PNNL-14838

Pacific Northwest
National Laboratory
Operated by Battelle for the
U.S. Department of Energy

2004 Initial Assessments for the T and TX-TY Tank Farms Field Investigation Report (FIR): Numerical Simulations

Z. F. Zhang
V. L. Freedman
S. R. Waichler

September 2004

Prepared for the U.S. Department of Energy
under Contract DE-AC06-76RL01830

DISCLAIMER

PACIFIC NORTHWEST NATIONAL LABORATORY
operated by
BATTELLE
for the
UNITED STATES DEPARTMENT OF ENERGY
under Contract DE-AC05-76RL01830

Printed in the United States of America

Available to DOE and DOE contractors from
the Office of Scientific and Technical Information,
P.O. Box 62, Oak Ridge, TN 37831-0062
www.osti.gov
ph: (865) 576-8401
fox: (865) 576-5728
email: reports@osti.gov

Available to the public from the National Technical Information Service
5301 Shawnee Rd., Alexandria, VA 22312
ph: (800) 553-NTIS (6847)
or (703) 605-6000
email: info@ntis.gov
Online ordering: http://www.ntis.gov

PNNL-14838

2004 Initial Assessments for the T and TX-TY Tank Farms Field Investigation Report (FIR): Numerical Simulations

Z. F. Zhang
V. L. Freedman
S. R. Waichler

September 2004

Prepared for
the U.S. Department of Energy
under Contract DE-AC06-76RL01830

Pacific Northwest National Laboratory
Richland, WA 99352

Summary

In support of CH2M HILL Hanford Group, Inc.'s (CHG) preparation of a Field Investigative Report (FIR) for the Hanford Site Single-Shell Tank Waste Management Area (WMA) T and TX-TY, a suite of numerical simulations of flow and solute transport was executed using the STOMP code to predict the performance of surface barriers for reducing long-term risks from potential groundwater contamination at the T and TX-TY WMA. The scope and parametric data for these simulations were defined by a modeling data package provided by CHG. This report documents the simulations involving 2-D cross sections through the T Tank Farm (T-106, T-105, and T-104) and the TX-TY Tank Farms (TX-105, TX-106, TX-107, and TX-108). Eight cases were carried out for the cross sections to simulate the effects of interim barrier, waterline leak, inventory distribution, and surface recharge on water flow and the transport of long-lived radionuclides (i.e., technecium-99 and uranium) and chemicals (i.e., nitrate and chromium). Fluid flow within the vadose zone is described by Richards' equation, whereas the contaminant transport is described by the conventional advective-dispersive transport equation with an equilibrium linear sorption coefficient (K_d) formulation.

For simulations with barriers, it was assumed that an interim barrier is in place by the year 2010. It was also assumed that, for all simulations, as part of tank farm closure, a closure barrier was in place by the year 2040. Placing a barrier is expected to significantly reduce infiltration of meteoric water and therefore arrival of contaminants at the water table. The modeling considers the estimated inventories of contaminants within the vadose zone and calculates the associated risk. It assumes that no tanks will leak in the future. Initial conditions for pressure head (and moisture) are established by allowing the vadose zone to equilibrate with an infiltration rate representative of natural infiltration for tank farm conditions. The data on infiltration rates with and without barriers are included in the discussion. Initial conditions for contaminant concentration are provided as part of inventory estimates for uranium, technetium-99, nitrate, and chromium. For moisture flow modeling, Neumann boundary conditions are prescribed at the surface with the flux equal to the recharge rate estimate. For transport modeling, a zero flux boundary is prescribed at the surface for uranium, technetium-99, nitrate, and chromium. The western and eastern boundaries are assigned no-flux boundaries for both flow and transport. The water table boundary is prescribed by water table elevations and the unconfined aquifer hydraulic gradient. No-flux boundaries are used for the lower boundary. Numerical results were obtained for compliance at the WMA boundary, 200 Areas boundary, exclusion boundary beyond the 200 Areas, and the Columbia River (DOE-RL 2000). Streamtube/analytical models were used to route computed contaminant concentrations at the water table to the downstream compliance points.

After the interim barrier was applied at 2010, saturation results indicate the soil desaturates gradually. The difference in saturation of the soil with and without the interim barrier was the largest at 2040, the time the closure barrier was applied. After this, the difference in saturation in the two cases became smaller with time. Generally, the solutes broke though faster if there was a waterline leak. A relatively small five-day leak (Case 4) had little effect on the peak concentration, while a large 20-yr leak (Case 3) increased the peak concentration significantly and reduced the solute travel in the vadose zone. The distribution of the inventory, either uniform or nonuniform, has little effect on peak arrival time; the peak concentrations of the conservative solutes varied by -6.9 to 0.2% for the T tank farm and by 11 to 49.4% for the TX tank farm. The reduction of the meteoric recharge before the barrier was applied led to less soil saturation, as expected, and thus longer solute travel time in the vadose zone and smaller peak

fenceline concentration. The effect on soil saturation lasted for about another 50 years after the barrier was applied at 2050. However, the reduced recharge rate affected the breakthough curve through the end of the simulation. The fenceline concentrations at the year 3000 were always higher for cases with reduced natural recharge than for those of the base case, which indicates that the fundamental impact of the reduced natural recharge is a smoothing of the breakthrough concentrations (lower peak concentration but higher tail concentration) at the compliance points.

Acronyms

ARH	Atlantic Richfield Hanford Comp
ASCII	American Standard Code for Information Interchange
bgs	below ground surface
BMI	Battelle Memorial Institute
BTCs	Break Through Curves
CA	Composite Analysis
CFEST	Coupled Fluid, Energy, and Solute Transport
CHG	CH2M HILL Hanford Group, Inc.
CR	Configuration report
DOE	U.S. Department of Energy
FIR	Field Investigation Report
GIS	Geographic Information System
IA	initial assessment
ICM	interim corrective measures
ILAW	Immobilized Low-Activity Waste
MDP	Modeling Data Package
NUREG	U.S. Nuclear Regulatory Commission regulation / Nuclear Regulatory Guide
ORP	Office of River Protection, U.S. Department of Energy
PNNL	Pacific Northwest National Laboratory
PNWD	Pacific Northwest Division
RCRA	Resource Conservation and Recovery Act
RPP	River Protection Project
SGM	Site-Wide Groundwater Model
SPLIB	A Library of Iterative Methods for Sparse Linear Systems
SST	Single-Shell Tank
STOMP	A flow simulator for **S**ubsurface **T**ransport **O**ver **M**ultiple **P**hases
TPA	The Tri-Party Agreement
WHC	Westinghouse Hanford Company
WMA	Waste Management Area

Table of Contents

Figures

Tables

1.0 Introduction

The U.S. Department of Energy (DOE) is charged with the cleanup of sites where the subsurface environment has been contaminated with dangerous constituents. Included among these sites are four of the seven Hanford Site Single-Shell Tank (SST) Waste Management Areas (WMAs) referred to as S-SX, B-BX-BY, T and TX-TY. In keeping with its charge, DOE has initiated a corrective action program that addresses the effects of previous and potential future leaks and releases of wastes from tanks at these four WMAs on the vadose zone environment. The Tank Farm Vadose Zone Project, a component of DOE's overall corrective action program, has begun a series of field investigations at the T and TX-TY WMA, which were called for by the Hanford Tri-Party Agreement (TPA M-45-98-03). By January 2005, the DOE Office of River Protection (ORP) is required to submit to the Washington State Department of Ecology (proposed TPA Milestone M-45-55-T03) a field investigation report (FIR) for WMAs T and TX-TY. As part of the FIR, interim corrective measures (ICMs) such as surface cover or barrier will be evaluated for their effects in reducing long-term risk from potential groundwater contamination at the T and TX-TY tank farms. Such an evaluation will be performed using numerical simulations. The specific objectives for FIR modeling are to 1) quantify the effects posed by past tank releases to the groundwater if no ICMs are implemented and 2) quantify the impacts for scenarios involving implementation of selected ICMs. Included in this report will be consideration of ICMs such as surface covers or barriers (Haass 1999). These considerations shall investigate, through numerical simulation, the performance of proposed ICMs with respect to their effectiveness in reducing long-term risks from potential groundwater contamination at the T and TX-TY WMA.

A series of numerical simulations was conducted to evaluate the performance of ICMs such as surface barriers for reducing long-term human health risks from potential groundwater contamination at the T and TX-TY WMA. The specific objectives of the numerical assessment were to quantify the risks posed by past tank releases if no ICMs were implemented and to determine the degree to which implementation of selected ICMs will decrease the risks posed by past tank releases. The assessments of this investigation specifically focus on the impacts to groundwater resources (i.e., the concentration of contaminants in the groundwater) and long-term risk to human health associated with groundwater use. The evaluations consider the current extent of contamination within the vadose zone, movement of contaminants through the vadose zone to the groundwater, and movement of contaminants through the groundwater to points of compliance. By providing quantitative comparisons between ICM concepts, the results from this evaluation may impact current operations or future decisions regarding the retrieval of tank waste and closure of the T and TX-TY WMA.

This report documents the initial investigations performed via numerical simulation of contaminant migration beneath the T and TX-TY WMA and the calculation of associated risks at point(s) of compliance. The scope and data required to perform these numerical simulations are documented in the modeling data package (MDP) (Khaleel et al. 2004) provided by CH2M HILL Hanford Group, Inc. (CHG). The numerical simulations reported herein were executed with the Subsurface Transport Over Multiple Phases (STOMP) simulator (White and Oostrom 2004) and consider the distribution of contaminants presently in the vadose zone, the migration of those contaminants to the groundwater under the influence of surface barriers, the further migration of contaminants through the groundwater to the point(s) of compliance, and the types of human activities at the point(s) of compliance. As specified by the MDP, four contaminant species (Tc-99, U-238, NO_3, and Cr), representing the range of mobile and

immobile constituents, were considered in these migration and risk analyses. All of the simulations reported were executed on two-dimensional (2-D) grids that represented cross sections traversing three SSTs within the T WMA (T-106, T-105, and T-104)[(a)] and four SSTs in the TX-TY WMA (TX-105, TX-106, TX-107, and TX-108). Initial contaminant inventories were developed for each cross section in accordance with the MDP. Grid resolutions for all simulations were 0.5 m both horizontally and vertically. All simulations were executed assuming isothermal conditions but with pressure-dependent liquid density. The vadose zone was modeled as an aqueous-gas porous media system where transport through the gas phase was neglected. All simulations used the infinite dilution assumption for coupling fluid flow and contaminant transport.

The principal objectives for these investigations were to execute the simulations specified in the MDP using proven, scientifically based, computational software and to report the generated results. To promote an open exchange of scientific knowledge and ideas, the software used to generate the reported results and a readable source code will be made available, upon request, to the U.S. government and its contractors. To ensure the capability to repeat these simulations in the future, the source coding, input files, and output files have been stored in electronic form and will also be made available to the government and its contractors. Although Battelle – Pacific Northwest Division maintains the copyright on the STOMP simulator, the government retains a paid-up, nonexclusive, irrevocable worldwide license to reproduce, prepare derivative works, perform and display publicly by or for the government, including the right to distribute to other government contractors. Numerical simulation of contaminant migration through the vadose zone and unconfined aquifer beneath the T and TX-TY WMA required converting information in the MDP into electronic input that could be interpreted by the STOMP simulator, executing the software, and translating the simulation output into graphical form for reporting. This report documents these three steps and summarizes the simulation results for each of the 16 cases executed.

Inventory estimates were considered a critical parameter of these analyses, and uncertainties in the initial inventory were considered. Jones (2000) provides details on inventory estimates for chemicals and radionuclides lost to the vadose zone in the T and TX-TY WMAs. Khaleel et al. (2004, Table 5-1) summarizes the inventory data for the selected cross sections. The data in their Table 5-1 for the four species (i.e., Tc-99, U-238, NO_3, and Cr) are distributed within the vadose zone based on information collected from boreholes near Tanks T-106, TX-104, TX-105 and TX-107. Because data analysis for the recently drilled boreholes near Tank T-106 is incomplete at this time, inventory for the cross section containing Tank T-106 is distributed based on the 1993 borehole concentration data for the three species (Freeman-Pollard 1994).

A principal assumption of the investigation is that no additional contaminant releases will occur in the future, and that waterline leaks from the existing piping in the T and TX-TY WMA have been addressed and resolved. Two simulation cases, however, did consider waterline leaks in the vicinity of Tanks T-104 and TX-105.

For simulations that considered surface barriers, it was assumed that interim barriers became effective in the year 2010 and closure barriers in the year 2040. Surface barriers were expected to significantly reduce the infiltration of meteoric water and delay the arrival of contaminants at the water table. The

(a) The names (numbers) of all Hanford underground storage tanks begin with the prefix 241-. In this report, as in common usage, the prefix has been omitted.

curved surface of the tank dome, impermeable tank wall, and water shedding by these surfaces were modeled in these simulations. Because of water shedding, soils between tank surfaces were predicted to have higher water contents than the sediments located outside the tank region. The sedimentary soils were assumed to have moisture-dependent anisotropy, where the ratio of horizontal to vertical relative permeability was defined to be a function of the soil saturation.

Two-dimensional cross sections were used to simulate fluid flow and contaminant transport through the vadose zone and groundwater. Two representations of west-east cross sections through the T and TX-TY tank farm were considered: 1) cross section through Tanks T-104, -105, and -106 and 2) cross section through Tanks TX-105, -106, -107, and -108.

Each transient simulation was preceded by a steady flow simulation to establish initial conditions. Steady flow conditions were established using a constant surface recharge of meteoric water and fixing the water table gradient across the cross section. No solute transport was considered during the steady flow simulations. Transient simulations involved both fluid flow and solute transport. The fluid flow transient started with the steady flow condition flow field and responded to changes in meteoric recharge caused by barrier emplacements. Two simulations additionally considered waterline leaks. The water table hydraulic gradient remained fixed throughout the transient simulation. The transient solute transport simulations conducted for each cross section generated a breakthrough curve (BTC) (a plot of dissolved solute concentration versus time) at the eastern boundaries (groundwater outflow region) of the T and TX-TY WMA. The temporal and spatial distributions of the BTCs by cross section were recognized, and the principle of superposition was used to generate a composite BTC across the T and TX-TY WMA compliance boundary. An analytical streamline approach was used to translate the BTCs from the T and TX-TY WMA boundary compliance points to the three remote compliance points. Solute concentrations at the compliance points were converted into dose estimates using conversion factors.

Fluid flow within the vadose zone was described using the Richard's equation, whereas contaminant transport was described using the conventional advective-dispersive transport equation with an equilibrium linear sorption coefficient formulation (i.e., K_d formulation). Stratigraphic information for the two representative cross sections was based on studies by Wood et al. (2001) and Price and Fecht (1976a, b). These cross sections include dipping strata, and, when combined with the Polmann model (Polmann 1990) for anisotropy in relative permeability for unsaturated soils, allow the simulator to model the enhanced spreading at the fine- to coarse-grained interfaces and the increased downslope movement of water along these interfaces.

Modeling parameters used to describe soil-moisture retention, phase relative permeability, saturated hydraulic conductivity (intrinsic permeability), and bulk density (porosity), for individual stratum were based on data collected from 200 Area soils (Khaleel et al. 2000). For each stratum (soil type) defined on the cross-section stratigraphy, the small-scale laboratory measurements were scaled spatially upward to obtain equivalent horizontal and vertical unsaturated hydraulic conductivities as a function of mean tension (Khaleel et al. 2000). This scaling technique yields a mathematical expression describing macroscopic anisotropy in the unsaturated hydraulic conductivity as a function of mean tension for each stratum. Arithmetic averaging of van Genuchten parameters (van Genuchten 1980) was used to define the soil-moisture retention function for each stratum. Where multiple soil samples were unavailable for a given stratum, data were used from soil samples taken from the same stratum but from sites near the T and TX-TY WMA. Hydraulic properties were determined from laboratory-measurements of both soil-

moisture retention and unsaturated hydraulic conductivity when available. This approach avoided extrapolating unsaturated hydraulic conductivities (van Genuchten 1980; Mualem 1976) to dry conditions, based on a saturated conductivity estimate (Khaleel et al. 1995). To reflect field conditions, laboratory data additionally were corrected for the presence of any gravel fraction in the sediment samples (Khaleel and Relyea 1997).

In keeping with the approach taken for modeling fluid flow, solute transport properties for bulk density, diffusivity, and dispersivity were specified for each stratum. Contaminant mobility was defined through an equilibrium linear sorption coefficient which was specified uniquely for each combination of solute and stratum. There is little doubt that the linear sorption coefficient (i.e., K_d) for Tc-99 is close to zero mL/g in Hanford sediments. This low K_d, coupled with its long half-life (2.03×10^5 yr), allows Tc-99 to migrate long distances in both the vadose zone and groundwater, posing a threat to groundwater quality for a long time.

Initial conditions for soil-moisture (expressed in terms of capillary pressure) and solute concentration were needed to initiate these transient flow and transport simulations. Initial soil-moisture was established through steady flow simulations. Steady flow simulations are pseudo-transient simulations that proceed from some soil-moisture distribution with constant boundary conditions until steady flow conditions are reached. In establishing the steady flow soil moisture profiles, constant recharge was used as the boundary condition along the ground surface, and a constant west-to-east hydraulic gradient was imposed for the groundwater. Vertical surfaces above the capillary fringe were considered zero-flux boundaries. Initial conditions for solute concentrations were based on contaminant concentrations and integrals of the inventory estimates for Tc-99, U-238, NO_3 and Cr (Khaleel et al. 2004) and the uniform and the nonuniform distribution models.

As noted above, 2-D west-to-east cross sections through the T and TX-TY WMA were used for modeling fluid flow and solute transport. The simulation domain extended horizontally to include the WMA boundaries and vertically from the ground surface to roughly 5 m below the water table, at a depth of about 85 m below ground surface. The geologic strata were assumed to be continuous across the cross sections but not of constant thickness.

.

2.0 Case Descriptions

The flow and solute transport simulations executed were specified in the MDP (Khaleel et al. 2004). This suite of simulations investigates the need for interim corrective measures (e.g., surface barriers) and the sensitivity of solute transport on waterline leaks, uniform and nonuniform distribution of initial concentration, and variation of surface recharge. Two-dimensional cross sections, representing east-west transects through the T and TX-TY tank farms, were used for the computational domains in all the cases. All the cases except Case 5 considered a spatially uniform inventory distribution of the contaminant inventory data in the MDP; Case 5 considered a nonuniform distribution. Cases 3 and 4 considered different volumes for waterline leaks, whereas Cases 6 through 8 considered varying estimates of natural recharge. Simulations were executed for a period of compliance of 1000 years. Each case involved the simulation of transient fluid flow and solute transport on two cross sections (T-106, -105, -104 and TX-105, -106, -107, -108).

- **Case 1: Base Case, No-Action Alternative.** Flow and transport runs for the two T-TY-TX cross sections (noted above) considering natural infiltration *only*, *no* waterline leak, *no* interim barrier, a closure barrier by the year 2040, and a uniform inventory distribution.
- **Case 2: Barrier Alternative and No Waterline Leak.** Flow and transport runs for the two T-TY-TX cross sections considering placement of an interim barrier by 2010; a closure barrier by 2040 (i.e., the interim barrier replaced by the closure barrier); no waterline leak, and a uniform inventory distribution.
- **Case 3: No Barrier and Waterline Leak of 1 gpm for 20 years.** Flow and transport runs for the two T-TY-TX cross sections considering natural infiltration, waterline leak (1 gpm for 20 yr starting 1/1/2000) for Tanks T-104 or TX-105 only, no interim barrier until closure, and a uniform inventory distribution.
- **Case 4: No Barrier and 200,000 gal Waterline Leak.** Flow and transport runs for the two T-TY-TX cross sections considering natural infiltration (100 mm/yr), waterline leak (200,000 gal in five days starting on 1/1/2000) for Tank T-104 or TX-105 only, no interim barrier until closure, and a uniform inventory distribution.
- **Case 5: Nonuniform Inventory Distribution and No Barrier.** Flow and transport runs for the two T-TY-TX cross sections considering natural infiltration only; no waterline leak; *no* barrier until closure; and a higher distribution of inventory at a few locations (e.g., a few nodes, with a high concentration, either at the same depth or at different depths).
- **Case 6: Base Case with 50 mm/yr Meteoric Recharge.** Flow and transport runs for the two T-TY-TX cross sections considering natural infiltration (50 mm/yr) only, no waterline leak, no interim barrier, a closure barrier by the year 2040, and a uniform inventory distribution.
- **Case 7: Base Case with 30 mm/yr Meteoric Recharge.** Flow and transport runs for the two T-TY-TX cross sections considering natural infiltration (30 mm/yr) only, no waterline leak, no interim barrier, a closure barrier by the year 2040, and a uniform inventory distribution.
- **Case 8: Base Case with 10 mm/yr Meteoric Recharge.** Flow and transport runs for the two T-TY-TX cross sections considering natural infiltration (10 mm/yr) only, no waterline leak, no interim barrier, a closure barrier by the year 2040, and a uniform inventory distribution.

3.0 Technical Approach

A multistep approach was used to execute the simulations described in the MDP (Khaleel et al. 2004). The approach involved converting information in the data package to a suite of input files, executing the STOMP (White and Oostrom 2004) simulator, translating the simulation results into graphical form, extrapolating solute concentrations at the modeling domain boundary to the compliance points, and computing doses at the compliance points from the extrapolated solute concentrations. This section provides first an overview and then more extensive review of these steps.

3.1 Overview

Three types of input files define a STOMP simulation: 1) a simulation control and material definition file, 2) a soil zonation file, and 3) an inventory file for each solute species. Modeling input data stored in these files were developed from the MDP in conjunction with the discretization of the physical domain. Physical domains were east-west 2-D cross sections of the T and TX-TY WMA. The physical domain was discretized using a Cartesian grid with uniform horizontal and vertical spacing of 0.5 m.

Graphical representations of geology interpretations and engineered structures in the T and TX-TY WMA were converted to zonation maps based on the Cartesian discretization of the physical domain. Tabular data describing the initial distribution of the four contaminants of concern (Tc-99, U-238, NO_3, and Cr) were interpolated onto the computational domain with two types of assumed solute distributions, that is, the uniform and nonuniform distribution, as described in Section 3.3.3.2. Hydrologic property, as defined in the MDP, for each of the five identified soils types and the transport property data for the four contaminants and five soil-type combinations were converted to input in the form of STOMP input cards. The conceptual model was then completed by converting boundary conditions and sources as specified in the MDP into STOMP input cards, specifying execution controls and requesting output data.

Time-varying surface recharge and waterline leaks required a transient flow simulation to be executed with the solute transport calculations. The initial condition of the simulations was achieved by a steady-state simulation that did not involve solute and under a constant recharge rate. The steady flow conditions represented the soil-water regime at preconstruction. The same approach was applied to both the T and TX cross sections. The same steady-state flow condition was applied to each of the eight cases associated with the corresponding cross section at the T or TX farm. The transient flow and transport simulations were then initiated using the steady flow solution. Both the steady flow and transient simulations were executed on workstations operating under Linux. For compatibility between platforms, the input, zonation, and inventory files were maintained as ASCII-formatted files.

Simulation results were written to three types of output files: 1) a file named '*output*' that reflected input and reference note information, 2) a series of *plot* files, and 3) a series of *surface-flux* files with user-given names. The '*output*' file contains a translation of the '*input*' file(s) as interpreted by the simulator (e.g., with unit conversions) and a time sequence of the simulation history and chosen variables (aqueous pressure, aqueous moisture content, solute concentrations, Darcy fluxes) at selected grid locations. *Plot* files contain variable data for all grid points at selected simulation times. These files are

used to generate color-scaled plots and animations through Tecplot,[(a)] a utility program used to translate STOMP plot files into Tecplot formatted input files. *Surface-flux* files contain rate and integral information about fluxes crossing user-defined internal or external boundaries. Solute fluxes and aqueous fluxes at the downgradient domain boundary, within the groundwater, are used to calculate average solute concentrations. Surface-flux files were also used to generate rate and integral plots of solutes entering the groundwater and exiting the computational domain. A utility program, *Surfcalc*, was used to translate STOMP surface-flux files into formatted input files suitable for plotting.

Solute BTCs, or solute concentrations as a function of time, for the aquifer at the compliance points outside the T or TX tank farm were computed by extrapolating solute concentrations exiting the STOMP computational domain. An analytical solution to the advection-dispersion equation for solute transport through a saturated porous media in three dimensions was used, following the approach described by Baetsle (1969) and documented in Domenico and Schwartz (1990). This approach assumed that the solute originated at a point source as a series of slugs released over time. The method of superposition was used to integrate the slug releases. The solute mass from each slug migrated from a point source, which was at the fenceline, by advective-dispersive transport in a steady, uniform flow field. As the solute mass was transported advectively with the flow, it spread longitudinally and transversely via hydrodynamic dispersion and molecular diffusion. The solute flux used as input was computed from the STOMP surface file output for mass flux exiting the 15-m-thick aquifer at the east side of the domain. Aquifer recharge along the groundwater flow path was neglected in translating solute concentrations to the compliance points.

3.2 Modeling Data Package

Meteoric recharge and parameters for vadose zone flow and transport were provided in the MDP. Selected data are repeated in this section.

3.2.1 Recharge Estimates

T and TX-TY tank farm surfaces are covered with gravel to prevent vegetative growth and provide radiation shielding for Site workers. Bare gravel surfaces, however, enhance net infiltration of meteoric water relative to undisturbed, naturally vegetated surfaces. Between-tank infiltration is further enhanced by the effect of recharge water being diverted by the impermeable sloping surface of the tank domes. Recharge estimates used in this investigation are shown in Table 3.1.

Table 3.1. Time Estimates for Interim and Closure Barriers at the T and TX-TY Tank Farms and Corresponding Recharge Estimates

Condition Simulated	Recharge Estimate (mm/yr)
No barrier [2000-2010]	100
Interim barrier [2010-2040]	0.5
Closure barrier [2040-2540]	0.1
Degraded closure barrier [2540-3000]	3.5

(a) Tecplot, Version 10.0, Amtec Engineering, Inc., Bellevue, WA.

3.2.2 Vadose Zone Flow and Transport Properties

Upscaled values of parameters for fluid flow and solute transport for the vadose zone were used in these investigations. Details for computing upscaled parameters are provided in Khaleel et al. (2004). Fluid flow parameters for the vadose zone include soil moisture retention characteristics and saturated hydraulic conductivity. Solute transport parameters include bulk density, diffusivity, sorption coefficients, and macrodispersivity. Table 3.2 lists the composite, fitted van Genuchten-Mualem (van Genuchten 1980; van Genuchten et al. 1991) parameters for various strata at the T and TX-TY tank farms. Note that the material type numbers are identical to those indicated in the MDP (Khaleel et al. 2004, Appendix B).

Table 3.2. Composite van Genuchten-Mualem Parameters for Various Strata at the T and TX-TY Tank Farms

Strata/Material Type	Number of Samples	θ_s	θ_r	α (1/cm)	n	l	K_s (cm/s)
Backfill (1)	10	0.1380	0.0100	0.0210	1.3740	0.5	5.60×10^{-4}
Sand (2)	12	0.3819	0.0443	0.1170	1.6162	0.5	9.88×10^{-5}
Gravelly Sand (3)	11	0.2126	0.0032	0.0141	1.3730	0.5	2.62×10^{-4}
Plio-Pleistocene (4)	4	0.4349	0.0665	0.0085	1.8512	0.5	2.40×10^{-4}
Sandy Gravel (5)	10	0.1380	0.0100	0.0210	1.3740	0.5	5.60×10^{-4}

3.2.3 Stochastic Model for Macroscopic Anisotropy

Variable tension-dependent anisotropy provides a framework for upscaling small-scale, laboratory-measured hydraulic properties to the effective (i.e., upscaled) properties for the large-scale tank farm vadose zone. A stochastic model (Polmann 1990) was used to evaluate tension-dependent anisotropy for sediments at the T and TX-TY WMA; details are in Khaleel et al. (2004, Appendix C). The following is a brief description of the variable anisotropy model used in this investigation.

Yeh et al. (1985) analyzed steady unsaturated flow through heterogeneous porous media using a stochastic model; parameters such as the saturated hydraulic conductivity were treated as random variables rather than deterministic quantities. The Gardner (1958) relationship was used by Yeh et al. (1985) to describe unsaturated hydraulic conductivity as a function of saturated hydraulic conductivity and tension according to Equation (3.1):

$$K(\psi) = K_s \exp(-\beta\psi) \tag{3.1}$$

where K is the unsaturated hydraulic conductivity, K_s is the saturated hydraulic conductivity, ψ is the tension, and β is a fitting parameter. Equation (3.1) can be written as shown in Equation (3.2). This form is referred to as the log-linear model:

$$\ln K(\psi) = \ln K_s - \beta\psi \tag{3.2}$$

because the log of the hydraulic conductivity is linearly related to the tension through a constant slope, β. A constant slope, however, is often inadequate for describing lnK(ψ) over the range of tension of interest for field applications. As an alterative, β can be approximated locally by straight lines over a range of tensions. The $\ln K_s$ term can then be derived by extrapolating the local slopes to zero tension.

Using a linear correlation model between the zero-tension intercept and β, Polmann (1990) presented a generalized model that accounts for the cross-correlation of the local soil property (i.e., $\ln K_s$ and β) residual fluctuations. Compared with the uncorrelated $\ln K_s$ and β model, partial correlation of the properties was shown to have a significant effect on the magnitude of the effective parameters derived from the stochastic theory. The Polmann (1990) equations for deriving the effective parameters for stratified soils with infinite horizontal correlation length are shown in Equations (3.3) through (3.6):

$$\langle \mathrm{LnK} \rangle = \langle \mathrm{LnK_s} \rangle - A\langle \psi \rangle - \frac{\sigma^2_{\mathrm{LnKs}} \lambda \left[p - p^2 \langle \psi \rangle - \zeta^2 \langle \psi \rangle \right]}{(1 + A\lambda)} \tag{3.3}$$

$$\sigma^2_{\mathrm{LnK}} = \frac{\sigma^2_{\mathrm{LnKs}} \left[(1 - p\langle \psi \rangle)^2 + \zeta^2 \langle \psi \rangle^2 \right]}{(1 + A\lambda)} \tag{3.4}$$

$$K_h^{eq} = \exp\left[\langle \mathrm{LnK} \rangle + \frac{\sigma^2_{\mathrm{LnK}}}{2} \right] \tag{3.5}$$

$$K_v^{eq} = \exp\left[\langle \mathrm{LnK} \rangle - \frac{\sigma^2_{\mathrm{LnK}}}{2} \right] \tag{3.6}$$

where

σ^2_{LnK} = the variance of log unsaturated conductivity

$\langle \psi \rangle$ = the mean tension

σ^2_{LnKs} = the variance of $\ln K_s$

$\langle \mathrm{LnK_s} \rangle$ = the mean of $\ln K_s$

p = the slope of the β versus $\ln K_s$ regression line

$\zeta = \dfrac{\sigma_\delta}{\sigma_{LnKs}}$

σ_δ = the standard deviation of the residuals in the β versus $\ln K_s$ regression

A = the mean slope, β, for $\ln K_s$ versus ψ

λ = the vertical correlation length for $\ln K_s$

K_h^{eq} = the equivalent unsaturated horizontal hydraulic conductivity

K_v^{eq} = the equivalent unsaturated vertical hydraulic conductivity.

Macroscopic anisotropy parameter estimates for the strata at the T and TX-TY WMA are listed in Table 3.3. Details on the derivation of these parameter estimates are included in Khaleel et al. (2004, Appendix C).

Table 3.3. Macroscopic Anisotropy Parameters Based on the Polmann Equations for Strata at the T and TX-TY WMA

Strata/Material Type	Number of Samples	$\langle \mathrm{LnK_s} \rangle$	σ^2_{LnKs}	p	ζ	λ (cm)	A
Backfill (1)	10	-15.76	3.56	-1.1e-4	1.84e-4	30	0.00371
Sand (2)	12	-14.6	1.5	-7.2e-4	6.55e-4	50	0.00620
Gravelly Sand (3)	11	-14.85	1.94	-2.6e-4	2.50e-4	30	0.00368
Plio-Pleistocene (4)	4	-10.43	1.01	2.4e-3	9.34e-4	50	0.0104
Sandy Gravel (5)	10	-15.76	3.56	-1.1e-4	1.84e-4	30	0.00371

3.2.4 Bulk Density and Retardation Coefficient

Both bulk density (ρ_b) and retardation coefficient (K_d) estimates were needed to calculate retardation factors for different solute species. The effective large-scale estimate for the product $\rho_b K_d$ was considered to be the average of the product of small-scale laboratory measurements for bulk density and retardation coefficient (Gelhar 1993). Effective, large-scale estimates of bulk density, retardation coefficient, and their product for U-238 are listed in Table 3.4. The average ρ_b, $E[\rho_b]$ estimates were based on data in Khaleel et al. (2000). The retardation coefficients for the remaining solutes (Tc-99, NO_3, and Cr) were estimated to be zero. Calculations of $E[\rho_b]$ and $E[\rho_b K_d]$ include corrections for the gravel fraction.

Table 3.4. Effective Parameter Estimates for the Product of Bulk Density and Retardation Coefficient for U-238 at T and TX-TY WMA

Strata/Material	K_d (mL/g)	$E[\rho_b]$ (g/cm^3)	$E[\rho_b K_d]$ (-)
Backfill (1)	0.6	1.94	0.59
Sand (2)	0.6	1.76	1.04
Gravelly Sand (3)	0.6	2.07	1.24
Plio-Pleistocene (4)	0.6	1.65	0.98
Sandy Gravel (5)	0.6	1.94	0.59

3.2.5 Diffusivity

It was assumed that the effective, large-scale diffusion coefficients for all strata at the T and TX-TY WMA were a function of volumetric moisture content and could be expressed using the Millington and Quirk (1961) empirical relation, as shown in Equation (3.7):

$$D_e(\theta) = D_o \frac{\theta^{10/3}}{\theta_s^2} \tag{3.7}$$

where D_e is the effective diffusion coefficient of an ionic species, D_0 is the molecular diffusion coefficient for the specie in water, θ is the water content, and θ_s is the saturated water content. The molecular diffusion coefficient for all species in pore water was assumed to be 2.5×10^{-5} cm^2/s (Kincaid et al. 1995).

3.2.6 Macrodispersivity

An extended review is provided in Appendix C of Khaleel et al. (2004) on the rationale for vadose zone macrodispersivity estimates. Macrodispersivity estimates were needed for both reactive (U-238) and nonreactive (Tc-99, NO_3, and Cr) species. Macrodispersivity estimates for the nonreactive species are listed in Table 3.5.

Table 3.5. Nonreactive Macrodispersivity Estimates for Strata at T and TX-TY WMA

Strata/Material	A_L, cm	A_T, cm
Backfill (1)	~150	15
Sand (2)	~150	15
Gravelly Sand (3)	~100	10
Plio-Pleistocene (4)	~50	5
Sandy Gravel (5)	~150	15

The net effect of specie sorption is to retard migration through geologic media. Soil sorption is a function of the specie and soil properties and varies spatially with soil properties (Gelhar 1993; Talbott and Gelhar 1994). Stochastic analysis results for macrodispersivity enhancement for the five strata are presented in Appendix C of Khaleel et al. (2004) for the reactive species (U-238). In this analysis the unsaturated hydraulic conductivities were evaluated at a tension of 100 cm via the fitted van Genuchten-Mualem relation. The macrodispersivity enhancement ranged from 1.07 for backfill sediments to about 2.35 for Plio-Pleistocene sediments.

3.3 Input File Generation

Three types of input files were used to drive the STOMP simulator: 1) a simulation control file and material definition (input), 2) a soil zonation file (zonation), and 3) a series of initial solute inventory files (inventory). All input files were written and stored in ASCII text format. The simulation control and material definition input files were assembled using a conventional text editor, whereas the zonation and inventory files were generated with a utility program.

3.3.1 Input File

As described in the STOMP User's Guide (White and Oostrom 2004), the input file is divided into cards that group common data (e.g., solution control, hydraulic properties, output control, boundary conditions).

3.3.2 Zonation File

The zonation file is an ordered listing (i.e., I,J,K indexing) of integers that identify the rock/soil type for every grid cell in the computational domain. Inactive nodes are assigned an integer value of zero, and rock/soil types are assigned numbers in accordance with the ordered listing of rock/soil types in the Rock/Soil Zonation Card. For example, an integer value of 1 in the zonation file refers to backfill, and a value of 4 refers to Plio-Pleistocene. Color delineated images of the zonation files are shown in Figures 3.1 and 3.2 for the T and TX farm cross sections, respectively.

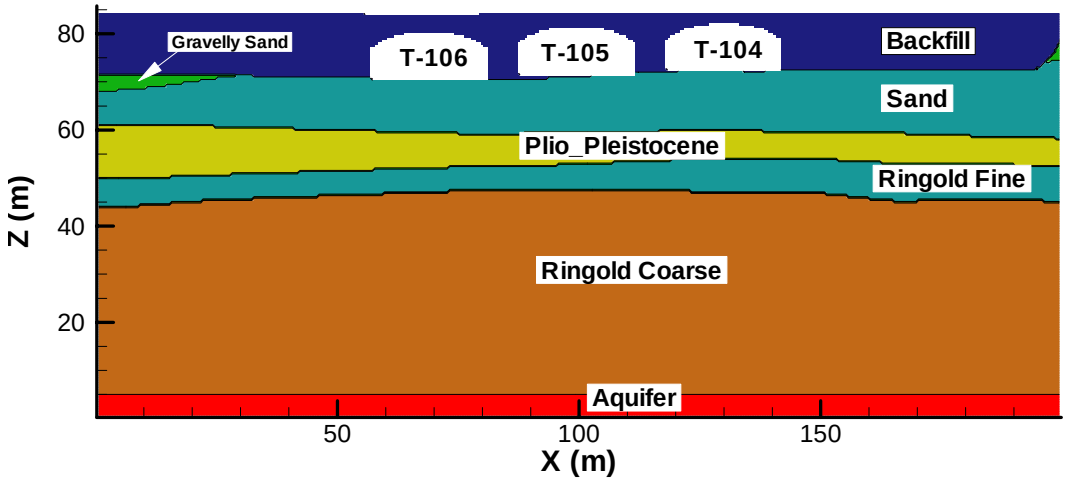

Figure 3.1. Rock/Soil Zonation for Cross Section Through T-104, T-105, and T-106

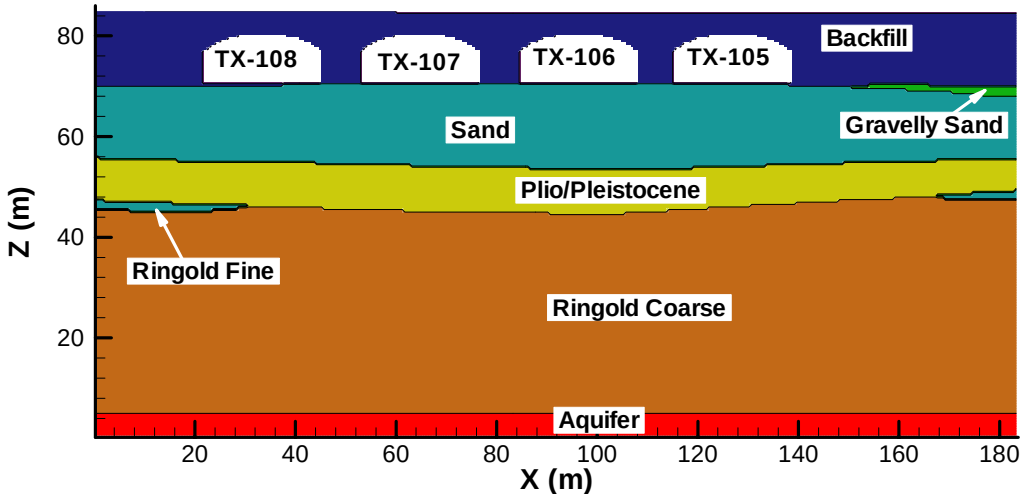

Figure 3.2. Rock/Soil Zonation for Cross section Through TX-105, TX-106, TX-107, and TX-108

3.3.3 Inventory File(s)

For both the T and TX-TY tank farms, the vadose zone inventory estimates of U-238, Tc-99, NO_3 and Cr were based on soil samples collected from boreholes located near Tanks T-101, T-103, T-106 and TX-107, as reported in Appendix D of the MDP. The MDP inventory values (concentration and total solute mass) are reported at discrete depths for each combination of tanks (e.g., T-106 and TX-107) and solute specie (Tc-99, U-238, NO_3, and Cr).

3.3.3.1 Node-centered discretization

Before translating to the computational grid, the discrete data were converted to contiguous binned data using *node-centered discretization* (each discrete depth was converted to a depth bin with the discrete depth centered in the depth bin). This discretization yielded depth bins that varied in height with elevation.

After converting those data reported as discrete depths to depth bins, the solute concentrations and inventory integrals were translated to the computational grid using an *overlapping approach* for each combination of tank and solute specie. The computational grids used vertical spacing of 0.5 m compared with the inventory depth bins that varied in height from 0.2 to 2.6 m. For these sets of dimensions, three domain overlapping conditions occurred: 1) computational grid totally within the inventory depth bin, 2) computational grid partially within the inventory depth bin, 3) depth bin totally within the computational grid. For the first two conditions, a fraction of the inventory in the depth bin was assigned to the grid horizon based on the fraction of overlap. For example, if a 0.5 m grid cell was completely enclosed by a 1.0 m depth bin, 50% of the mass within this depth bin would be in the grid horizon. For the third condition the entire inventory integral for the depth bin would be in the grid horizon. The overlapping approach distributes the inventory vertically across the computational domain according to the MDP and exactly preserves the total inventory for each tank and specie combination.

3.3.3.2 Inventory distributions

To determine the inventory profiles, two inventory distributions were used during these investigations: *uniform distribution* (also called variable-diameter distribution) and *nonuniform distribution* (also called fixed-diameter distribution) (Figure 3.3). The uniform distribution (Figure 3.3a) comprised a series of concentric stacked disks with varying solute concentration and diameters with depth; the solute concentration within each disk equaled the value in the MDP, and the disk diameter was sized so that the total inventory is the same as that in the MDP. The nonuniform distribution (Figure 3.3b) comprised a series of concentric stacked disks of equal diameter. This distribution honored the total solute mass reported in the MDP for the depth but altered the concentration according to the disk diameter.

For a 2-D simulation using uniform or nonuniform distribution, the cylinder-shaped volume (Figure 3.4a) was converted to a slice of unit thickness (Figure 3.4b) and width equal to the diameter of the cross section of cylinder d. The inventory I was then uniformly assigned to the slice. We assumed that the inventory was uniformly distributed in a cylinder-shape volume (Figure 3.4a). For the uniform inventory horizontal distribution, the diameter of the cross-sectional area of the i^{th} horizon is determined by:

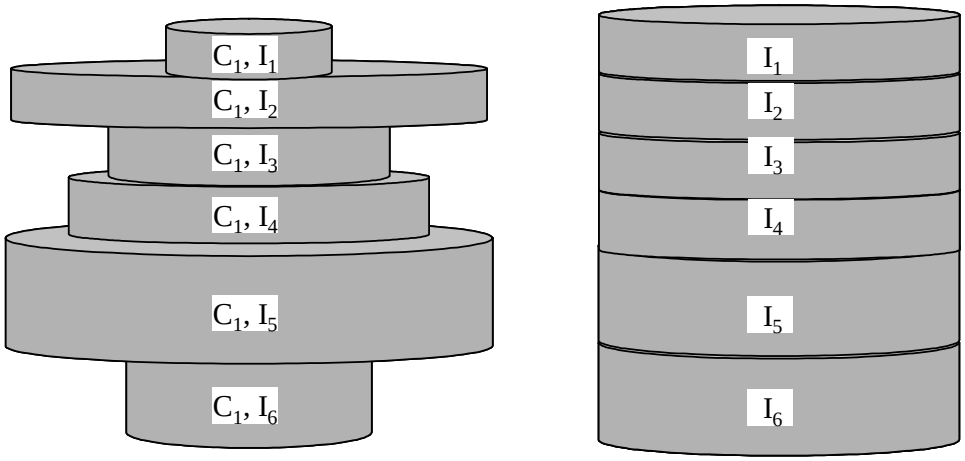

(a) Uniform (variable-diameter) distribution

(b) Nonuniform (fixed-diameter) distribution

Figure 3.3. Uniform and Nonuniform Distributions of Inventory

$$d_i = 2\left(\frac{I_i}{\pi C_{si} L_i \rho_{b_i}}\right)^{1/2} \tag{3.8}$$

where I is the total inventory (Ci or μg) and ρ_b is the average soil bulk density (kg/m^3). If the calculated cylinder diameter is larger than the simulation domain, the smaller value of the horizontal domain size was assigned as the diameter of the cylinder, and the concentration with this cylinder was scaled up to match its size.

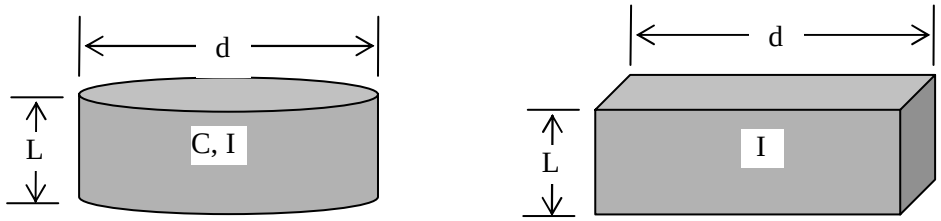

(a) (b)

Figure 3.4. Converting (a) a 3-D Volumetric Inventory to (b) an Inventory of a 2-D Slice

For the fixed-diameter inventory horizontal distribution, the diameters of the cross-sectional area for all layers were the same (see Figure 3.3b). The concentration within the ith cylinder was computed by

$$C_{si} = \frac{4I_i}{\pi d^2 L_i \rho_{b_i}} \tag{3.9}$$

where C_s is the inventory concentration per unit mass of soil (Ci/kg or μg/kg soil).

3.3.3.3 Inventory aqueous concentration

Specie inventories provided in the MDP were expressed in soil concentration, C_s (μg/g soil, pCi/g soil). These concentrations were converted to aqueous phase concentrations, C_a, based on soil bulk density (i.e., from grain density and porosity) and the initial saturation:

$$C_a = \frac{C_s \rho_s (1 - n_t) \kappa_a}{s n_d} \tag{3.10}$$

where ρ_s is the soil grain density, n_t is the total porosity, n_d is the diffusive porosity, s is the aqueous-phase saturation, and κ is the equilibrium fraction of solute in the aqueous phase.

3.3.3.4 Inventory files

Inventory files were used to initialize the solute concentrations across the computational domain. These files contain ordered listings (using I, J, K indexing) of initial solute inventory for every grid cell in the computational domain. A unique inventory file was developed for each combination of solute specie, cross section, and initial inventory distribution. Inventory file names were made of three parts connected by underscores. The first part is either *un* or *nu*, representing the uniform or nonuniform distribution, respectively; the middle part is the name of the specie; and the last part is either *t* or *tx* representing the T or TX farms. For example, the initial concentration for Tc-99 for the Case 1 simulation (uniform distribution) for the cross section of the TX farm is contained in the file "*un_tc99_tx*."

A utility program called *InvSTOMP* was used to convert tabulated values of contaminant concentrations and integrals, as reported in the MDP, into inventory files. *InvSTOMP* read an input file that contained a description of the computational domain (formatted as a STOMP grid card), the distribution of rock/soil types (formatted as a STOMP Rock/Soil zonation card) and the distribution of solute concentration and integrated inventory. The utility then used these data to compute solute distributions in one of two ways: uniform distribution (variable-diameter) and nonuniform distribution (fixed diameter). The distribution of each solute will be shown in Section 4.

3.3.3.5 Implementation features

In the FY 2000 initial assessments for S-SX FIR (White et al. 2001), the STOMP simulator was modified to extend its capabilities for modeling solute concentration dependent density and viscosity, saturation dependent anisotropy, enhanced macrodispersivity, and specialized Courant number control.

The reported simulations were executed on two workstations operating under LINUX system. All executables, however, were generated from a single source code that is readable and available in electronic form (Section 6). Executing the simulator required two steps: 1) compiling the source coding with a *parameters* definition file and 2) executing the compiled code on a workstation or personal computer. The executable forms of the STOMP simulator for these investigations were generated using the default level of optimization for each compiler. STOMP was coded following ASCII Fortran 77 protocols and yielded no warning or error messages during compilation. The size of the computational domains, 40,000 to 100,000 nodes, necessitates using a conjugate gradient linear system solver with a

compact storage scheme for the Jacobian matrix. The STOMP simulator uses the SPLIB solver (Bramley and Wang 1995) for sparse linear systems for solutions implementing conjugate gradient solvers. The SPLIB solver is a collection of libraries that must be assembled on the executing computer and linked to the STOMP simulator during compilation. The SPLIB files and instructions necessary to complete the compilation and execution of the STOMP simulator will be available in electronic form (Section 6).

3.3.3.6 Result translation

For these investigations, the STOMP simulator reads in a series of input files and generates an output file, surface-flux file, and a series of plot files. As described previously, the STOMP output file contains reflected data from the input files, simulation progression information, and reference-node output. The output files were only used for verification and simulation tracking. No reported data were derived from the output files, but these result files will be available in electronic form (Section 6).

Surface-flux surfaces were defined for the downgradient, vertical boundary in the unconfined aquifer, which represented the fenceline. The surface-flux output for this surface includes the aqueous volumetric flux rate and integral and the solute flux rate and integral crossing the surface (i.e., exiting the computational domain through the unconfined aquifer). Surface flux files are located in the simulation case directories (Section 6). Surface flux output was converted to BTCs at the WMA boundary compliance point and provided input to the streamtube model.

The results of the 2-D simulations executed in this investigation were converted into the values of three-dimensional (3-D) simulations by considering the dimensional scaling factor and the inventory scaling factor.

3.3.4 Two-Dimensional Cross-Section Concentrations

Cross-section concentrations, C_{2d} (pCi /L or μg/L), were initially calculated from the mass fluxes by the following equation:

$$C_{2d} = \frac{J_s}{J_w} \tag{3.11}$$

where J_s is the solute mass flux (pCi /yr or μg/yr), and J_w is the water mass flux (L/yr). These concentrations were later scaled to match the total inventory estimate. The equation to calculate the total mass flux is outlined in Section 3.5.3.

3.3.5 Inventory Scaling Factor

For both the T and TX farm the cross sections, the initial lateral extent of all the concentration profiles were explicitly in the uniform or nonuniform distribution. Integrating the vertical concentration data over the total volume of the 2-D slice yielded a fixed inventory for the 0.5-m-thick cross section. This calculated 2-D inventory was expanded to a 3-D volume large enough to account for the total inventory estimate. This was accomplished by multiplying the cross-section solute mass flux by an inventory scaling factor (f_{inv}) given as

$$f_{inv} = \frac{Inv_{total}}{Inv_{x\,sect}} \tag{3.12}$$

where Inv_{total} is the total estimated leak inventory (Ci or kg) and Inv_{xsect} represents the initial inventory in the cross section (Ci or kg). This approach is the same as the one used in the S-SX FIR modeling (White et al. 2001). The inventory scaling factors for each of the solutes are summarized in Table 3.6.

Table 3.6. The Inventory Scaling Factors

Solutes	T		TX	
	Uniform	Nonuniform	Uniform	Nonuniform
Tc-99	109.89	5.81	136.88	9.45
U-238	274.19	6.98	334.03	12.43
NO_3	105.73	6.40	72.24	9.79
Cr	312.91	8.03	294.15	10.88

3.3.6 Fenceline Cumulative Mass Flux

The cumulative mass flux at the fenceline, Q_{fl} (Ci or kg) was calculated by multiplying the cumulative mass flux from the 2-D simulations (Q_{2d}) by the inventory scaling factor in Equation (3.12):

$$Q_{fl} = f_{inv} Q_{2d} \tag{3.13}$$

3.3.7 Dimensional Scaling Factor and Fenceline Concentrations

The dimensional scaling factor accounts for the effects of flow dimensionality on solute concentration due to the restriction of flow and transport in the simulation. For example, when a 2-D simulation is carried out, the flow and transport are not allowed to occur at the third dimension. In reality, the media for both flow and transport to occur is 3-D. Consequently, a 2-D simulation tends to overestimate the solute concentration. This effect may be accounted for by a dimensional scaling factor defined as

$$f_{dim} = C_{2d}/C_{3d} \tag{3.14}$$

where C_{2d} is the solute concentration from a 2-D simulation of the system with unit thickness and C_{3d} is that from a 3-D simulation of the same system with the same source strength.

In the numerical simulations for the S-SX tank farm, Zhang et al. (2004) compared the results of the 2- and 3-D simulations of a retrieval leak of 4,000 gallons at the lower-right corner of Tank S-103 that began on the first day of the year 2000. The leak lasted for 14 days and contained a unit release of Tc-99 and U-238. The main difference between the 2-D and 3-D simulations was the thickness of the simulation domain in the horizontal (y) direction perpendicular to the groundwater flow direction. In the 2-D simulation, a unit width (1 m) was used. In 3-D, the width was 153 m discretized into 3-m units. Hence, water and solute migration occurred in the y direction for the 3-D simulation, whereas it was absent in the 2-D simulation.

To examine the relationship between the concentrations for the two simulations, the fenceline aqueous concentrations of Tc-99 and U-238 with K_d = 0.03 mL/g were plotted along the y direction for the 3-D simulation when the peak concentrations occurred. Figure 3.5 shows that the highest concentrations occurred at the center line of Tanks S-101, S-102, and S-103 (y = 125 m), and, as the distance from the tank centerline increased, the concentrations decreased. Note that the concentration along the y direction was nearly symmetrical along the centerline of the tank. Approximately 99.4% of Tc-99 and 98.3% of U-238 were within 40 m of the centerline of the tank (from 105 to 145 m).

Figure 3.6 compares the 2- and 3-D BTCs of Tc-99 and U-238 with K_d = 0.03 mL/g. For both Tc-99 and U-239, the shapes of the BTCs from the 2-D simulations were very similar to those from the 3-D simulations. The dimensional scaling factor (f_{dim}) was 41.1 for peak Tc-99 concentrations and 36.6 for U-238 with K_d = 0.03 mL/g. The average value of f_{dim} was 38.85.

In the 2-D simulations for the T and TX-TY tank farm, the thickness of the 2-D slice was 0.5 m (Δy_2 = 0.5 m), which was different from that in Zhang et al. (2004). A thinner slice will produce higher concentration if the same amount of mass is applied. After considering all the effects of inventory, domain dimensionality, and thickness of a 2-D slice, the fenceline concentration was calculated by

$$C_{fl} = C_{xsect} \frac{f_{inv} \Delta y_1}{f_{dim} \Delta y_2} \tag{3.15}$$

Substituting the average value of f_{dim} and the values of Δy into 3.15 produces

$$C_{fl} = C_{xsect} \frac{f_{inv}}{77.7} \tag{3.16}$$

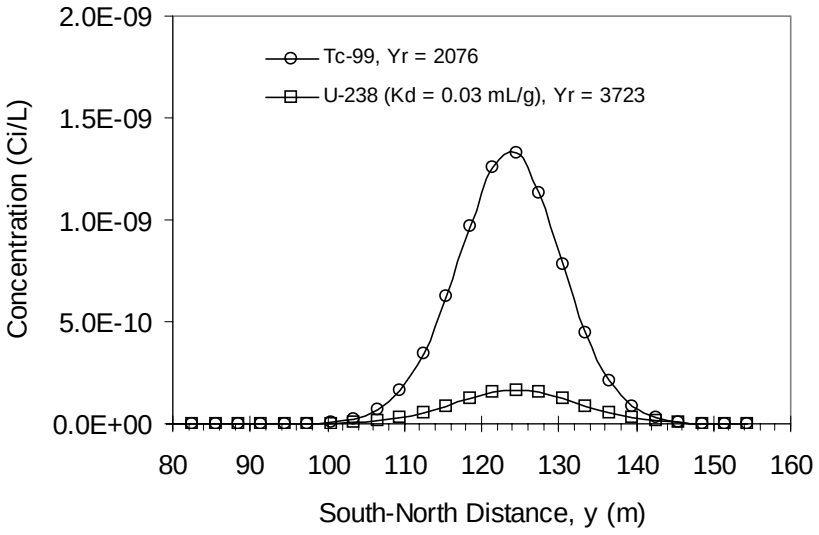

Figure 3.5. Fenceline Aqueous Concentration Perpendicular to Flow Direction (after Zhang et al. 2004)

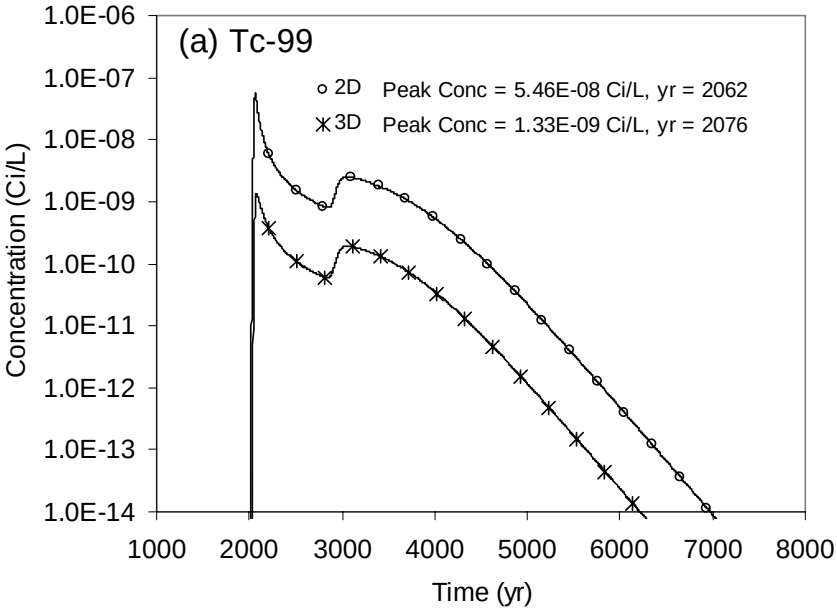

Figure 3.6a. Comparison of BTCs of Tc-99 Simulated with 2- and 3-D (after Zhang et al. 2004)

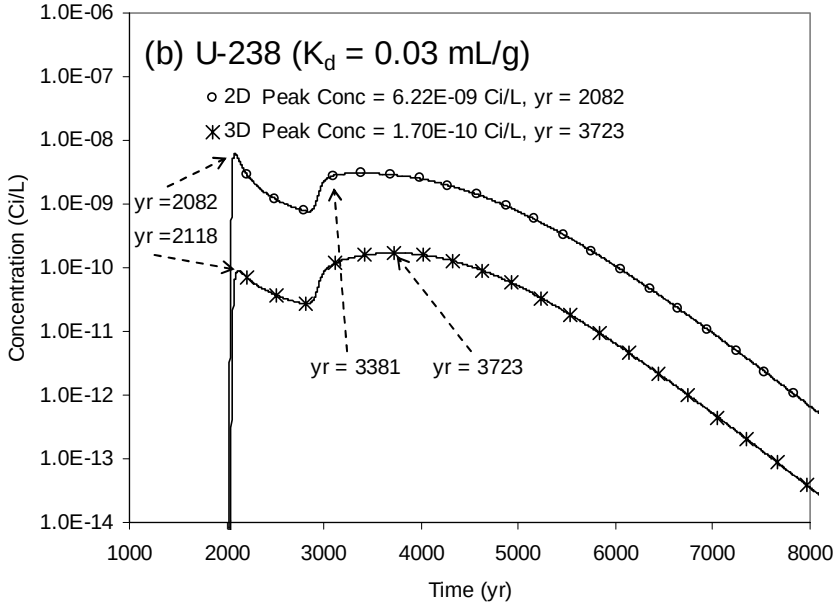

Figure 3.6b. Comparison of BTCs of U-238 with K_d = 0.03 mL/g Simulated with 2- and 3-D (after Zhang et al. 2004)

3.4 Analytical Groundwater Transport Modeling

An instantaneous point source model (Baetslé 1969) was used to calculate the concentration of contaminant species originating at the T and TX-TY WMA and monitored in the model at three remote compliance points along two groundwater flow paths. The analytical groundwater model assumed transport from a point source from a series of solute slugs and considers longitudinal and horizontal transverse dispersion, molecular diffusion, and first-order decay. The method of superposition was used to integrate the individual slug sources. The instantaneous point source model for a 3-D space, as reported by Domenico and Schwartz (1990), is shown in Equation (3.17):

$$C(x,y,z,t) = \left[\frac{C_0 V_0}{\left(8(\pi t)^{3/2} \left(D_x D_y D_z \right)^{1/2} \right)} \right] exp\left[- \frac{(x - vt)^2}{4D_x t} - \frac{y^2}{4D_y t} - \frac{z^2}{4D_z t} - \lambda t \right] \quad (3.17)$$

where $C(x, y, z)$ is the solute concentration (pCi/L or μg/L) as a function of position and time, C_0V_0 is the instantaneous source of solute mass (pCi or μg), D_x,D_y, and D_z are spatial components of the hydrodynamic dispersion coefficient (m^2/yr), x, y, and z are spatial distances from the solute source (m), t is the time (yr), λ is the solute species radioactive decay half-life (yr), and v is the pore water velocity (m/yr). The spatial components of hydrodynamic dispersion coefficients include dispersive and diffusive elements according to Equation (3.17):

$$D_i = \alpha_i v + D_m \quad for \quad i = x, y, z \quad (3.18)$$

where α_i is the dispersivity (m), and D_m is the molecular diffusion coefficient (m^2/yr). If the soil sorption of solute is assumed to be linear, the transport of a reactive solute can also be described by Equation (3.18). For a reactive solute, its dispersivities, D^*, and pore-water velocity, v^*, relate to those, D and v, of a conservative solute by

$$D^* = D/R \text{ and } v^* = v/R \quad (3.19)$$

where R is the retardation factor defined as

$$R = 1 + \rho_b K_d/\theta \quad (3.20)$$

and θ is volumetric soil water content.

The instantaneous point source model (Equation 3.17) was used to calculate the concentration of contaminant species originating at the T and TX-TY tank farm and traveling to three remote compliance points along two groundwater flow paths. The three compliance points are located at 1) the 200 West Area boundary, 2) the exclusion boundary, and 3) the Columbia River. The distance to each compliance point along the groundwater flow path was based on streamlines derived from the Coupled Fluid, Energy, and Solute Transport (CFEST) Site-wide groundwater model (Gupta et al. 1987; Gupta 1997), as described in Section 5. Values for the y and z directions are assigned as zero, signifying that the point of observation was along the longitudinal centerline.

The concentration at compliance points is calculated by a FORTRAN code *(point_3d.f)* that implements the instantaneous pulse equation. The streamtube model requires both inputs from screen and a file. The screen inputs include all the parameter values and were facilitated so they are contained in a *C* shell script. The input from file provided solute mass flux across T and TX-TY tank farm as a function of time for Tc-99, U-238, NO_3, and Cr. The 1,000-year period for the T and TX-TY tank analysis, between years 2000 and 3000, was modeled using 2,000 uniformly spaced solute release events.

4.0 Simulation Results

Reported simulation results are focused on key fluid flow and solute transport behavior, BTCs at the fenceline (T and TX-TY WMA boundary), and mass balance errors. Peak aqueous concentration, arrival time of peak concentration, and maximum initial aqueous concentration are summarized in this section. The mean aqueous phase saturation and maximum aqueous initial concentration values, which were based on the inventory estimates of Khaleel et al. (2004), are presented for comparison with the computed peak aqueous concentrations. The peak mass fluxes and arrival times at the groundwater table and the fenceline are also summarized. The peak concentrations and arrival times at the groundwater table, the fenceline, the 200-West boundary, the exclusion boundary, and the Columbia River along the north and south paths are presented. The STOMP mass balance within the 2-D simulation domain for each contaminant in each case is summarized.

Saturation and inventory profiles for the T-103, -104 and -105 cross section are shown in Appendix A. BTCs at the T WMA for the various cases are presented in Appendix B. Saturation and inventory profiles for the TX-105, -106, -107 and -108 cross section are shown in Appendix C. BTCs at the TX WMA for the various cases are presented in Appendix D. Translation of the BTC results to the downgradient compliance points via streamtube modeling is described in Section 5.

Simulation results were written to three types of output: 1) reference node, 2) plot file, and 3) surface flux. For more complete analyses, electronic copies of the reference node, plot file, and surface flux outputs will be available for each simulation case and cross section in STOMP simulator output format and converted *Tecplot* formats (Section 6). The simulations were initialized using a steady flow solution defined by a constant upper-surface recharge rate and a constant hydraulic gradient in the unconfined aquifer. A detailed description of the simulation is given in Section 3.1. Plot file outputs for all the simulations were generated at years 2000, 2001, 2010, 2040, 2100, 2200, 2300, 2400, 2500, 2540, 2600, 2800 and 3000 and include values for the aqueous saturation (i.e., θ/θ_s, where θ is the moisture content and θ_s is the saturated moisture content), aqueous pressure, aqueous moisture content, and concentrations for the four solute species.

Due to the significant sorption effects on the transport of U-238 (K_d = 0.6 mL/g) for all the cases except Case 3, U-238 had not migrated to the groundwater by the end of the simulation—year 3000. To show this effect, the peak concentrations of U-238 along with the other solutes are summarized in tables while the discussion focuses mainly on the three conservation solutes, Tc-99, NO_3, and Cr.

4.1 Initial Conditions

The saturation field was dependent on the surface recharge, hydrologic parameters, soil distribution, and impermeable structures (e.g., SSTs). The preconstruction moisture conditions (year 1945 for T farm and 1949 for TX farm) were achieved by running a simulation for the two cross sections using a recharge rate of 3.5 mm/yr for 1000 years or longer. The simulations were run without the tanks in place because it represented the preconstruction period of T and TX-TY tank farm. Once the tanks were in place in 1945 or 1949, recharge rates increased to 100 mm/yr. The soil moisture condition at year 2000, shown in Figure 4.1, was used as the initial saturation condition for all eight cases.

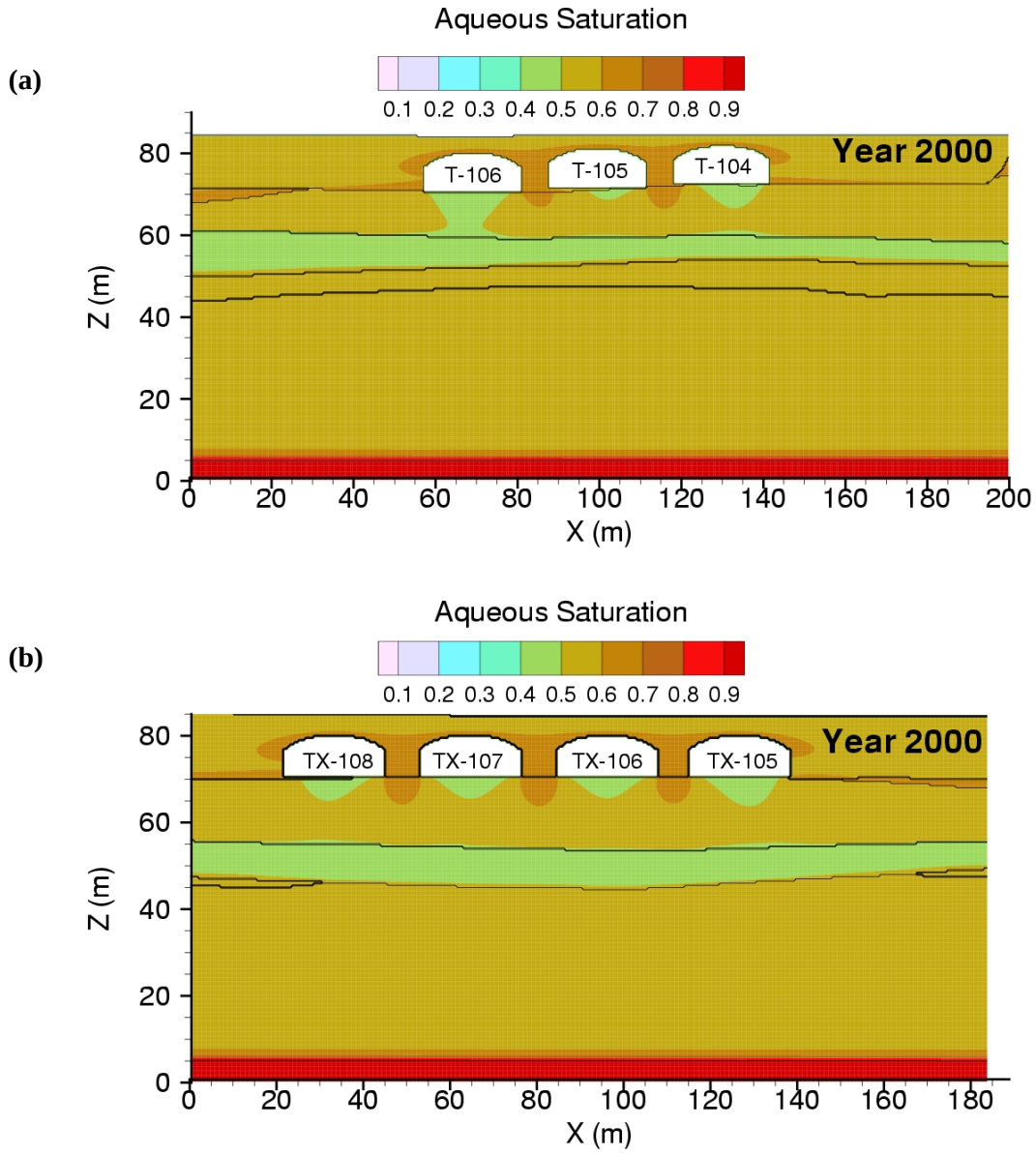

Figure 4.1. Aqueous-Phase Saturation at 2000 for (a) Cross Section T-104, -105, -106 and (b) Cross Section TX-105, -106, -107, -108

The data for the measured concentrations and inventory at different depths are given in Khaleel et al. (2004, Table D-1). Total inventory for Tc-99, U-238, NO_3, and Cr are repeated in Table 4.1. Because of significant uncertainties with inventory estimates, as described in Section 3, both uniform (variable-diameter) and nonuniform (fixed-diameter) distributions of the inventory were considered. All cases except Case 5 used a uniform inventory distribution. For the cross section with Tanks T-104, -105, and -106, the total inventory was distributed uniformly in the lateral direction across the diameter of Tank T-106 only (Figures 4.2a to 4.5a). For the cross section with Tanks TX-105, -116, -107 and -108, the total inventory was distributed uniformly in the lateral direction across the diameter of Tanks TX-106, -107, and -108 (Figures 4.2b to 4.5b).

Table 4.1. Total Inventory for Tc-99, U-238, NO_3, and Cr (after Khaleel et al. 2004)

Cross section	Tc-99 (Ci)	U-238 (Ci)	NO_3 (Kg)	Cr (Kg)
T	61.932	0.11711	36700	1013
TX	4.57	0.0185	7560	131

(a)

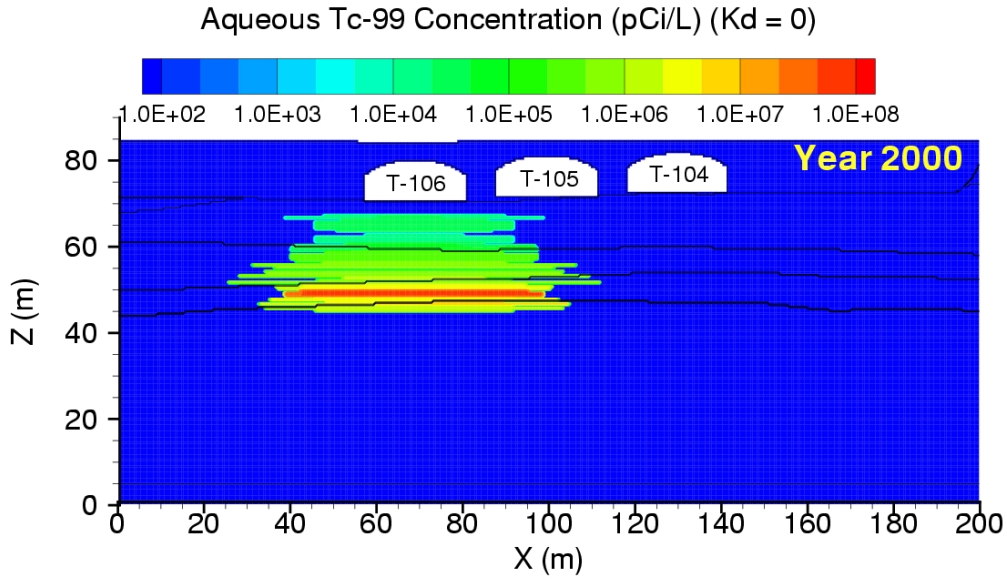

(b)

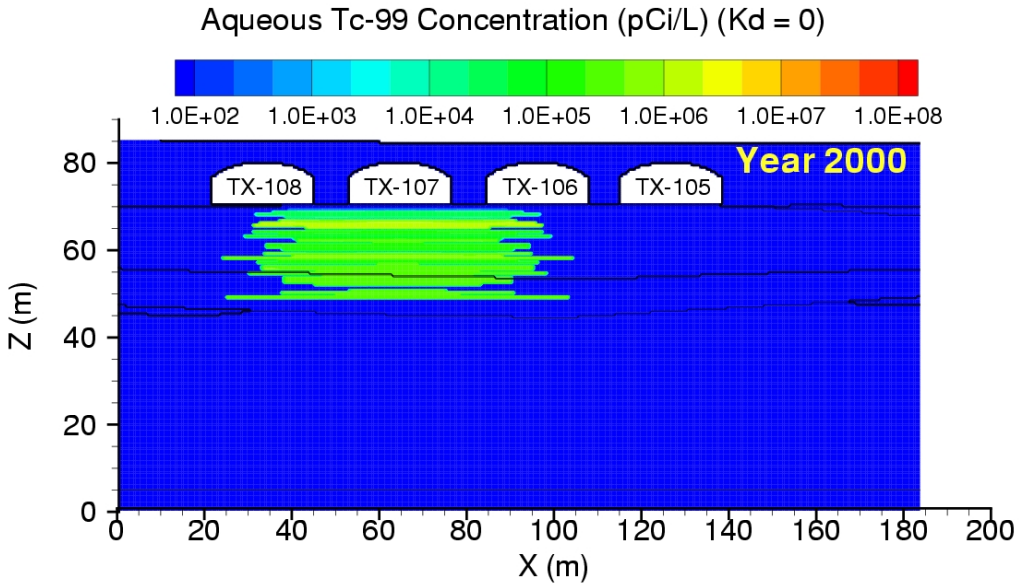

Figure 4.2. Aqueous-Phase Tc-99 Concentration at 2000 if Inventory Assigned as Uniform Distribution for (a) Cross Section T-104, -105, -106 and (b) Cross Section TX-105, -106, -107, -108

(a)

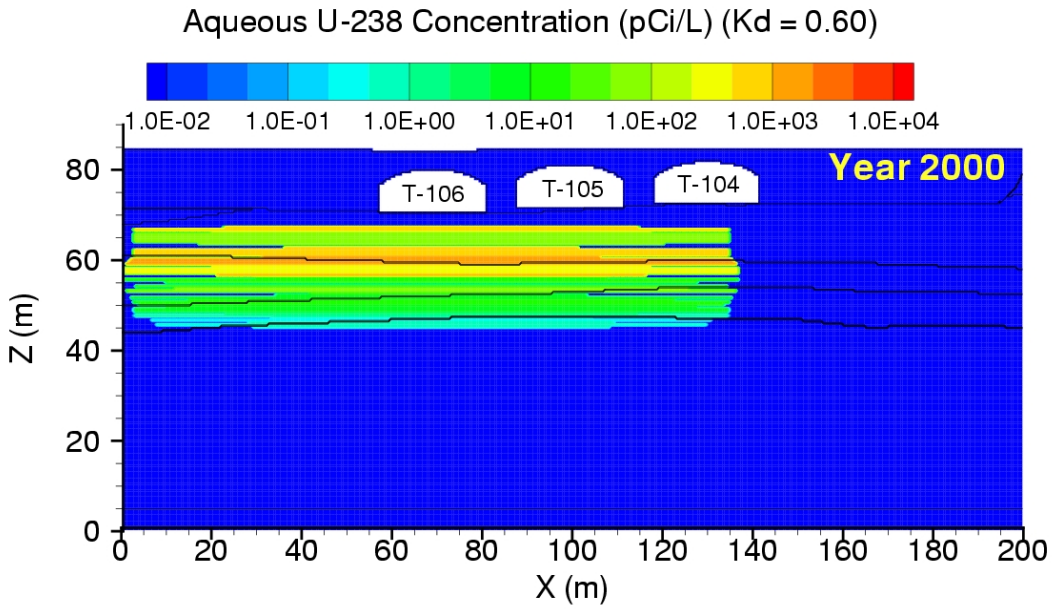

(b)

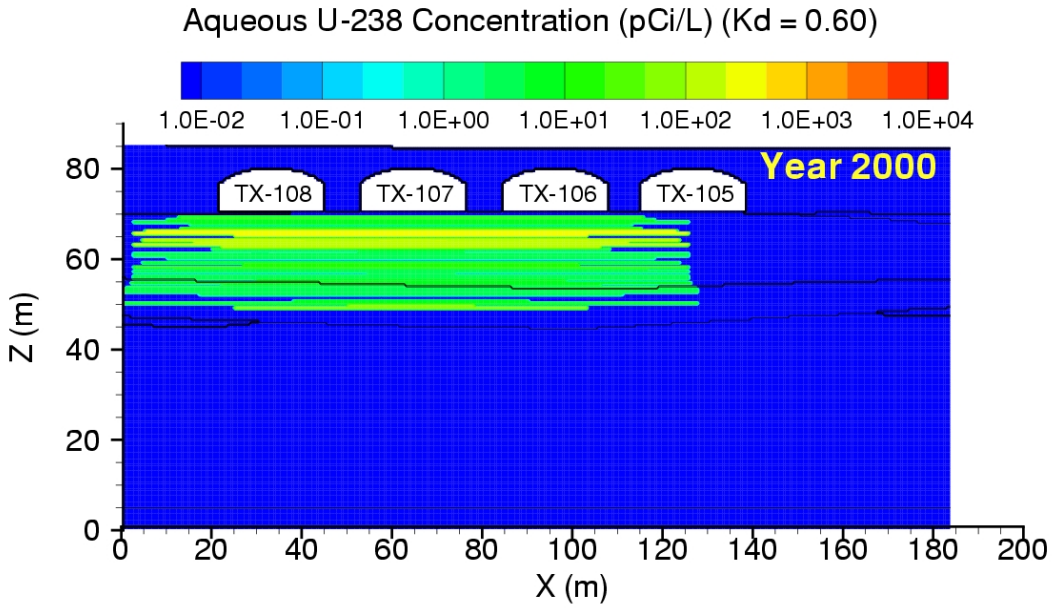

Figure 4.3. Aqueous-Phase U-238 Concentration at 2000 if Inventory Assigned as Uniform Distribution for (a) Cross Section T-104, -105, -106 and (b) Cross Section TX-105, -106, -107, -108

The nonuniform inventory distribution was used for Case 5. For the cross section with Tanks T-104, -105 and -106, the total inventory for each depth was distributed in the lateral direction within one-half the space *only* between Tanks T-105 and -106, beginning on the eastern edge of Tank T-106 (Figures 4.6a to 4.9a). For the cross section with Tanks TX-105, -116, -107 and -108, the total inventory for each depth was distributed in the lateral direction within one-half the space *only* between Tanks TX-107 and -108, beginning on the eastern edge of Tank TX-108 (Figures 4.6b to 4.9b).

(a)

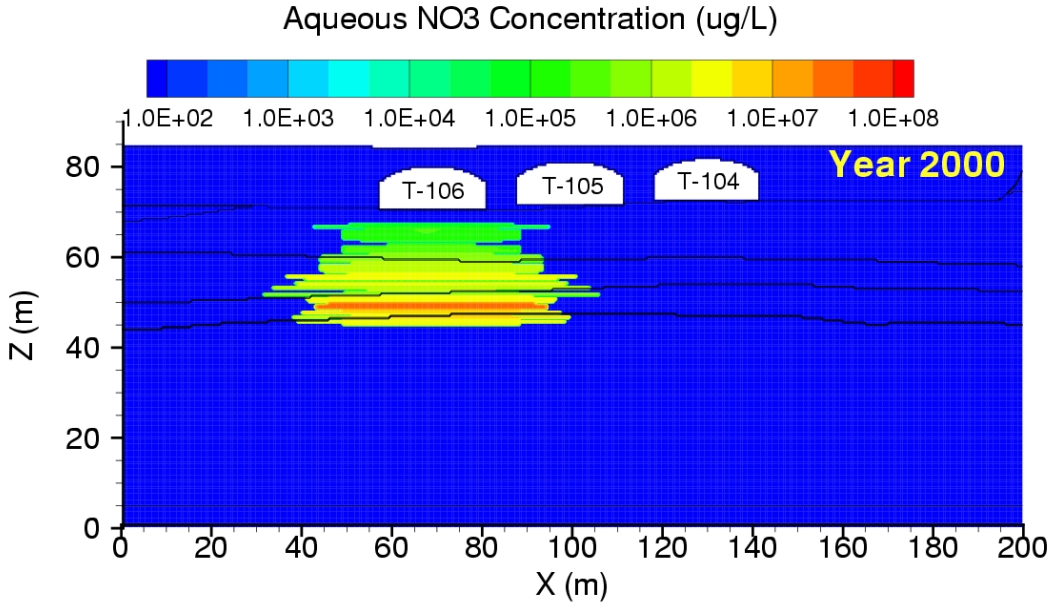

(b)

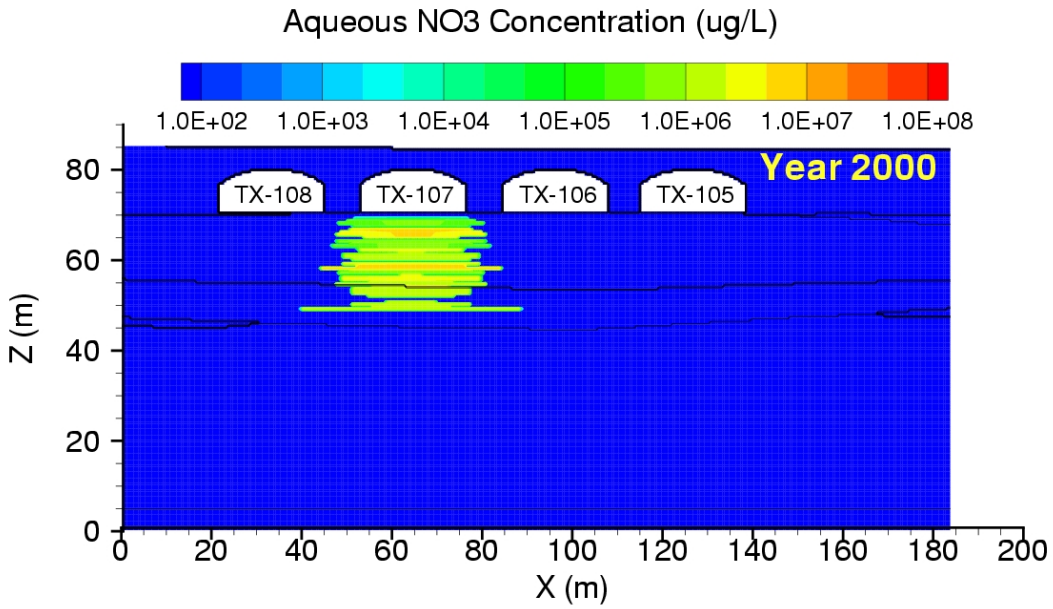

Figure 4.4. Aqueous-Phase NO_3 Concentration at 2000 if Inventory Assigned as Uniform Distribution for (a) Cross Section T-104, -105, -106 and (b) Cross Section TX-105, -106, -107, -108

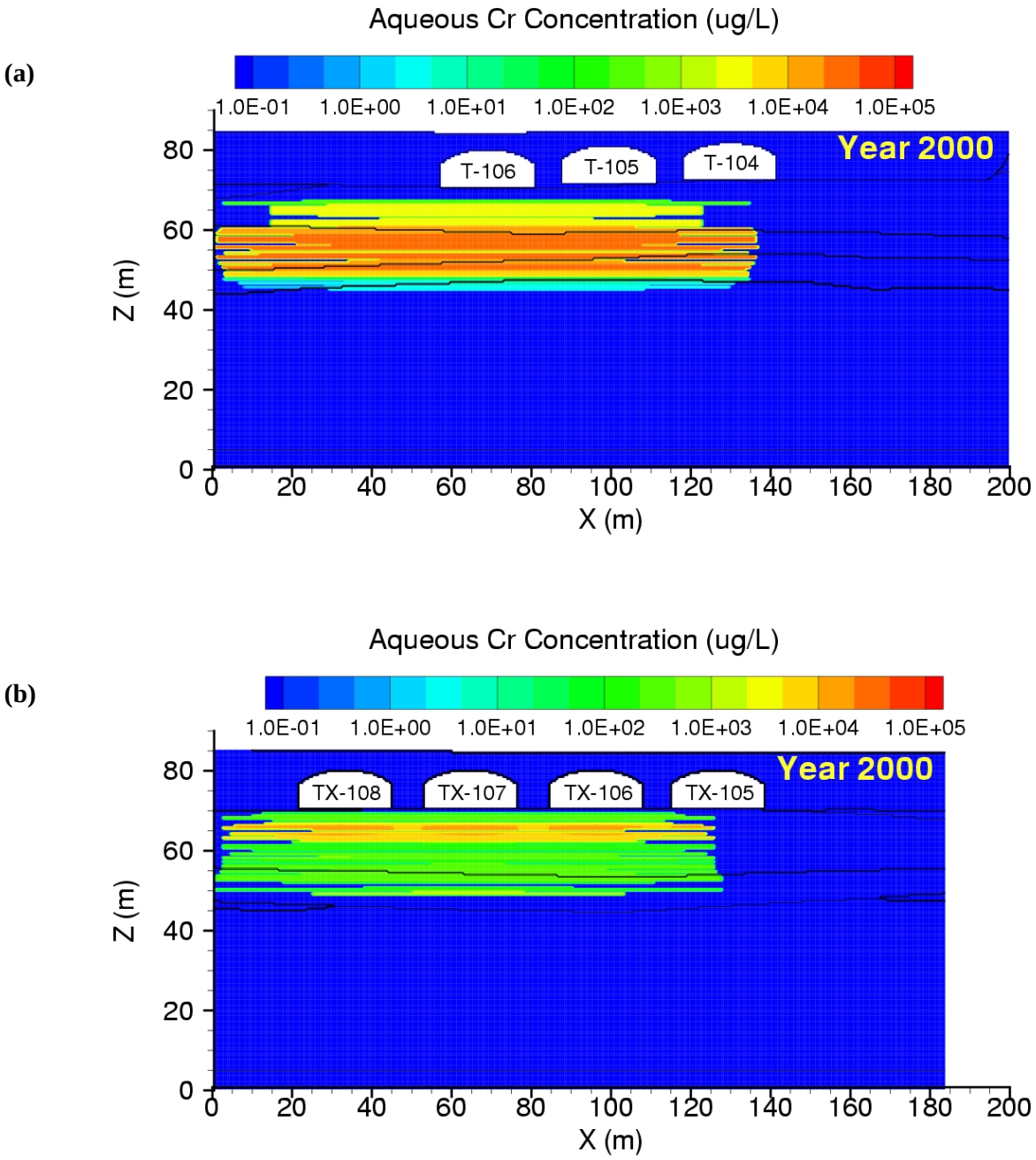

Figure 4.5. Aqueous-Phase Cr Concentration at 2000 if Inventory Assigned as Uniform Distribution for (a) Cross Section T-104, -105, -106 and (b) Cross Section TX-105, -106, -107, -108

(a)

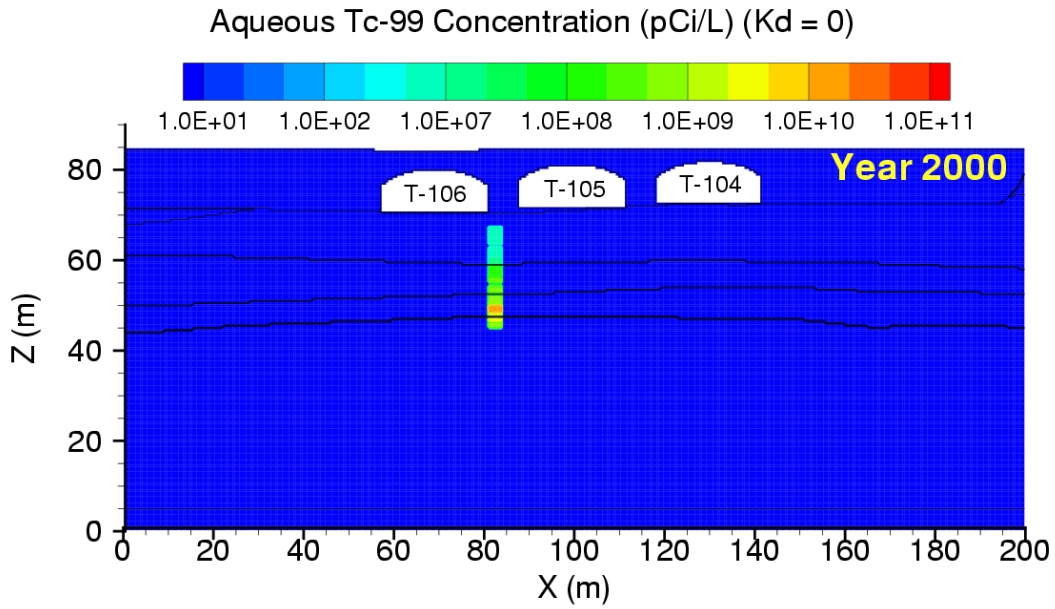

(b)

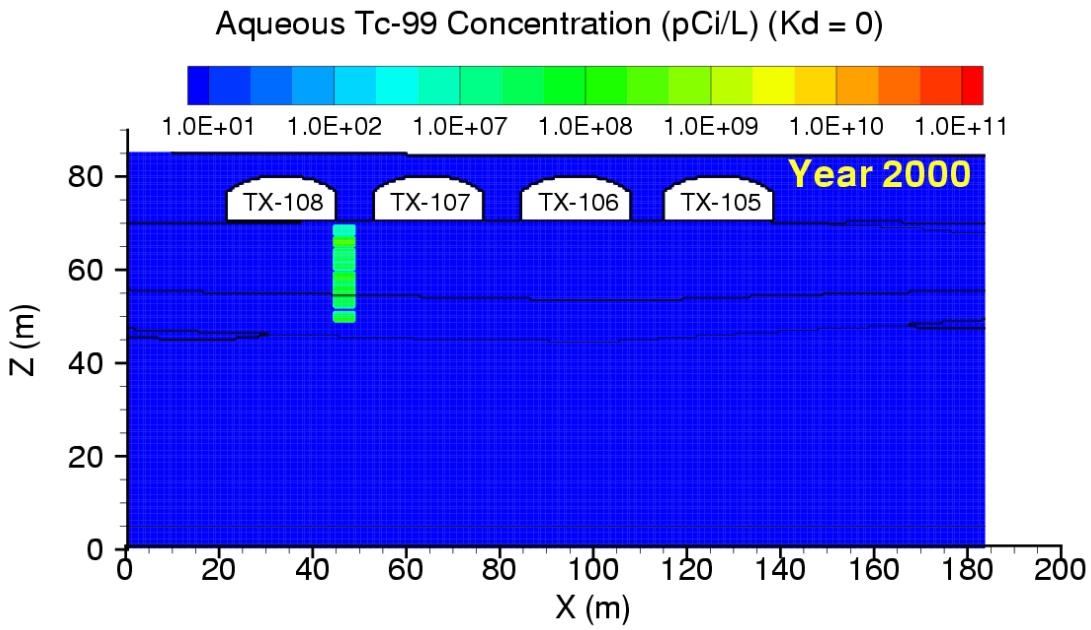

Figure 4.6. Aqueous-Phase Tc-99 Concentration at 2000 if Inventory Assigned as Nonuniform Distribution for (a) Cross Section T-104, -105, -106 and (b) Cross Section TX-105, -106, -107, -108

(a)

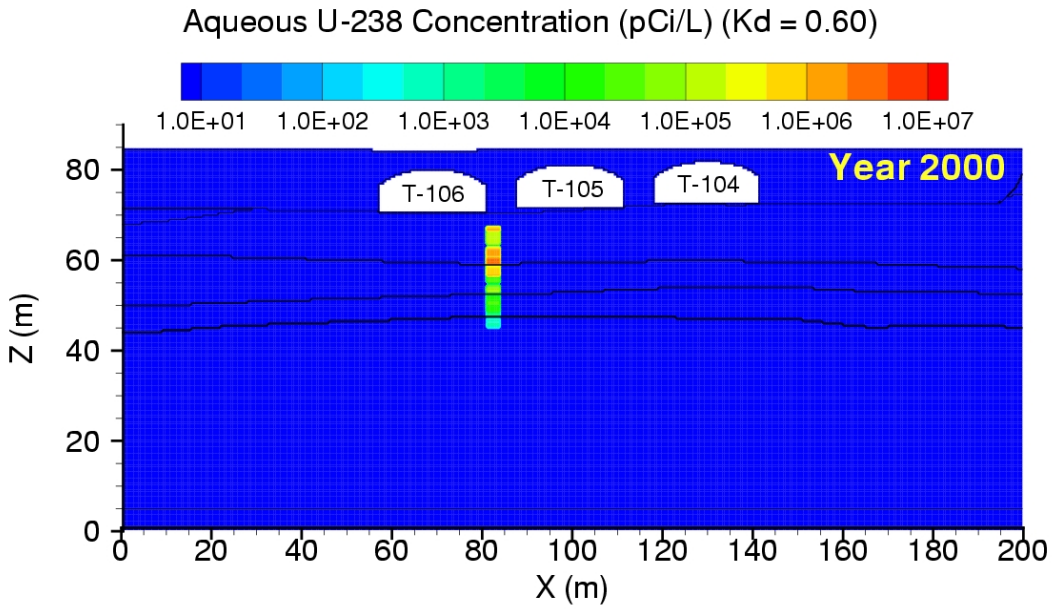

(b)

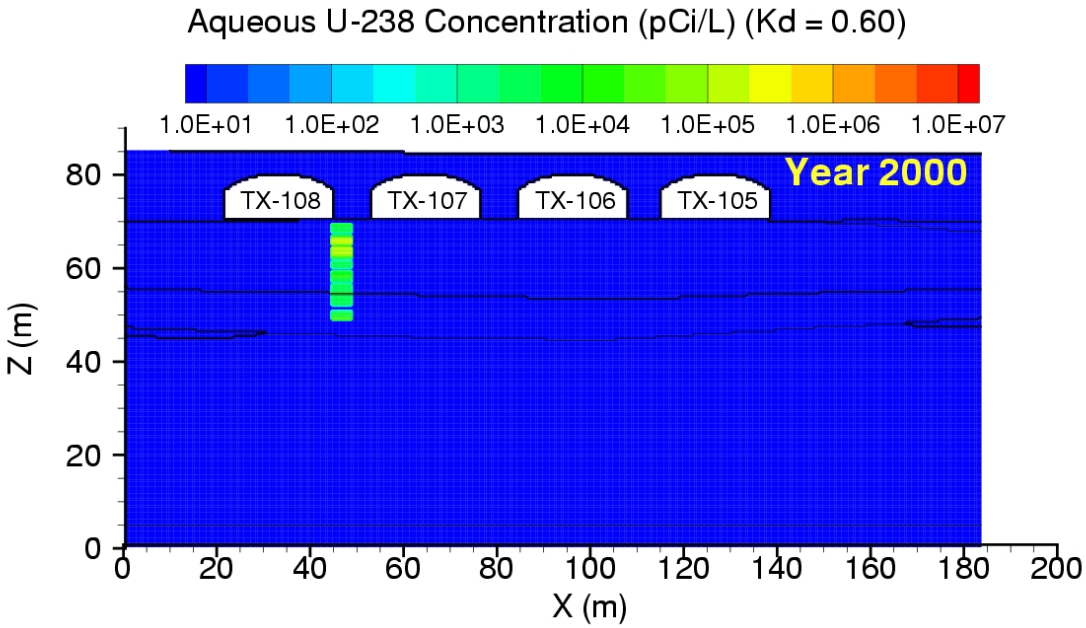

Figure 4.7. Aqueous-Phase U-238 Concentration at 2000 if Inventory Assigned as Nonuniform Distribution for (a) Cross Section T-104, -105, -106 and (b) Cross Section TX-105, -106, -107, -108

(a)

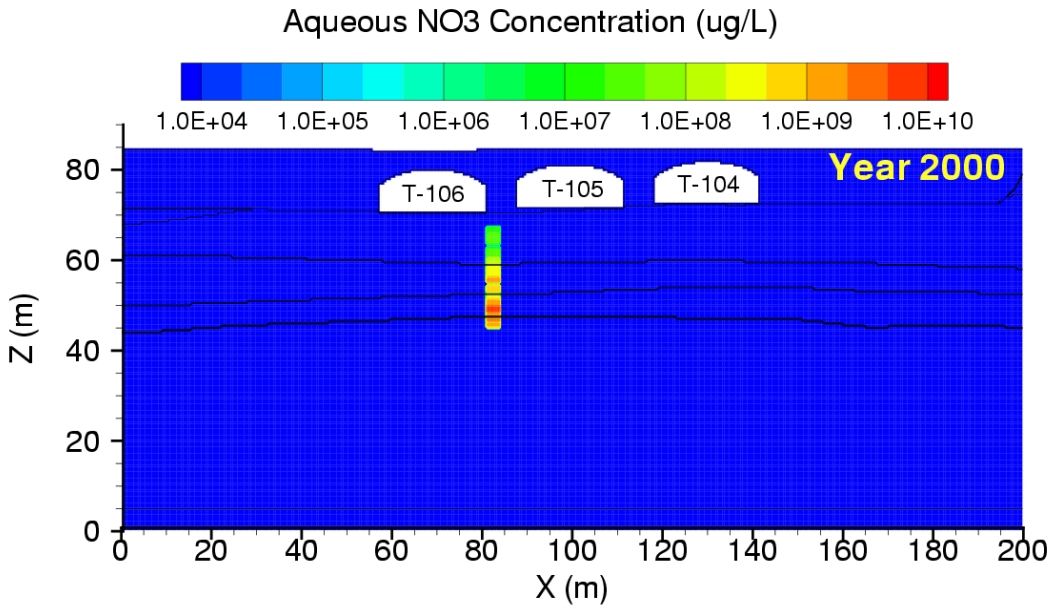

(b)

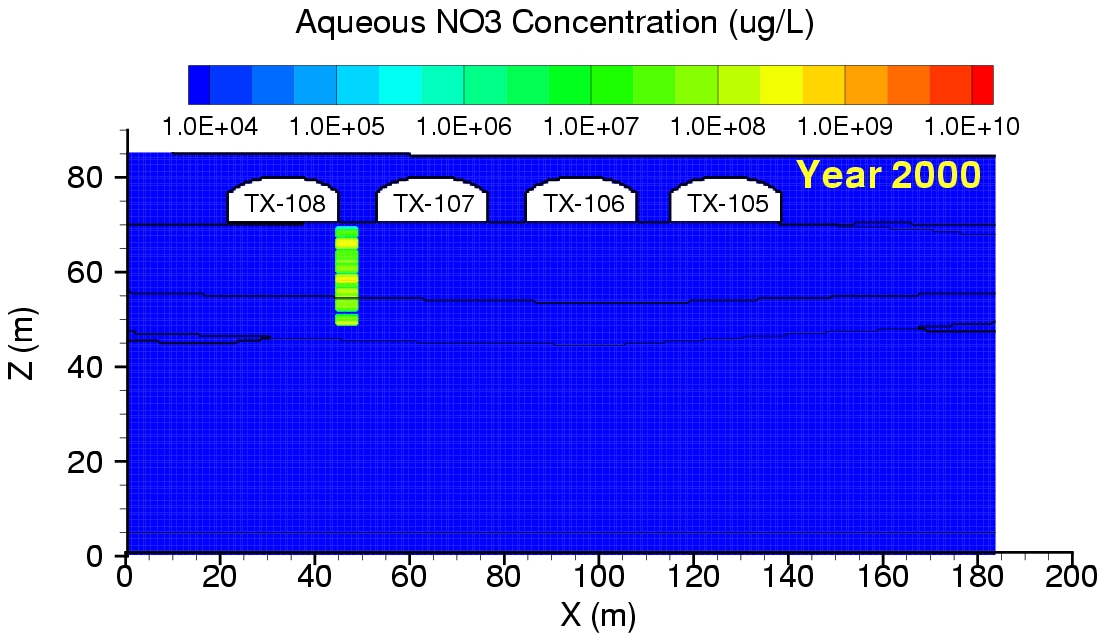

Figure 4.8. Aqueous-Phase NO_3 Concentration at 2000 if Inventory Assigned as Nonuniform Distribution for (a) Cross Section T-104, -105, -106 and (b) Cross Section TX-105, -106, -107, -108

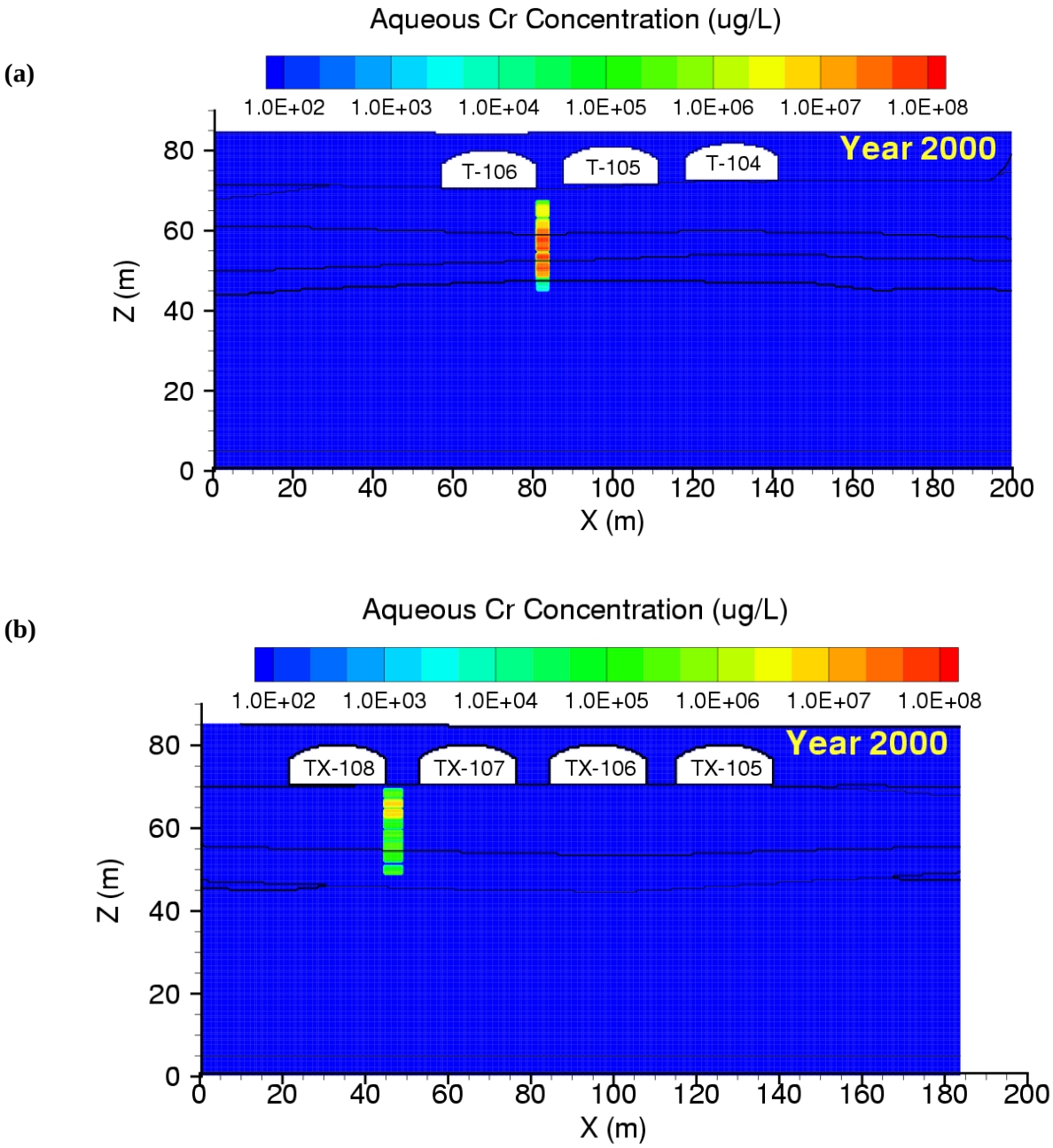

Figure 4.9. Aqueous-Phase Cr Concentration at 2000 if Inventory Assigned as Nonuniform Distribution for (a) Cross Section T-104, -105, -106 and (b) Cross Section TX-105, -106, -107, -108

4.2 Base Case (No-Action Alternative)

The Base Case (Case 1) suite of simulations investigated solute transport through two cross sections in the T and TX-TY WMA considering natural surface infiltration with no waterline leaks and no interim surface barriers but with a closure barrier by the year 2040. These simulations were initialized using a steady-flow solution defined by the upper surface recharge rate of 100 mm/yr (Figure 4.1) and a constant

hydraulic gradient in the unconfined aquifer. Inventories of the four contaminant species were initialized using the uniform distribution pattern (Figures 4.2 through 4.5).

The aqueous saturation field is dependent on the surface recharge, hydrologic parameters, soil distribution, and impermeable structures (e.g., SSTs). The steady-flow saturation field at year 2040 for the T farm cross section with 100 mm/yr of meteoric recharge is shown in Figure 4.10. This field shows the impacts of the tanks on the aqueous saturation, where higher than ambient saturations occur above and between the tanks and lower than ambient saturations occur just below the tanks. In 2040 a closure barrier was assumed to be active, which lowered the meteoric recharge from 100 mm/yr to 0.1 mm/yr. The aqueous saturation field dried in response to the change in surface recharge. The closure barrier was assumed to remain effective for 500 years, at which time, it begins to degrade, allowing meteoric recharge to increase to 3.5 mm/yr. In the 500-year period between 2040 and 2540, the aqueous saturation field continued to slowly dry reaching a minimum average level at 2540, as shown in Figure 4.11. The shielding impact of the impermeable tanks on the aqueous saturation was reduced, as shown in comparing Figures 4.10 and 4.11. In the 460 years between 2540 and 3000, the aqueous saturation field wetted in response to the increased meteoric recharge of 3.5 mm/yr for the degraded surface barrier. The aqueous saturation at year 3000 is shown in Figure 4.12.

The water table level showed little variation with the rate of surface recharge; therefore, the mean aqueous saturation in the cross section gives a general indication of the effect of surface recharge on the hydrologic environment. Mean aqueous phase saturations at selected times during the simulation period are shown in Table 4.2 for the two cross sections. As expected, the mean saturations follow the trends in surface recharge (i.e., higher mean saturations at higher surface recharge), but the rate of change in mean saturation was slow, as evidenced by the gradual decrease in saturation between the transition from 100 to 0.1 mm/yr in 2040 until the next rate change in 2540. In contrast, the aqueous flow field changes nearly immediately to variations in the surface recharge. The saturation values in Table 4.2 show little variation between cross sections.

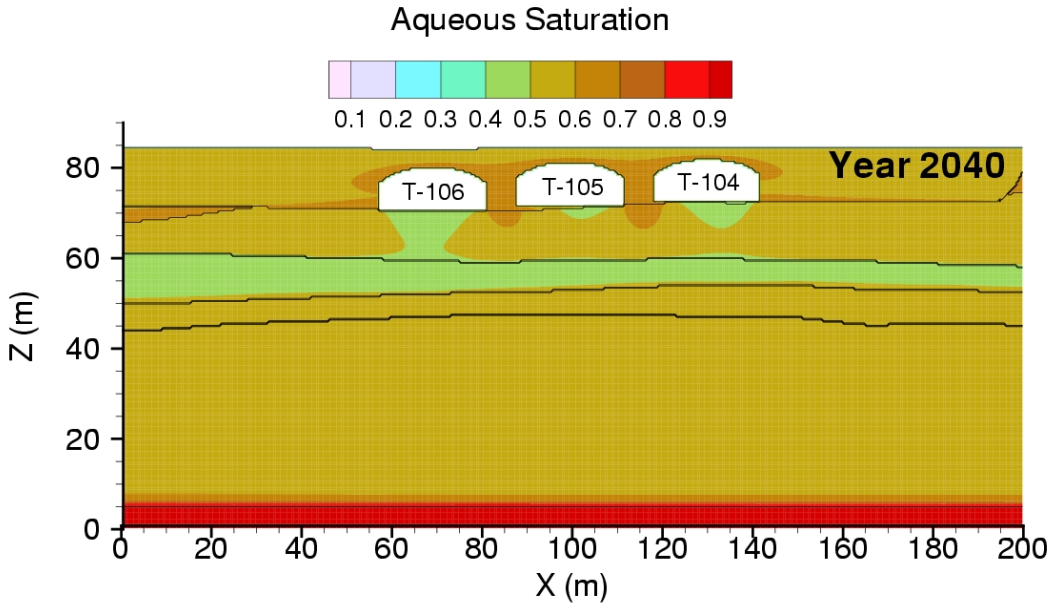

Figure 4.10. Aqueous-Phase Saturation at 2040 (100 mm/yr) for Cross Section T-104, -105, -106

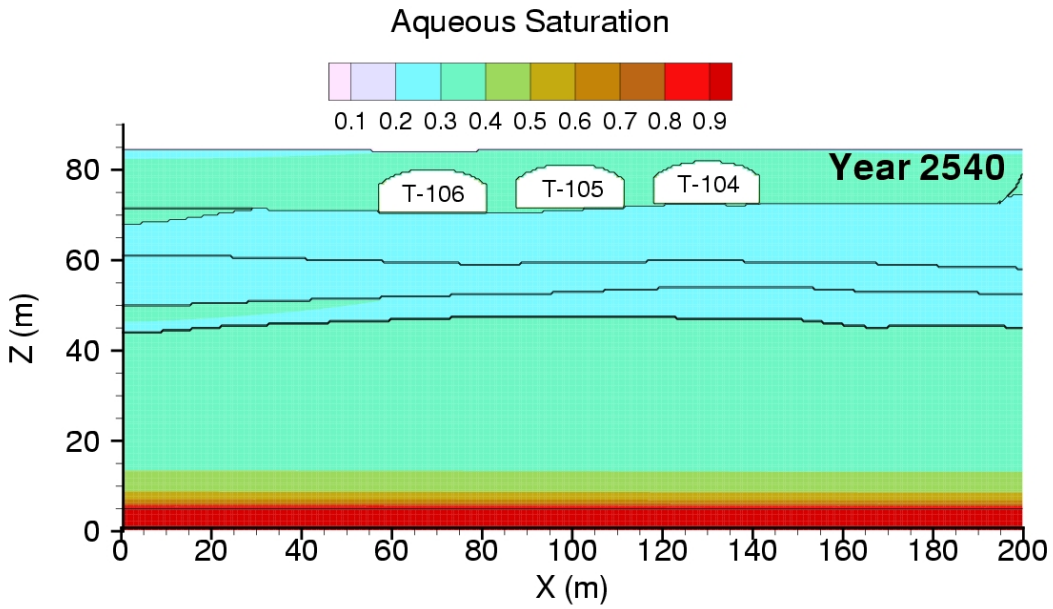

Figure 4.11. Aqueous-Phase Saturation at 2540 (0.1 mm/yr) for Cross Section T-104, -105, -106

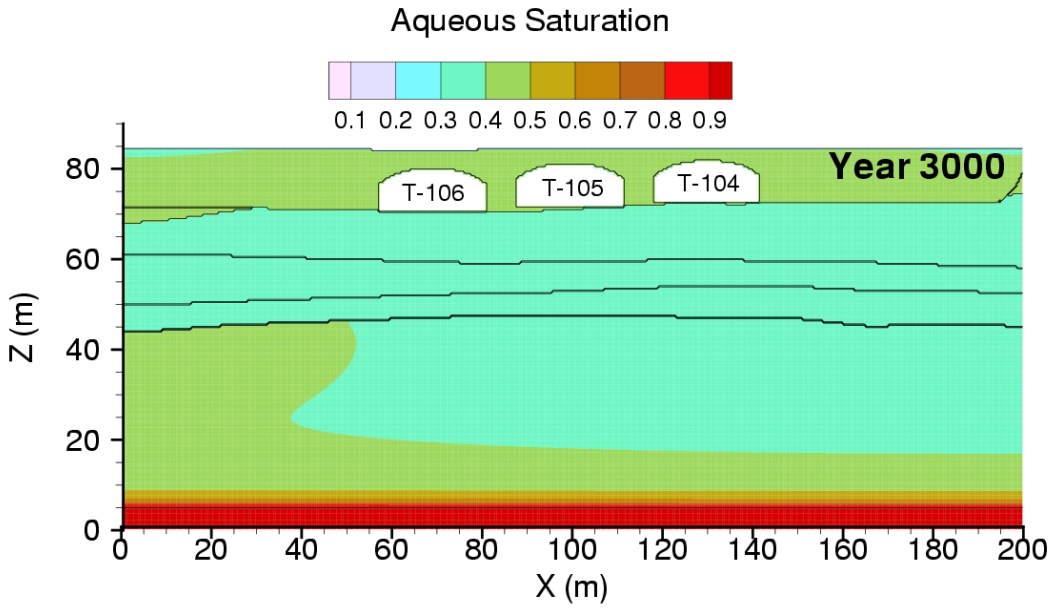

Figure 4.12. Aqueous-Phase Saturation at 3000 (3.5 mm/yr) for Cross Section T-104, -105, -106

The distribution of the aqueous concentration of the contaminants for cross section T-104, -105, -106 at year 2040 (3000 for U-238) is shown as color images in Figures A.8 through A.11 in logarithmic scale. The concentration distribution for cross section TX-105, -106, -107, -108 at year 2040 (3000 for U-238) is shown in Figures C.8 through C.11. The three conservative solutes (i.e., Tc-99, NO_3, and Cr) migrated downward at similar velocity, while U-238 had not reached the groundwater table by the end of the simulation (i.e., year 3000).

Table 4.2. Mean Aqueous-Phase Saturation

Year	Meteoric Recharge	Cross Section T-104, -105, -106	Cross Section TX-105, -106, -107, -108
2000	100 mm/yr	0.579	0.573
2001	100 mm/yr	0.579	0.573
2010	100 mm/yr	0.579	0.573
2040	100 to 0.1 mm/yr	0.579	0.573
2100	0.1 mm/yr	0.451	0.447
2200	0.1 mm/yr	0.414	0.412
2300	0.1 mm/yr	0.399	0.397
2400	0.1 mm/yr	0.389	0.388
2500	0.1 mm/yr	0.383	0.382
2540	0.1 to 3.5 mm/yr	0.381	0.380
2600	3.5 mm/yr	0.392	0.392
2800	3.5 mm/yr	0.408	0.408
3000	3.5 mm/yr	0.432	0.431

Figures B.1 through B.6 plot mass flux, cumulative mass, and BTCs for the three conservative contaminants for cross section T-104, -105, -106 and Figures D.1 through D.6 for cross section TX-105, -106, -107, -108. Breakthrough times and peak aqueous concentrations at the fenceline are shown in Table-4.3 along with maximum initial aqueous concentrations. Compared with the peak inventory concentration, the peak fenceline concentration of the three solutes was reduced by a factor of 3~37 for T farm and 18~89 for TX farm as the solutes migrated through the vadose zone and across the unconfined aquifer within T and TX-TY WMA. Almost no U-238 migrated outside the fenceline. It took 41 to 49 years in T farm and 50 to 58 years in TX farm for the conservative solutes to migrate to groundwater and further to the fenceline. Arrival times show a weak dependence on cross-section geology.

4.3 Barrier Alternative and No Waterline Leaks

The Barrier Alternative and No Waterline Leaks (Case 2) suite of simulations investigated solute transport through two cross sections in the T and TX-TY tank farms considering natural surface infiltration and no waterline leaks. This suite of simulations differs from the Base Case simulations in that an interim surface barrier was implemented between the years 2010 and 2040. These simulations were initialized using the flow solution defined by the upper surface recharge rate of 100 mm/yr and a constant hydraulic gradient in the unconfined aquifer (Figure 4.1). Inventories of the four contaminant species were initialized using the uniform distribution pattern (Figures 4.2 through 4.5).

The distribution of the aqueous concentration of contaminants for cross section T-104, -105, -106 at year 2040 (3000 for U-238) is shown in color images in Figures A.12 through A.15 in logarithmic scale.

Table 4.3. Peak Concentrations and Arrival Times at the Fenceline (T and TX-TY WMA Boundary) for Case 1

Cross Section	T-104, -105, -106	TX-105, -106, -107, -108
Tc-99		
Arrival time	2041 yr	2050 yr
Peak concentration	1.40×10^{6} pCi/L	4.65×10^{4} pCi/L
Maximum initial concentration[(a)]	5.23×10^{7} pCi/L	1.29×10^{6} pCi/L
U-238		
Arrival time	>= 3000 yr	>= 3000 yr
Peak concentration	1.19×10^{-13} pCi/L	5.76×10^{-15} pCi/L
Maximum initial concentration	1.20×10^{3} pCi/L	2.49×10^{2} pCi/L
NO_3		
Arrival time	2042 yr	2051 yr
Peak concentration	7.13×10^{5} μg/L	8.14×10^{4} μg/L
Maximum initial concentration	2.20×10^{7} μg/L	7.22×10^{6} μg/L
Cr		
Arrival time	2049 yr	2058 yr
Peak concentration	1.72×10^{4} μg/L	6.76×10^{2} μg/L
Maximum initial concentration	4.72×10^{4} μg/L	1.21×10^{4} μg/L
(a) Initial aqueous concentrations were based on inventory data and are listed for comparison with the peak arrival concentrations.		

The concentration distribution for cross section TX-105, -106, -107, -108 at year 2040 (3000 for U-238) is shown in Figures C.12 through C.15. The three conservative solutes (Tc-99, NO_3, and Cr) migrated downward at similar velocities, but U-238 had not reached the groundwater table by the end of the simulation (year 3000).

Figures B.7 through B.12 plot the mass flux, cumulative mass, and BTCs for each of the three conservative contaminants for cross section TX-105, -106, -107, -108 and Figures D.7 through D.12 for cross section TX-105, -106, -107, -108. The fenceline concentrations at the year 3000 were always higher for the case with the interim barrier (Case 2) than those of the Base Case (without interim barrier, Case 1), which indicates that the fundamental impact of the interim barrier is a smoothing of the breakthrough concentrations at the compliance points. Breakthrough times and peak aqueous concentrations at the fenceline are shown in Table 4.4, along with the maximum initial aqueous concentrations. Compared with the Base Case (Case 1), the application of the interim barrier prolonged the solute travel time by 0~6 years for T farm and 10~16 years for TX farm; the peak concentrations reduced by 70.7 ~86.6% for T farm and 90.9~92.7% for TX farm. For Cr at TX farm, the concentration at year 3000 was higher than the peak concentration at about 2070. The higher value is reported but not compared with the Base Case.

The effects of the interim barrier on mean saturation are illustrated by Figure 4.3. When the interim barrier was applied at 2010, the soil was desaturated gradually. The difference in saturation between the soil with (Case 2) and without (Case 1) the interim barrier was largest at 2040, the time the closure barrier was applied. After this, the difference in saturation between the two cases became smaller with time.

Table 4.4. Peak Concentrations and Arrival Times at the Fenceline (i.e., T and TX-TY WMA Boundary) for Case 2

Cross Section	T-104, -105, -106	TX-105, -106, -107, -108
Tc-99		
Arrival Time	2042 yr (1)[(a)]	2060 yr (10)
Peak Concentration	4.09×10^5 pCi/L (-70.7%)	4.20×10^3 pCi/L (-90.9%)
Maximum Initial Concentration[(b)]	5.23×10^7 pCi/L	1.29×10^6 pCi/L
U-238		
Arrival Time	>= 3000 yr (0)	>= 3000 yr (0)
Peak Concentration	0.00×10^0 pCi/L (-100%)	0.00×10^0 pCi/L (-100%)
Maximum Initial Concentration[(b)]	1.20×10^3 pCi/L	2.49×10^2 pCi/L
NO_3		
Arrival Time	2042 yr (0)	2067 yr (16)
Peak Concentration	1.96×10^5 µg/L (-72.4%)	5.94×10^3 µg/L (-92.7%)
Maximum Initial Concentration[(b)]	2.20×10^7 µg/L	7.22×10^6 µg/L
Cr		
Arrival Time	2055 yr (6)	>= 3000 yr (942)
Peak Concentration	2.30×10^3 µg/L (-86.6%)	5.06×10^1 µg/L (-92.5%)
Maximum Initial Concentration[(b)]	4.72×10^4 µg/L	1.21×10^4 µg/L

(a) Numbers in parentheses indicate change from Base Case.
(b) Maximum initial concentration is based on inventory data and listed for comparison with the simulated peak concentration at the compliance boundary.

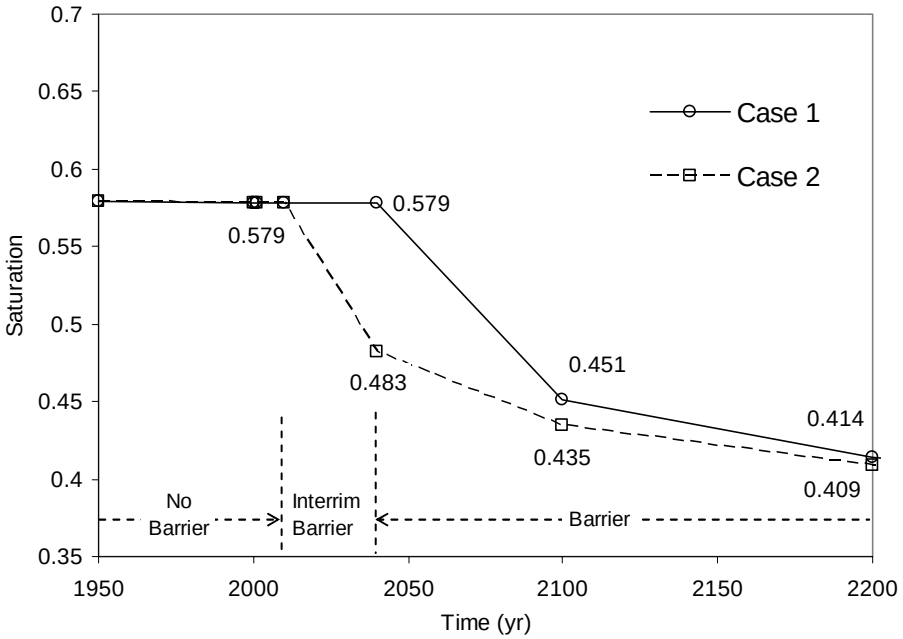

Figure 4.13. Effects of the Interim Cover on the Mean Saturation of the T Tank Farm

4.4 Waterline Leak and No Interim Barrier

The simulation cases, Cases 3 and 4, investigated transport behavior for contaminants originating from the waterline leaks. Two leak rates were simulated: Case 3 investigated the leak of 1 gpm for 20 years and Case 4 the leak of 200,000 gal for five days. The Cases 3 and 4 suites of simulations investigated solute transport through the two cross sections in T and TX-TY tank farms considering natural surface infiltration and a closure barrier by the year 2040. These suites of simulations differ from the Base Case in that a waterline leak occurred for Tank T-104 or TX-105 in the cross sections. The waterline leak was modeled as a cylinder-shaped source of water spread over a 6.5-m-diameter area between Tanks T-104 and T-105 or over a 7.0-m-diameter area between Tanks TX-105 and TX-106. The circular leak areas were translated to the 2-D simulation using a computational grid width of 0.5 m and assuming the centers of the circular leak areas were situated on the centerline between tanks. This approach results in a 2-D waterline leak rate of 0.097941 gpm per node for T farm and 0.090945 gpm for TX farm.

4.4.1 Case 3 No Barrier and Waterline Leak of 1 gpm for 20 Years

The flow environment of T tank farm following the 20-yr waterline leak event is shown in Figure 4.14. The soil below the leak position was saturated or near-saturated. The flow moved at the flux near the saturated hydraulic conductivity. Consequently, the inventory below the leak position was transported to the groundwater by the leak water at an enhanced rate. The water fluxes at the groundwater table beneath T tank farm are shown in Figure 4.15. It took about 0.6 years (at year 2000.6) for the leaked water to move down to the groundwater. As the leak continued, the water flux increased very quickly and reached 83% of the maximum value at year 2001 and 97% at 2002. There was no noticeable difference between the two tank farms.

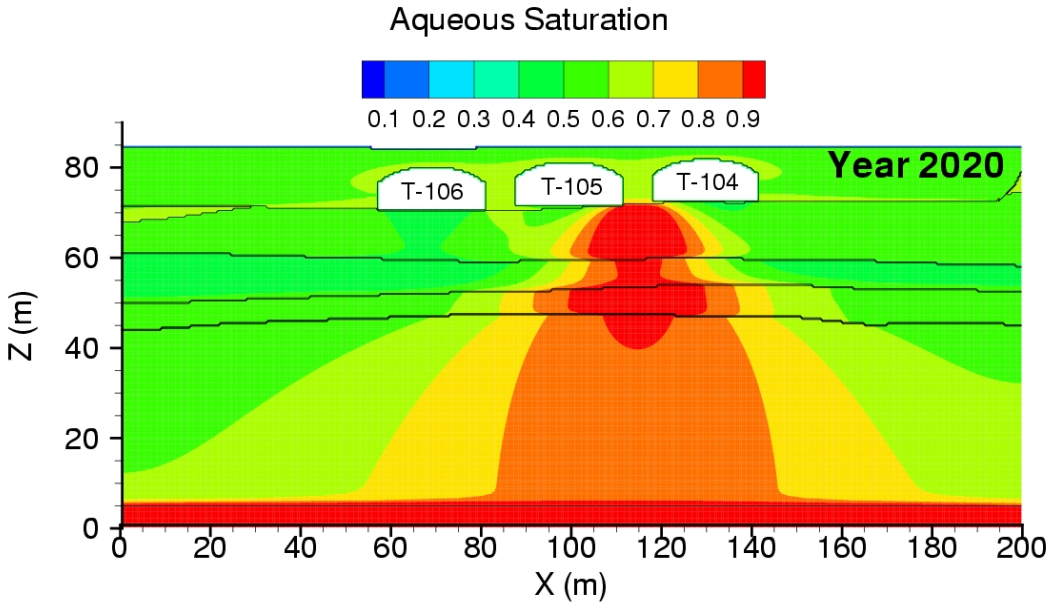

Figure 4.14. Aqueous-Phase Saturation for Cross Section T-104, -105, -106 at the End of the Waterline Leak for Case 3 (year 2020)

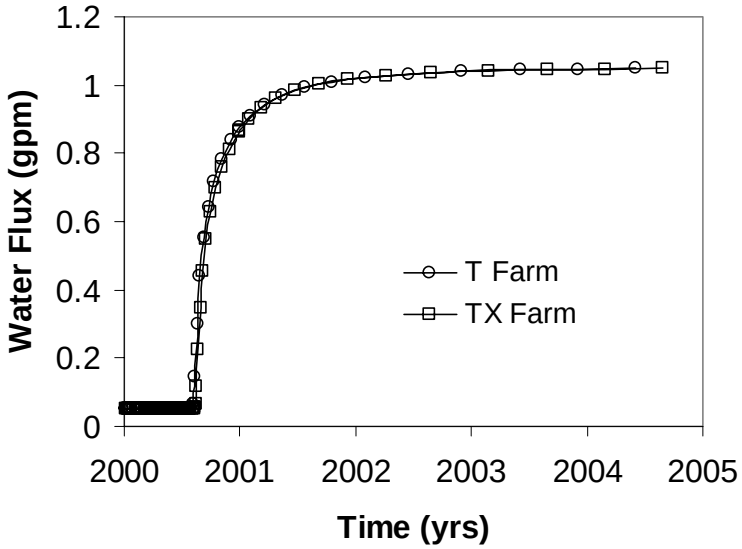

Figure 4.15. Variation of Water Flux (gmp) at the Groundwater Table for Case 3 Due to the Pipeline Leak

The distribution of the aqueous concentration of the contaminants for cross section T-104, -105, -106 at year 2040 (3000 for U-238) is shown as color images in Figures A.16 through A.19 in logarithmic scale. The concentration distribution for cross section TX-105, -106, -107, -108 at year 2040 (2010 for U-238) is shown in Figures C.16 through C.19. Due to the pipeline leak occurred between Tanks T-104 and T-105 or Tanks TX-105 and TX-106, the inventory in the soil beneath the leak position was flushed by the leak water and migrated at the enhanced rate into groundwater, while the inventory elsewhere was moving at a much slower rate. In the figures of concentration contours, this is shown by skewed distribution (Figures A.16 A.18, C.16 and C.18) or by a U-shaped flushed low concentration region (Figures A.17 A.19, C.17 and C.19).

Figures B.13 through B.20 plot the mass flux, cumulative mass, and BTCs for each of the four contaminants for cross section T-104, -105, -106 and Figures D.13 through D.20 for cross section TX-105, -106, -107, -108. Breakthrough times and peak aqueous concentrations at the fenceline are shown in Table 4.5, along with the maximum initial aqueous concentrations. Compared with the Base Case (Case 1), the 20-year pipeline leak reduced the conservative solutes travel time by 13~21 years for T farm and 23 ~31 years for TX farm; the peak concentrations of the conservative solutes increased by 284 ~537% for T farm and 94 ~679% for the TX farm. Due to the leak water, like the conservation tracers, the U-238 inventory beneath the leak position was also flushed into groundwater but at a much lower concentration.

4.4.2 Case 4 No Barrier and 200,000 gal Waterline Leak

This case differs from Case 3 in that the leak volume was smaller (1.9% of Case 3), the intensity was larger (about 28 times), and the duration was much shorter (five days versus 20 years). The flow

Table 4.5. Peak Concentrations and Arrival Times at the Fenceline for Case 3

Cross Section	T-104, -105, -106	TX-105, -106, -107, -108
Tc-99		
Arrival Time	2028 yr (-13)[(a)]	2027 yr (-23)
Peak Concentration	8.64×10^6 pCi/L (517.5%)	1.94×10^5 pCi/L (317.1%)
Maximum Initial Concentration[(b)]	5.23×10^7 pCi/L	1.29×10^6 pCi/L
U-238		
Arrival Time	2075 yr (-925)	2062 yr (-938)
Peak Concentration	1.22×10^2 pCi/L (1.0×10^{15})	1.17×10^1 pCi/L (2.0×10^{15})
Maximum Initial Concentration	1.20×10^3 pCi/L	2.49×10^2 pCi/L
NO_3		
Arrival Time	2028 yr (-14)	2027 yr (-24)
Peak Concentration	4.54×10^6 μg/L (536.8%)	1.58×10^5 μg/L (94%)
Maximum Initial Concentration	2.20×10^7 μg/L	7.22×10^6 μg/L
Cr		
Arrival Time	2028 yr (-21)	2027 yr (-31)
Peak Concentration	6.62×10^4 μg/L (284.3%)	5.27×10^3 μg/L (679.4%)
Maximum Initial Concentration	4.72×10^4 μg/L	1.21×10^4 μg/L

(a) Numbers in parentheses indicate change from Base Case.
(b) Maximum initial concentration is based on inventory data and listed for comparison with the simulated peak concentration at the compliance boundary.

environment following the five-day waterline leak event at T tank farm is shown in Figure 4.16. The large volume forced the flow to move in all directions, even upward. The soil around the leak position was saturated or nearly saturated. Different from Case 3, at the end of the leak, all the leaked water remained in the top part of the vadose zone. This water then moved slowly down to the groundwater.

The distribution of the aqueous concentration of the contaminants for cross section T-104, -105, -106 at year 2040 (3000 for U-238) is shown as color images in Figures A.20 through A.23 in logarithmic scale. The concentration distribution for cross section TX-105, -106, -107, -108 at year 2040 (2010 for U-238) is shown in Figures C.20 through C.23. Compared with Case 3, due to the much smaller total volume of the pipeline leak (1.9% of Case 3) occurring between Tanks T-104 and T-105 or Tanks TX-105 and -106, the flush effect was much weaker. It had almost no effect on the transport of U-238.

Figures B.21 through B.26 plot mass flux, cumulative mass, and BTCs for the three conservative contaminants for cross section T-104, -105, -106 and Figures D.21 through D.26 for cross section TX-105, -106, -107, -108. Breakthrough times and peak aqueous concentrations at the fenceline are shown in Table 4.6 along with the maximum initial aqueous concentrations. Compared with the Base Case (Case 1), the five-day pipeline leak reduced the travel time of the conservative solutes by just 1 ~5 years; the peak concentrations of the conservative solutes were reduced by 6.7 ~15.7% for T farm but increased by 3.9 ~32.7% for TX farm. In spite of the leak water, very little U-238 inventory was flushed into the groundwater.

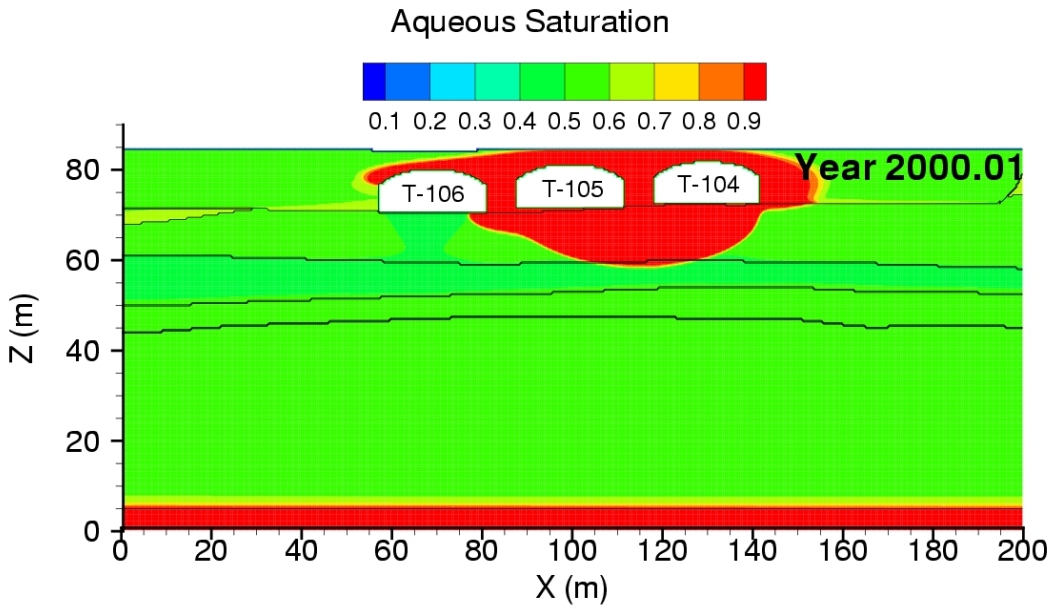

Figure 4.16. Aqueous-Phase Saturation for Cross Section T-104, -105, -106 at the End of the Waterline Leak for Case 4 (year 2000 plus five days)

Table 4.6. Peak Concentrations and Arrival Times at the Fenceline for Case 4

Cross Section	T-104, -105, -106	TX-105, -106, -107, -108
Tc-99		
Arrival Time	2036 yr (-5)[(a)]	2049 yr (-1)
Peak Concentration	1.27×10^{6} pCi/L (-9.2%)	4.87×10^{4} pCi/L (4.7%)
Maximum Initial Concentration[(b)]	5.23×10^{7} pCi/L	1.29×10^{6} pCi/L
U-238		
Arrival Time	>= 3000 yr (0)	>= 3000 yr (0)
Peak Concentration	6.28×10^{-12} pCi/L (5183.9%)	3.53×10^{-12} pCi/L (61184.6%)
Maximum Initial Concentration	1.20×10^{3} pCi/L	2.49×10^{2} pCi/L
NO_3		
Arrival Time	2038 yr (-4)	2050 yr (-1)
Peak Concentration	6.65×10^{5} µg/L (-6.7%)	8.46×10^{4} µg/L (3.9%)
Maximum Initial Concentration	2.20×10^{7} µg/L	7.22×10^{6} µg/L
Cr		
Arrival Time	2047 yr (-2)	2053 yr (-5)
Peak Concentration	1.45×10^{4} µg/L (-15.7%)	8.98×10^{2} µg/L (32.7%)
Maximum Initial Concentration	4.72×10^{4} µg/L	1.21×10^{4} µg/L

(a) Numbers in parentheses indicate change from Base Case.
(b) Maximum initial concentration is based on inventory data and listed for comparison with the simulated peak concentration at the compliance boundary.

4.4.3 Effects of Waterline Leak

When a waterline leak occurred, additional water was introduced into the system. Figure 4.17 shows the average saturation of the system without (Case 1) and with (Cases 3 and 4) a waterline leak. Average saturation increased right after a leak started. For Cases 3 and 4 this effect diminished at year 2040.

Generally, the solutes broke though faster if there was a waterline leak. A relative small five-day leak (Case 4) did not affect the peak concentration much, while a large 20-yr leak (Case 3) significantly increased the peak concentration and reduced the solute travel in the vadose zone. As an example, a comparison of Tc-99 BTCs for T farm with and without the pipeline leak is shown in Figure 4.18.

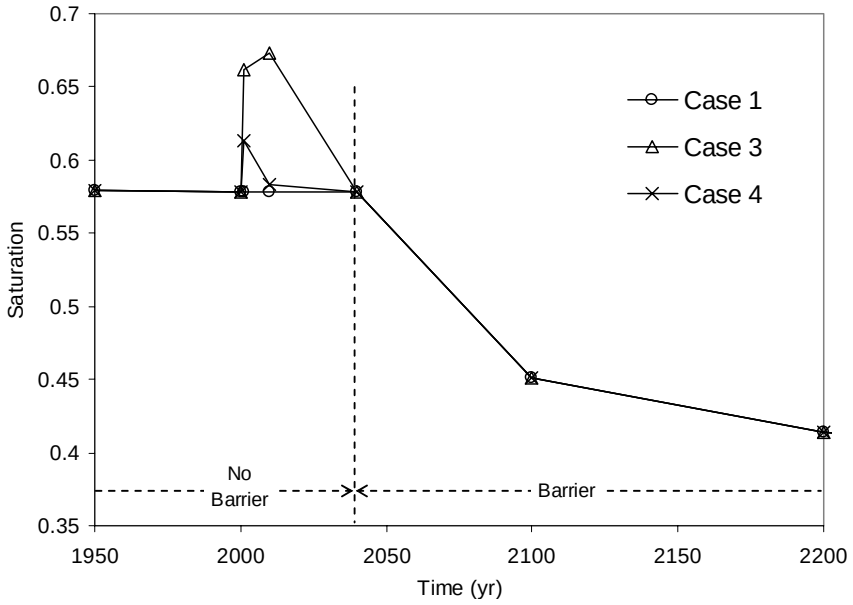

Figure 4.17. Effects of Waterline Leaks on the Mean Saturation of T Tank Farm

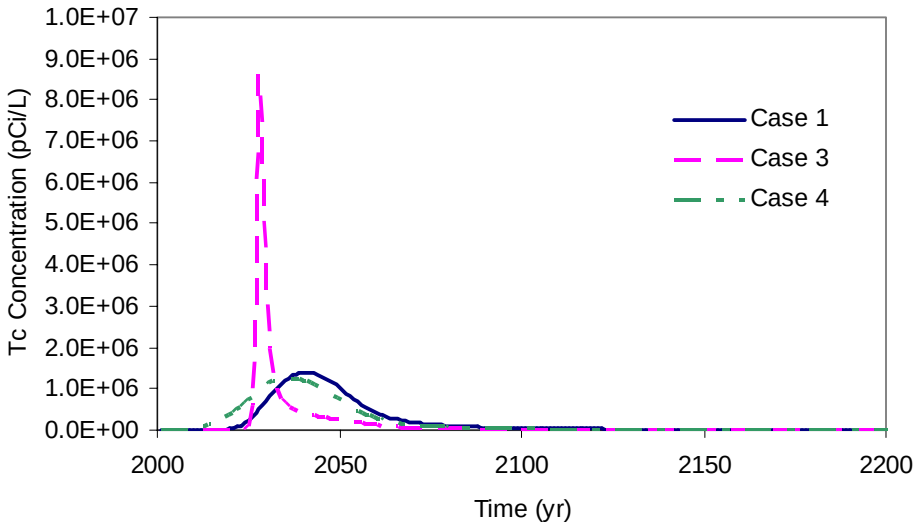

Figure 4.18. Effects of Waterline Leaks on Tc-99 Concentration at the Fenceline of T Tank Farm

4.5 No Interim Barrier and Nonuniform Inventory Distribution

This suite of simulations (Case 5) investigated solute transport through two cross sections in the T and TX-TY WMA considering natural surface infiltration with no waterline leaks or interim surface barriers but with a closure barrier by the year 2040. Different from the Base Case (Case 1), inventories of the four contaminant species were initialized using the nonuniform distribution pattern (Figures 4.6 through 4.9). The aqueous saturation field was the same as that of the Base Case.

The distribution of the aqueous concentration of the contaminants for cross section T-104, -105, -106 at year 2040 (3000 for U-238) is shown as color images in Figures A.24 through A.27 in logarithmic scale. The concentration distribution for cross section TX-105, -106, -107, -108 at year 2040 (3000 for U-238) is shown in Figures C.24 through C.27. Similar to the Base Case, the three conservative solutes (Tc-99, NO_3, and Cr) migrated downward at similar velocity, while U-238 had not reached the groundwater table by the end of the simulation (year 3000).

Figures B.27 through B.32 plot the mass flux, cumulative mass, and BTCs for the three conservative contaminants for cross section T-104, -105, -106; Figures D.27 through D.32 plot cross section TX-105, -106, -107, -108. Breakthough times and peak aqueous concentrations at the fenceline are shown in Table 4.7 along with the maximum initial aqueous concentrations. Compared with the Base Case, the distribution of inventory, uniform or nonuniform, has little effect on peak arrival time; the peak concentrations of the conservative solutes varied by -6.9% to 0.2% for T tank farm and 11% to 49.4% for TX tank farm. The differences were possibly due to geology.

Table 4.7. Peak Concentrations and Arrival Times at the WMA Fenceline for Case 5

Cross Section	T-104, -105, -106	TX-105, -106, -107, -108
Tc-99		
Arrival Time	2040 yr (-1)[(a)]	2052 yr (2)
Peak Concentration	1.39×10^{6} pCi/L (-0.2%)	5.16×10^{4} pCi/L (11%)
Maximum Initial Concentration[(b)]	2.00×10^{10} pCi/L	2.59×10^{9} pCi/L
U-238		
Arrival Time	>= 3000 yr (0)	>= 3000 yr (0)
Peak Concentration	9.63×10^{-15} pCi/L (-91.8%)	3.46×10^{-15} pCi/L (-39.9%)
Maximum Initial Concentration	2.22×10^{6} pCi/L	2.03×10^{5} pCi/L
NO_3		
Arrival Time	2042 yr (0)	2052 yr (1)
Peak Concentration	7.15×10^{5} µg/L (0.2%)	9.62×10^{4} µg/L (18.2%)
Maximum Initial Concentration	6.22×10^{9} µg/L	5.97×10^{9} µg/L
Cr		
Arrival Time	2050 yr (1)	2057 yr (-1)
Peak Concentration	1.60×10^{4} µg/L (-6.9%)	1.01×10^{3} µg/L (49.4%)
Maximum Initial Concentration	8.42×10^{7} µg/L	8.44×10^{6} µg/L

(a) Numbers in parentheses indicate change from Base Case.
(b) Maximum initial concentration is based on inventory data and listed for comparison with the simulated peak concentration at the compliance boundary.

4.6 Base Case with Reduced Meteoric Recharge

This suite of simulations (Cases 6, 7, and 8) investigated solute transport through two cross sections in the T and TX-TY WMA considering reduced surface infiltration (50 mm/yr for Case 6, 30 mm/yr for Case 7, and 10 mm/yr for Case 8), with no waterline leaks and no interim surface barriers but with a closure barrier by the year 2040. Inventories of the four contaminant species were initialized using the uniform distribution pattern (Figures 4.2 through 4.5).

4.6.1 Case 6, Base Case with 50 mm/yr Meteoric Recharge

Distribution of the aqueous concentration of contaminants for cross section T-104, -105, -106 at year 2040 (3000 for U-238) is shown as color images in Figures A.28 through A.31 in logarithmic scale. The concentration distribution for cross section TX-105, -106, -107, -108 at year 2040 (3000 for U-238) is shown in Figures C.28 through C.31. The three conservative solutes (Tc-99, NO_3, and Cr) migrated downward at similar velocity, while U-238 had not reached the groundwater table by the end of the simulation (year 3000).

Figures B.33 through B.38 plot mass flux, cumulative mass, and BTCs for the three conservative contaminants for cross section T-104, -105, -106; Figures D.33 through D.38 plot TX-105, -106, -107, -108. Breakthrough times and peak aqueous concentrations at the fenceline are shown in Table 4.8, along with the maximum initial aqueous concentrations. Compared with the base case (Case 1), the reduced natural recharge from 100 mm to 50 mm/yr increased the conservative solute travel time by

Table 4.8. Peak Concentrations and Arrival Times at the WMA Fenceline for Case 6

Cross Section	T-104, -105, -106	TX-105, -106, -107, -108
Tc-99		
Arrival Time	2057 yr (16)[(a)]	2066 yr (16)
Peak Concentration	7.86×10^5 pCi/L (-43.8%)	1.23×10^4 pCi/L (-73.4%)
Maximum Initial Concentration[(b)]	5.23×10^7 pCi/L	1.29×10^6 pCi/L
U-238		
Arrival Time	>= 3000 yr (0)	>= 3000 yr (0)
Peak Concentration	0.00×10^0 pCi/L (-100%)	0.00×10^0 pCi/L (-100%)
Maximum Initial Concentration	1.20×10^3 pCi/L	2.49×10^2 pCi/L
NO_3		
Arrival Time	2058 yr (16)	2069 yr (18)
Peak Concentration	3.86×10^5 µg/L (-45.9%)	1.89×10^4 µg/L (-76.8%)
Maximum Initial Concentration	2.20×10^7 µg/L	7.22×10^6 µg/L
Cr		
Arrival Time	2064 yr (15)	>= 3000 yr (942)
Peak Concentration	6.09×10^3 µg/L (-64.6%)	8.45×10^1 µg/L (-87.5%)
Maximum Initial Concentration	4.72×10^4 µg/L	1.21×10^4 µg/L

(a) Numbers in parentheses indicate change from Base Case.
(b) Maximum initial concentration is based on inventory data and listed for comparison with the simulated peak concentration at the compliance boundary.

15~16 yr for T farm and 16~18 yr for TX farm; peak concentrations reduced by 43.8 ~64.6% for T farm and 73.4 ~87.5% for TX farm. For Cr at TX farm, the concentration at year 3000 was higher than the peak concentration at about 2070. The higher value is reported but not compared with the Base Case.

4.6.2 Case 7 Base Case with 30 mm/yr Meteoric Recharge

Distribution of the aqueous concentration of contaminants for cross section T-104, -105, -106 at year 2100 (3000 for U-238) is shown as color images in Figures A.32 through A.35 in logarithmic scale. The concentration distribution for cross section TX-105, -106, -107, -108 at year 2040 (3000 for U-238) is shown in Figures C.32 through C.35. The three conservative solutes (Tc-99, NO_3, and Cr) migrated downward at similar velocity while U-238 had not reached the groundwater table by the end of the simulation (year 3000).

Figures B.39 through B.44 plot mass flux, cumulative mass, and BTCs for the three conservative contaminants for cross section T-104, -105, -106 and Figures D.39 through D.44 for cross section TX-105, -106, -107, -108. Breakthrough times and peak aqueous concentrations at the fenceline are shown in Table 4.9 along with maximum initial aqueous concentrations. Compared with the Base Case, the reduced natural recharge from 100 to 30 mm/yr increased the conservative solute travel time by 29 ~33yr for T farm and 35 ~41 yr for TX farm; peak concentrations reduced by 68.6 ~84.2% for T farm and 88.9 ~90.9% for TX farm. For Cr at TX farm, the concentration at year 3000 was higher than the peak concentration at about 2070. The higher value is reported but not compared with the Base Case.

Table 4.9. Peak Concentrations and Arrival Times at the WMA Fenceline for Case 7

Cross Section	T-104, -105, -106	TX-105, -106, -107, -108
Tc-99		
Arrival Time	2070 yr (29)[(a)]	2085 yr (35)
Peak Concentration	4.38×10^5 pCi/L (-68.6%)	5.13×10^3 pCi/L (-88.9%)
Maximum Initial Concentration[(b)]	5.23×10^7 pCi/L	1.29×10^6 pCi/L
U-238		
Arrival Time	>= 3000 yr (0)	>= 3000 yr (0)
Peak Concentration	0.00×10^0 pCi/L (-100%)	0.00×10^0 pCi/L (-100%)
Maximum Initial Concentration	1.20×10^3 pCi/L	2.49×10^2 pCi/L
NO_3		
Arrival Time	2071 yr (29)	2092 yr (41)
Peak Concentration	2.11×10^5 µg/L (-70.3%)	7.37×10^3 µg/L (-90.9%)
Maximum Initial Concentration	2.20×10^7 µg/L	7.22×10^6 µg/L
Cr		
Arrival Time	2082 yr (33)	>= 3000 yr (942)
Peak Concentration	2.72×10^3 µg/L (-84.2%)	6.21×10^1 µg/L (-90.8%)
Maximum Initial Concentration	4.72×10^4 µg/L	1.21×10^4 µg/L

(a) Numbers in parentheses indicate change from Base Case.
(b) Maximum initial concentration is based on inventory data and listed for comparison with the simulated peak concentration at the compliance boundary.

4.6.3 Case 8, Base Case with 10 mm/yr Meteoric Recharge

Distribution of the aqueous concentration of contaminants for cross section T-104, -105, -106 at year 2100 (3000 for U-238) is shown as color images in Figures A.36 through A.39 in logarithmic scale. The concentration distribution for cross section TX-105, -106, -107, -108 at year 2100 (3000 for U-238) is shown in Figures C.36 through C.39. The three conservative solutes (Tc-99, NO_3, and Cr) migrated downward at similar velocity, while U-238 had not reached the groundwater table by the end of the simulation (year 3000).

Figures B.45 through B.50 plot mass flux, cumulative mass, and BTCs for the three conservative contaminants for cross section T-104, -105, -106 and Figures D.45 through D.50 for cross section TX-105, -106, -107, -108. Breakthrough times and peak aqueous concentrations at the fenceline are shown in Table 4.10 along with the maximum initial aqueous concentrations. Compared with the Base Case, the reduced natural recharge from 100 to 10 mm/yr increased the conservative solute travel time by 58 ~79 yr for T farm; the peak concentrations reduced by 87.5 ~94.5% for T farm and 95.1 ~96.5% for TX farm. For TX farm, the concentrations of conservative solutes at year 3000 were higher than the peak concentration at about 2070; the higher value is reported but not compared with the Base Case.

Table 4.10. Peak Concentrations and Arrival Times at the WMA Fenceline for Case 8

Cross Section	T-104, -105, -106	TX-105, -106, -107, -108
Tc-99		
Arrival Time	2099 yr (58)[(a)]	>= 3000 yr (950)
Peak Concentration	1.74×10^5 pCi/L (-87.5%)	2.27×10^3 pCi/L (-95.1%)
Maximum Initial Concentration[(b)]	5.23×10^7 pCi/L	1.29×10^6 pCi/L
U-238		
Arrival Time	>= 3000 yr (0)	>= 3000 yr (0)
Peak Concentration	0.00×10^0 pCi/L (-100%)	0.00×10^0 pCi/L (-100%)
Maximum Initial Concentration	1.20×10^3 pCi/L	2.49×10^2 pCi/L
NO_3		
Arrival Time	2100 yr (58)	>= 3000 yr (949)
Peak Concentration	8.37×10^4 μg/L (-88.2%)	4.18×10^3 μg/L (-94.8%)
Maximum Initial Concentration	2.20×10^7 μg/L	7.22×10^6 μg/L
Cr		
Arrival Time	2128 yr (79)	>= 3000 yr (942)
Peak Concentration	9.47×10^2 μg/L (-94.5%)	2.34×10^1 μg/L (-96.5%)
Maximum Initial Concentration	4.72×10^4 μg/L	1.21×10^4 μg/L

(a) Numbers in parentheses indicate change from Base Case.
(b) Maximum initial concentration is based on inventory data and listed for comparison with the simulated peak concentration at the compliance boundary.

4.6.4 Effects of Meteoric Recharge

The reduction in meteoric recharge before the barrier was applied led to smaller soil saturation (Figure 4.19), as expected, and thus longer solute travel time in the vadose zone and smaller peak fenceline concentration (Figure 4.20). The effect on soil saturation lasted for about 50 more years after the barrier was applied in 2050. However, the reduced recharge rate affected the BTCs until the end of the simulation. The fenceline concentrations at year 3000 were higher for cases with reduced natural recharge (Cases 6, 7, and 8) than for those of the Base Case, indicating that the fundamental impact of reduced natural recharge is a smoothing of breakthrough concentrations at compliance points.

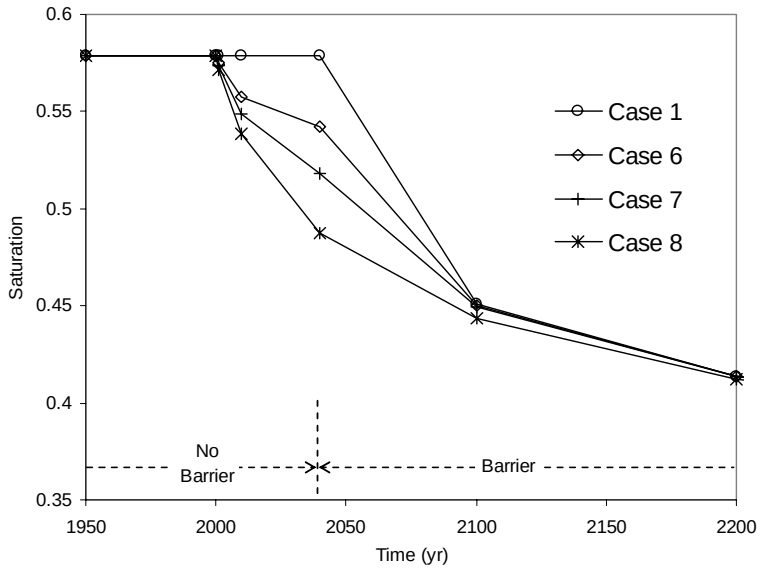

Figure 4.19. Effects of Reduced Meteoric Recharge on the Mean Saturation of T Tank Farm

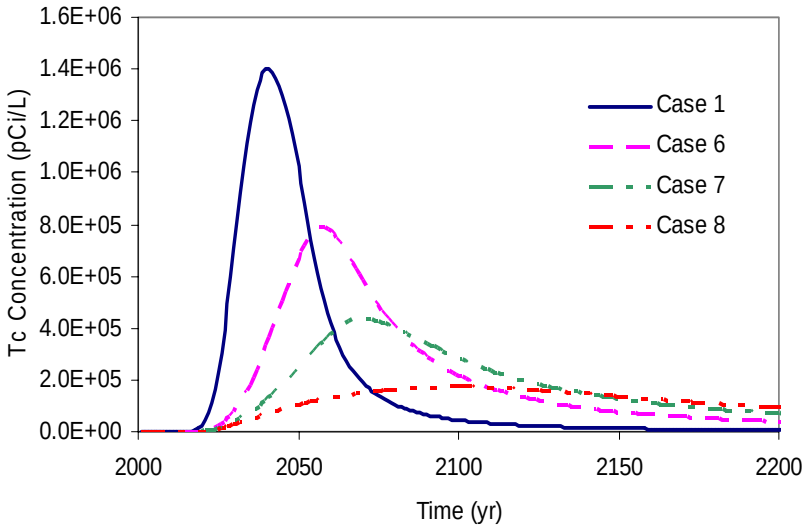

Figure 4.20. Effect of Reduced Meteoric Recharge on Tc-99 Concentration at the Fence Line of T Tank Farm

4.7 Solute Mass Balance

Mass balance checks were performed on the four solutes (Tc-99, U-238, NO_3, and Cr) for each simulation case at year 3000 using this expression:

$$m_{error} = \frac{m_{released} - m_{domain} - m_{exit}}{m_{released}} \times 100\% \tag{4.1}$$

where m_{error} is the mass balance error in percent, $m_{released}$ is the total amount of solute released in the system, m_{domain} is the solute inventory in the domain computed from the STOMP plot file output at year 3000, and m_{exit} is the integrated solute inventory, leaving the computational domain computed from the STOMP surface flux output. The amount of each solute released into the system was the inventory at the 2-D slice. The solute mass leaving the computational domain through the aquifer was determined using surface flux output on the eastern side of the domain. The surface-flux output provided both the solute flux rate and cumulative mass. Other than solving the solute mass conservation equations, the STOMP simulator contains no algorithms for correcting local or global mass. Therefore, mass balance errors represent the actual mass balance errors from the conservation equations. Expressed as percent error, mass balance errors were small, no more than 0.2% except in T Case 5 (2.6%), as shown in Tables 4.11 through 4.22 for the four contaminants.

Table 4.11. Predicted Peak Tc-99 Flux, Arrival Time, and Cumulative Mass

Case	Groundwater Table			Fenceline		
	Flux (pCi/yr)	Arrival Time (yr)	Cumulative Mass (pCi)	Flux (Ci/yr)	Arrival Time (yr)	Cumulative Mass (pCi)
T Case 1	3.07E+12	2037	6.19E+13	3.07E+12	2041	6.17E+13
T Case 2	7.51E+11	2037	5.65E+13	7.37E+11	2041	5.62E+13
T Case 3	2.90E+12	2016	6.18E+13	2.00E+13	2028	6.17E+13
T Case 4	2.80E+12	2032	6.19E+13	2.78E+12	2036	6.18E+13
T Case 5	1.62E+11	2037	6.19E+13	1.62E+11	2040	6.17E+13
T Case 6	1.50E+12	2053	6.03E+13	1.48E+12	2057	6.01E+13
T Case 7	7.85E+11	2066	5.80E+13	7.78E+11	2070	5.78E+13
T Case 8	2.96E+11	2094	5.23E+13	2.96E+11	2098	5.21E+13
TX Case 1	1.31E+11	2047	3.85E+12	1.27E+11	2050	3.83E+12
TX Case 2	9.86E+09	2054	1.73E+12	9.78E+09	2058	1.71E+12
TX Case 3	1.12E+11	2019	3.98E+12	5.94E+11	2027	3.96E+12
TX Case 4	1.38E+11	2046	3.97E+12	1.35E+11	2048	3.96E+12
TX Case 5	9.91E+09	2047	4.16E+12	9.65E+09	2051	4.13E+12
TX Case 6	3.04E+10	2061	2.66E+12	2.99E+10	2064	2.65E+12
TX Case 7	1.21E+10	2080	1.91E+12	1.20E+10	2083	1.90E+12
TX Case 8	5.15E+09	>=3000	1.15E+12	5.09E+09	>=3000	1.14E+12

Table 4.12. Predicted Peak U-238 Flux, Arrival Time, and Cumulative Mass

Case	Groundwater Table			Fenceline		
	Flux (pCi/yr)	Arrival Time (yr)	Cumulative Mass (Ci)	Flux (pCi/yr)	Arrival Time (yr)	Cumulative Mass (pCi)
T Case 1	1.11E-06	>=3000	4.04E-05	4.93E-07	>=3000	2.35E-05
T Case 2	0.00E+00	>=3000	0.00E+00	0.00E+00	>=3000	0.00E+00
T Case 3	4.37E+09	2009	1.47E+10	3.09E+09	2013	1.46E+10
T Case 4	5.82E-05	>=3000	3.28E-03	2.60E-05	>=3000	2.22E-03
T Case 5	1.86E-09	>=3000	2.58E-06	1.02E-09	>=3000	1.72E-06
T Case 6	0.00E+00	>=3000	0.00E+00	0.00E+00	>=3000	0.00E+00
T Case 7	0.00E+00	>=3000	0.00E+00	0.00E+00	>=3000	0.00E+00
T Case 8	0.00E+00	>=3000	0.00E+00	0.00E+00	>=3000	0.00E+00
TX Case 1	6.07E-08	>=3000	1.52E-06	3.16E-08	>=3000	9.11E-07
TX Case 2	0.00E+00	>=3000	0.00E+00	0.00E+00	>=3000	0.00E+00
TX Case 3	6.14E+08	2010	1.76E+09	4.62E+08	2013	1.76E+09
TX Case 4	2.85E-05	>=3000	1.14E-03	1.94E-05	>=3000	7.90E-04
TX Case 5	1.45E-09	>=3000	1.01E-06	7.07E-10	>=3000	6.09E-07
TX Case 6	0.00E+00	>=3000	0.00E+00	0.00E+00	>=3000	0.00E+00
TX Case 7	0.00E+00	>=3000	0.00E+00	0.00E+00	>=3000	0.00E+00
TX Case 8	0.00E+00	>=3000	0.00E+00	0.00E+00	>=3000	0.00E+00

Table 4.13. Predicted Peak NO_3 Flux, Arrival Time, and Cumulative Mass

Case	Groundwater Table			Fenceline		
	Flux (µg/yr)	Arrival Time (yr)	Cumulative Mass (µg/yr)	Flux (Ci/yr)	Arrival Time (yr)	Cumulative Mass (µg)
T Case 1	1.50E+12	2039	3.63E+13	1.50E+12	2042	3.62E+13
T Case 2	3.47E+11	2037	3.09E+13	3.40E+11	2041	3.08E+13
T Case 3	1.58E+12	2015	3.64E+13	1.01E+13	2028	3.63E+13
T Case 4	1.41E+12	2034	3.64E+13	1.40E+12	2038	3.63E+13
T Case 5	9.14E+10	2039	3.64E+13	9.13E+10	2042	3.63E+13
T Case 6	7.07E+11	2054	3.44E+13	6.97E+11	2057	3.43E+13
T Case 7	3.65E+11	2066	3.22E+13	3.62E+11	2070	3.20E+13
T Case 8	1.37E+11	2094	2.77E+13	1.37E+11	2099	2.76E+13
TX Case 1	1.63E+10	2047	8.72E+11	1.59E+10	2050	8.67E+11
TX Case 2	9.90E+08	2061	3.91E+11	9.83E+08	2065	3.88E+11
TX Case 3	1.25E+10	2047	8.74E+11	3.46E+10	2027	8.70E+11
TX Case 4	1.70E+10	2046	8.86E+11	1.66E+10	2049	8.82E+11
TX Case 5	1.91E+10	2047	6.97E+12	1.86E+10	2051	6.93E+12
TX Case 6	3.30E+09	2064	6.15E+11	3.25E+09	2067	6.11E+11
TX Case 7	1.23E+09	2086	4.39E+11	1.22E+09	2090	4.36E+11
TX Case 8	6.80E+08	>=3000	2.50E+11	6.72E+08	>=3000	2.47E+11

Table 4.14. Predicted Peak Cr Flux, Arrival Time, and Cumulative Mass

Case	Groundwater Table			Fenceline		
	Flux (µg/yr)	Arrival Time (yr)	Cumulative Mass (µg/yr)	Flux (Ci/yr)	Arrival Time (yr)	Cumulative Mass (µg)
T Case 1	1.07E+11	2045	9.84E+11	1.05E+11	2048	9.77E+11
T Case 2	1.16E+10	2048	6.80E+11	1.15E+10	2053	6.75E+11
T Case 3	2.86E+11	2001	9.92E+11	4.36E+11	2028	9.91E+11
T Case 4	9.30E+10	2042	9.96E+11	9.01E+10	2046	9.89E+11
T Case 5	2.55E+09	2046	9.80E+11	2.50E+09	2049	9.76E+11
T Case 6	3.24E+10	2059	8.61E+11	3.18E+10	2063	8.56E+11
T Case 7	1.36E+10	2076	7.28E+11	1.35E+10	2080	7.24E+11
T Case 8	4.55E+09	2121	5.19E+11	4.54E+09	2126	5.14E+11
TX Case 1	3.86E+09	2053	9.49E+10	3.73E+09	2056	9.43E+10
TX Case 2	2.49E+08	>=3000	1.72E+10	2.44E+08	>=3000	1.70E+10
TX Case 3	1.71E+10	2002	1.07E+11	3.47E+10	2027	1.06E+11
TX Case 4	5.53E+09	2048	1.04E+11	5.18E+09	2051	1.03E+11
TX Case 5	2.13E+08	2052	1.12E+11	2.07E+08	2056	1.11E+11
TX Case 6	4.12E+08	>=3000	4.47E+10	4.08E+08	>=3000	4.42E+10
TX Case 7	3.05E+08	>=3000	2.08E+10	3.00E+08	>=3000	2.06E+10
TX Case 8	1.16E+08	>=3000	6.72E+09	1.13E+08	>=3000	6.61E+09

Table 4.15. Predicted Peak Tc-99 Aqueous Concentrations (pCi/L) and Arrival Time (yr) Summary

Case	Groundwater		Fenceline		200 West (south)		Exclusion Boundary (south)		Columbia River (south)		Exclusion Boundary (north)		Columbia River (north)	
	Conc.	Time	Conc.	Time	Conc.	Time	Conc.	Time	Conc.	Time	Conc.	Time	Conc.	Time
T Case 1	1.40E+06	2037	1.40E+06	2041	1.35E+04	2138	1.20E+03	2267	4.03E+02	2354	1.00E+04	2172	4.26E+02	2827
T Case 2	4.10E+05	2038	4.09E+05	2042	5.61E+03	2156	4.88E+02	2281	1.58E+02	2366	4.48E+03	2193	2.44E+02	2858
T Case 3	7.53E+05	2029	8.64E+06	2028	1.48E+04	2125	1.32E+03	2254	4.48E+02	2342	1.07E+04	2159	4.41E+02	2814
T Case 4	1.28E+06	2032	1.27E+06	2036	1.37E+04	2133	1.21E+03	2262	4.04E+02	2349	1.01E+04	2166	4.31E+02	2821
T Case 5	1.40E+06	2037	1.39E+06	2040	7.15E+02	2138	6.35E+01	2267	2.13E+01	2354	5.28E+02	2171	2.25E+01	2827
T Case 6	7.86E+05	2054	7.86E+05	2057	9.19E+03	2160	8.07E+02	2287	2.65E+02	2373	7.09E+03	2195	3.43E+02	2854
T Case 7	4.39E+05	2066	4.38E+05	2070	6.27E+03	2178	5.42E+02	2303	1.75E+02	2389	5.01E+03	2213	2.69E+02	2876
T Case 8	1.74E+05	2095	1.74E+05	2099	3.19E+03	2208	2.66E+02	2330	8.34E+01	2414	2.68E+03	2244	1.69E+02	2911
TX Case 1	4.63E+04	2047	4.65E+04	2050	6.32E+02	2153	6.07E+01	2280	1.93E+01	2364	3.88E+02	2240	2.43E+01	2832
TX Case 2	4.21E+03	2056	4.20E+03	2060	9.15E+01	2181	8.52E+00	2302	2.57E+00	2383	6.78E+01	2278	5.01E+00	2878
TX Case 3	3.22E+04	2047	1.94E+05	2027	6.89E+02	2140	6.61E+01	2266	2.09E+01	2350	4.27E+02	2226	2.66E+01	2817
TX Case 4	4.87E+04	2046	4.87E+04	2049	6.97E+02	2149	6.68E+01	2276	2.12E+01	2360	4.25E+02	2235	2.64E+01	2826
TX Case 5	5.11E+04	2048	5.16E+04	2052	4.83E+01	2154	4.64E+00	2281	1.47E+00	2365	2.97E+01	2241	1.86E+00	2833
TX Case 6	1.24E+04	2062	1.23E+04	2066	2.24E+02	2180	2.12E+01	2304	6.53E+00	2387	1.54E+02	2272	1.07E+01	2869
TX Case 7	5.15E+03	2081	5.13E+03	2085	1.10E+02	2203	1.02E+01	2325	3.09E+00	2407	8.06E+01	2299	5.90E+00	2897
TX Case 8	2.29E+03	>=3000	2.27E+03	>=3000	4.07E+01	2251	3.69E+00	2371	1.09E+00	2453	3.22E+01	2349	2.52E+00	2947

Table 4.16. Predicted Peak U-238 Aqueous Concentrations (pCi/L) and Arrival Time (yr) Summary

Case	Groundwater		Fenceline		200 West (south)		Exclusion Boundary (south)		Columbia River (south)		Exclusion Boundary (north)		Columbia River (north)	
	Conc.	Time	Conc.	Time	Conc.	Time	Conc.	Time	Conc.	Time	Conc.	Time	Conc.	Time
T Case 1	2.67E-13	>=3000	1.19E-13	>=3000	9.97E-16	2870	5.49E-41	>=3000	0.00E+00	>=3000	6.15E-16	>=3000	0.00E+00	>=3000
T Case 2	0.00E+00	>=3000	0.00E+00	>=3000	0.00E+00	>=3000	0.00E+00	>=3000	0.00E+00	>=3000	0.00E+00	>=3000	0.00E+00	>=3000
T Case 3	1.21E+02	2009	1.22E+02	2075	4.36E+01	2630	6.62E-09	>=3000	0.00E+00	>=3000	3.26E+01	2828	0.00E+00	>=3000
T Case 4	1.40E-11	>=3000	6.28E-12	>=3000	3.66E-13	>=3000	1.51E-30	>=3000	0.00E+00	>=3000	2.50E-13	>=3000	0.00E+00	>=3000
T Case 5	1.77E-14	>=3000	9.63E-15	>=3000	2.24E-18	>=3000	1.43E-41	>=3000	0.00E+00	>=3000	8.12E-19	>=3000	0.00E+00	>=3000
T Case 6	0.00E+00	>=3000	0.00E+00	>=3000	0.00E+00	>=3000	0.00E+00	>=3000	0.00E+00	>=3000	0.00E+00	>=3000	0.00E+00	>=3000
T Case 7	0.00E+00	>=3000	0.00E+00	>=3000	0.00E+00	>=3000	0.00E+00	>=3000	0.00E+00	>=3000	0.00E+00	>=3000	0.00E+00	>=3000
T Case 8	0.00E+00	>=3000	0.00E+00	>=3000	0.00E+00	>=3000	0.00E+00	>=3000	0.00E+00	>=3000	0.00E+00	>=3000	0.00E+00	>=3000
TX Case	1.11E-14	>=3000	5.76E-15	>=3000	2.57E-18	>=3000	0.00E+00	>=3000	0.00E+00	>=3000	9.35E-35	>=3000	0.00E+00	>=3000
TX Case	0.00E+00	>=3000	0.00E+00	>=3000	0.00E+00	>=3000	0.00E+00	>=3000	0.00E+00	>=3000	0.00E+00	>=3000	0.00E+00	>=3000
TX Case	1.41E+01	2010	1.17E+01	2062	6.29E+00	2625	1.53E-09	>=3000	0.00E+00	>=3000	1.79E+00	>=3000	0.00E+00	>=3000
TX Case	5.20E-12	>=3000	3.53E-12	>=3000	1.17E-13	>=3000	7.90E-31	>=3000	0.00E+00	>=3000	6.05E-16	>=3000	0.00E+00	>=3000
TX Case	7.10E-15	>=3000	3.46E-15	>=3000	7.42E-19	>=3000	0.00E+00	>=3000	0.00E+00	>=3000	1.95E-22	>=3000	0.00E+00	>=3000
TX Case	0.00E+00	>=3000	0.00E+00	>=3000	0.00E+00	>=3000	0.00E+00	>=3000	0.00E+00	>=3000	0.00E+00	>=3000	0.00E+00	>=3000
TX Case	0.00E+00	>=3000	0.00E+00	>=3000	0.00E+00	>=3000	0.00E+00	>=3000	0.00E+00	>=3000	0.00E+00	>=3000	0.00E+00	>=3000
TX Case	0.00E+00	>=3000	0.00E+00	>=3000	0.00E+00	>=3000	0.00E+00	>=3000	0.00E+00	>=3000	0.00E+00	>=3000	0.00E+00	>=3000

Table 4.17. Predicted Peak NO_3 Aqueous Concentrations (μg/L) and Arrival Time (yr) Summary

Case	Groundwater		Fenceline		200 West (south)		Exclusion Boundary (south)		Columbia River (south)		Exclusion Boundary (north)		Columbia River (north)	
	Conc.	Time	Conc.	Time	Conc.	Time	Conc.	Time	Conc.	Time	Conc.	Time	Conc.	Time
T Case 1	7.12E+05	2039	7.13E+05	2042	7.15E+03	2140	6.34E+02	2269	2.12E+02	2356	5.32E+03	2174	2.31E+02	2830
T Case 2	1.97E+05	2038	1.96E+05	2042	2.65E+03	2157	2.30E+02	2282	7.44E+01	2367	2.13E+03	2194	1.18E+02	2861
T Case 3	4.08E+05	2029	4.54E+06	2028	7.86E+03	2127	7.03E+02	2255	2.38E+02	2342	5.76E+03	2160	2.42E+02	2816
T Case 4	6.68E+05	2034	6.65E+05	2038	7.32E+03	2136	6.47E+02	2264	2.16E+02	2351	5.45E+03	2169	2.36E+02	2824
T Case 5	7.15E+05	2039	7.15E+05	2042	4.35E+02	2140	3.86E+01	2269	1.29E+01	2355	3.24E+02	2174	1.41E+01	2830
T Case 6	3.86E+05	2054	3.86E+05	2058	4.50E+03	2162	3.94E+02	2288	1.29E+02	2375	3.49E+03	2197	1.73E+02	2857
T Case 7	2.12E+05	2067	2.11E+05	2071	2.98E+03	2179	2.57E+02	2304	8.28E+01	2390	2.39E+03	2215	1.31E+02	2879
T Case 8	8.38E+04	2095	8.37E+04	2100	1.49E+03	2208	1.24E+02	2330	3.88E+01	2415	1.25E+03	2245	7.96E+01	2913
TX Case 1	8.11E+04	2048	8.14E+04	2051	7.70E+01	2154	7.40E+00	2281	2.35E+00	2365	4.72E+01	2241	2.95E+00	2833
TX Case 2	5.96E+03	2063	5.94E+03	2067	9.66E+00	2189	8.93E-01	2309	2.67E-01	2390	7.30E+00	2287	5.50E-01	2887
TX Case 3	6.22E+04	2048	1.58E+05	2027	7.64E+01	2147	7.29E+00	2273	2.29E+00	2357	4.76E+01	2232	2.99E+00	2824
TX Case 4	8.44E+04	2047	8.46E+04	2050	8.17E+01	2151	7.84E+00	2278	2.49E+00	2363	4.97E+01	2237	3.09E+00	2829
TX Case 5	9.53E+04	2048	9.62E+04	2052	9.05E+01	2154	8.70E+00	2281	2.76E+00	2366	5.53E+01	2241	3.44E+00	2832
TX Case 6	1.90E+04	2065	1.89E+04	2069	2.58E+01	2185	2.44E+00	2309	7.46E-01	2391	1.81E+01	2278	1.27E+00	2875
TX Case 7	7.39E+03	2088	7.37E+03	2092	1.18E+01	2211	1.09E+00	2332	3.28E-01	2414	8.84E+00	2308	6.59E-01	2907
TX Case 8	4.23E+03	>=3000	4.18E+03	>=3000	4.05E+00	2264	3.66E-01	2383	1.08E-01	2465	3.25E+00	2363	2.57E-01	2963

Table 4.18. Predicted Peak Cr Aqueous Concentrations (μg/L) and Arrival Time (yr) Summary

Case	Groundwater		Fenceline		200 West (south)		Exclusion Boundary (south)		Columbia River (south)		Exclusion Boundary (north)		Columbia River (north)	
	Conc.	Time	Conc.	Time	Conc.	Time	Conc.	Time	Conc.	Time	Conc.	Time	Conc.	Time
T Case 1	1.72E+04	2045	1.72E+04	2049	5.06E+02	2147	4.48E+01	2275	1.49E+01	2362	3.81E+02	2181	1.72E+01	2839
T Case 2	2.31E+03	2051	2.30E+03	2055	1.10E+02	2175	9.34E+00	2297	2.97E+00	2381	9.06E+01	2213	5.55E+00	2885
T Case 3	9.38E+03	2001	6.62E+04	2028	5.19E+02	2132	4.54E+01	2259	1.50E+01	2346	3.95E+02	2165	1.80E+01	2820
T Case 4	1.49E+04	2042	1.45E+04	2047	5.30E+02	2140	4.65E+01	2268	1.54E+01	2354	4.01E+02	2173	1.81E+01	2829
T Case 5	1.60E+04	2046	1.60E+04	2050	1.23E+01	2149	1.09E+00	2277	3.63E-01	2363	9.34E+00	2183	4.29E-01	2841
T Case 6	6.10E+03	2060	6.09E+03	2064	2.37E+02	2175	2.06E+01	2300	6.69E+00	2385	1.89E+02	2211	1.02E+01	2876
T Case 7	2.73E+03	2078	2.72E+03	2082	1.28E+02	2198	1.09E+01	2321	3.47E+00	2405	1.06E+02	2236	6.39E+00	2906
T Case 8	9.47E+02	2123	9.47E+02	2128	5.17E+01	2242	4.25E+00	2362	1.33E+00	2446	4.43E+01	2280	3.04E+00	2953
TX Case 1	6.79E+02	2054	6.76E+02	2058	2.31E+01	2169	2.21E+00	2294	6.89E-01	2377	1.52E+01	2258	1.01E+00	2853
TX Case 2	5.16E+01	>=3000	5.06E+01	>=3000	9.47E-01	2200	8.67E-02	2316	2.57E-02	2395	7.50E-01	2308	5.94E-02	2915
TX Case 3	5.39E+02	2052	5.27E+03	2027	3.12E+01	2135	2.98E+00	2259	9.27E-01	2343	2.06E+01	2223	1.34E+00	2815
TX Case 4	9.28E+02	2049	8.98E+02	2053	3.09E+01	2156	2.95E+00	2282	9.24E-01	2366	1.97E+01	2243	1.27E+00	2836
TX Case 5	1.01E+03	2054	1.01E+03	2057	1.18E+00	2167	1.13E-01	2292	3.56E-02	2376	7.62E-01	2256	4.97E-02	2849
TX Case 6	8.53E+01	>=3000	8.45E+01	>=3000	3.56E+00	2220	3.25E-01	2338	9.63E-02	2418	2.78E+00	2320	2.16E-01	2921
TX Case 7	6.32E+01	>=3000	6.21E+01	>=3000	1.12E+00	2222	1.02E-01	2339	3.04E-02	2418	8.84E-01	2331	7.03E-02	2940
TX Case 8	2.40E+01	>=3000	2.34E+01	>=3000	3.67E-01	2253	3.33E-02	2372	9.82E-03	2453	2.93E-01	2352	2.31E-02	2953

Table 4.19. STOMP Mass Balance Within the 2-D Slice for Tc-99

Case	Released	Domain	Exit	Error
	(pCi)	(pCi)	(pCi)	%
T Case 1	5.636040E+11	2.505895E+09	5.616255E+11	-9.4E-02
T Case 2	5.636040E+11	5.149437E+10	5.118448E+11	4.7E-02
T Case 3	5.636040E+11	1.155483E+09	5.616910E+11	1.3E-01
T Case 4	5.636040E+11	1.676278E+09	5.623230E+11	-7.0E-02
T Case 5	1.065779E+13	4.630890E+10	1.062123E+13	-9.1E-02
T Case 6	5.636040E+11	1.637662E+10	5.472093E+11	3.2E-03
T Case 7	5.636040E+11	3.733314E+10	5.259267E+11	6.1E-02
T Case 8	5.636040E+11	8.846953E+10	4.744973E+11	1.1E-01
TX Case 1	3.340084E+10	5.401643E+09	2.799375E+10	1.6E-02
TX Case 2	3.340084E+10	2.079815E+10	1.252439E+10	2.3E-01
TX Case 3	3.340084E+10	4.408755E+09	2.893396E+10	1.7E-01
TX Case 4	3.340084E+10	4.497644E+09	2.890229E+10	2.7E-03
TX Case 5	4.837548E+11	4.635556E+10	4.374740E+11	-1.5E-02
TX Case 6	3.340084E+10	1.401143E+10	1.933133E+10	1.7E-01
TX Case 7	3.340084E+10	1.948065E+10	1.384441E+10	2.3E-01
TX Case 8	3.340084E+10	2.498692E+10	8.323283E+09	2.7E-01

Table 4.20. STOMP Mass Balance Within the 2-D Slice for U-238

Case	Released	Domain	Exit	Error
	(pCi)	(pCi)	(pCi)	%
T Case 1	4.270510E+08	4.270690E+08	8.579583E-08	-4.2E-03
T Case 2	4.270510E+08	4.270665E+08	0.000000E+00	-3.6E-03
T Case 3	4.270510E+08	3.737201E+08	5.339012E+07	-1.4E-02
T Case 4	4.270510E+08	4.270669E+08	8.109307E-06	-3.7E-03
T Case 5	1.678651E+10	1.678645E+10	2.458804E-07	3.5E-04
T Case 6	4.270510E+08	4.270677E+08	0.000000E+00	-3.9E-03
T Case 7	4.270510E+08	4.270680E+08	0.000000E+00	-4.0E-03
T Case 8	4.270510E+08	4.270695E+08	0.000000E+00	-4.3E-03
TX Case 1	5.538398E+07	5.538306E+07	2.727694E-09	1.7E-03
TX Case 2	5.538398E+07	5.538284E+07	0.000000E+00	2.1E-03
TX Case 3	5.538398E+07	5.011995E+07	5.262545E+06	2.7E-03
TX Case 4	5.538398E+07	5.538294E+07	2.363797E-06	1.9E-03
TX Case 5	1.488830E+09	1.488824E+09	4.901457E-08	4.3E-04
TX Case 6	5.538398E+07	5.538290E+07	0.000000E+00	2.0E-03
TX Case 7	5.538398E+07	5.538310E+07	0.000000E+00	1.6E-03
TX Case 8	5.538398E+07	5.538298E+07	0.000000E+00	1.8E-03

Table 4.21. STOMP Mass Balance Within the 2-D Slice for NO_3

Case	Released	Domain	Exit	Error
	(μg)	(μg)	(μg)	%
T Case 1	3.469352E+11	4.920564E+09	3.424225E+11	-1.2E-01
T Case 2	3.469352E+11	5.596822E+10	2.911043E+11	-4.0E-02
T Case 3	3.469352E+11	3.302787E+09	3.432087E+11	1.2E-01
T Case 4	3.469352E+11	3.686142E+09	3.435789E+11	-9.5E-02
T Case 5	5.731172E+12	6.349271E+10	5.674289E+12	-1.2E-01
T Case 6	3.469352E+11	2.262914E+10	3.244589E+11	-4.4E-02
T Case 7	3.469352E+11	4.397557E+10	3.030357E+11	-2.2E-02
T Case 8	3.469352E+11	8.612448E+10	2.608857E+11	-2.2E-02
TX Case 1	1.046440E+11	1.612470E+10	8.860980E+10	-8.6E-02
TX Case 2	1.046440E+11	6.506165E+10	3.960225E+10	-1.9E-02
TX Case 3	1.046440E+11	1.564787E+10	8.888213E+10	1.1E-01
TX Case 4	1.046440E+11	1.466650E+10	9.006868E+10	-8.7E-02
TX Case 5	7.723272E+11	6.513699E+10	7.079110E+11	-9.3E-02
TX Case 6	1.046440E+11	4.225544E+10	6.241218E+10	-2.3E-02
TX Case 7	1.046440E+11	6.017728E+10	4.448619E+10	-1.9E-02
TX Case 8	1.046440E+11	7.938604E+10	2.527469E+10	-1.6E-02

Table 4.22. STOMP Mass Balance Within the 2-D Slice for Cr

Case	Released	Domain	Exit	Error
	(μg)	(μg)	(μg)	%
T Case 1	3.237322E+09	1.084285E+08	3.122180E+09	2.1E-01
T Case 2	3.237322E+09	1.080481E+09	2.157523E+09	-2.1E-02
T Case 3	3.237322E+09	6.414661E+07	3.167416E+09	1.8E-01
T Case 4	3.237322E+09	7.022455E+07	3.159865E+09	2.2E-01
T Case 5	1.231172E+11	4.784422E+09	1.214922E+11	-2.6E+00
T Case 6	3.237322E+09	5.002710E+08	2.736826E+09	6.9E-03
T Case 7	3.237322E+09	9.250806E+08	2.312897E+09	-2.0E-02
T Case 8	3.237322E+09	1.595466E+09	1.642717E+09	-2.7E-02
TX Case 1	4.453501E+08	1.248920E+08	3.204223E+08	8.1E-03
TX Case 2	4.453501E+08	3.876992E+08	5.769947E+07	-1.1E-02
TX Case 3	4.453501E+08	8.388903E+07	3.613521E+08	2.4E-02
TX Case 4	4.453501E+08	9.444154E+07	3.509112E+08	-5.9E-04
TX Case 5	1.204570E+10	1.860280E+09	1.019311E+10	-6.4E-02
TX Case 6	4.453501E+08	2.950251E+08	1.504077E+08	-1.9E-02
TX Case 7	4.453501E+08	3.755453E+08	6.986725E+07	-1.4E-02
TX Case 8	4.453501E+08	4.229101E+08	2.246115E+07	-4.8E-03

5.0 Numerical Groundwater Transport Modeling Results

This section describes the two types of simulations performed with the 3-D numerical aquifer model of the Hanford Site. The first two simulations were for point sources that determined peak concentrations at the compliance boundaries and their respective travel times. This analysis was carried out to determine velocities needed as input to the analytical streamtube model (reported in Tables 5.1 and 5.2). The second set of cases represented the Base Case scenarios at the T and TX tank farms. While the analytical model was used to predict concentrations of several constituents, including Tc-99, U-238, NO_3 and Cr, the numerical model simulations were only conducted for Tc-99 to yield the most conservative concentration estimates. Model comparisons were made at three locations that included the eastern boundary of the 200 West Area, the exclusion boundary, and the Columbia River.

The Hanford Site-Wide Groundwater Model (SGM) is the 3-D numerical groundwater flow and contaminant transport process model and was used in this study for comparison with the analytical model results. The SGM is a finite element model based on the CFEST code (Gupta et al. 1987; Gupta 1997). This model and its conceptual basis are fully described in Wurstner et al. (1995) and Cole et al. (1997). It was most recently used in the Hanford Site Composite Analysis (Cole et al. 1997; Kincaid et al. 1998; Bergeron et al. 2001) and ILAW Performance Assessment (Bergeron and Wurstner 2000; Mann et al. 2001). Cole et al. (2001) contains a complete discussion of the uncertainties in the conceptual model as they are currently understood.

In the sections that follow, the SGM that was implemented in this analysis is presented. This is followed by a description of the point source simulation and how the results were used to obtain travel times (i.e., groundwater velocities) for the analytical streamtube model. In the final sections of this chapter, numerical modeling results are presented and compared with the results obtained with the analytical streamtube model.

5.1 The Site-Wide Groundwater Model (SGM)

The CFEST SGM that was used in this analysis is the same as the one implemented in the S-SX closure investigation (Zhang et al. 2004). Thus, only a brief description of the SGM is presented in this report. For a more detailed description of the SGM, the reader is referred to Zhang et al. (2004).

In this work, the SGM is implemented with a refined grid based on the composite analysis grid (Kincaid et al. 1998). This grid maintains a 750-m spacing in the southern and western areas of the Site (Figure 5.1), but the majority of the central plateau is discretized into 249 m units. The 200 West Area is further refined into 83 m nodal spacing.

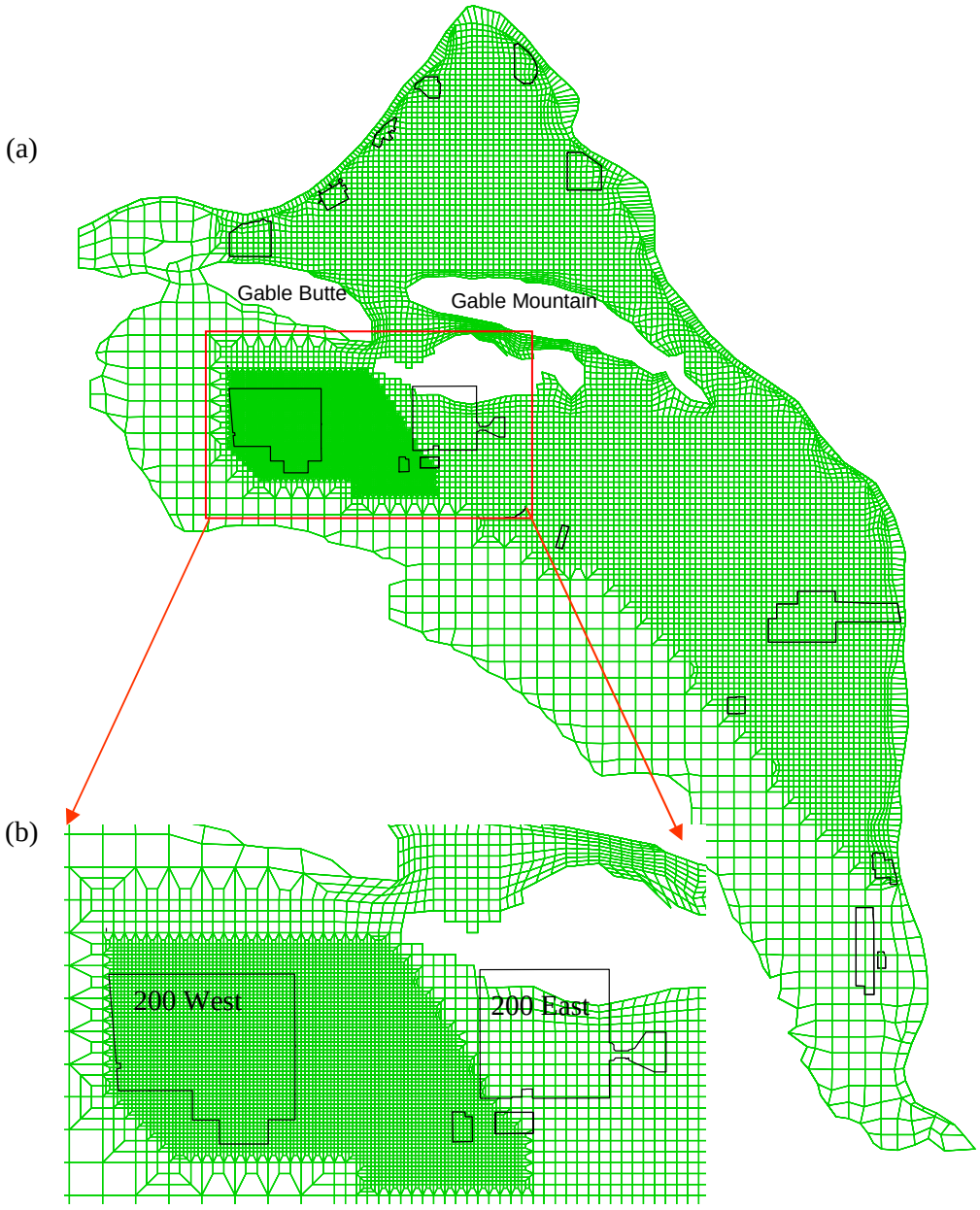

Figure 5.1. (a) Refined Composite Analysis Grid (red square denotes area of smallest grid refinement); (b) 200 Areas with 83 m Nodal Spacing in 200 W and 249 m in 200 E

Current field data indicate that for post-Hanford operations, the dissipation of the groundwater mounds in the 200 Areas causes flow to be cut off through the gap between Gable Butte and Gable Mountain. This reduction in flow is caused by basalt outcrops that impede flow when the water table is lowered. As a result, groundwater flows predominately in an easterly direction toward the Columbia River. To simulate this flow behavior, grid nodes were deleted in the gap, but their removal was based on a new interpretation of the location of the basalt outcrops for post-Hanford conditions (Figure 5.2). Although the deletion of grid nodes significantly reduced northward flow, contaminant transport from both T and TX farms is still significant given their proximity to the gap. Thus, peak concentrations and

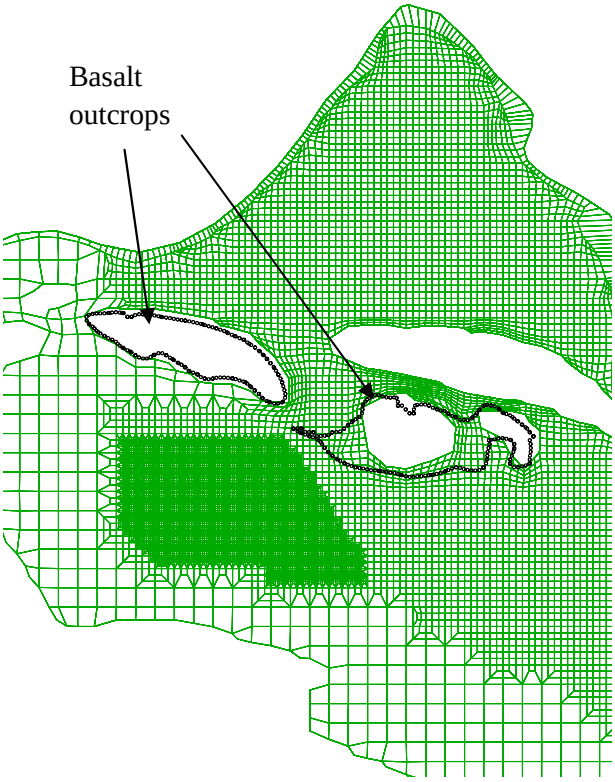

Figure 5.2. New Interpretation of the Basalt Outcrop Locations for Post-Hanford Operations Flow Conditions (outlined in black). Nodes within the black outlines were deleted from the grid.

arrival times for two flow paths are presented in this section. The first represents an eastern flow path that is south of the gap. The second flow path travels north through the gap before arriving at the Columbia River. These travel paths are described in more detail in Section 5.3 and are shown in Figure 5.5.

As in the S-SX closure effort, this analysis involves steady-state flow with transient transport. This setup represents future "Post-Hanford" conditions with no artificial recharge, when the effects of the disposal mounds from Hanford operations have ceased.

5.2 Flow and Transport Parameters for the SGM

To model groundwater flow, the distribution of hydraulic properties, including both horizontal and vertical hydraulic conductivity and porosity, were required for each hydrogeologic unit defined in the model (Figure 5.3). The procedure used to calibrate the current detailed process model is described in Cole et al. (2001). The resulting hydraulic conductivity distribution determined for the upper part of the aquifer is provided in Figure 5.4.

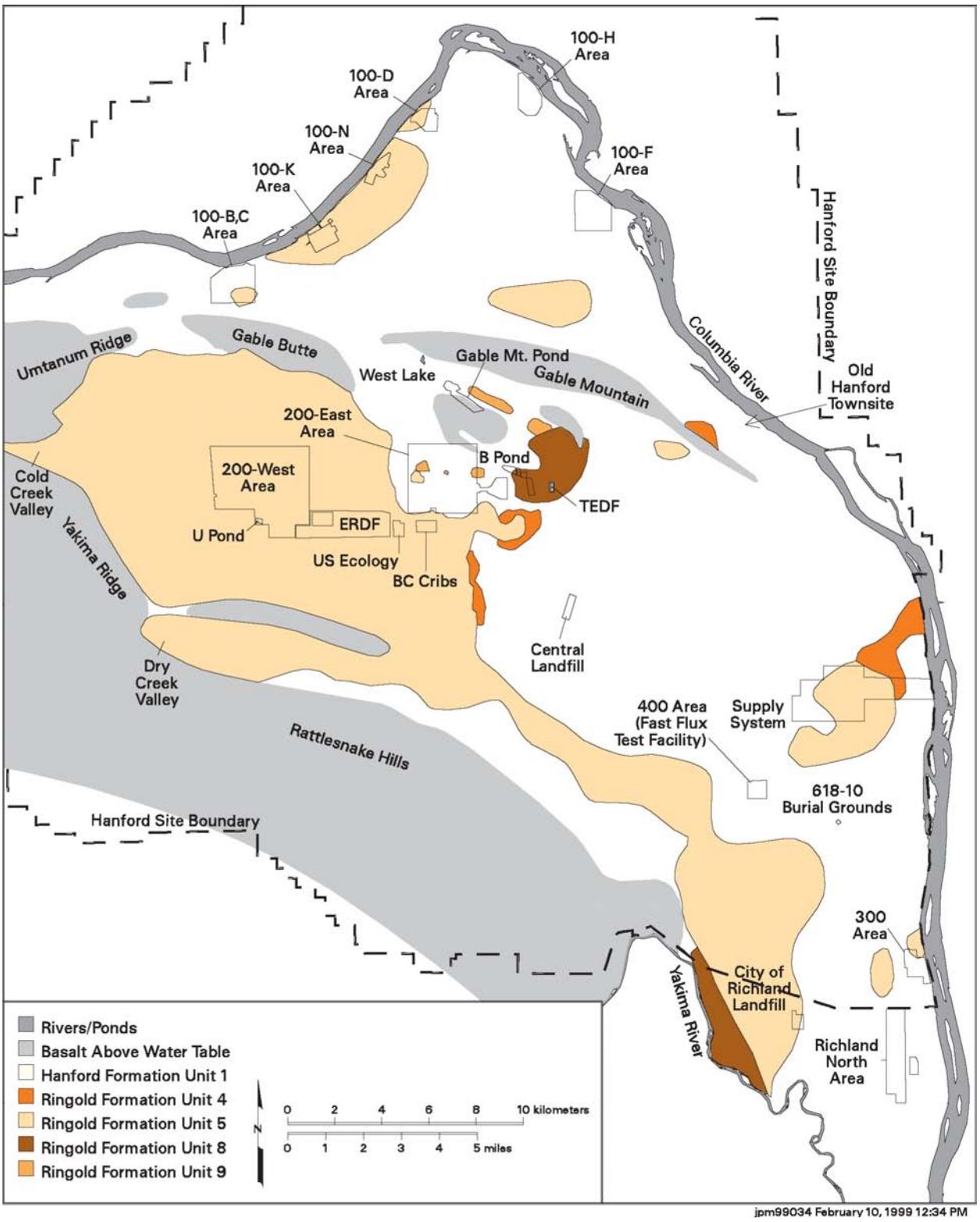

Figure 5.3. Map of SGM Hydrogeologic Units Containing Water Table in March 1999 (Hartman 2000)

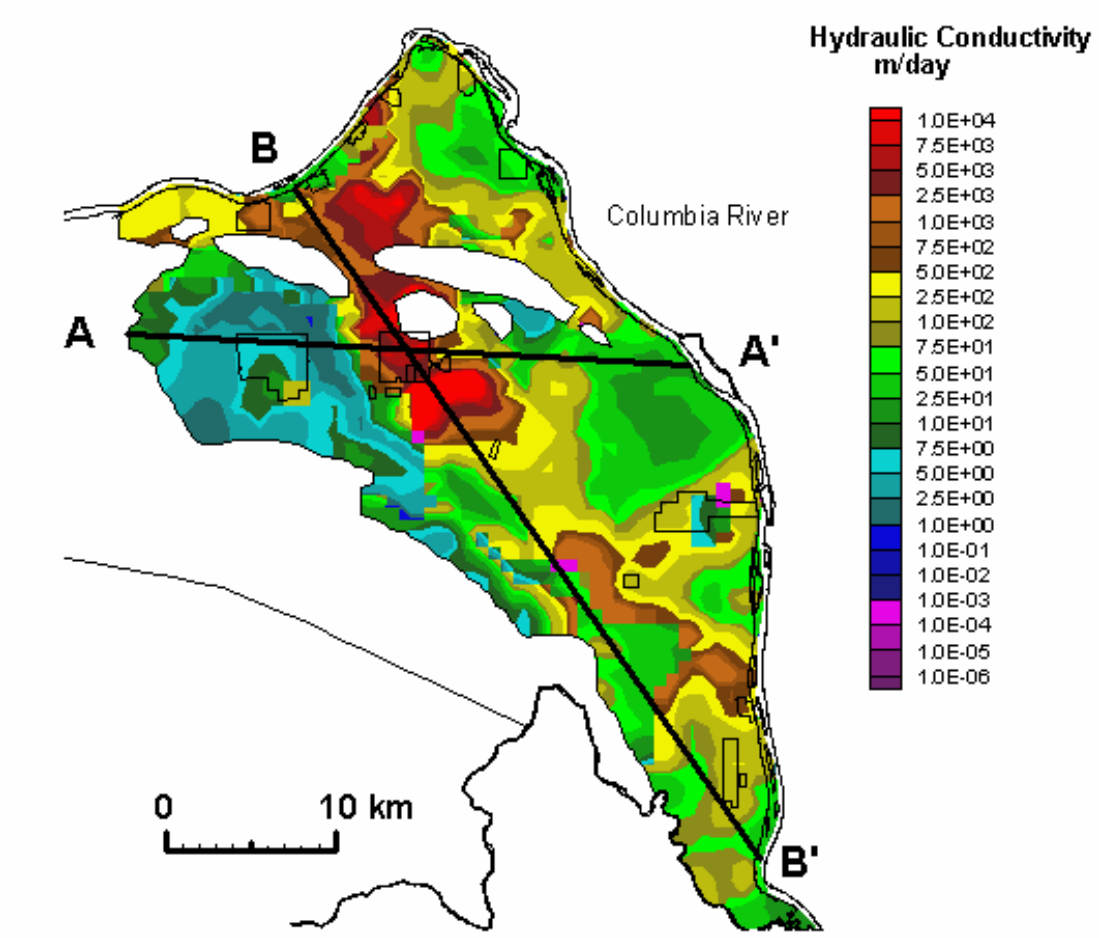

Figure 5.4. Hydraulic Conductivity Distribution (Cole et al. 2001)

To simulate movement of contaminant plumes, the required transport properties include contaminant-specific distribution coefficients, bulk density, effective porosity, and the longitudinal and transverse dispersivities (α_l and α_t), which are the components of the dispersion tensor generally used to represent dispersion in a porous media that is isotropic with respect to dispersivity. As described in White et al. (2001), several difficulties are associated with determining appropriate values of dispersivity at a site-wide scale. Although dispersivity is often determined by inverse modeling of onsite tracer test BTCs, no field tests have been conducted at the Hanford Site to develop an estimate for this parameter at the scale of transport appropriate for the SGM.

Dispersivity is likely to vary across the Site depending on the degree of heterogeneity and the temporal variability of flow gradients. In the Composite Analysis, uniform dispersivity values (e.g., longitudinal dispersivity, α_l = 95 m and transverse dispersivity, α_t, = 19 m) were used. With the finer mesh used in the current model, dispersivities were reduced to satisfy the grid Peclet number. In the 200 West Area, the area of greatest refinement, a longitudinal dispersivity of 30 m and a transverse dispersivity of 6 m were used for the Ringold Formation. For the other units, a 62.5 m longitudinal dispersivity and a 12.5 m transverse dispersivity were implemented.

5.3 Unit Source Analysis

A CFEST simulation of the SGM was used to determine solute transport velocities for the analytical streamtube model described in Section 3.8. A unit point source (1 Ci) simulation was performed to determine velocities and travel distances to the downstream compliance points (the eastern boundary of the 200 West Area, the exclusion boundary, and the Columbia River). Using a steady-state flow field to represent post-Hanford conditions, a unit source simulation was carried out for each tank farm by injecting a unit source as a pulse over a single time step into four surface nodes (Figure 5.5). 500-year transient transport simulations were carried out using one-year time steps.

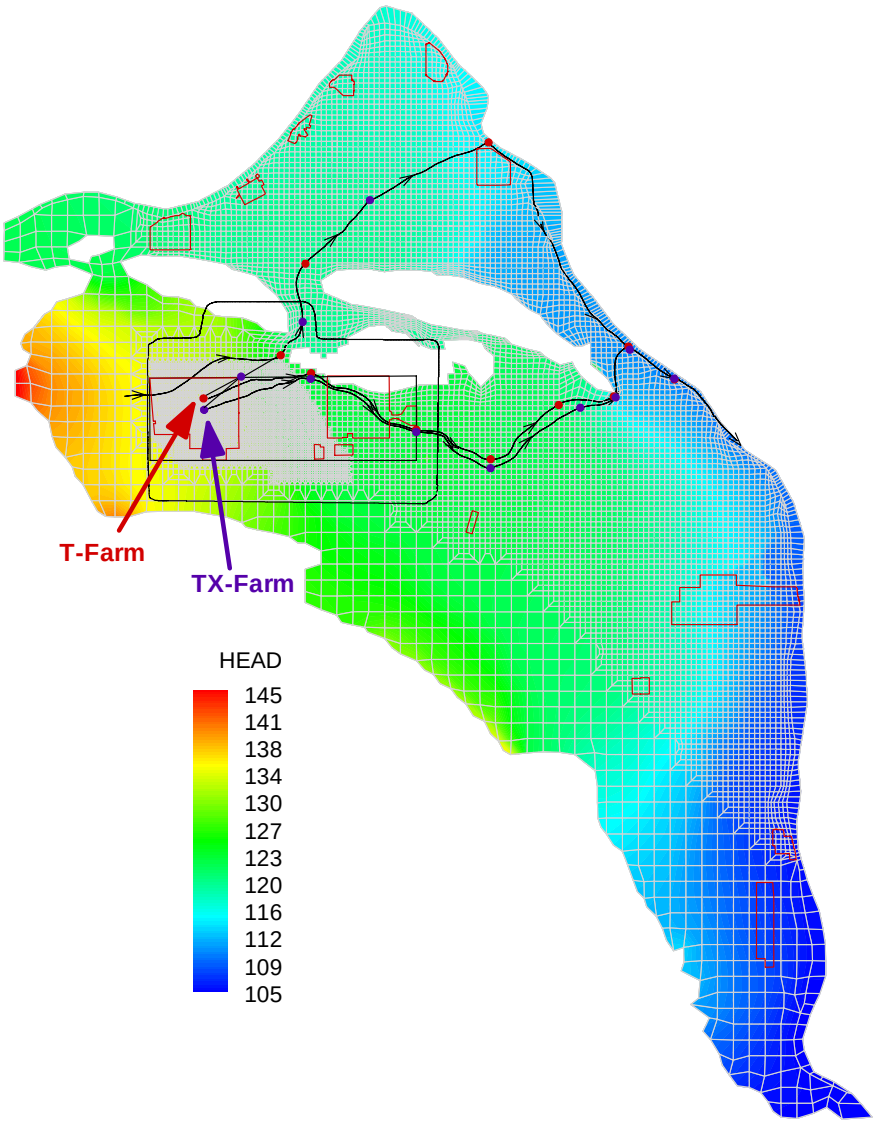

Figure 5.5. Post-Hanford Operations, Steady-State Potentiometric Surface for SGM, and Streamtrace Along Peak Concentration Pathways. Red markers indicate where travel distances were computed for sources originating at T farm; purple markers indicate where travel distances were computed for sources originating at T farm. Northward flow paths through the gap were nearly identical for T and TX farms.

To determine average flow velocities, the peak concentrations were determined for two flow paths. The east flow path included the eastern boundaries of 200 West and the exclusion boundary as well as the Columbia River. The north flow path included the northern boundary of the exclusion zone and the Columbia River. The arrival time of the peak concentrations at the boundaries was assumed to be the travel time from the source. The travel distance was then determined using streamlines generated by Tecplot. Figure 5.5 shows the streamtraces that were used to calculate travel distances. Red markers on the streamtrace were used to calculate travel distances along the east path, south of the gap for the unit source originating at T farm. Purple markers were used to calculate travel distances for the streamtrace south of the gap for the source originating at TX farm. As shown in Figure 5.5, the streamtraces for the north flow path through the gap were nearly identical for both the T and TX farms. Because of the tortuous nature of flow, all flow path distances were greater than the straight line distance. The flow velocity was then calculated using the time and distance data. Tables 5.1 and 5.2 show the peak concentrations and peak arrival times resulting from the unit source simulations.

Table 5.1. Travel Distances, Travel Times and Average Velocities for Streamtube Model at T Farm

Compliance Points	Distance (km)	Travel Time (yr)	Velocity (m/yr)
East Flow Path, South of Gap			
200 West Boundary	1.634	104	15.71
Exclusion Boundary	11.04	226	48.84
Columbia River	26.23	312	84.09
North Flow Path, Through the Gap			
200 West Boundary/ Exclusion Boundary	1.96	138	14.19
Columbia River	19.21	788	24.38

Table 5.2. Travel Distances, Travel Times and Average Velocities for Streamtube Model at TX Farm

Compliance Points	Distance (km)	Travel Time (yr)	Velocity (m/yr)
East Flow Path, South of Gap			
200 West Boundary	1.713	104	16.47
Exclusion Boundary	10.84	226	47.96
Columbia River	26.58	310	85.75
North Flow Path, Through the Gap			
200 West Boundary/ Exclusion Boundary	2.36	190	12.44
Columbia River	19.62	772	25.41

5.4 Modeling Results

The same scenario (Case 1) was modeled for T and TX farms with the conservative species Tc-99. Case 1 for both farms represented the Base Case scenario, with an interim barrier in the year 2010 and a closure barrier in year 2040. In the STOMP vadose zone modeling, emplacement of the interim barrier reduced the recharge rate from 100 mm/yr to 0.5 mm/yr in the year 2010. The recharge rate was further reduced to 0.1 mm/yr once the closure barrier was in place. After 500 years the barrier degraded, and the recharge rate increased to 3.5 mm/yr. These changes in recharge affected Tc-99 transport to the groundwater. As in streamtube modeling, sources at the fenceline were used as input to the SGM.

5.4.1 Case 1: T Tank Farm

To simulate contaminant transport for Case 1, STOMP mass fluxes were used as input into the CFEST SGM beginning in the year 2000. Using a steady-state flow field to represent post-Hanford conditions, the annual mass fluxes from STOMP were injected as dry mass into four surface nodes at T tank farm. Tc-99 transport was simulated for 1000 years using two year time steps subdivided into one-year time steps for transport calculations.

Figure 5.6 shows the BTCs predicted by the CFEST SGM at the 200 West, exclusion and Columbia River boundaries for both east and north flow paths. Figures 5.7 and 5.8 illustrate the plan view concentration contours at the water table when the peak concentration occurred at the exclusion boundaries and the Columbia River for the east and north flow paths, respectively. At the source, Table 5.3 shows the peak concentrations and time of occurrence at the fenceline. Although the peak arrival times differ by only three years, the concentration at the fenceline for the streamtube model is 9.2 times greater than the source concentration in the CFEST model. This large difference in the initial source concentration occurs because the mass flux input into the CFEST model is mixed with the groundwater. In the streamtube model, no mixing occurs with an existing volume of water.

At the downstream compliance points, dilution occurred for both CFEST and streamtube models. As shown in Table 5.3, the peak concentration predicted by the analytical model (1.35E+04 pCi/L) was 2.6 times higher than the SGM at the 200 West boundary, 2.8 times higher at the exclusion boundary (1.20E+03 pCi/L), and 3.1 times higher at the Columbia River (4.03E+02 pCi/L) for the east flow path. The SGM predicted ~92% reduction in peak concentration at the exclusion boundary relative to its peak at 200 West and a 69% decrease at the river relative to the peak predicted at the exclusion boundary. Similarly, the streamtube model predicted a 91% decrease in the peak concentration from 200 West to the exclusion boundary and a 69% decrease at the river. Although the streamtube model predicted the peak at the 200 West boundary 18 years earlier than the SGM, the predicted arrival was only three years earlier at the exclusion boundary (2267) and four years earlier at the river (2354).

For the north flow path, peak concentrations and arrival times had larger differences than those of the east flow path. Although the streamtube predicted peak concentration at the exclusion boundary was 2.6 times higher (1.00E+04 pCi/L) than the SGM, its arrival time was predicted 12 years earlier (year 2172) as well. The gap in predictions was further widened at the Columbia River, where the peak concentration predicted by the streamtube model was 35 years earlier (year 2827) and 5.8 times higher (4.26E+02 pCi/L) than the SGM.

a)

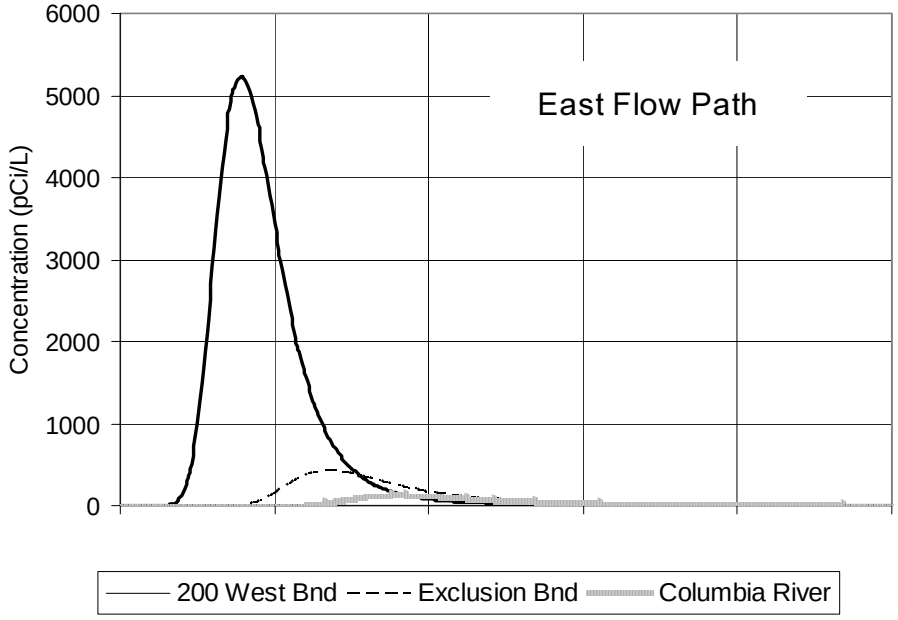

b)

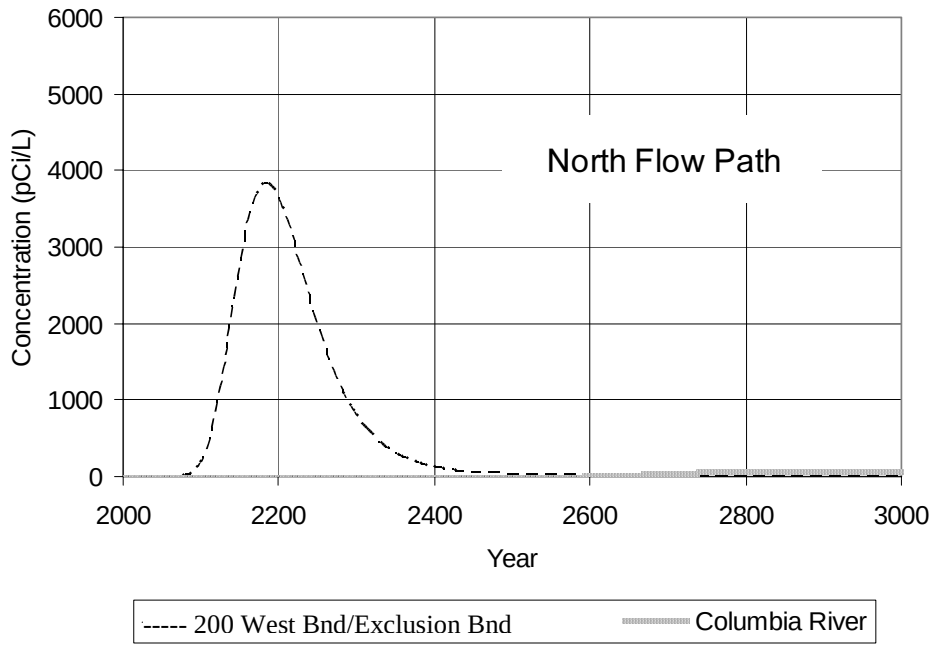

Figure 5.6. BTCs Simulated by CFEST Site-Wide Model for T-Farm Case 1 at (a) 200 West, Exclusion, and Columbia River Boundaries for East Flow Path; and (b) Exclusion and Columbia River Boundaries for North Flow Path

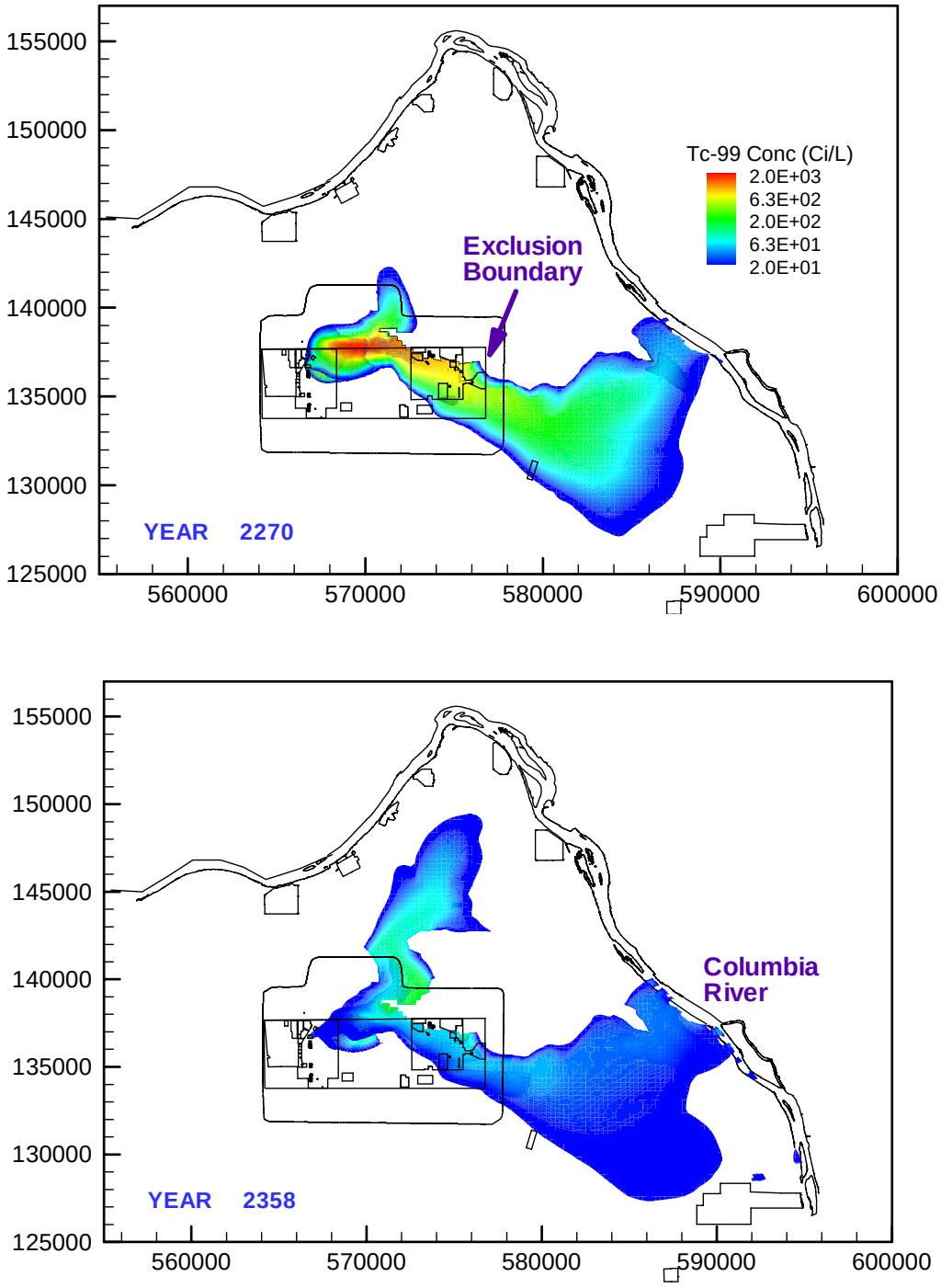

Figure 5.7. Composite SGM Results for Case 1, T Tank Farm Illustrating Plan-View Concentration Contours when Peak Concentrations Occurred at the Exclusion Boundary (top) and Columbia River (bottom) for the East Flow Path

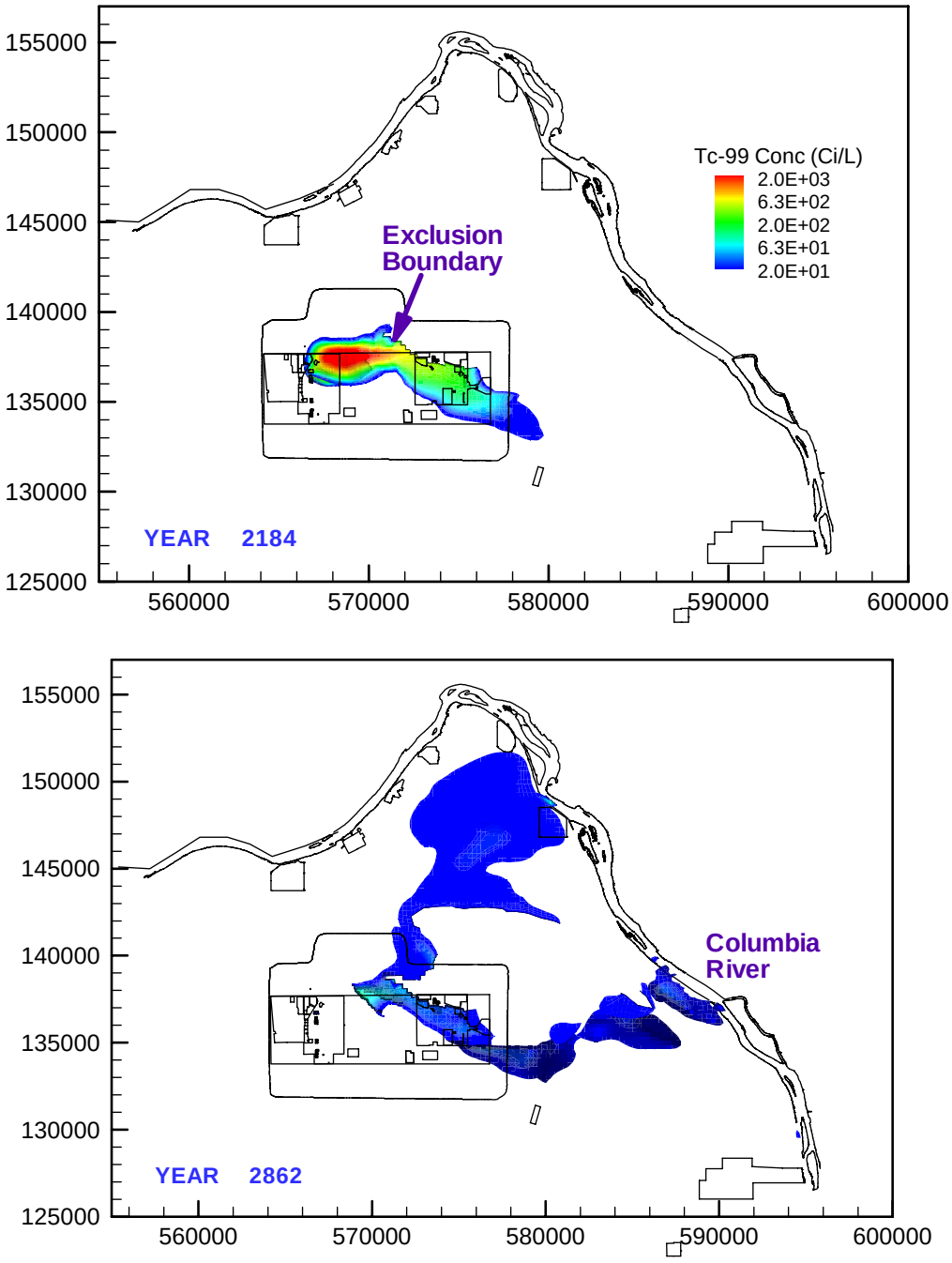

Figure 5.8. Composite SGM Results for Case 1, T Tank Farm, Illustrating Plan-View Concentration Contours when the Peak Concentrations Occurred at the Exclusion Boundary (top) and the Columbia River (bottom) for the North Flow Path (through the gap)

Table 5.3. Peak Tc-99 Concentrations at the 200 West Eastern Boundary, the Exclusion Boundary, and the Columbia River for Case 1, T Tank Farm

Models	Fenceline		200 West Area		Exclusion Boundary		Columbia River	
	Time (yr)	Conc (pCi/L)	Time (yr)	Conc (pCi/L)	Time (yr)	Conc (pCi/L)	Time (yr)	Conc (pCi/L)
East Flow Path, South of Gap								
Streamtube	2041	1.40E+06	2138	1.35E+04	2267	1.20E+03	2354	4.03E+02
SGM (CFEST)	2044	1.52E+05	2156	5.23E+03	2270	4.25E+02	2358	1.32E+02
North Flow Path, Through the Gap								
Streamtube	2041	1.40E+06	2172	1.00E+04	2172	1.00E+04	2827	4.26E+02
SGM (CFEST)	2044	1.52E+05	2184	3.83E+03	2184	3.83E+03	2862	7.29E+01

Although the streamtube model was calibrated with parameters from the SGM, the streamtube model predictions were more conservative in time (3~35 years earlier) and also represented more conservative estimates of the peaks. This result occurred due to differences in advective transport between the two models. For example, in the one-dimensional analytical model, advective transport occurred in only one direction, whereas in the SGM, it occurred in all three dimensions. Moreover, advective transport in the analytical model did not account for any heterogeneity. Hence, concentrations predicted by the SGM were more dilute than the concentrations predicted by the analytical model.

5.4.2 Case 1: TX Tank Farm

As in the Case 1 groundwater simulation for T tank farm, contaminant transport at TX farm (Case 1) was simulated using STOMP mass fluxes as input into the CFEST SGM beginning in the year 2000. Using a steady-state flow field to represent post-Hanford conditions, the annual mass fluxes from STOMP were injected as dry mass into four surface nodes at TX tank farm. Tc-99 transport was simulated for 1000 years using two-year time steps subdivided into one-year time steps for transport calculations.

Figure 5.9 shows the BTCs predicted by the CFEST SGM at the 200 West, exclusion, and Columbia River boundaries for both the east and north flow paths. Figures 5.10 and 5.11 illustrate the plan view concentration contours at the water table when the peak concentration occurred at the exclusion boundary and the Columbia River for the east and north flow paths, respectively. At the source, Table 5.4 shows the peak concentrations and time of occurrence at the fenceline. Similar to T Farm simulation results, peak arrival times for the fenceline were similar and differed by only two years. However, the concentration at the fenceline for the streamtube model was 8.7 times greater than the source concentration in the CFEST model. This large difference in the initial source concentration occurs because the mass flux input into the CFEST model is mixed with the groundwater. In the streamtube model, no mixing occurs with an existing volume of water.

Although source concentrations at TX tank farm were more dilute than at T farm, solute transport behavior was similar between the two cases. For example, both the streamtube model and SGM predicted similar decreases in peak concentrations as Tc-99 was transported to the downstream compliance boundaries. For the east flow path, the SGM predicted ~89% reduction in the peak concentrations at the

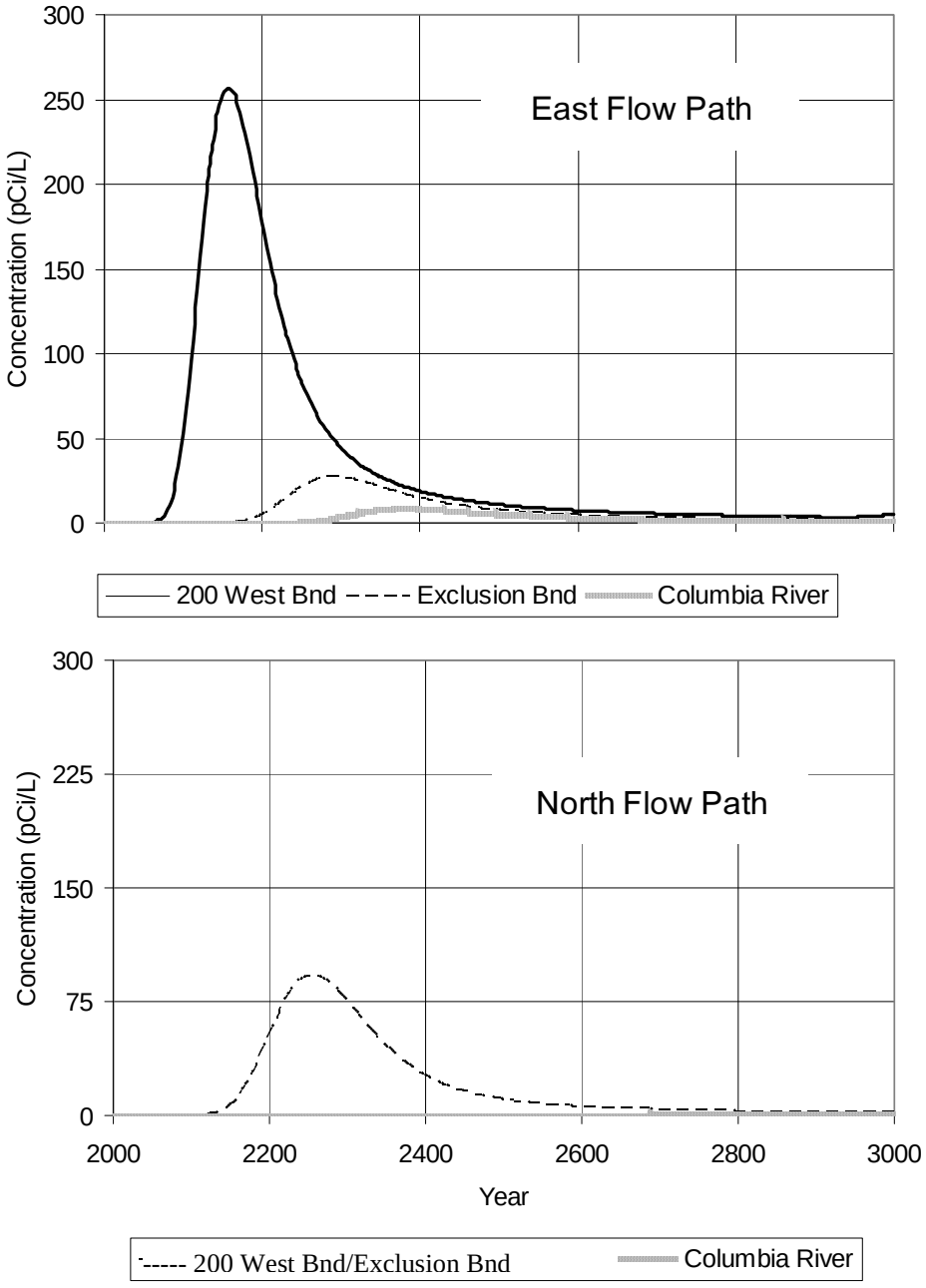

Figure 5.9. BTCs Simulated by CFEST Site-Wide Model for TX-Farm Case 1 at a) 200 West Area, Exclusion and Columbia River Boundaries for East Flow Path; and (b) Exclusion and Columbia River Boundaries for the North Flow Path

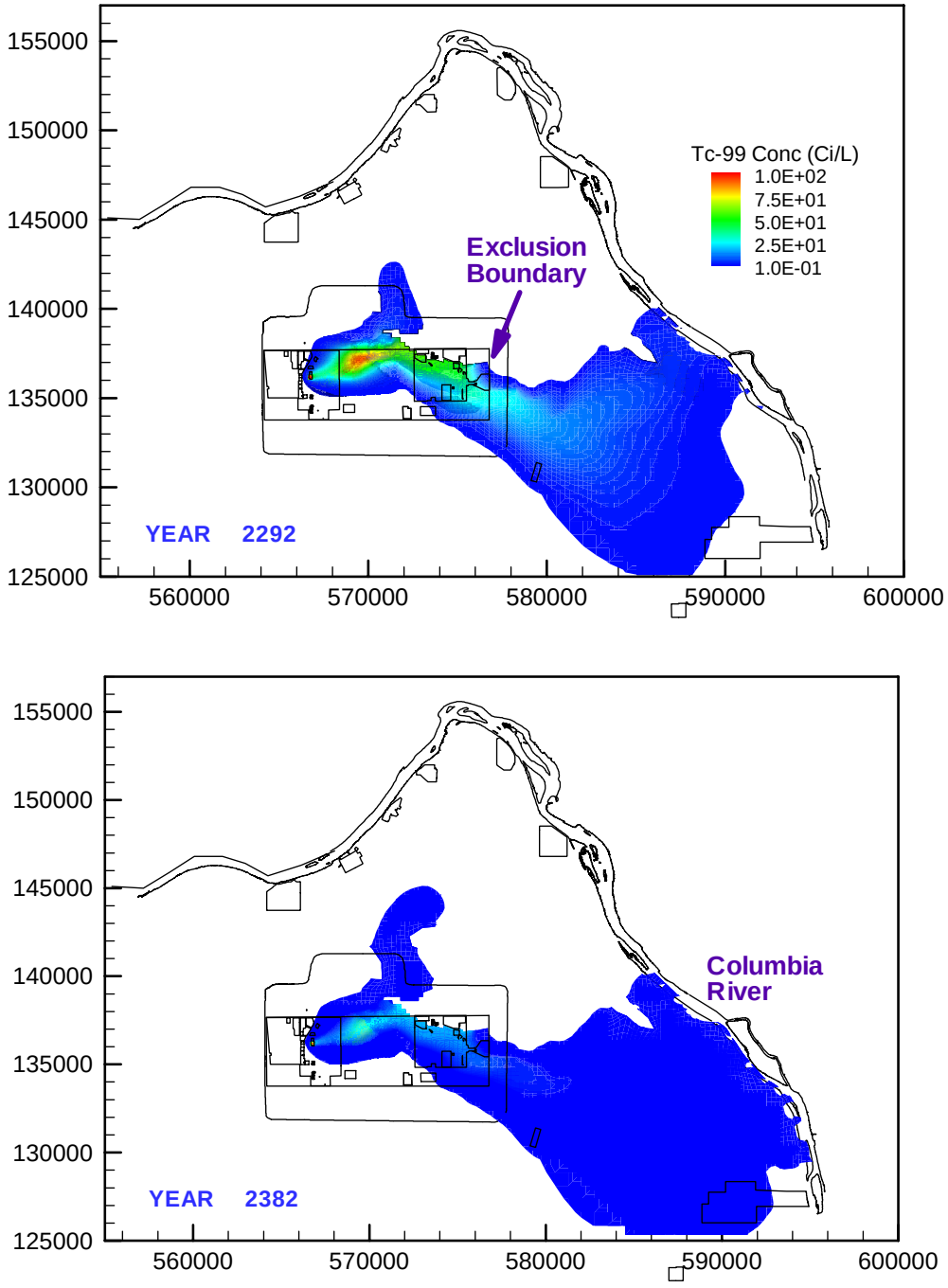

Figure 5.10. Composite SGM Results for Case 1, TX Tank Farm, Illustrating Plan-View Concentration Contours when Peak Concentrations Occurred at Exclusion Boundary (top) and Columbia River (bottom) for East Flow Path

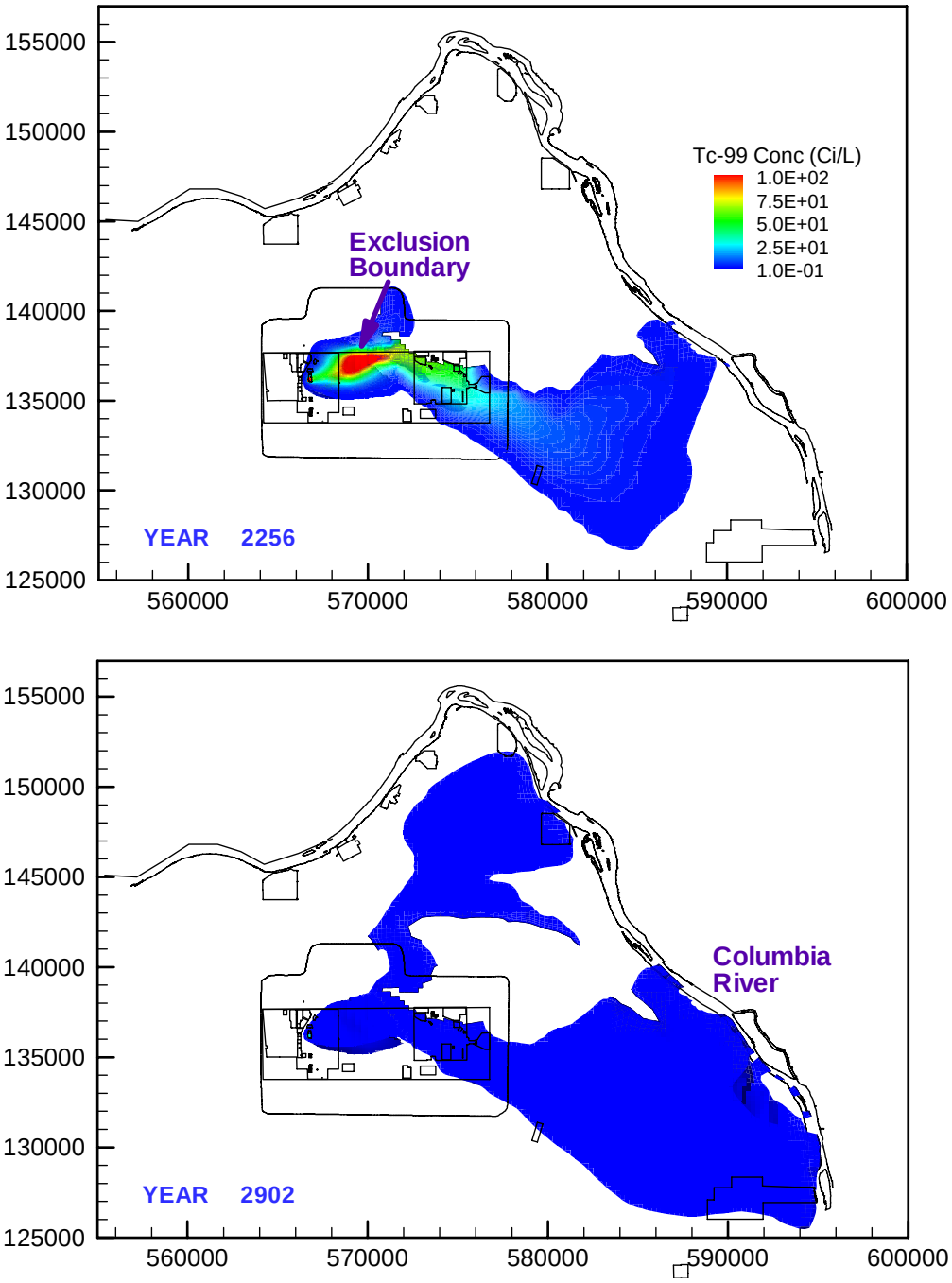

Figure 5.11. Composite SGM Results for Case 1, TX Tank Farm, Illustrating Plan-View Concentration Contours when Peak Concentrations Occurred at the Exclusion Boundary (top) and Columbia River (bottom) for the North Flow Path

Table 5.4. Peak Tc-99 Concentrations at the 200 West Eastern Boundary, the Exclusion Boundary, and the Columbia River for Case 1, TX Tank Farm

Models	Fenceline		200 West Area		Exclusion Boundary		Columbia River	
	Time (yr)	Conc (pCi/L)	Time (yr)	Conc (pCi/L)	Time (yr)	Conc (pCi/L)	Time (yr)	Conc (pCi/L)
East Flow Path, South of Gap								
Streamtube	2050	4.65E+04	2153	6.32E+02	2280	6.07E+01	2364	1.93E+01
SGM (CFEST)	2052	5.34E+03	2158	2.56E+02	2292	2.72E+01	2382	8.73E+00
North Flow Path, Through the Gap								
Streamtube	2050	4.65E+04	2240	3.88E+02	2240	3.88E+02	2832	2.43E+01
SGM (CFEST)	2052	5.34E+03	2256	9.22E+01	2256	9.22E+01	2902	1.33E+00

exclusion boundary relative to its peak at 200 West (versus 91% for T farm), and a 68% decrease at the Columbia River relative to the peak predicted at the exclusion boundary (versus 69% for T farm). Similarly, the streamtube model predicted a 90% decrease in the peak concentration from 200 West to the exclusion boundary (versus 91% for T farm), and a 68% decrease at the Columbia River (versus 69% for T farm). As in the T-farm simulation, peak concentrations predicted by the streamtube model were higher than predicted by the SGM. On average, peak concentration predictions were 2.3 times higher for the streamtube model (6.32E+02 pCi/L at 200 West, 6.07E+01 pCi/L at the exclusion boundary, and 1.93E+01 pCi/L at the Columbia River) than those predicted by the SGM along the east flow path. Peak arrival times were also earlier (5~18 years) for the streamtube model.

Similar to T farm results, larger differences in peak concentrations and arrival times resulted for the north flow path. For example, the streamtube predicted peak concentration at the exclusion boundary was 4.2 times higher (3.88E+02 pCi/L) than the SGM, and its predicted arrival time was 16 years earlier (year 2240). The gap in predictions was further widened at the Columbia River, where the peak concentration predicted by the streamtube model was 70 years earlier (year 2832) and 18.2 times higher (2.43E+01 pCi/L) than the SGM.

Both T and TX simulation results demonstrate that the streamtube model predictions are more similar to the CFEST-based SGM for the east flow path than they are for the north flow path. This result is likely due to heterogeneities in the aquifer thickness that occur along the north flow path. Because the aquifer thins in the gap and then thickens in the area just north of the gap, the contaminant spreads vertically and dilution occurs. Since these heterogeneities are not represented in the streamtube model, its ability to predict peak concentrations and their arrival times is limited along the north flow path.

6.2 Geology and Initial Inventory

Zonation files to define the rock/soil-type and inactive-node distributions were provided with the MDP (Khaleel et al. 2004). These lithologic descriptions were based on inferences drawn from groundwater monitoring wells near the S-SX tank farm and from grain size data and supplemented by information from tank farm drywells and excavation (e.g., Price and Fecht 1976a, 1976b). Zonation files are stored in the individual case directories as *tf*_withtank.dat and *tf*_notank.dat, where *tf* designates tank farm (t or tx) and "withtank" designates the configuration with tanks present and "notank" designates the configuration with tanks absent, as before 1945 for T Farm and 1949 for TX Farm. Within the zonation file is information on the inactive nodes that define the tanks and cross-section boundaries. Rock/soil zonation files can be visualized as 2-D color-scaled images with Tecplot by opening the layout file for the cross section.

Contaminant inventories for the initial concentrations in STOMP are saved in files named as un_*_*tf* and nu_*_*tf*, where "un" refers to the uniform distribution used in all cases except Case 5, and "nu" refers to the nonuniform distribution used in Case 5, and *tf* is t or tx for the appropriate tank farm.

6.3 Steady Flow Simulations

A steady flow simulation was executed to generate initial condition flow fields for each of the transient solute transport simulations. This simulation is found in the "case0" directory and was executed with the STOMP simulator, which produced a "restart" file that described the steady flow field. The input, output, and restart files are catalogued in Table 6.2.

Table 6.2. Steady Flow Initial Condition Files

File Name	Description	File Type
input	STOMP input file	Text
output	STOMP reference-node output file	Text
plot	STOMP plot-file output file	Text
restart	STOMP restart file	Text

6.4 Coupled Vadose Zone and Unconfined Aquifer Modeling

Coupled vadose zone and unconfined aquifer modeling files are stored in directories named according to case number (e.g., directory case2 holds files associated with the Case 2 simulations). The case directories hold input files, zonation files, reference-node output files, plot-file output files, and surface-flux output files. Also within the case directories are subdirectories containing converted plot-file output, Tecplot layout files, solute concentration and mass flux data files, and image files. The "btc" subdirectory contains files of timeseries output and the flux and concentration timeseries graph files in encapsulated postscript (*.eps) and portable network graphics (*.png) formats. The "tecplot" subdirectory contains Tecplot data files (*.plt), Tecplot macros files (*.mcr), and *.eps, *.png files of the cross-section contour plots at distinct points in time. Table 6.3 summarizes the naming conventions for the files stored under each case directory.

Table 6.3. Coupled Vadose Zone and Unconfined Aquifer Modeling Files

File Name	Description	File Type
Input	STOMP simulator input	Text
Output	STOMP simulator reference-node output	Text
fn.srf	STOMP simulator surface-flux output	Text
*fn*_tot.srf	Modified STOMP simulator surface-flux output so that the cumulative flux is continuous between stages 1 and 2	Text
yr.plt	Tecplot data file at time *yr*	Tecplot binary
*yr_type_**.eps	Tecplot graph showing concentration or saturation profiles at distinct points in time	Text
*yr_type_**.png	Image file showing concentration or saturation profiles at distinct points in time (generated with convert –density 200x200 *eps *png)	Image
prepsurf_fenceline_*tf_cd*.csh, prepsurf_gwtable_*tf_cd*.csh	C-Shell scripts for computing BTCs at the fenceline or groundwater table, respectively (executes Surfcalc for each contaminant). *tf* is tank farm ("t" or "tx") and *cd* is uniform ("un") or nonuniform ("nu") contaminant distribution.	Text
*_*location*_mf.dat	Solute mass flux breakthrough data at the fenceline	Text
*_*location*_mf.eps,	Mass flux and concentration BTCs, respectively. Encapsulated postscript file generated using rungnu.csh	Text/Image
*_*location*_mf.png	Image file containing mass flux and concentration BTCs, respectively (generated using convert –density 200x200 *eps *png)	Image

Notes:
is the plot file number indicator (e.g., plot.175, plot.3462, etc.).
fn is the user-defined filename.
yr represents the calendar year plotted in the image file.
* is the plot variable (e.g., sat (saturation), ac_tc (aqueous conc tc), vc_U_0.10 (u total conc w/ K_d =0.10).
location represents the fenceline or the gwtable (groundwater table) locations.

For each transient flow and solute transport simulation, the STOMP simulator read an input file, restart file, zonation file, and solute inventory file and generated one reference-node output file, one or more plot-file output files, and one or more surface-flux output files. The STOMP-generated plot file output files were converted to Tecplot ASCII format using the PlotTec utility. These ASCII files were rendered with Tecplot to generate color-scaled images of saturation and solute concentration for selected points in time. The STOMP-generated surface flux output files were translated to ASCII mass flux and concentration timeseries *.dat files. The *.dat files were used as input to the analytical advection-dispersion ("streamtube") model to generate concentrations at downgradient points over time.

6.5 Analytical Groundwater Transport Modeling

Input and output files for the analytical groundwater transport ("streamtube") model were archived in the case BTC directories. C-Shell scripts for running the streamtube model and generating plots are included in a main folder called 2_btc_figs. Execution of the streamtube model and subsequent post-processing creates output files for each species that contains the time and calculated concentrations at each compliance point in columns.

The scripts used to run the model and relevant utility programs are shown in Table 6.4. Script runpoint.csh contains the flow-path length, velocity, and hydraulic parameters, runs the streamtube model, and creates output files for each species that contain the time and calculated concentrations at each compliance point in columns. Script combine_timeseries.csh combines as columns in one file the time series data year, mass flux to groundwater table, concentration at groundwater table, cumulative mass flux to groundwater table, mass flux to fenceline, concentration at fenceline, cumulative mass flux to fenceline, concentration at 200 West boundary along the east pathway, concentration at exclusion boundary along the east pathway, concentration at the Columbia River along the east pathway, concentration at the exclusion boundary along the north pathway, and concentration at the Columbia River along the north pathway. These scripts were executed for each case directory to generate the encapsulated postscript files for the plots used in this report.

Table 6.4. Analytical Groundwater Transport Modeling Files

File Name	Description	File Type
run_allmodels.csh	C-Shell script for executing series of c-shell scripts used to generate BTCs. .	Text
runpoint.csh	C-Shell script for executing the streamtube model (includes model parameters).	Text
combine_timeseries.csh	C-Shell script for combining breakthrough data at the groundwater table, fenceline, 200 W boundary, exclusion boundaries, and Columbia River points into one file	Text
run_gnu.csh	C-Shell script for generating BTC plot files	
dir_loc_*.btc	Solute-concentration breakthrough data for contaminant * at location *loc* ("200W," "excl," or "riv") along pathway *dir* ("north" or "east")	Text
all_*.dat	Solute concentration breakthrough data for contaminant * at all locations in east and north pathways	Text
all_*_log-friendly.dat	Solute concentration breakthrough data for all locations in east and north pathways; zeros replaced with 9999e-30 to facilitate plotting with logarithmic scale	Text
*__conc_*dir*path.eps, *.png	Postscript or image file containing concentration BTC data at the fenceline, exclusion boundary, and Columbia River for the *dir* ("north" or "east") flow path	Text/Image
* Indicates the solute species (e.g., tc, u_0.60, no3, cr).		

6.6 STOMP Execution and Post-Processing

STOMP runs and all of the postprocessing steps can be executed using the shell scripts described in this section, and each of these steps may be executed individually at the command line to obtain the vadose zone and streamtube modeling results and graphics. To provide further automation to the processing, R scripts were developed to provide a "wrapper" to the existing programs. R was used to simplify and generalize the selection of specific steps and cases for execution, and provide all necessary intermediate steps with a single command line execution. The actual computations at each of the processing steps described previously were accomplished with the existing C and Fortran programs, and shell, Tecplot, and Gnuplot scripts. A few additional processing steps were included in the R scripts, such as graphics file format conversions and finding appropriate y-axis limits for the BTC plots at the beginning of the project. To execute certain processing steps for one or more case runs, options are set in the main R script run_cases.r, which is found in the sfarm root directory. For example, if only one case is needed to be run, then this option is set in the run_cases.r script. The actual postprocessing steps are coded in another R script, template.r. With a single command line execution, the following steps may be executed. For each case:

- Run STOMP.
- Plot BTCs with Gnuplot.
- Find years in which the peak concentration occurred at the fenceline for each contaminant.
- Plot concentration distributions with Tecplot.

R is essentially an expanded and open source version of the commercially distributed S-plus, the statistics, graphing, and general purpose programming environment. R is a mature product that is well supported and documented and is available at no cost for all of the usual operating systems (http://www.R-project.org). Help in using R can be found in the program and in Venables and Smith (2001), Krause and Olson (2000), and Venables and Ripley (1999, 2000). The R script can be executed two ways: 1) from the R shell or 2) direct from the command line. For method 1, start R by entering R at the command line, then enter 'source ("run_cases.r").' For method 2, enter the following at the command line: 'R –slave –no-save < run_cases.r.'

7.0 References

Baetslé LH. 1969. "Migration of radionuclides in porous media." *Progress in Nuclear Energy Series XII, Health Physics*, AMF Duhamel, ed. Pergamon Press, Elmsford, NY, pp. 707–730.

Bergeron MP and SK Wurstner. 2000. *Groundwater Calculations Supporting the 2001 Immobilized Low-Activity Waste Disposal Facility Performance Assessment at the Hanford Site in Southeastern Washington*. PNNL-13400, Pacific Northwest National Laboratory, Richland, WA.

Bergeron MP, E Freeman, S Wurstner, CT Kincaid, FM Coony, D Strenge, R Aaberg, and P Eslinger. 2001. *Addendum to Composite Analysis for Low-Level Waste Disposal in the 200 Area Plateau of the Hanford Site*. PNNL-11800-Addendum 1, Pacific Northwest National Laboratory, Richland, WA.

Bramley R and X Wang. 1995. *SPLIB: A Library of Iterative Methods for Sparse Linear Systems*. Indiana University, Bloomington, IN

Cole CR, MP Bergeron, SK Wurstner, PD Thorne, S. Orr, and MI McKinley. 2001. *Transient Inverse Calibration of Hanford Site-Wide Groundwater Model to Hanford Operational Impacts—1943 to 1996.* PNNL-13447, Pacific Northwest National Laboratory, Richland, WA.

Cole CR, SK Wurstner, MP Bergeron, MD Williams, and PD Thorne. 1997. *Three-Dimensional Analysis of Future Groundwater Flow Conditions and Contaminant Plume Transport in the Hanford Site Unconfined Aquifer System: FY 1996 and 1997 Status Report.* PNNL-11801, Pacific Northwest National Laboratory, Richland, WA.

Domenico PA and FW Schwartz. 1990. *Physical and Chemical Hydrogeology*. John Wiley & Sons, New York, pp. 824.

Freeman-Pollard JR. 1994. *Engineering Evaluation of the GAO/RCED-89-157, Tank 241-T-106 Vadose Zone Investigation*. WHC-SD-EN-EE-013, Westinghouse Hanford Company, Richland, WA.

Gardner WR. 1958. "Some steady-state solutions of the unsaturated moisture flow equation with applications to evaporation from a water table." *Soil Science*, 85:228-232.

Gelhar LW. 1993. *Stochastic Subsurface Hydrology*, Prentice Hall, New York.

Gupta SK, CR Cole, CT Kincaid, and AM Monti. 1987. *Coupled Fluid, Energy, and Solute Transport (CFEST) Model: Formulation and User's Manual.* BMI/ONWI-660, Battelle Memorial Institute, Columbus, OH.

Gupta SK. 1996. *Draft User's Manual, CFEST-96 Flow and Solute Transport, Constant/Variable Densit,y Computationally Efficient, and Low Disk PC/Unix Version.* Environmental System Technologies, Irvine, CA.

Haass CC. 1999. *Engineering Report: Single-Shell Tank Farms Interim Measures to Limit Infiltration Through the Vadose Zone*. RPP-5002 Rev. 0, Lockheed Martin Hanford Corp., Richland, WA.

Hartman MJ. 2000. *Hanford Site Groundwater Monitoring: Setting, Sources and Methods.* PNNL-13080, Pacific Northwest National Laboratory, Richland, WA.

Jones TL. 2000. *Inventory Estimates for Single-Shell Tank Leaks in S and SX Tank Farms.* RPP-6285 Rev. 0, CH2M Hill Hanford Group, Inc., Richland, WA.

Khaleel R, JF Relyea, and JL Conca. 1995. "Evaluation of van-Genuchten-Mualem relationships to estimate unsaturated conductivity at low water contents." *Water Resources Research,* 31:2659-2668.

Khaleel R and JF Relyea. 1997. "Correcting laboratory-measured moisture retention data for gravels." *Water Resources Research,* 33:1875-1878.

Khaleel R, TE Jones, AJ Knepp, FM Mann, DA Myers, PM Rogers, RJ Serne, and MI Wood. 2000. *Modeling Data Package for S–SX Field Investigation Report (FIR).* RPP-6296 Rev. 0, CH2M Hill Hanford Group, Inc., Richland, WA.

Khaleel R, FJ Anderson, MP Connelly, TE Jones, FM Mann, DA Myers, MI Wood. 2004. Modeling Data Package For T-TX-TY Field Investigation Report (FIR). RPP-17393 Rev. 0, CH2M Hill Hanford Group, Inc., Richland, WA.

Kincaid CT, JW Shade, GA Whyatt, MG Piepho, K Rhoads, JA Voogd, JH Westsik Jr, MD Freshley, KA Blanchard, and BG Lauzon. 1995. *Performance Assessment of Grouted Double-Shell Tank Waste Disposal at Hanford*. WHC-SD-WM-EE-004 Rev. 1, Westinghouse Hanford Company, Richland, WA.

Kincaid CT, MP Bergeron, CR Cole, MD Freshley, NL Hassig, VG Johnson, DI Kaplan, RJ Serne, GP Streile, DL Strenge, PD Thorne, LW Vail, GA Whyatt, and SK Wurstner. 1998. *Composite Analysis for Low-Level Waste Disposal in the 200-Area Plateau of the Hanford Site.* PNNL-11800, Pacific Northwest National Laboratory, Richland, WA.

Krause A and M Olson. 2000. *The Basics of S and S-plus*, 2nd edition. Springer, New York.

Mann FM, RJ Puigh II, SH Finfrock, EJ Freeman, R Khaleel, DH Bacon, MP Bergeron, BP McGrail, and SK Wurstner. 2001. *Hanford Immobilized Low-Activity Tank Waste Performance Assessment, 2001 Version*. DOE/ORP-2000-24, U.S. Department of Energy Office of River Protection, Richland, WA.

Millington RJ and JP Quirk. 1961. "Permeability of porous media." *Nature,* 183:387-388.

Mualem Y. 1976. "A new model for predicting the hydraulic conductivity of unsaturated porous media." *Water Resources Research,* 12:513-522.

Polmann DJ. 1990. *Application of Stochastic Methods to Transient Flow and Transport in Heterogeneous Unsaturated Soils*. Ph.D. Thesis, Massachusetts Institute of Technology, Cambridge, MA.

Price WH and KR Fecht. 1976a. *Geology of the 241-S Tank Farm*. ARH-LD-133, Atlantic Richfield Hanford Company, Richland, WA.

Price WH and KR Fecht. 1976b. *Geology of the 241-SX Tank Farm*. ARH-LD-134, Atlantic Richfield Hanford Company, Richland, WA.

Talbott ME and LW Gelhar. 1994. *Performance Assessment of a Hypothetical Low-Level Waste Facility: Groundwater Flow and Transport Simulation.* NUREG/CR-6114 Vol. 3, U.S. Nuclear Regulatory Commission, Washington, DC.

van Genuchten MTh. 1980. "A closed-form equation for predicting the hydraulic conductivity of unsaturated soils." *Soil Science Society of America Journal*, 44:892-898.

van Genuchten MT. 1980. "A Closed-Form Equation for Predicting the Hydraulic Conductivity of Unsaturated Soils." *Soil Science Society of America Journal* 44:892-898.

Venables W and B Ripley. 1999. *Modern Applied Statistics with S-plus*, 3rd edition. Springer, New York.

Venables W and B Ripley. 2000. *S Programming*. Springer, New York.

Venables W and D Smith. 2001. *An Introduction to R.* Network Theory Limited, Bristol, UK.

White MD and M Oostrom. 2004. *STOMP Subsurface Transport Over Multiple Phases, Version 3.1, User's Guide.* PNNL-14478, Pacific Northwest National Laboratory, Richland, WA.

White MD, M Oostrom, and MD Williams. 2001. *FY00 Initial Assessments for S-SX Field Investigation Report (FIR): Simulations of Contaminant Migration with Surface Barriers.* PNWD-3111, Pacific Northwest National Laboratory, Richland, WA.

Wood, MI, TE Jones, R Schalla, BN Bjornstad, and FN Hodges. 2001. *Subsurface Conditions Description Report for the T & TX-TY Waste Management Areas*, RPP-7123 Rev. 0, CH2M HILL Hanford Group, Inc., Richland, Washington.

Wurstner SK, PD Thorne, MA Chamness, MD Freshley, and MD Williams. 1995. *Development of a Three-Dimensional Groundwater Model of the Hanford Site Unconfined Aquifer System: FY 1995 Status Report.* PNL-10886, Pacific Northwest Laboratory, Richland, WA.

Yeh TCJ, LW Gelhar, and AL Gutjahr. 1985. "Stochastic analysis of unsaturated flow in heterogeneous soils, 2. Statistically anisotropic media with variable α." *Water Resources Research,* 21:457-464.

Zhang ZF, VL Freedman, SR Waichler, and MD White. 2004. *2004 Initial assessments of closure for the S-SX Tank Farm: numerical simulations.* PNNL-14604, Pacific Northwest National Laboratory, Richland, WA.

Appendix A

T Tank Farm Cross-Section Plots

(a)

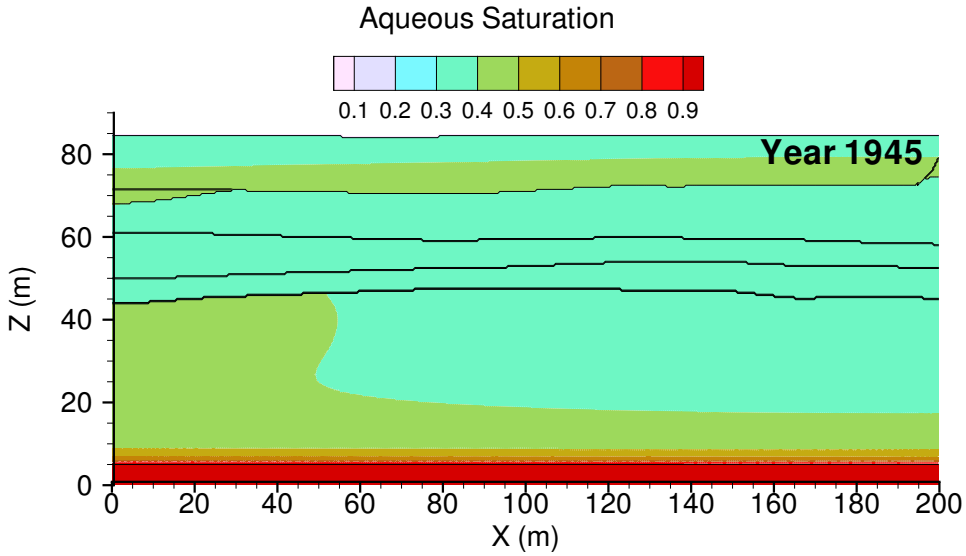

(b)

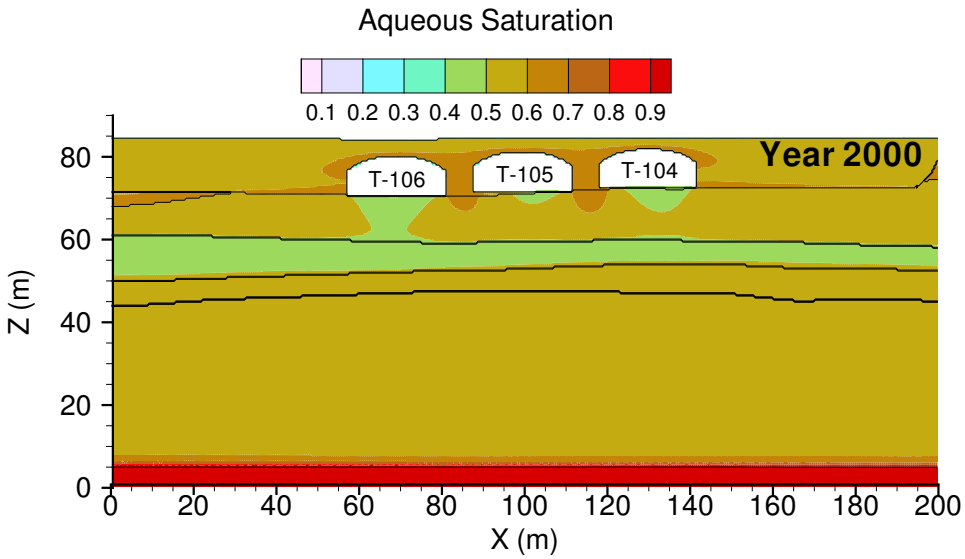

Figure A.1. T baseline aqueous saturation at (a) year 1945 and (b) 01/01/2000

(a)

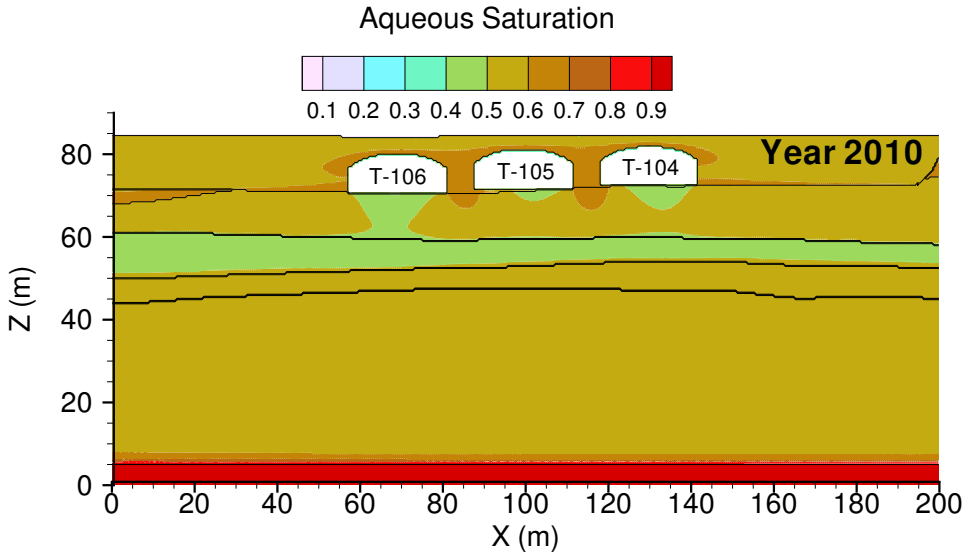

(b)

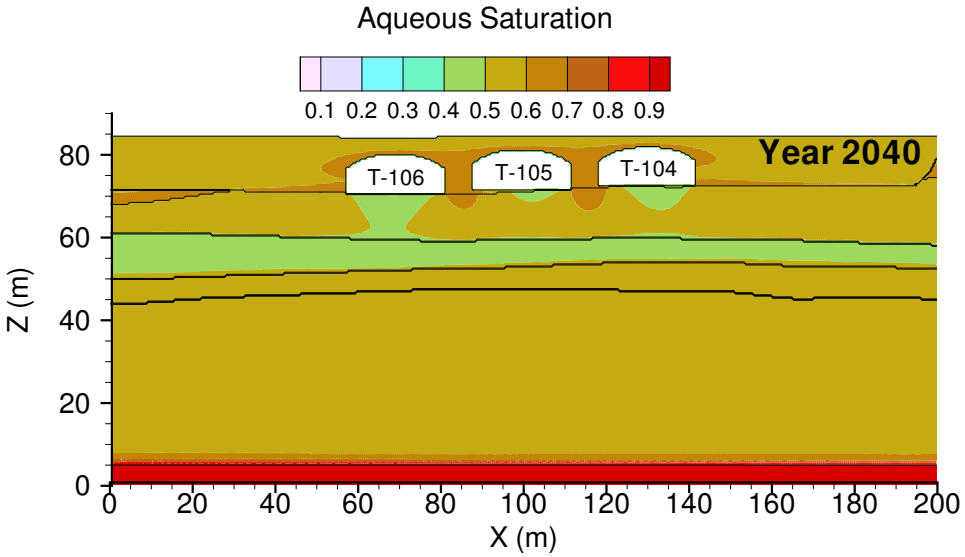

Figure A.2. T baseline aqueous saturation at (a) year 2010 (current conditions) and (b) year 2040 (no interim barrier)

(a)

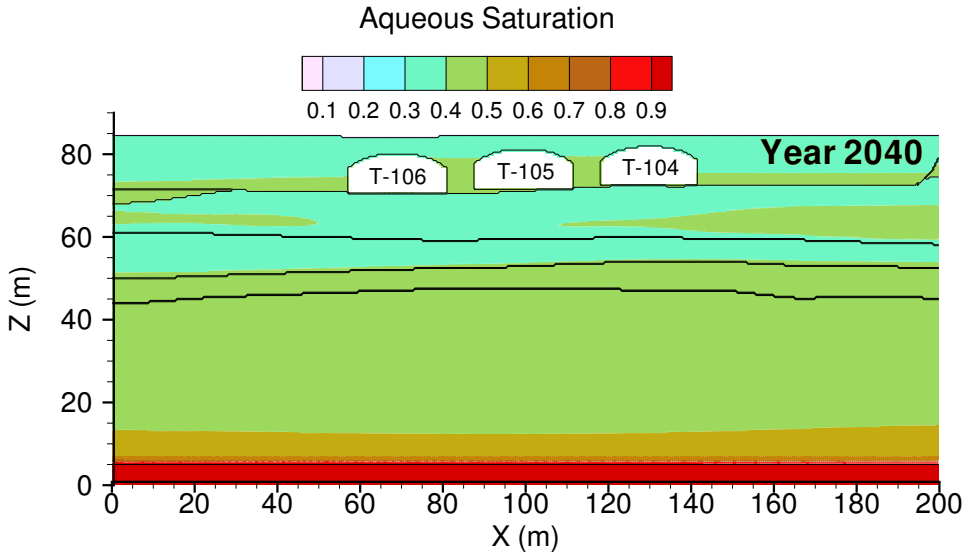

(b)

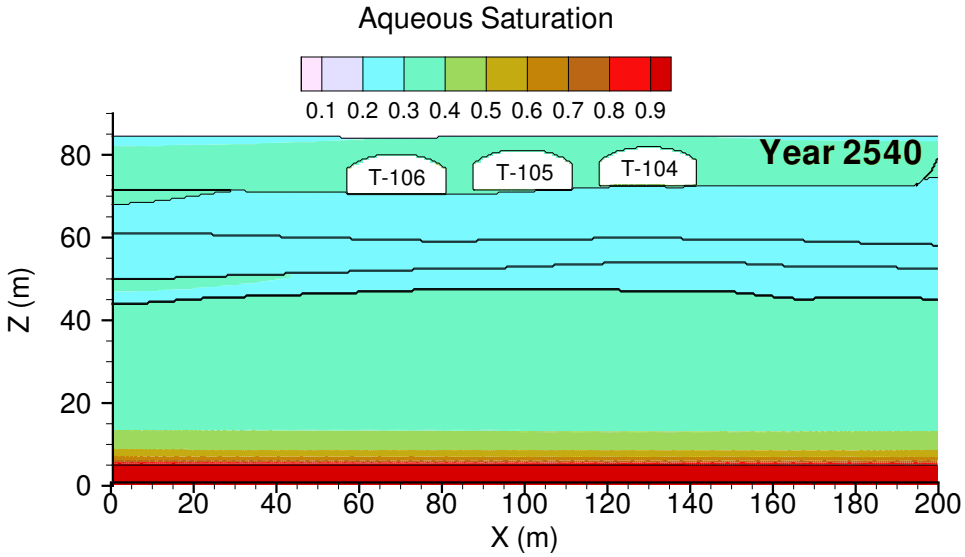

Figure A.3. T baseline aqueous saturation at (a) year 2040 (interim barrier) and (b) year 2540 (closure barrier)

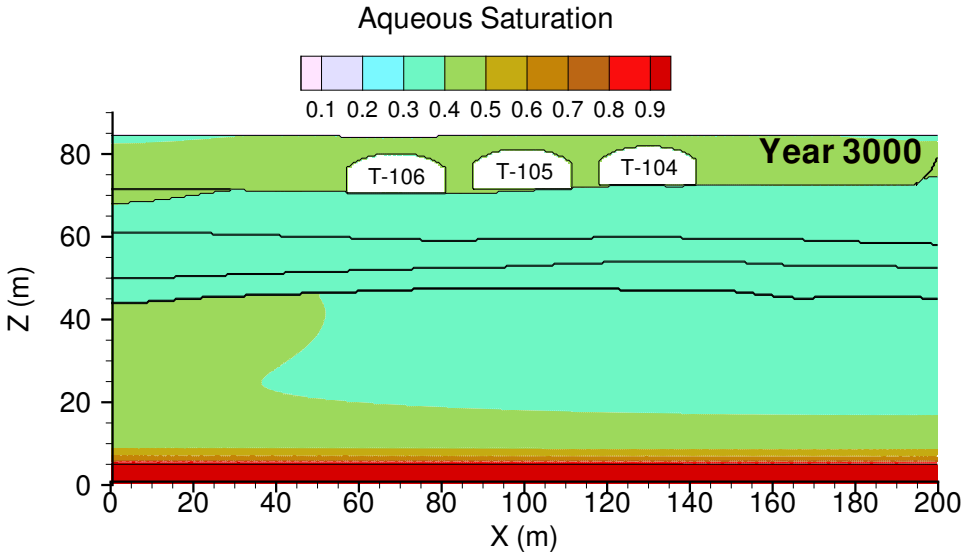

Figure A.4. T baseline aqueous saturation at year 3000 (degraded barrier)

(a)

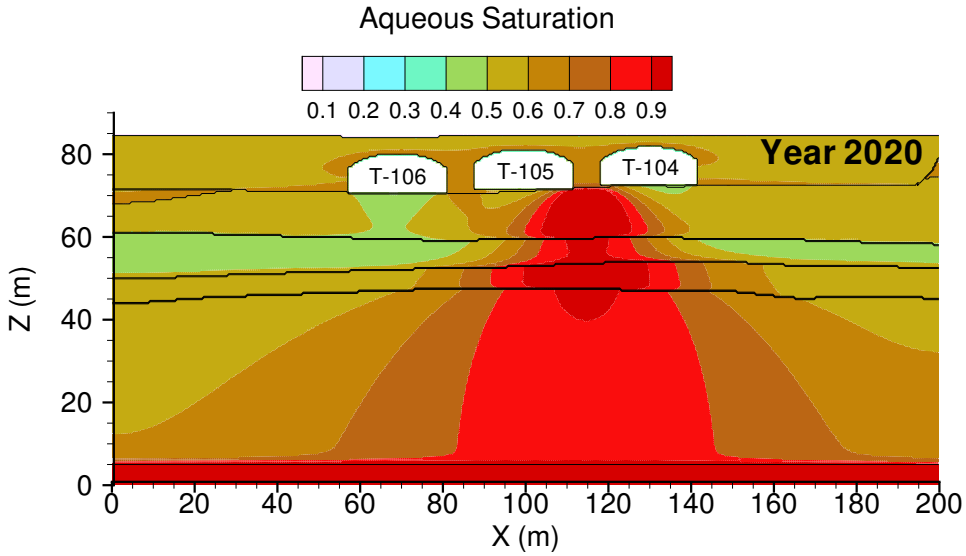

(b)

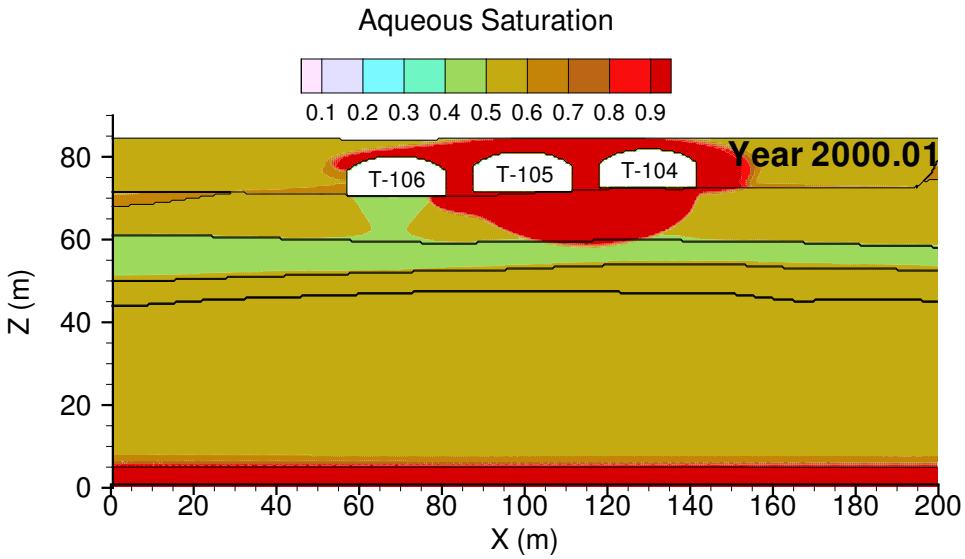

Figure A.5. T baseline aqueous saturation: (a) Case 3, year 2020 and (b) Case 4, 1/5/2000

(a)

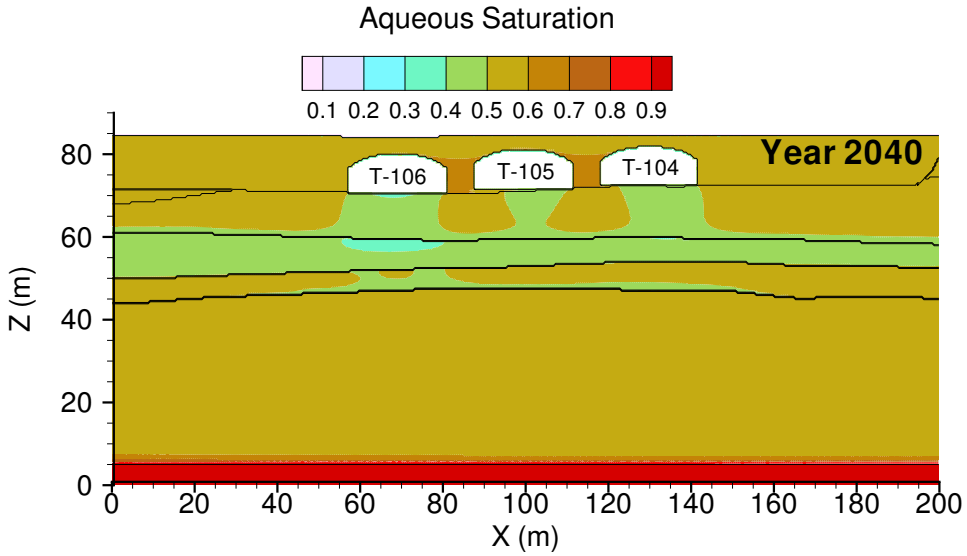

(b)

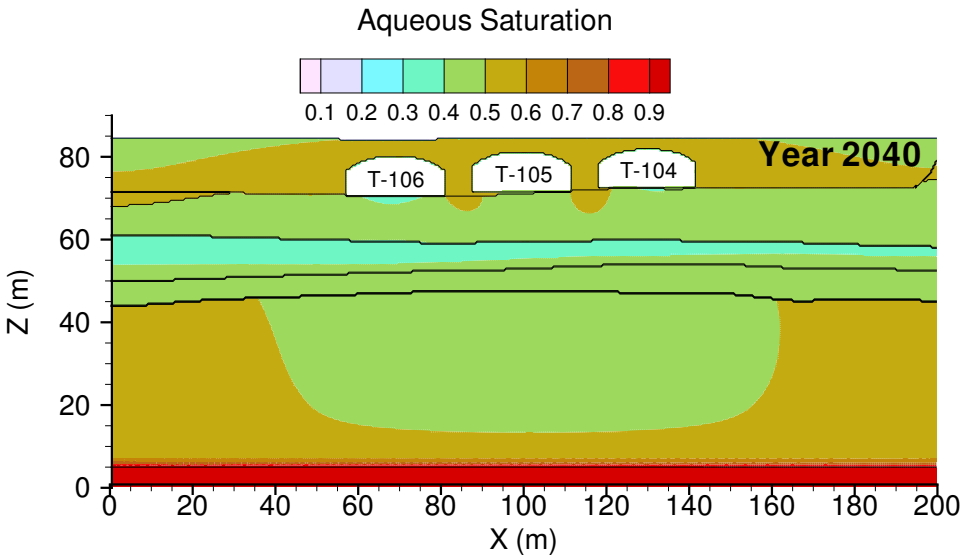

Figure A.6. T baseline aqueous saturation at year 2040: (a) Case 6 and (b) Case 7

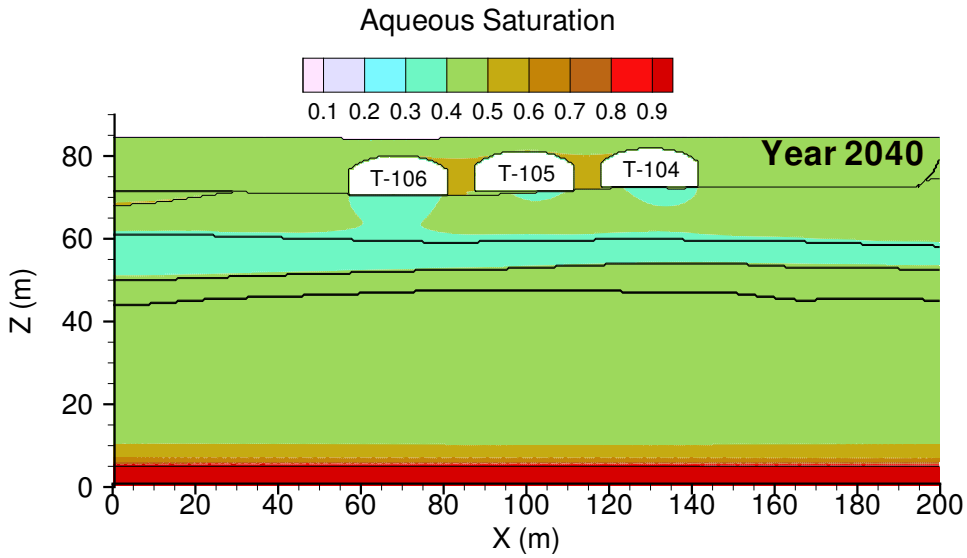

Figure A.7. T baseline aqueous saturation at year 2040 for Case 8

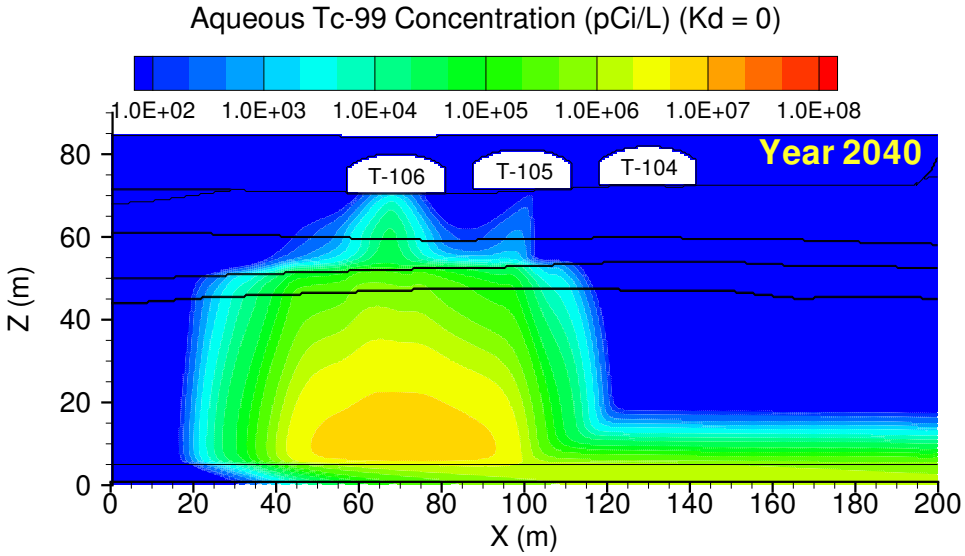

Figure A.8. T Case 1, **Tc-99** aqueous concentration at year 2040. Year of maximum concentration at fenceline was 2041.

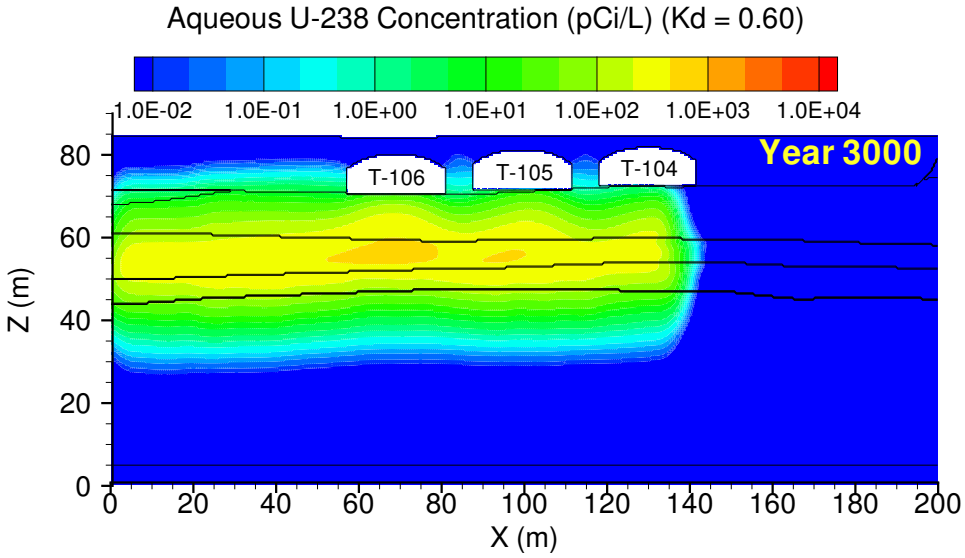

Figure A.9. T Case 1, **U-238** (K_d = 0.60) aqueous concentration at year 3000. Year of maximum concentration at fenceline was 3000.

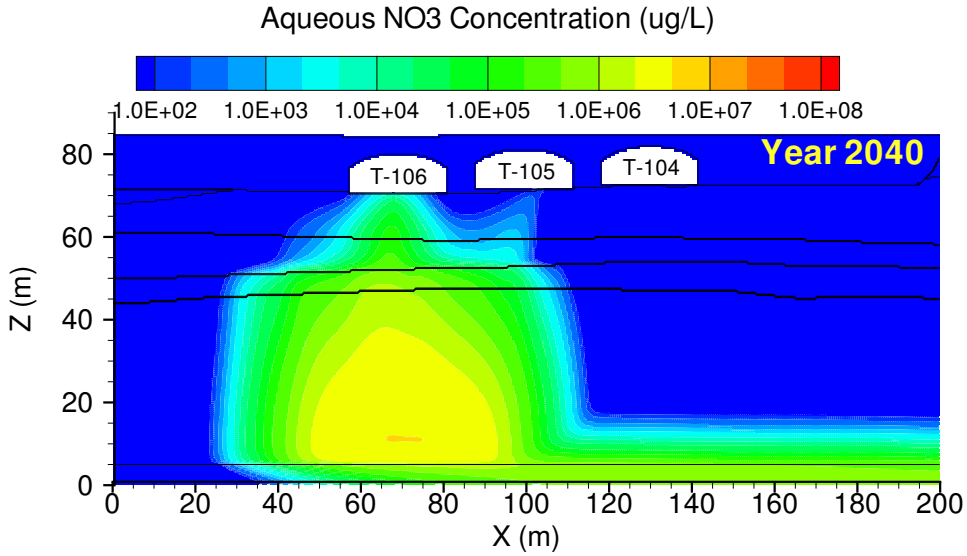

Figure A.10. T Case 1, **NO_3** aqueous concentration at year 2040. Year of maximum concentration at fenceline was 2042.

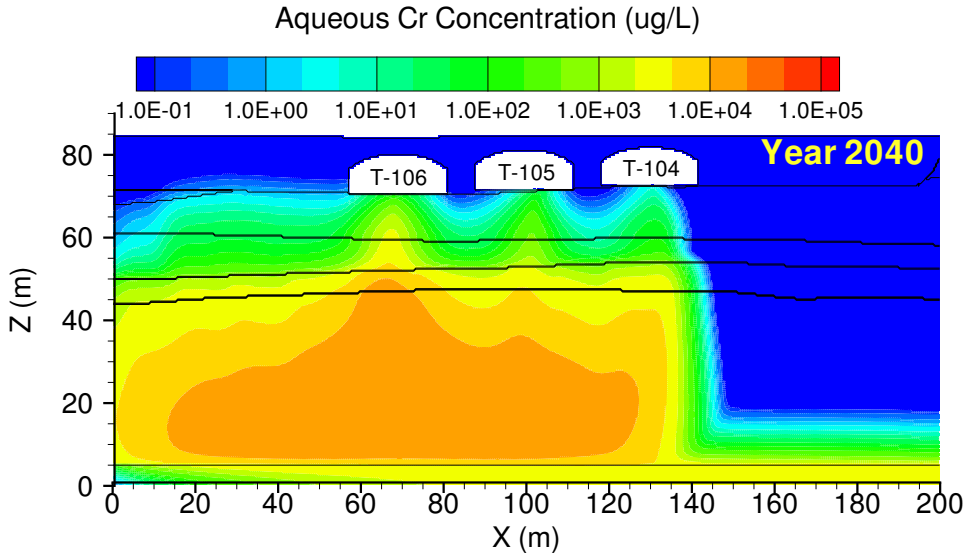

Figure A.11. T Case 1, **Cr** aqueous concentration at year 2040. Year of maximum concentration at fenceline was 2049.

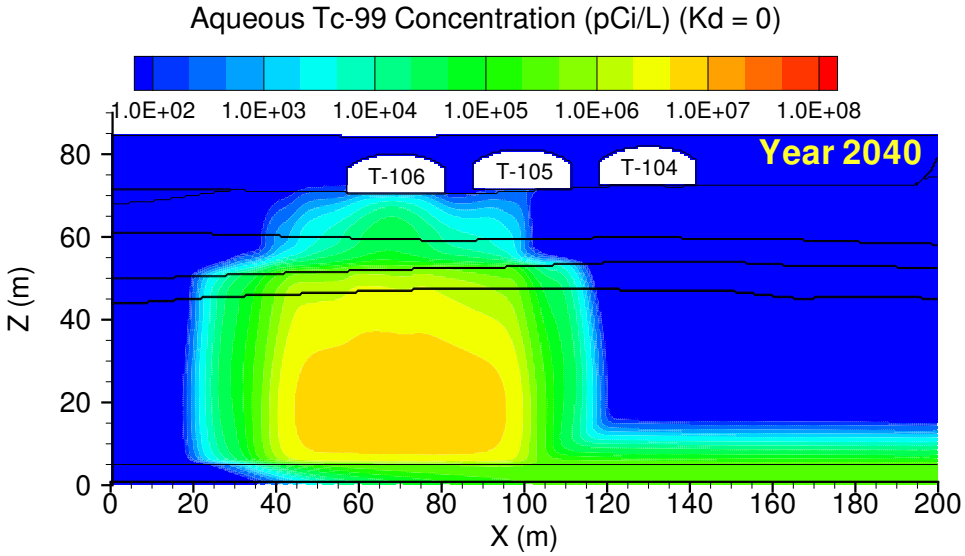

Figure A.12. T Case 2, **Tc-99** aqueous concentration at year 2040. Year of maximum concentration at fenceline was 2042.

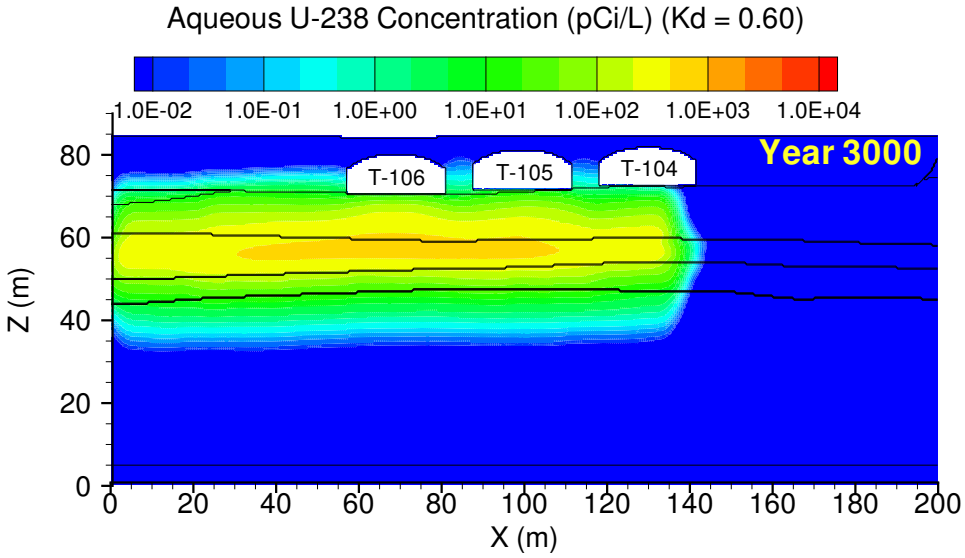

Figure A.13. T Case 2, **U-238** (K_d = 0.60) aqueous concentration at year 3000. Year of maximum concentration at fenceline was 3000.

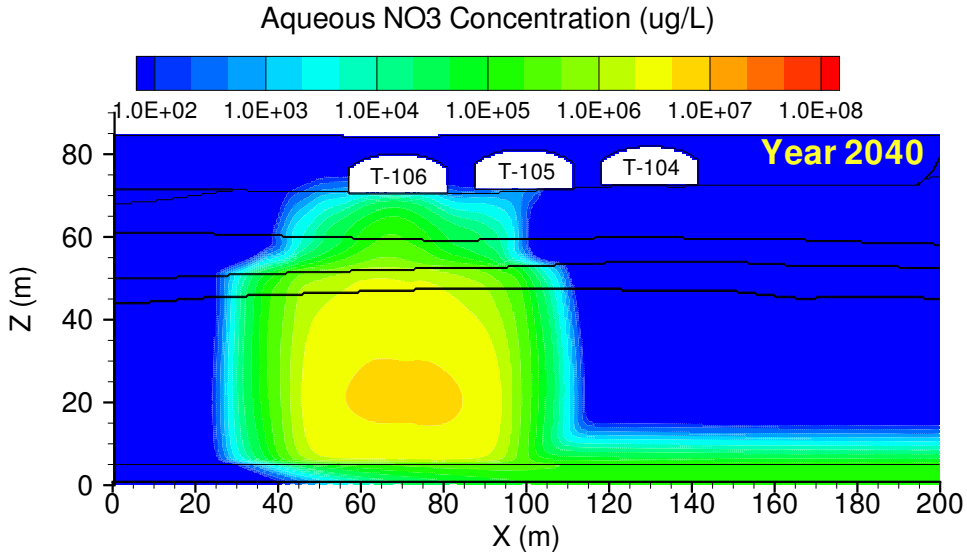

Figure A.14. T Case 2, **NO_3** aqueous concentration at year 2040. Year of maximum concentration at fenceline was 2042.

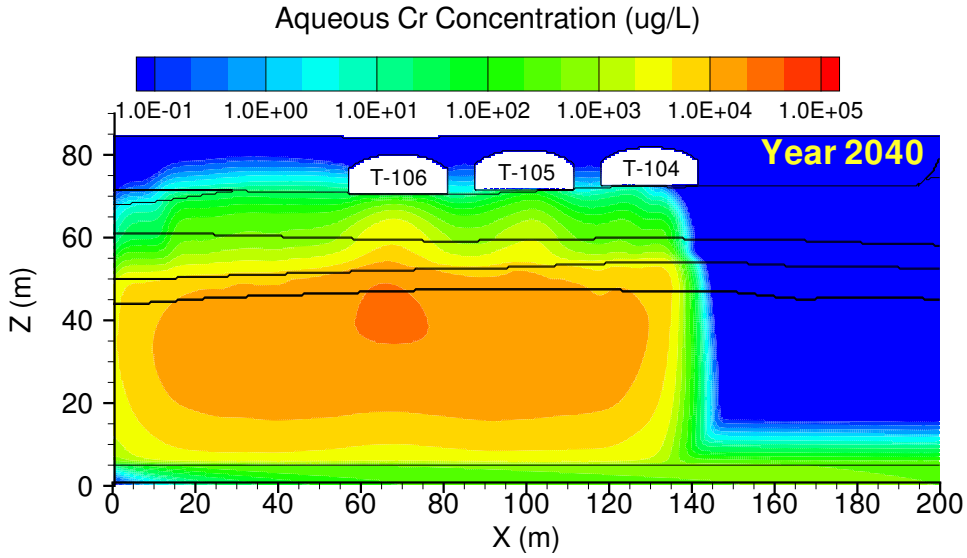

Figure A.15. T Case 2, **Cr** aqueous concentration at year 2040. Year of maximum concentration at fenceline was 2055.

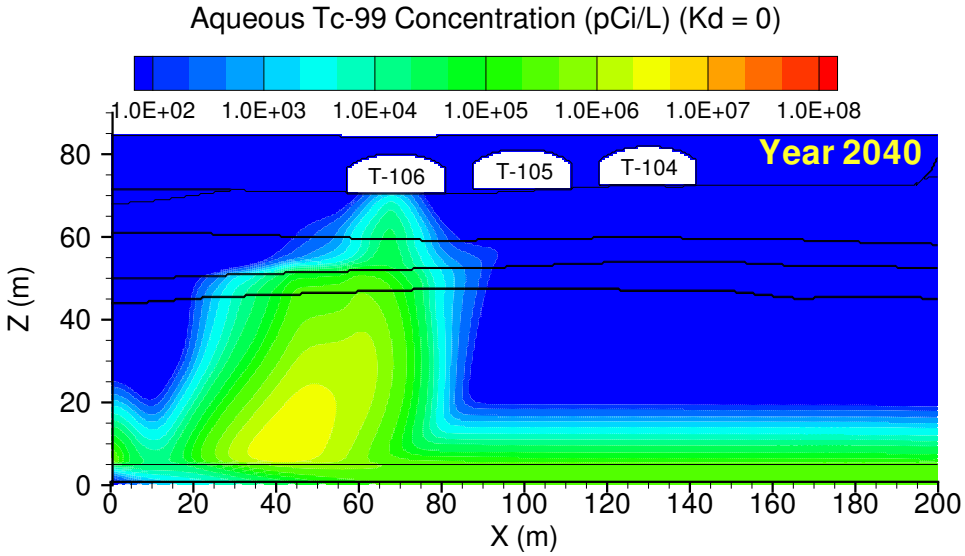

Figure A.16. T Case 3, **Tc-99** aqueous concentration at year 2040. Year of maximum concentration at fenceline was 2028.

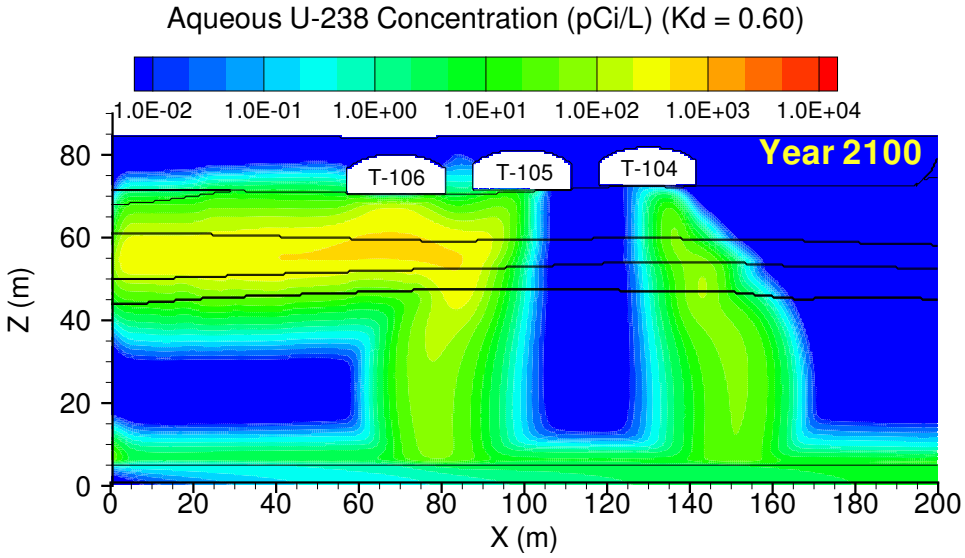

Figure A.17. T Case 3, **U-238** (K_d = 0.60) aqueous concentration at year 2100. Year of maximum concentration at fenceline was 2075.

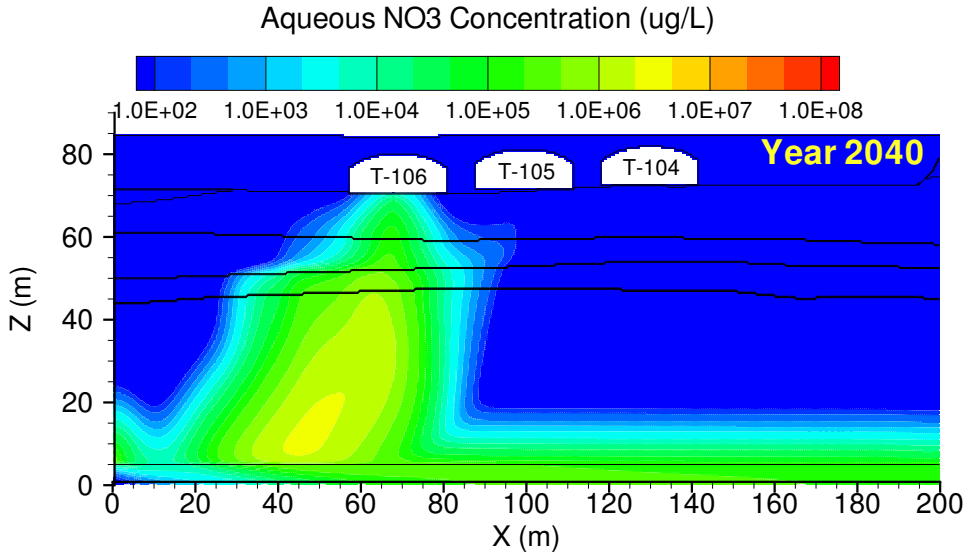

Figure A.18. T Case 3, **NO_3** aqueous concentration at year 2040. Year of maximum concentration at fenceline was 2028.

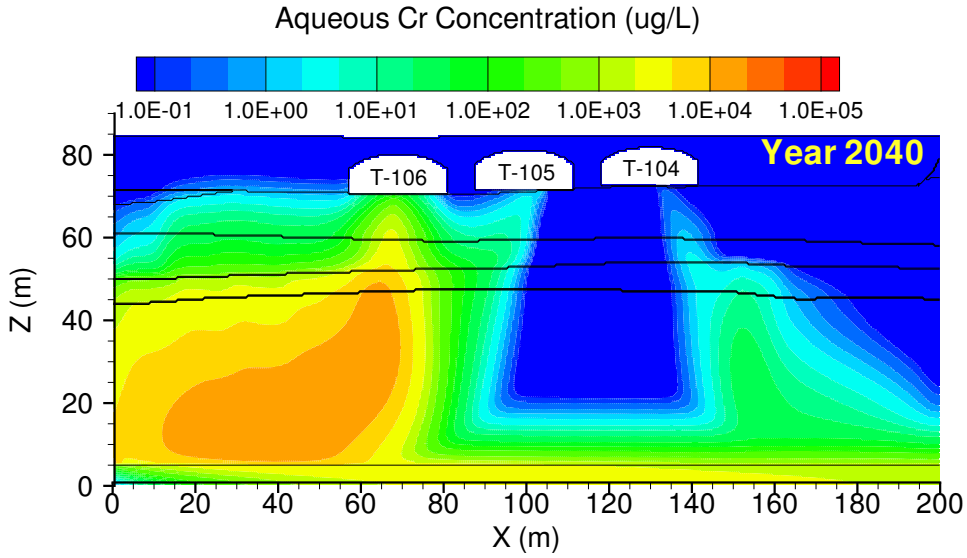

Figure A.19. T Case 3, **Cr** aqueous concentration at year 2040. Year of maximum concentration at fenceline was 2028.

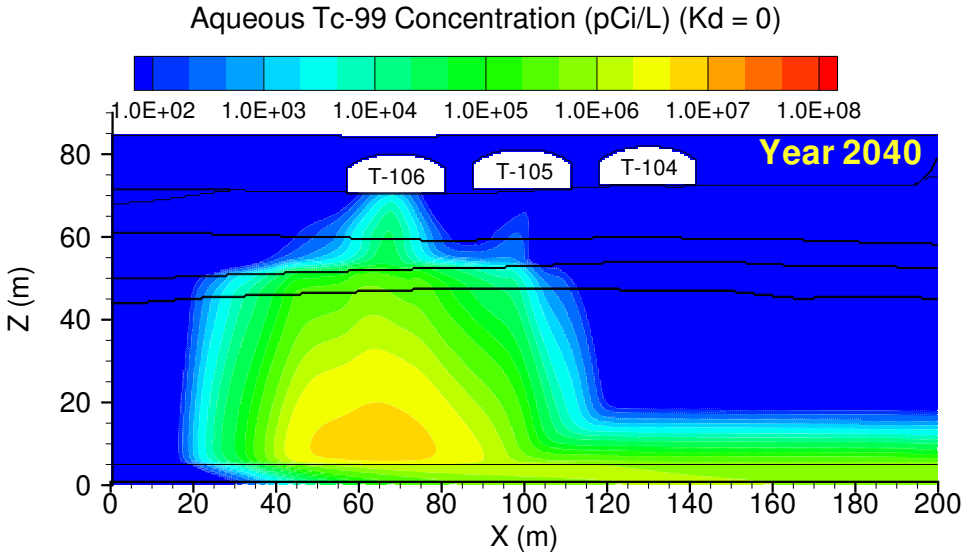

Figure A.20. T Case 4, **Tc-99** aqueous concentration at year 2040. Year of maximum concentration at fenceline was 2036.

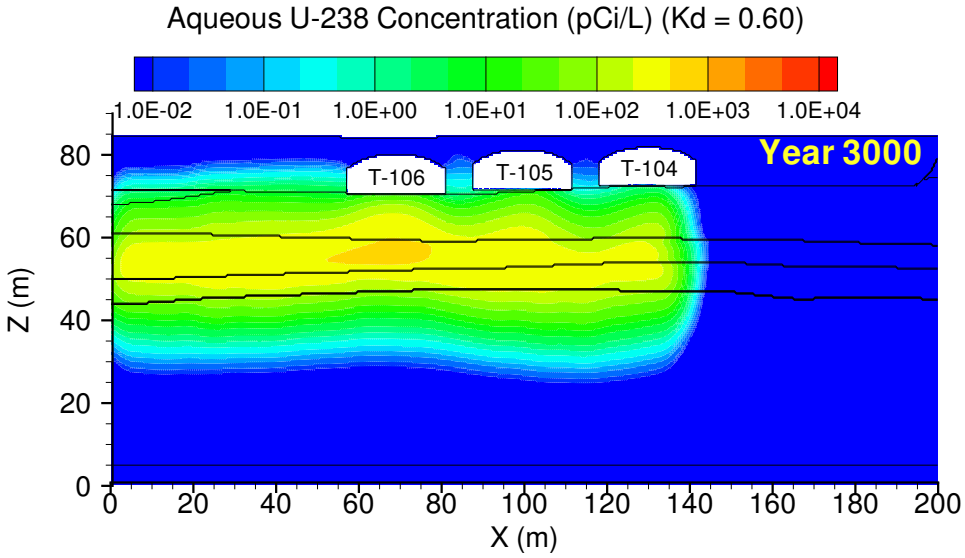

Figure A.21. T Case 4, **U-238** (K_d = 0.60) aqueous concentration at year 3000. Year of maximum concentration at fenceline was 3000.

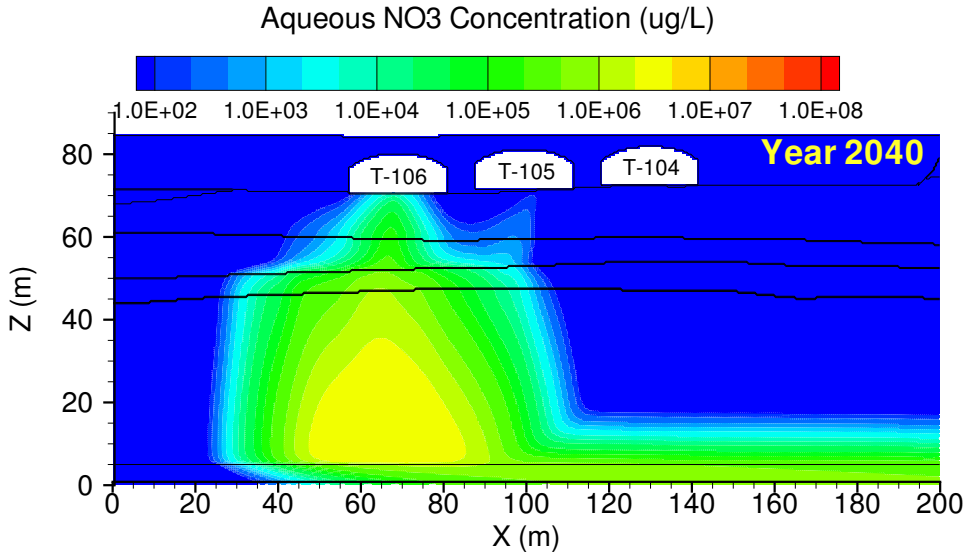

Figure A.22. T Case 4, **NO_3** aqueous concentration at year 2040. Year of maximum concentration at fenceline was 2038.

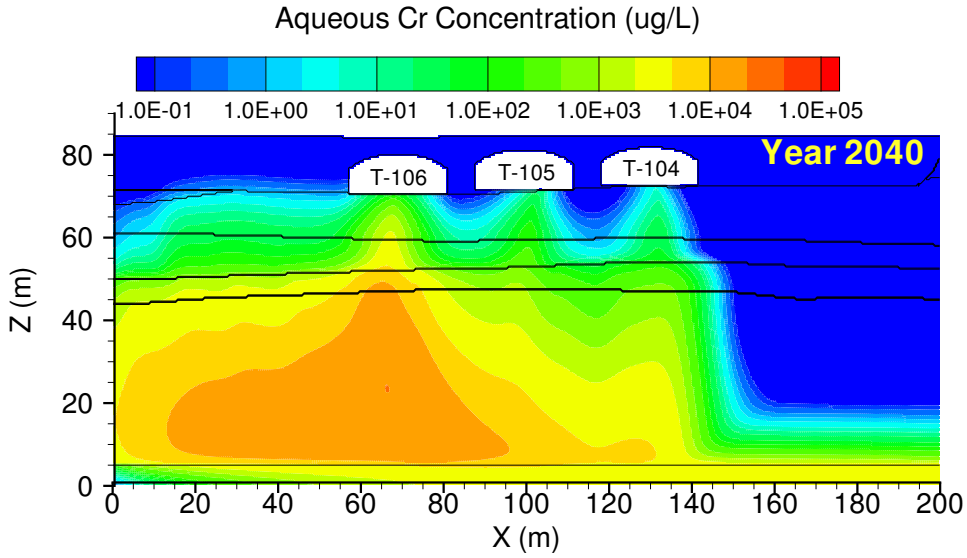

Figure A.23. T Case 4, **Cr** aqueous concentration at year 2040. Year of maximum concentration at fenceline was 2047.

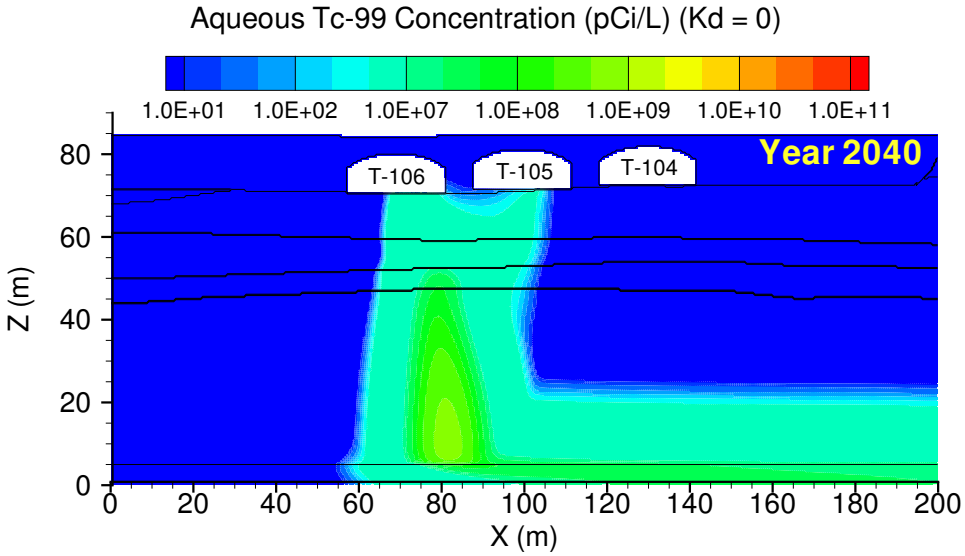

Figure A.24. T Case 5, **Tc-99** aqueous concentration at year 2040. Year of maximum concentration at fenceline was 2040.

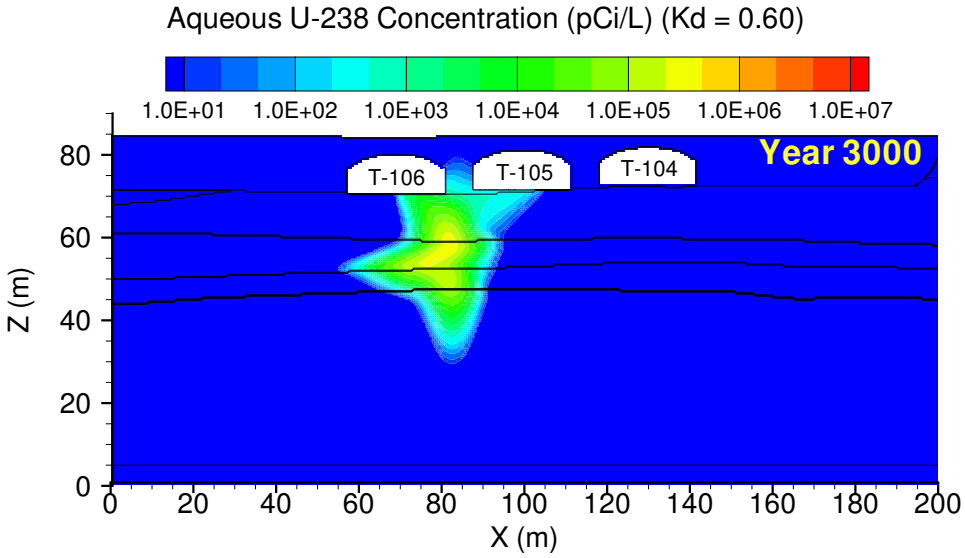

Figure A.25. T Case 5, **U-238** (K_d = 0.60) aqueous concentration at year 3000. Year of maximum concentration at fenceline was 3000.

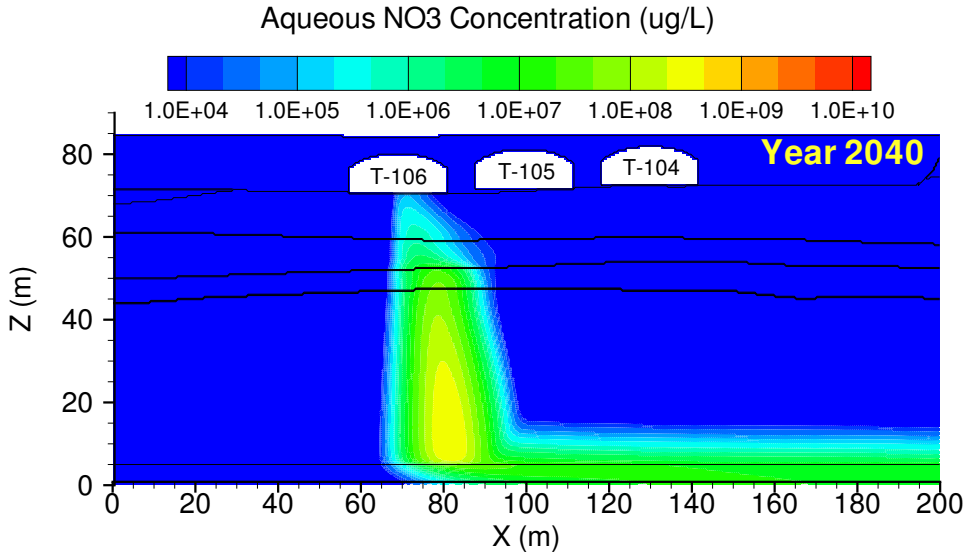

Figure A.26. T Case 5, **NO_3** aqueous concentration at year 2040. Year of maximum concentration at fenceline was 2042.

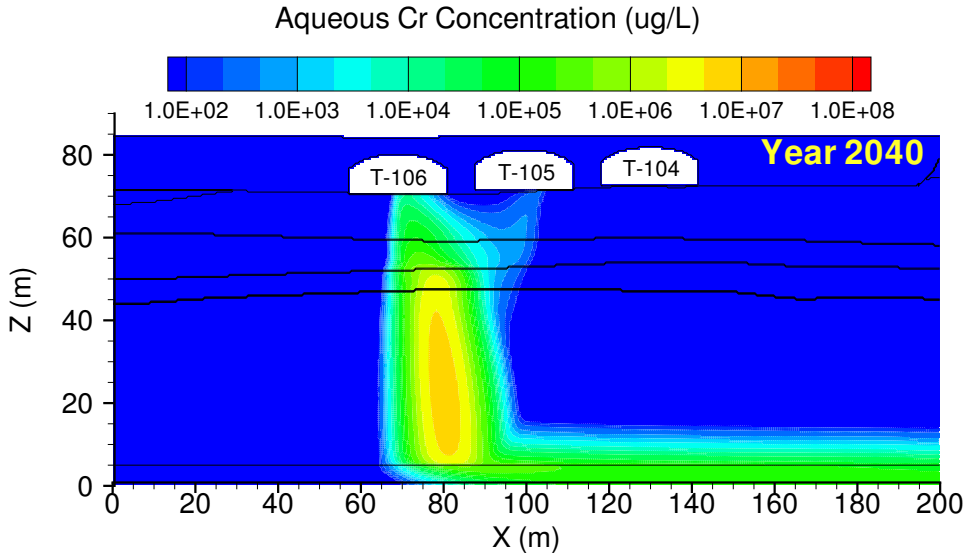

Figure A.27. T Case 5, **Cr** aqueous concentration at year 2040. Year of maximum concentration at fenceline was 2050.

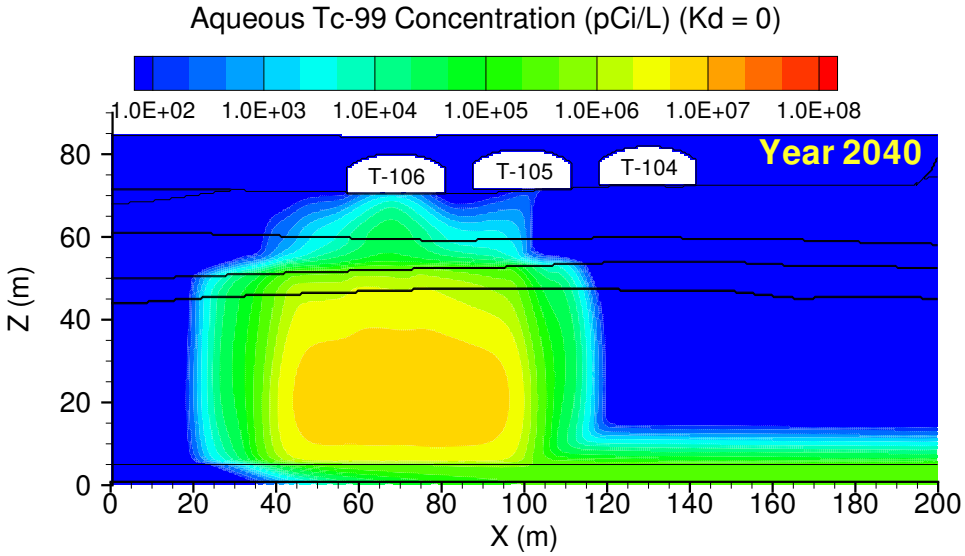

Figure A.28. T Case 6, **Tc-99** aqueous concentration at year 2040. Year of maximum concentration at fenceline was 2057.

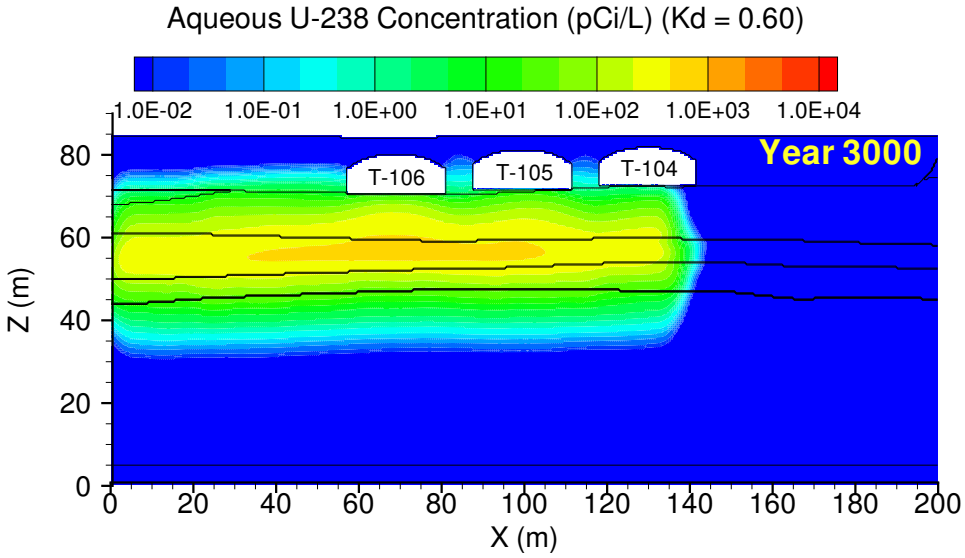

Figure A.29. T Case 6, **U-238** (K_d = 0.60) aqueous concentration at year 3000. Year of maximum concentration at fenceline was 3000.

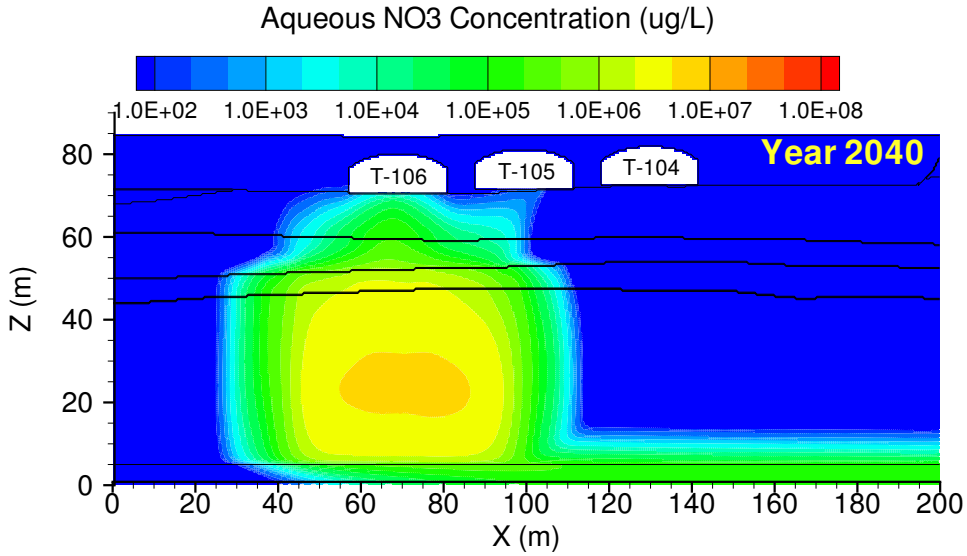

Figure A.30. T Case 6, **NO_3** aqueous concentration at year 2040. Year of maximum concentration at fenceline was 2058.

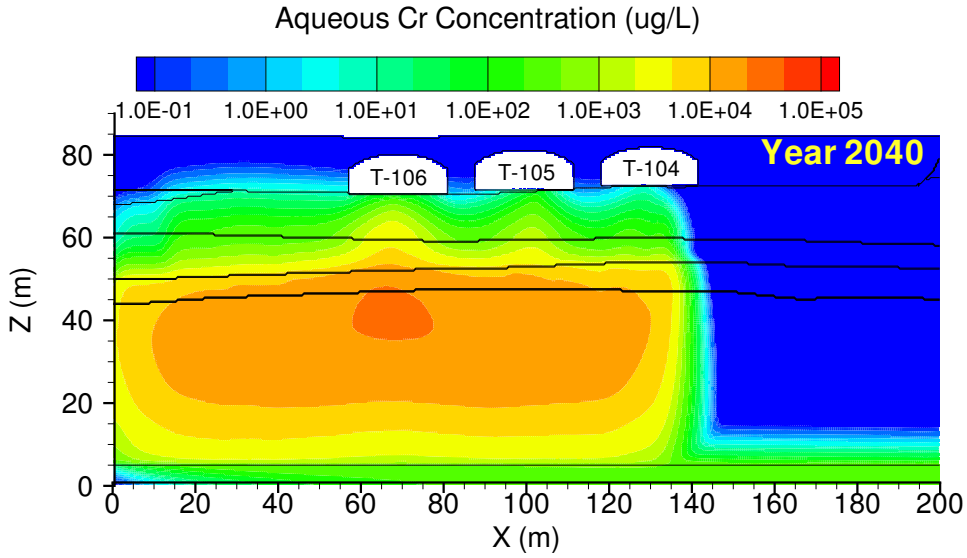

Figure A.31. T Case 6, **Cr** aqueous concentration at year 2040. Year of maximum concentration at fenceline was 2064.

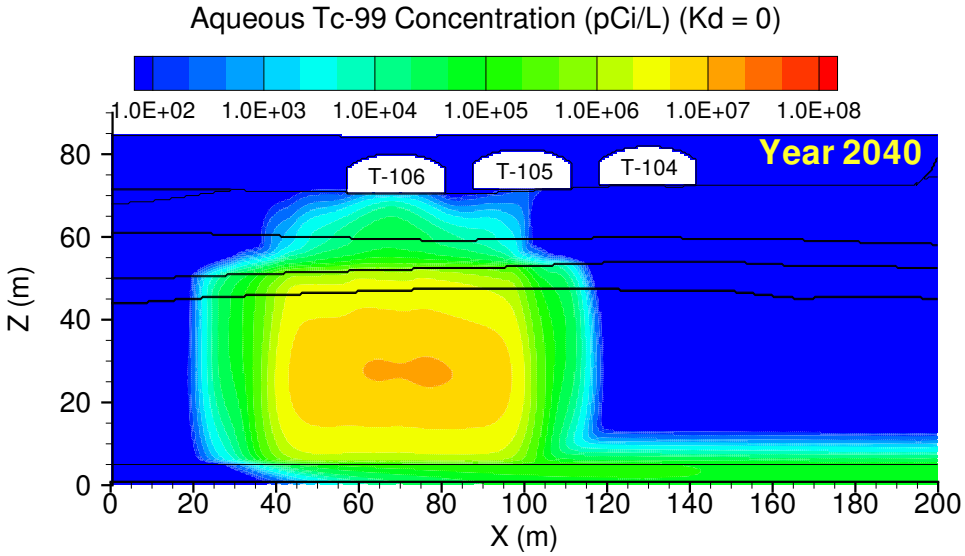

Figure A.32. T Case 7, **Tc-99** aqueous concentration at year 2040. Year of maximum concentration at fenceline was 2070.

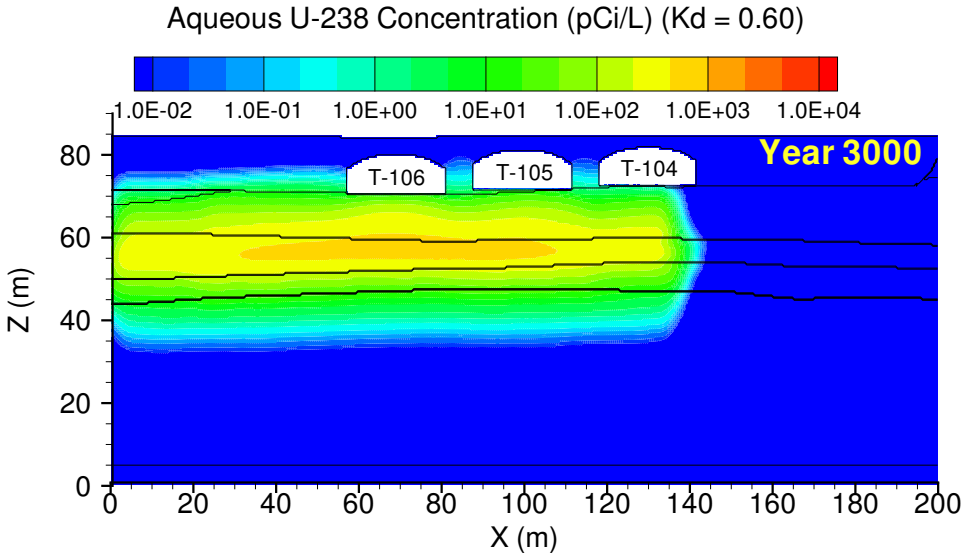

Figure A.33. T Case 7, **U-238** (K_d = 0.60) aqueous concentration at year 3000. Year of maximum concentration at fenceline was 3000.

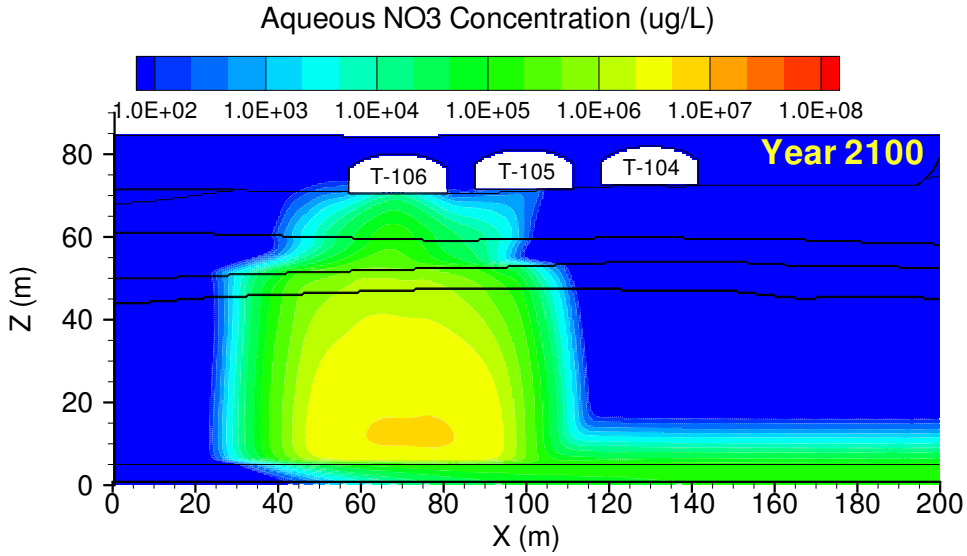

Figure A.34. T Case 7, **NO_3** aqueous concentration at year 2100. Year of maximum concentration at fenceline was 2071.

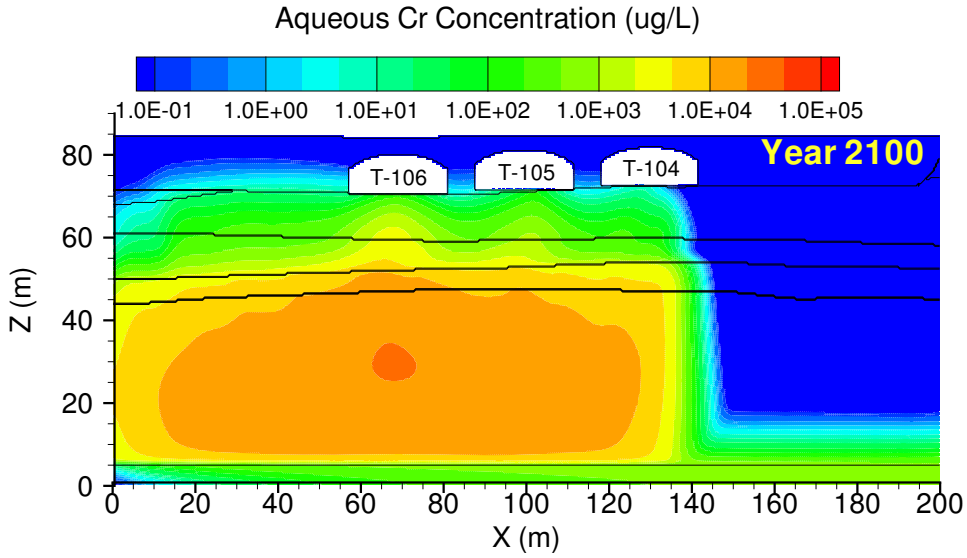

Figure A.35. T Case 7, **Cr** aqueous concentration at year 2100. Year of maximum concentration at fenceline was 2082.

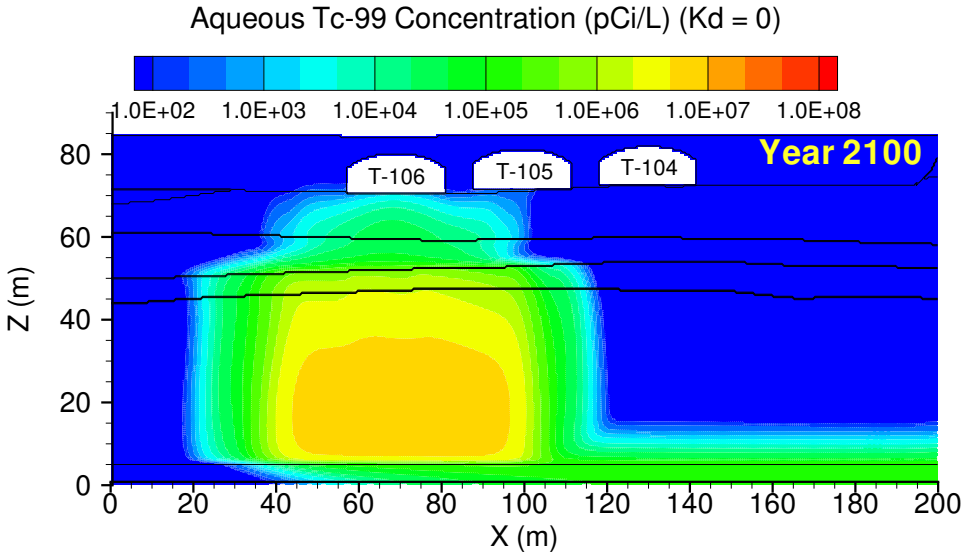

Figure A.36. T Case 8, **Tc-99** aqueous concentration at year 2100. Year of maximum concentration at fenceline was 2099.

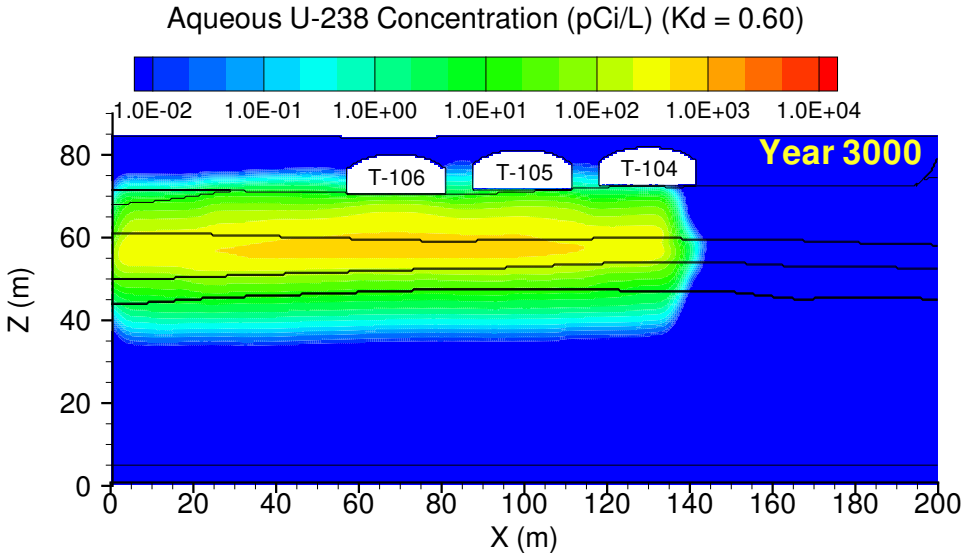

Figure A.37. T Case 8, **U-238** (K_d = 0.60) aqueous concentration at year 3000. Year of maximum concentration at fenceline was 3000.

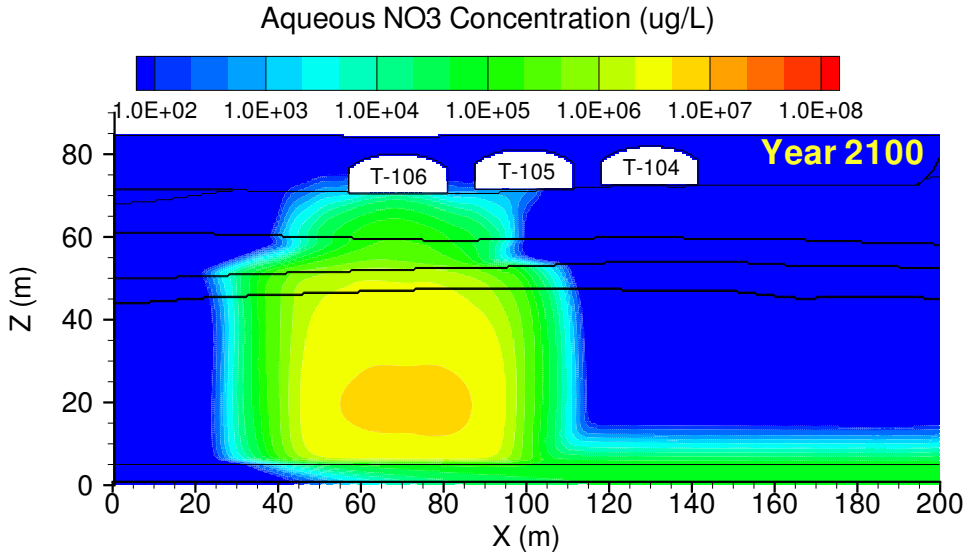

Figure A.38. T Case 8, **NO_3** aqueous concentration at year 2100. Year of maximum concentration at fenceline was 2100.

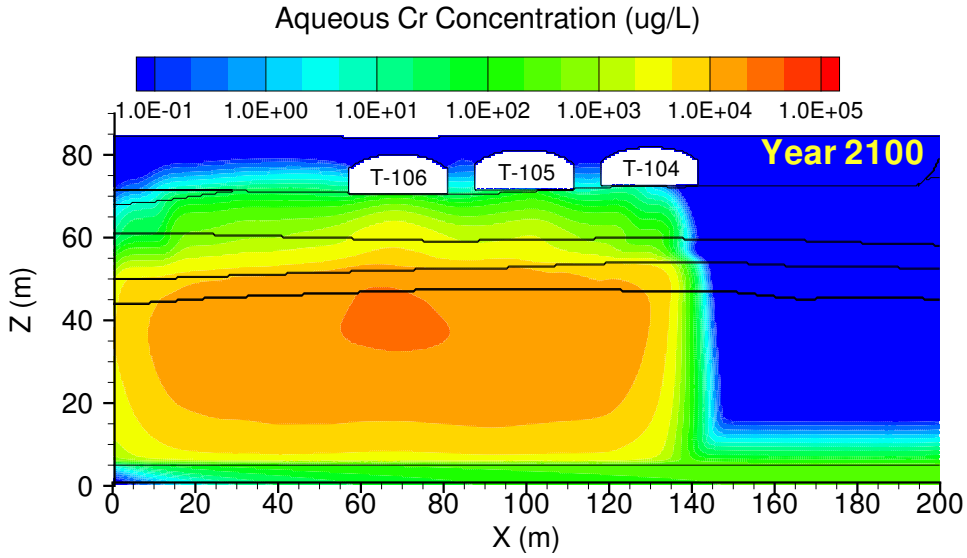

Figure A.39. T Case 8, **Cr** aqueous concentration at year 2100. Year of maximum concentration at fenceline was 2128.

Appendix B

T Tank Farm
Contaminant Breakthrough Curves

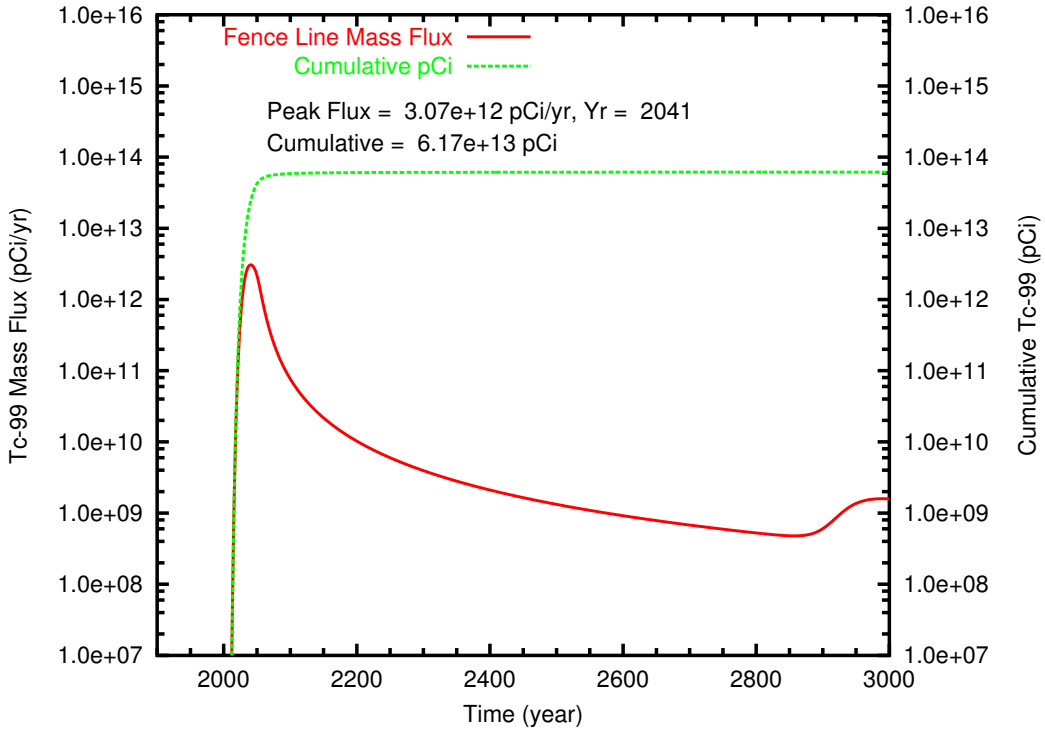

Figure B.1. T Case 1 **Tc-99** mass flux and cumulative mass at fenceline

(a)

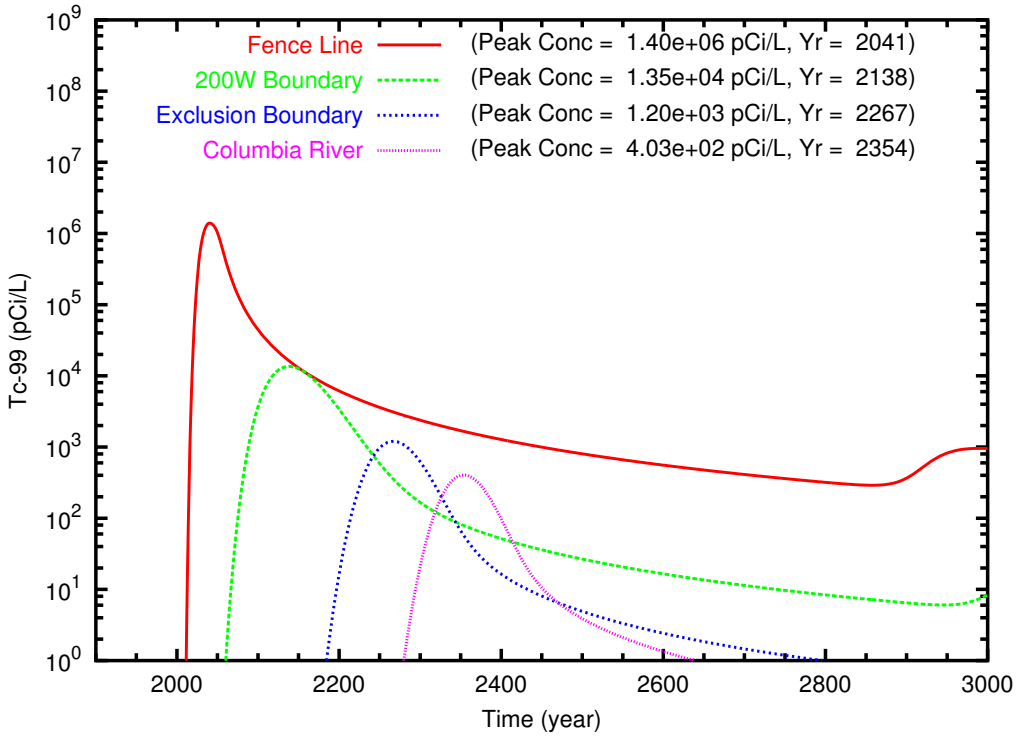

(b)

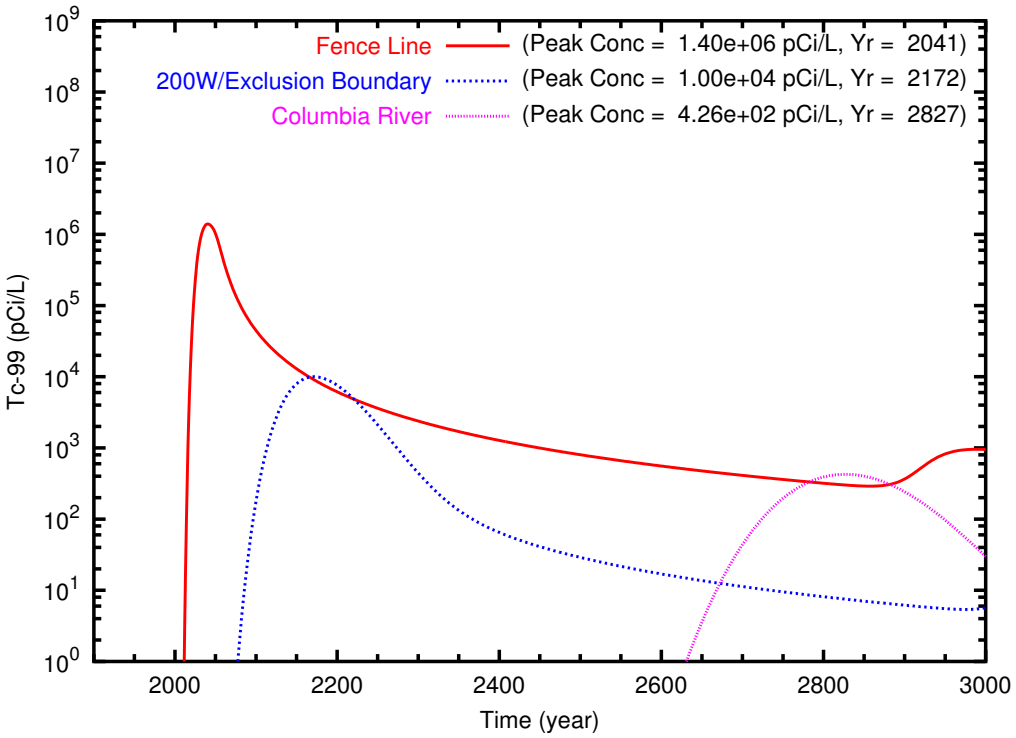

Figure B.2. T Case 1 **Tc-99** breakthrough curves at fenceline and downgradient points along (a) east path and (b) north path

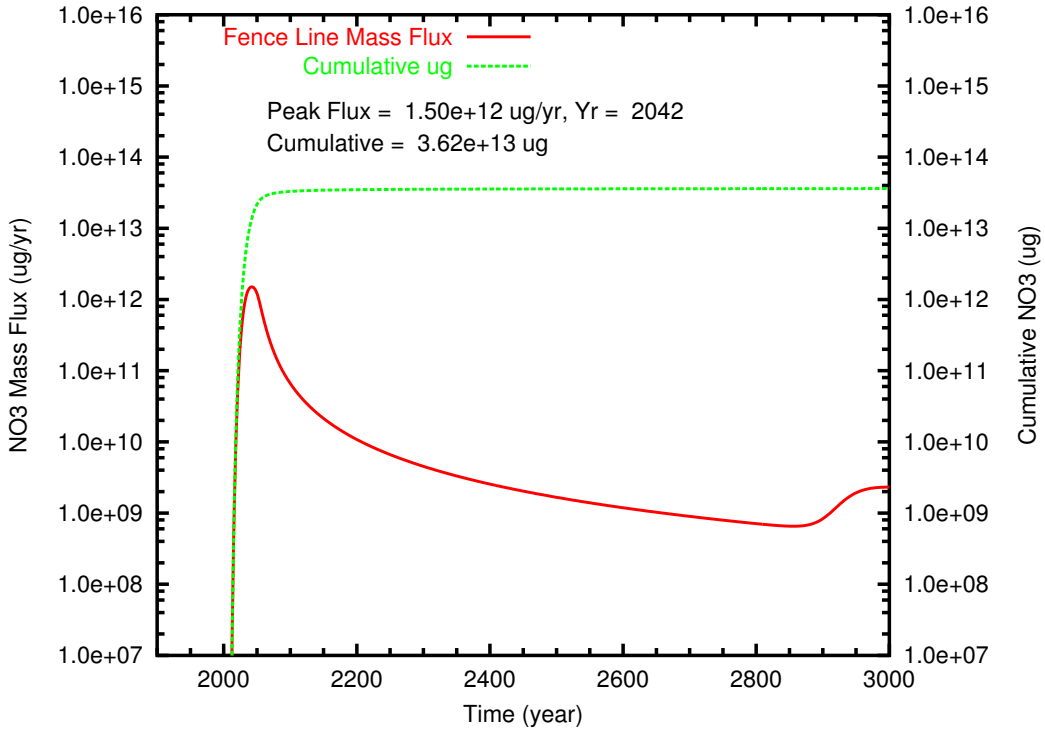

Figure B.3. T Case 1 $\mathbf{NO_3}$ mass flux and cumulative mass at fenceline

(a)

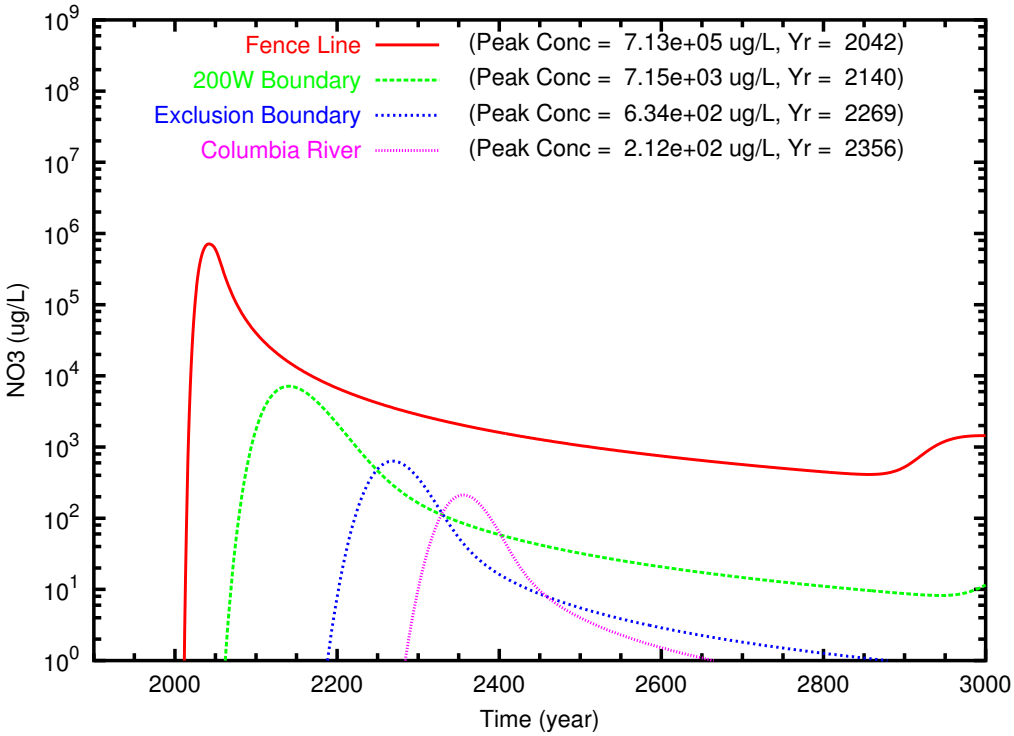

(b)

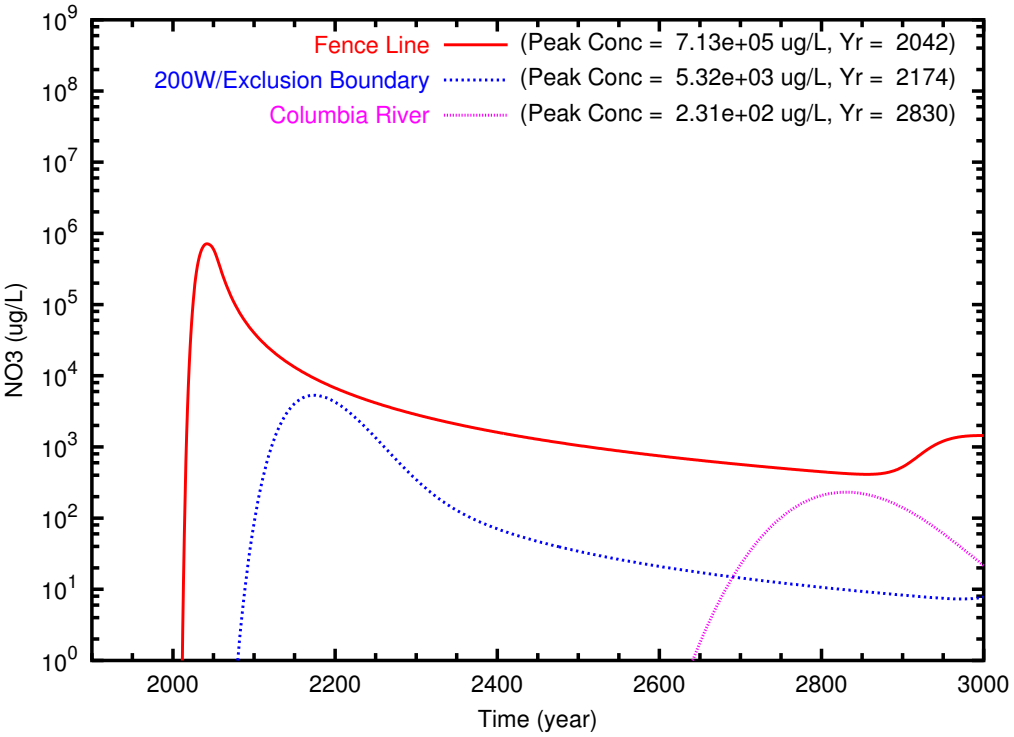

Figure B.4. T Case 1 **NO_3** breakthrough curves at fenceline and downgradient points along (a) east path and (b) north path

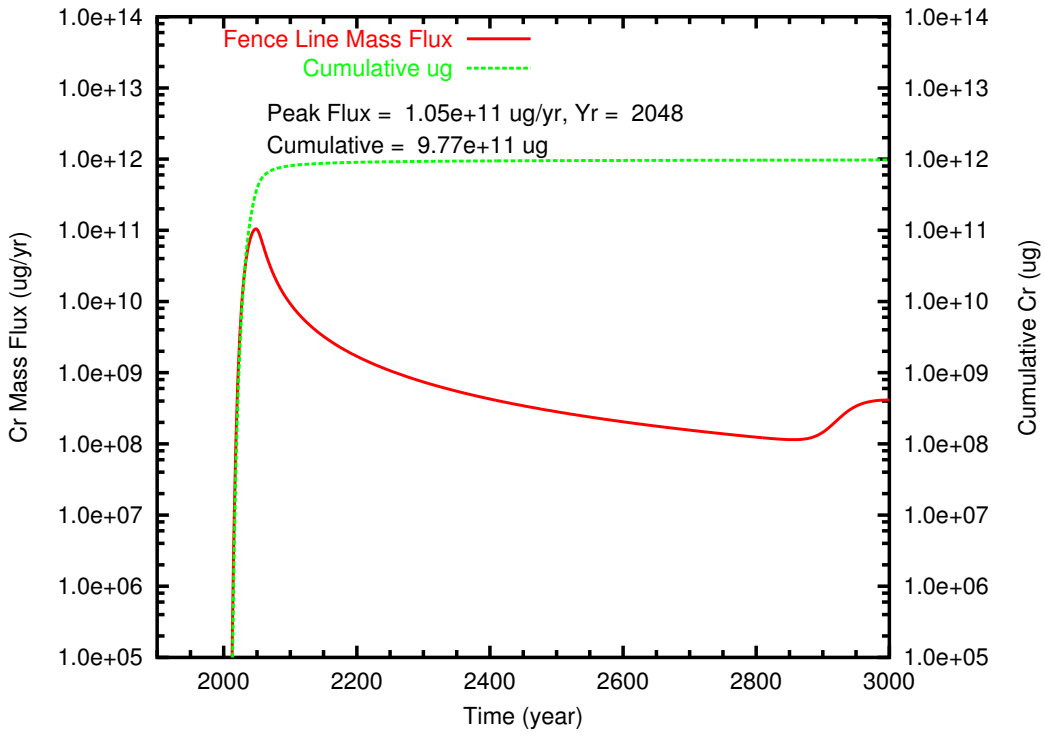

Figure B.5. T Case 1 **Cr** mass flux and cumulative mass at fenceline

(a)

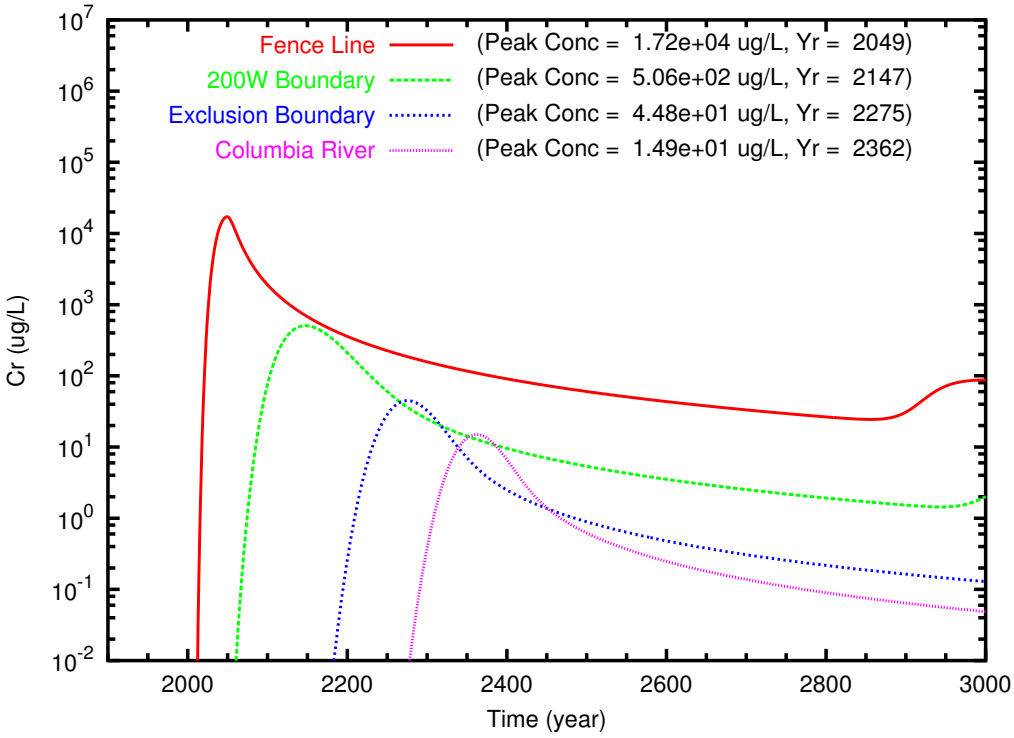

(b)

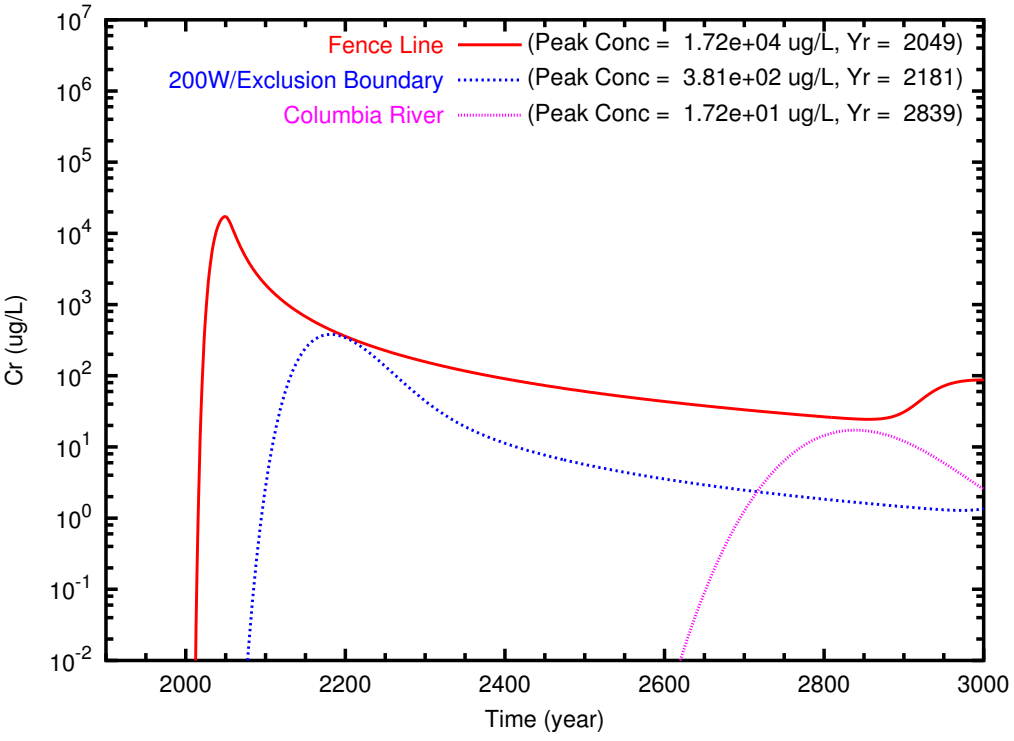

Figure B.6. T Case 1 **Cr** breakthrough curves at fenceline and downgradient points along (a) east path and (b) north path

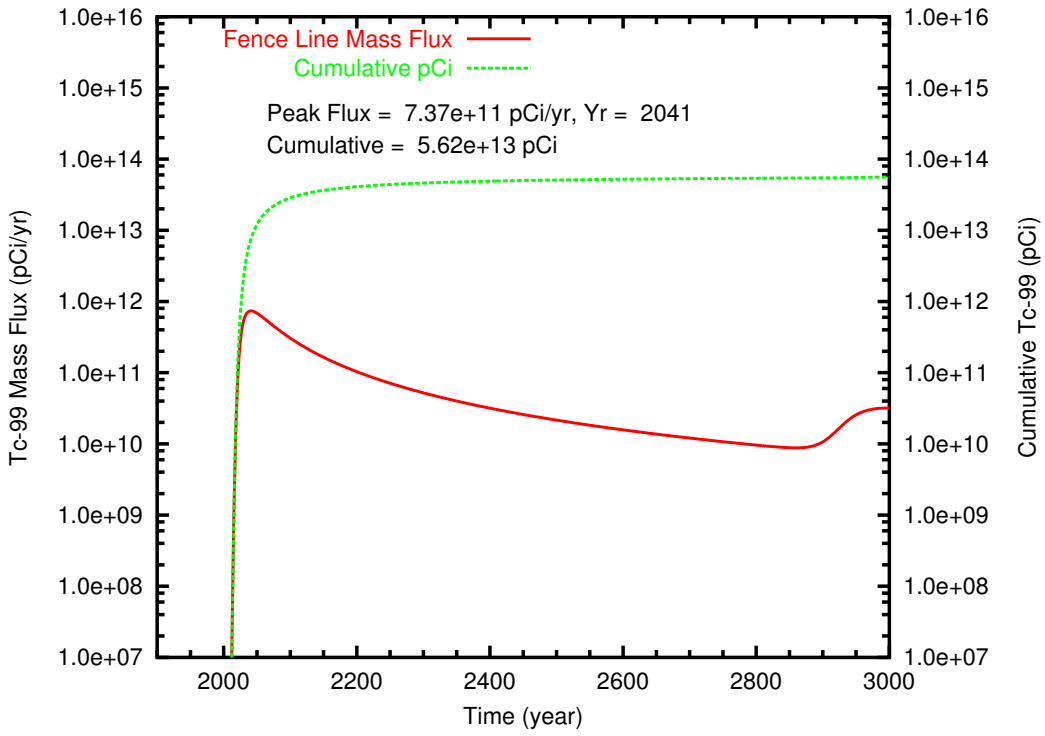

Figure B.7. T Case 2 **Tc-99** mass flux and cumulative mass at fenceline

(a)

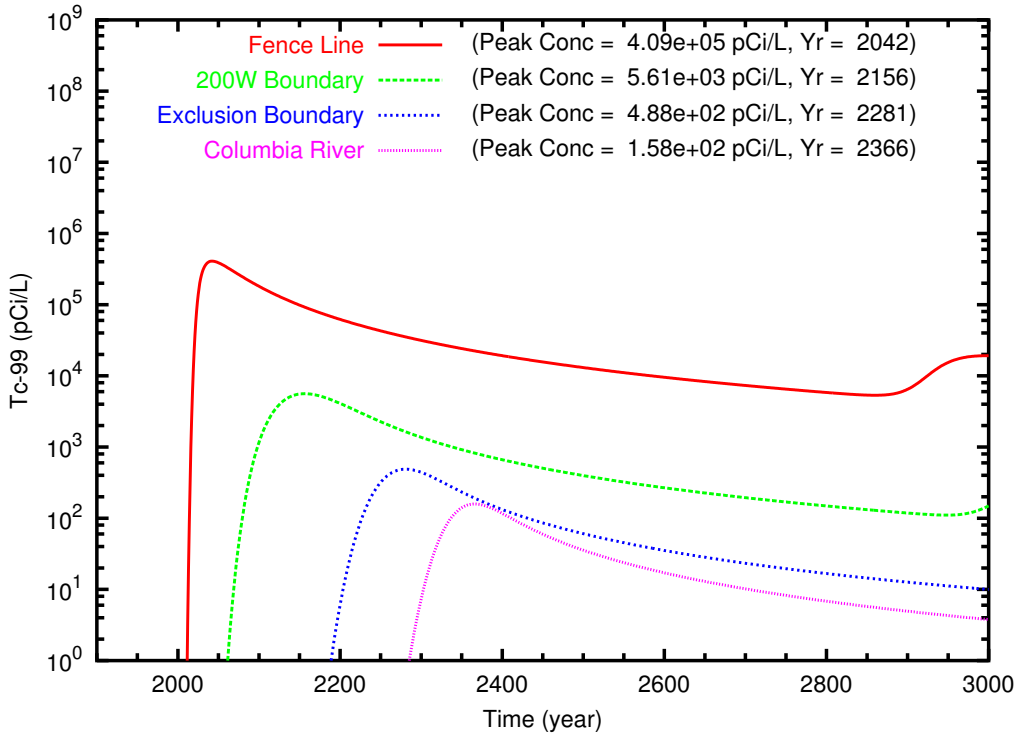

(b)

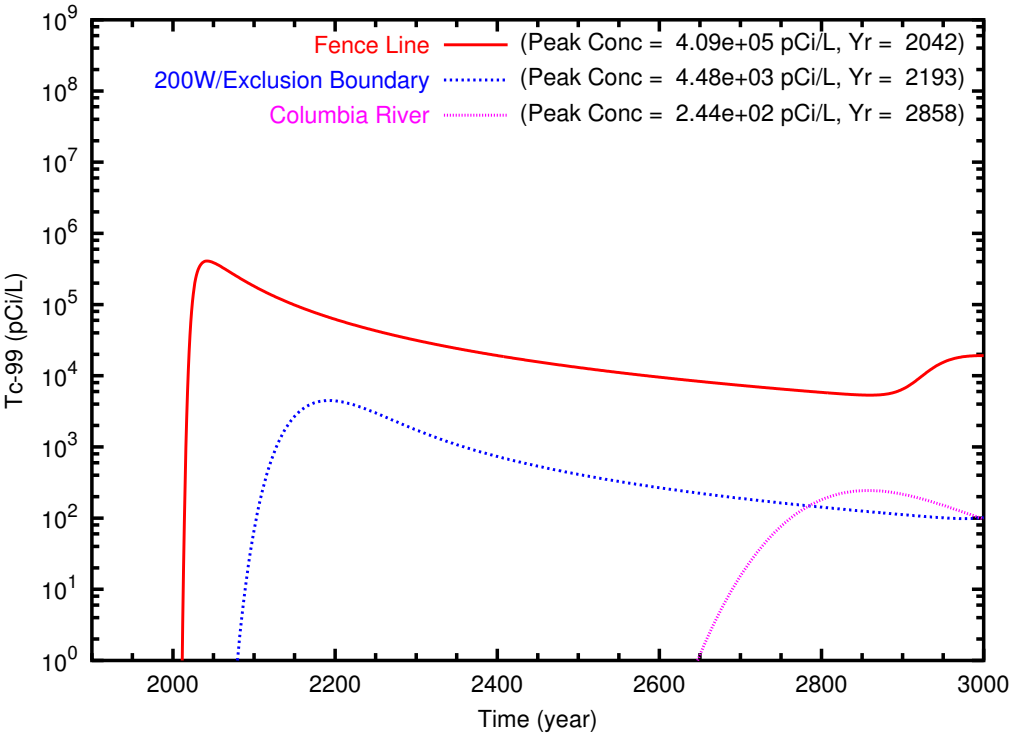

Figure B.8. T Case 2 **Tc-99** breakthrough curves at fenceline and downgradient points along (a) east path and (b) north path

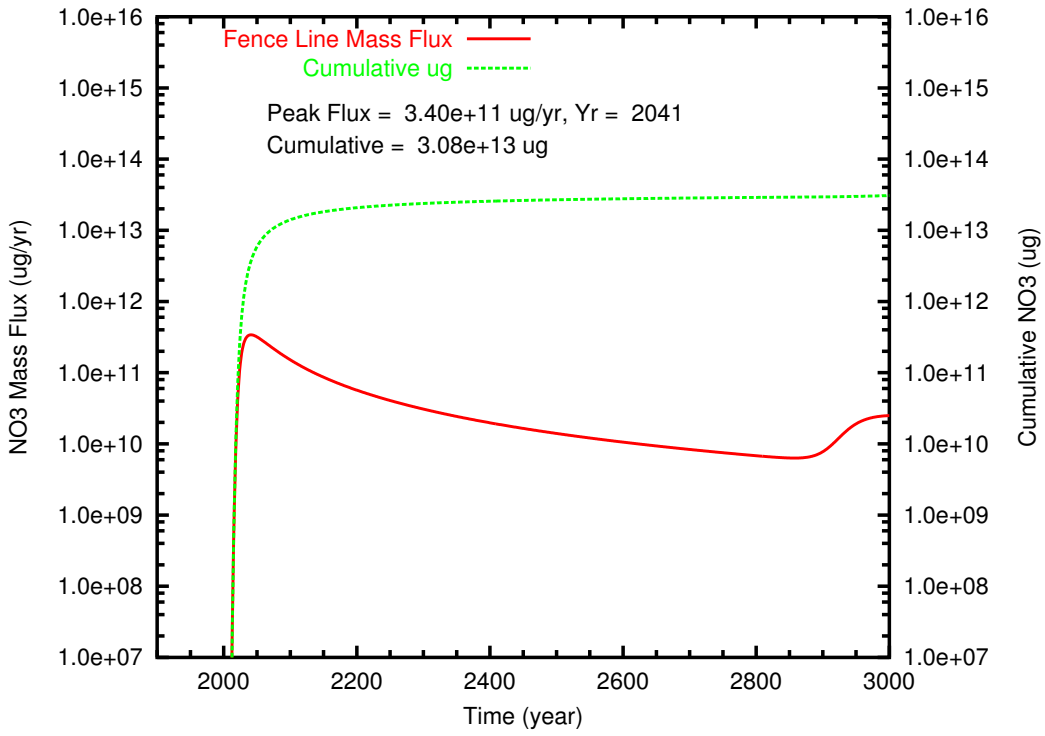

Figure B.9. T Case 2 $\mathbf{NO_3}$ mass flux and cumulative mass at fenceline

(a)

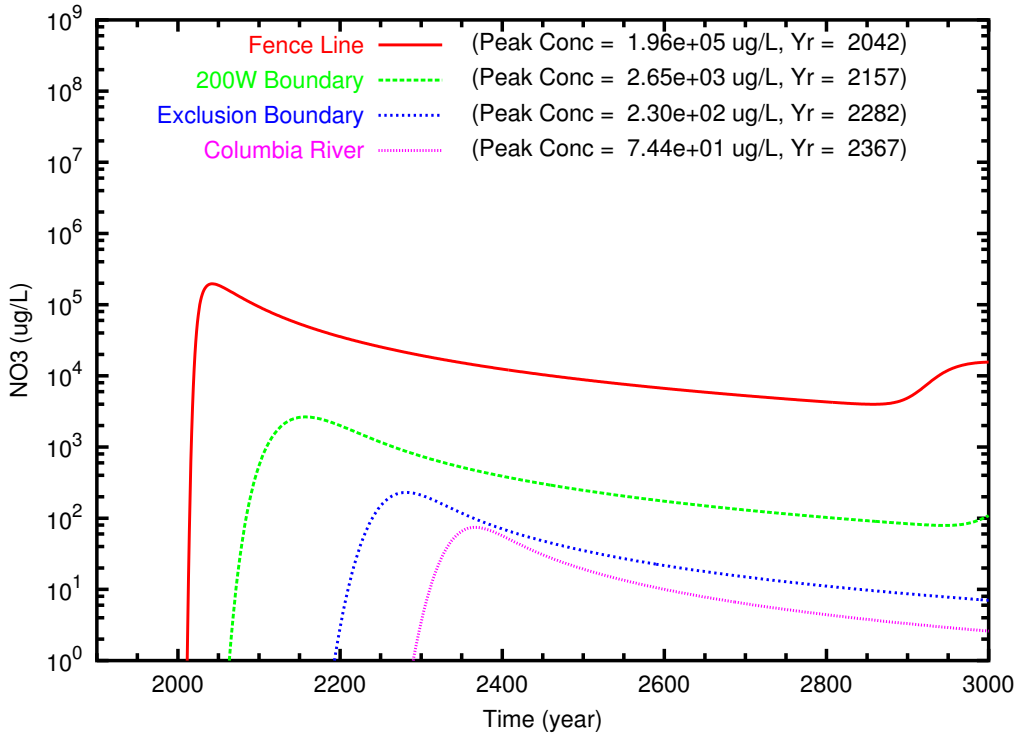

(b)

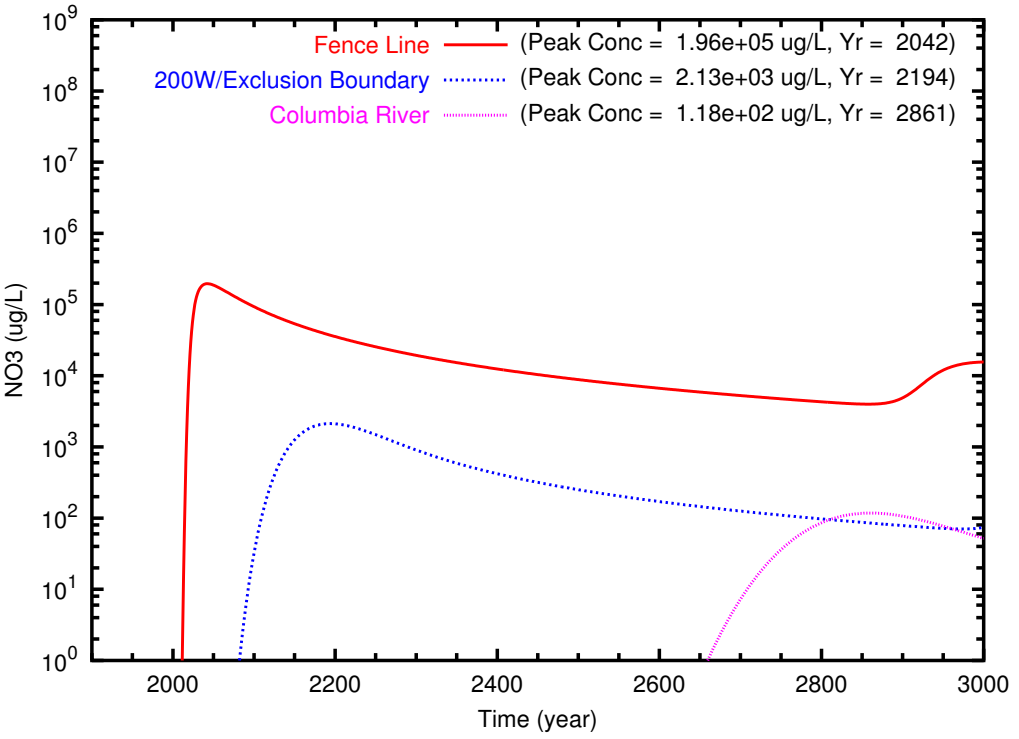

Figure B.10. T Case 2 **NO_3** breakthrough curves at fenceline and downgradient points along (a) east path and (b) north path

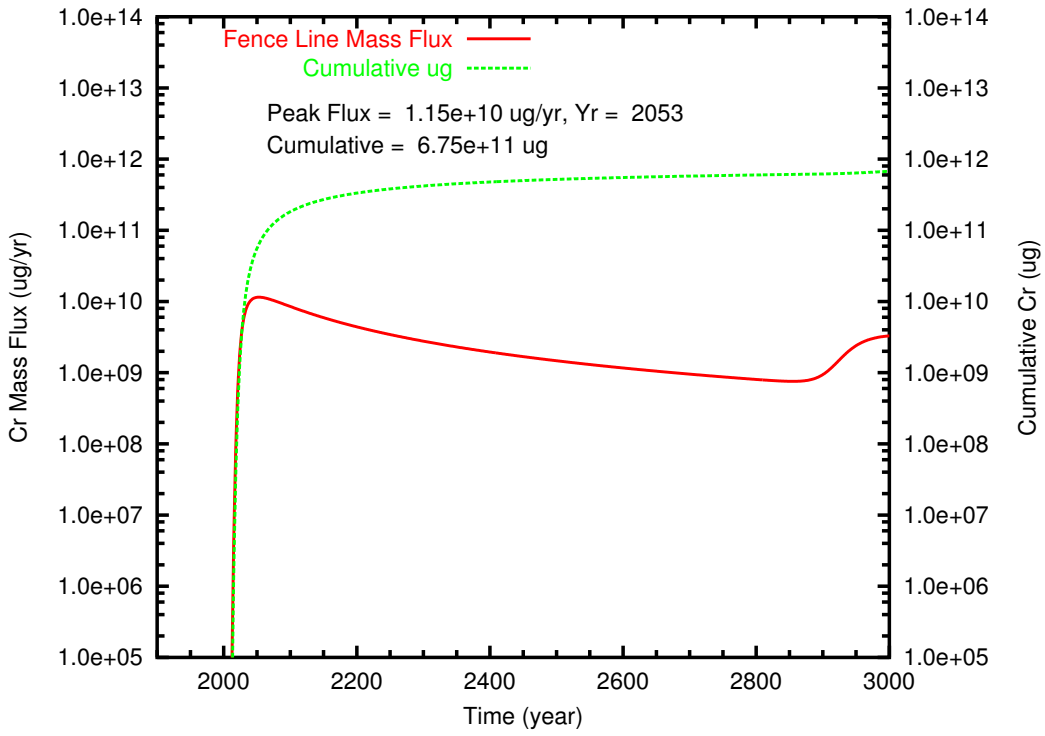

Figure B.11. T Case 2 **Cr** mass flux and cumulative mass at fenceline

(a)

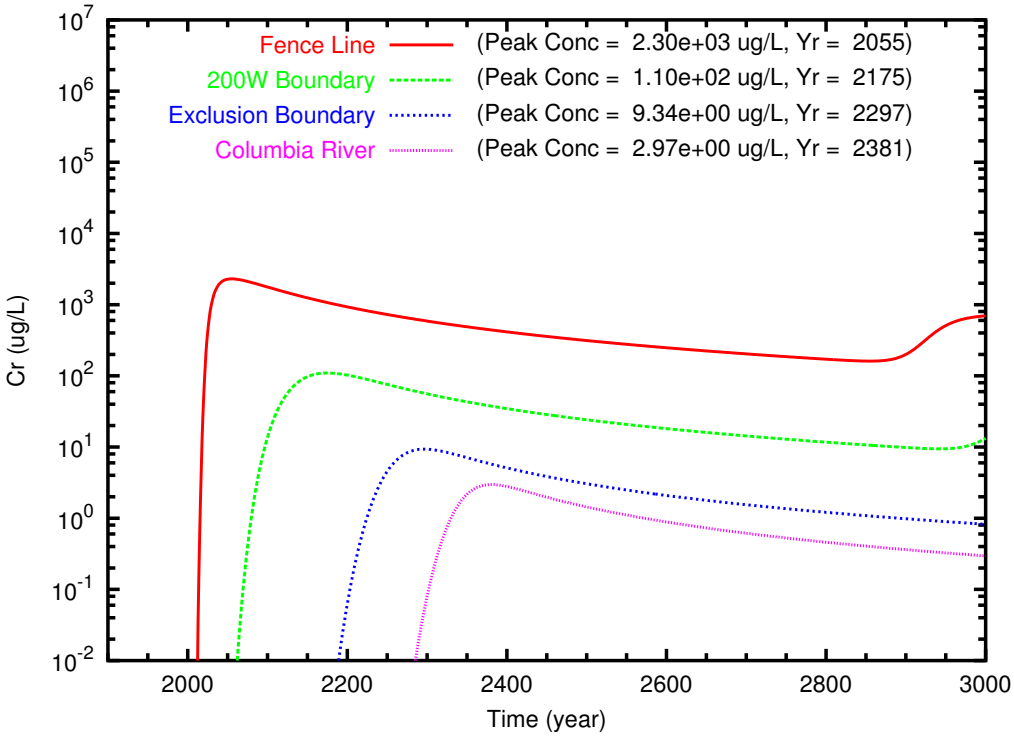

(b)

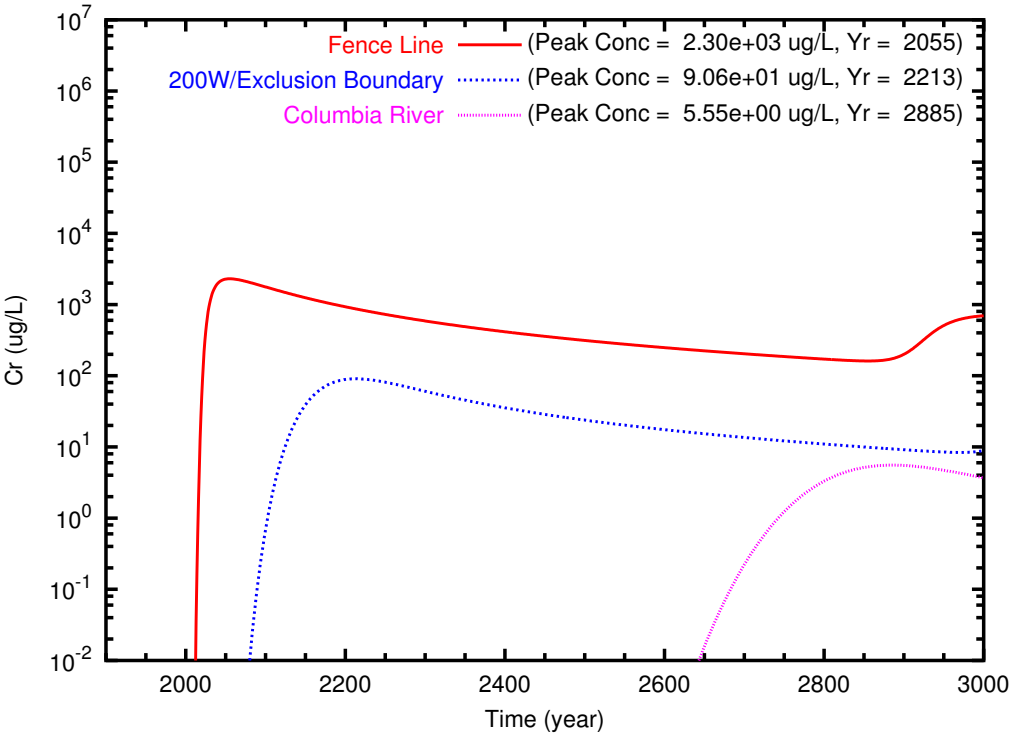

Figure B.12. T Case 2 **Cr** breakthrough curves at fenceline and downgradient points along (a) east path and (b) north path

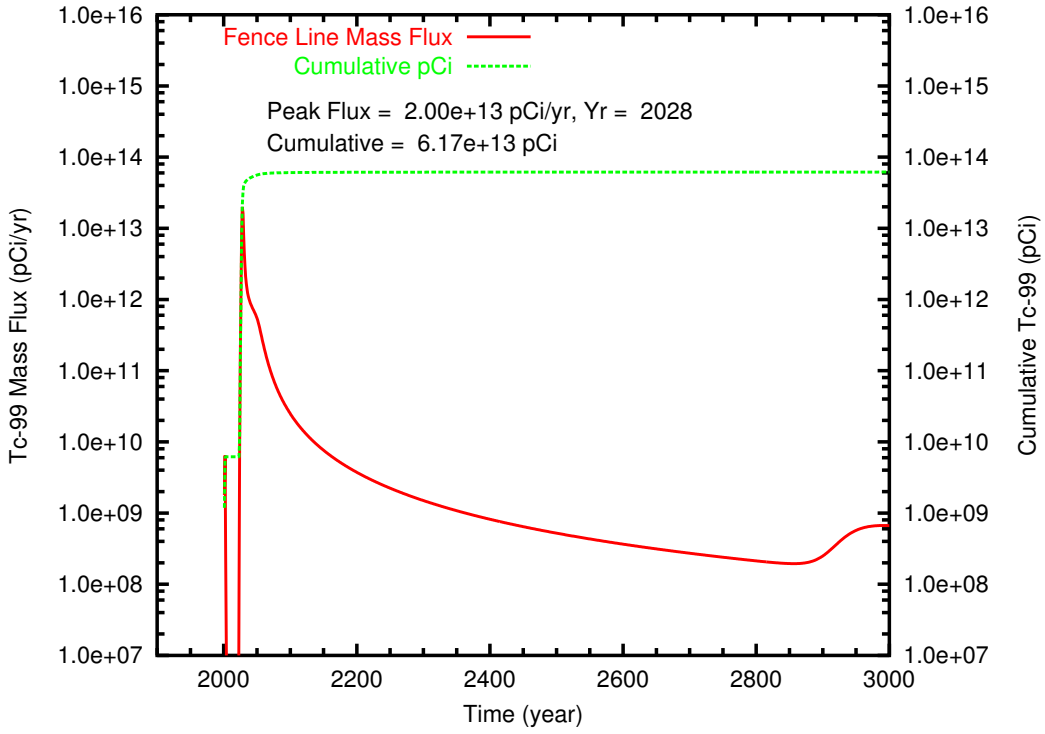

Figure B.13. T Case 3 **Tc-99** mass flux and cumulative mass at fenceline

(a)

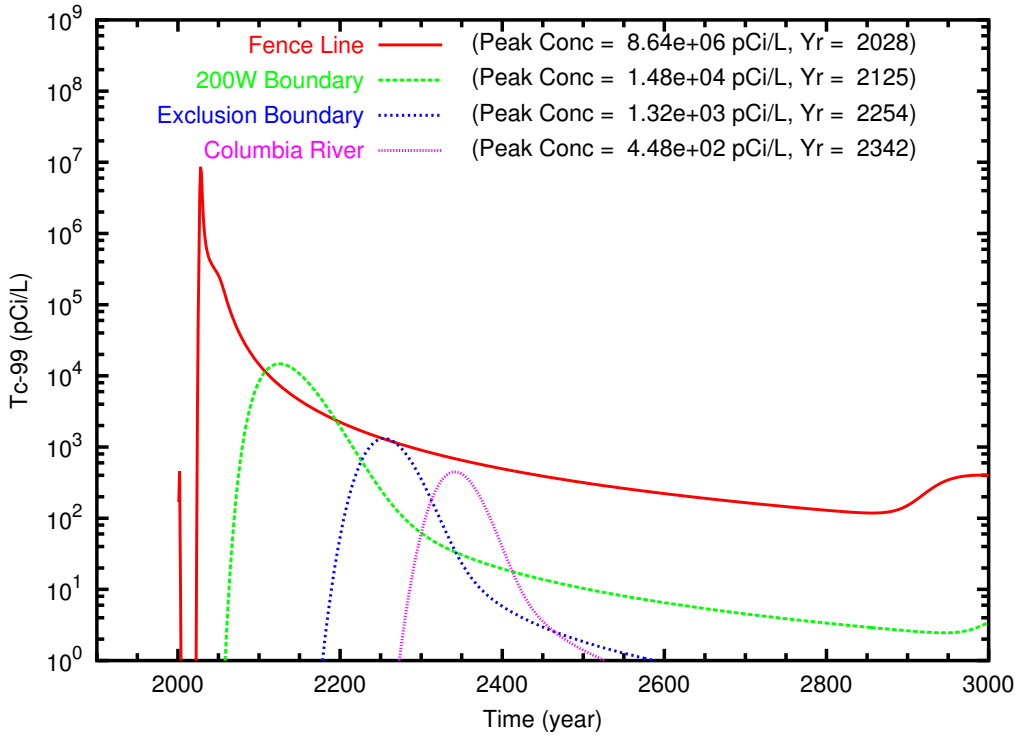

(b)

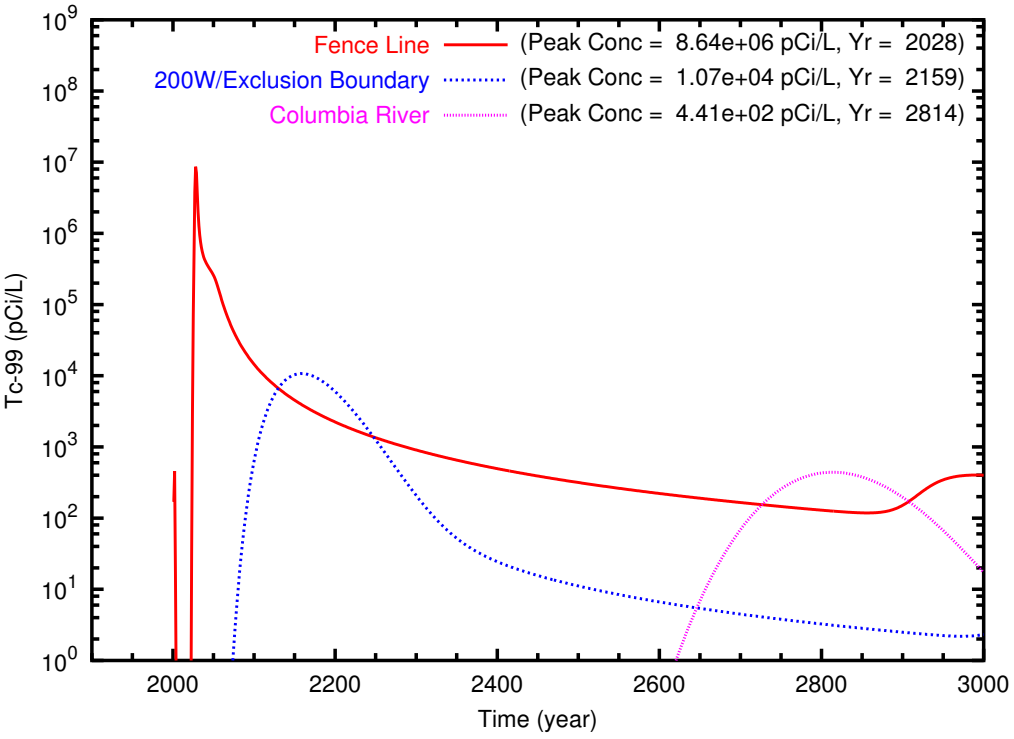

Figure B.14. T Case 3 **Tc-99** breakthrough curves at fenceline and downgradient points along (a) east path and (b) north path

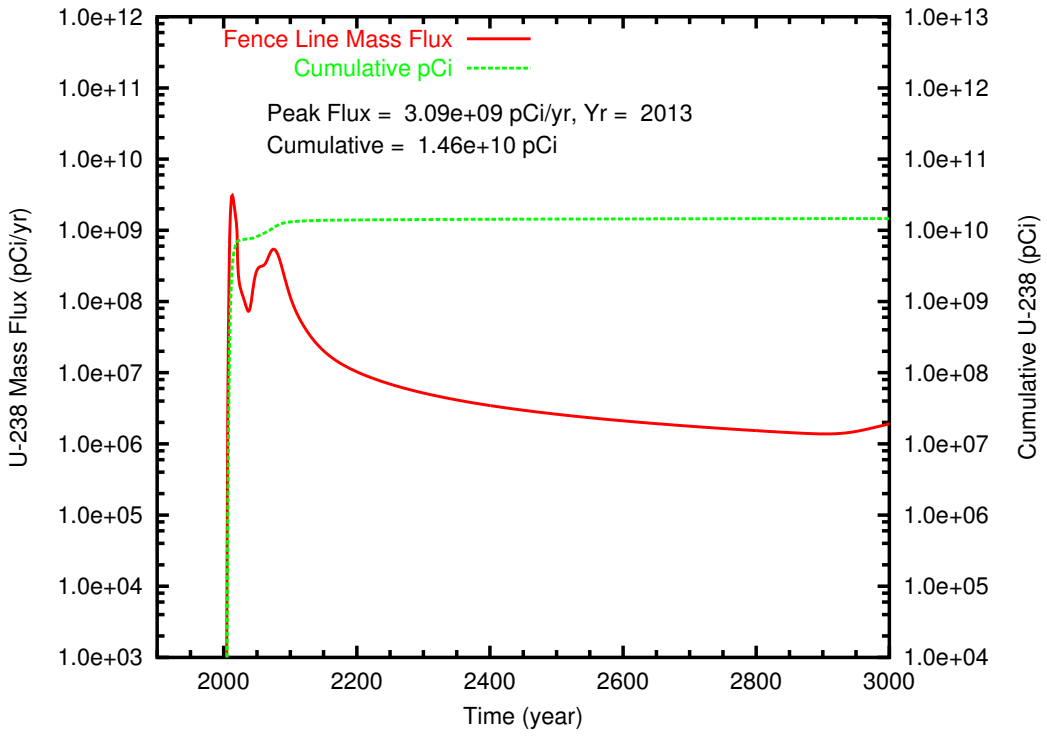

Figure B.15. T Case 3 **U-238** (K_d = 0.60) mass flux and cumulative mass at fenceline

(a)

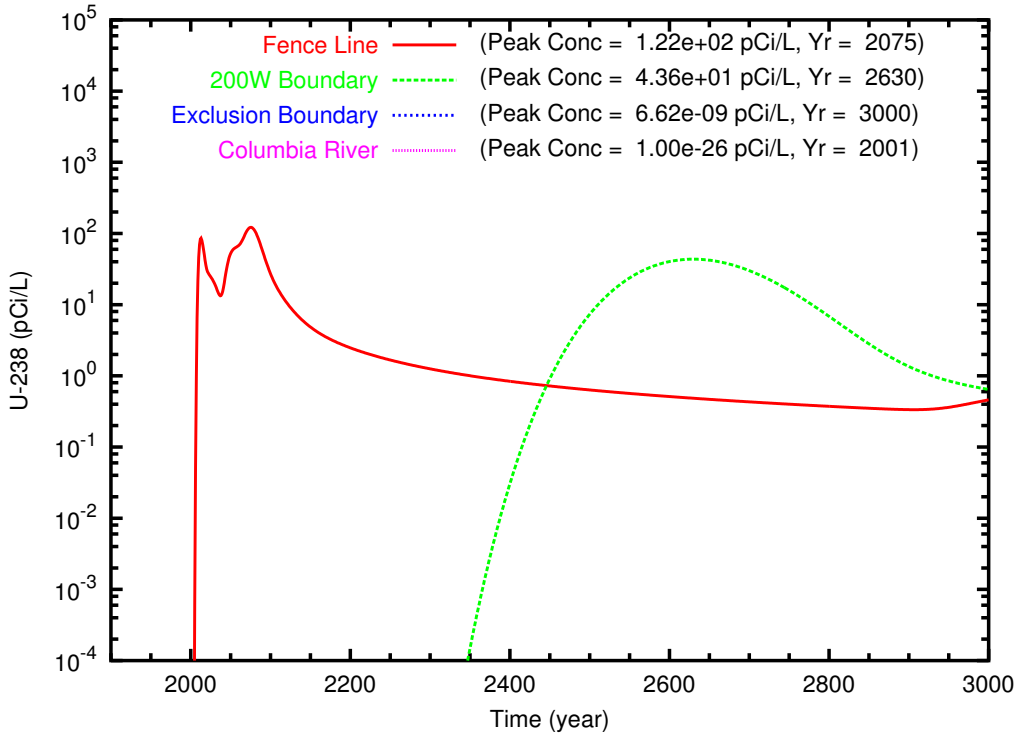

(b)

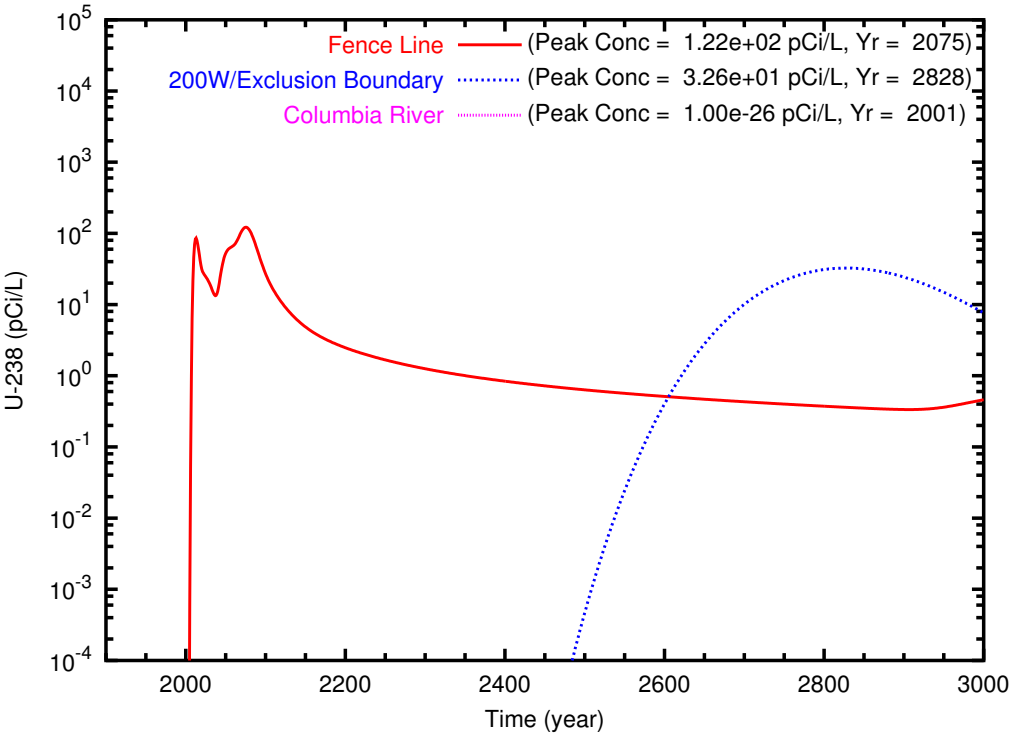

Figure B.16. T Case 3 **U-238** (K_d = 0.60) breakthrough curves at fenceline and downgradient points along (a) east path and (b) north path

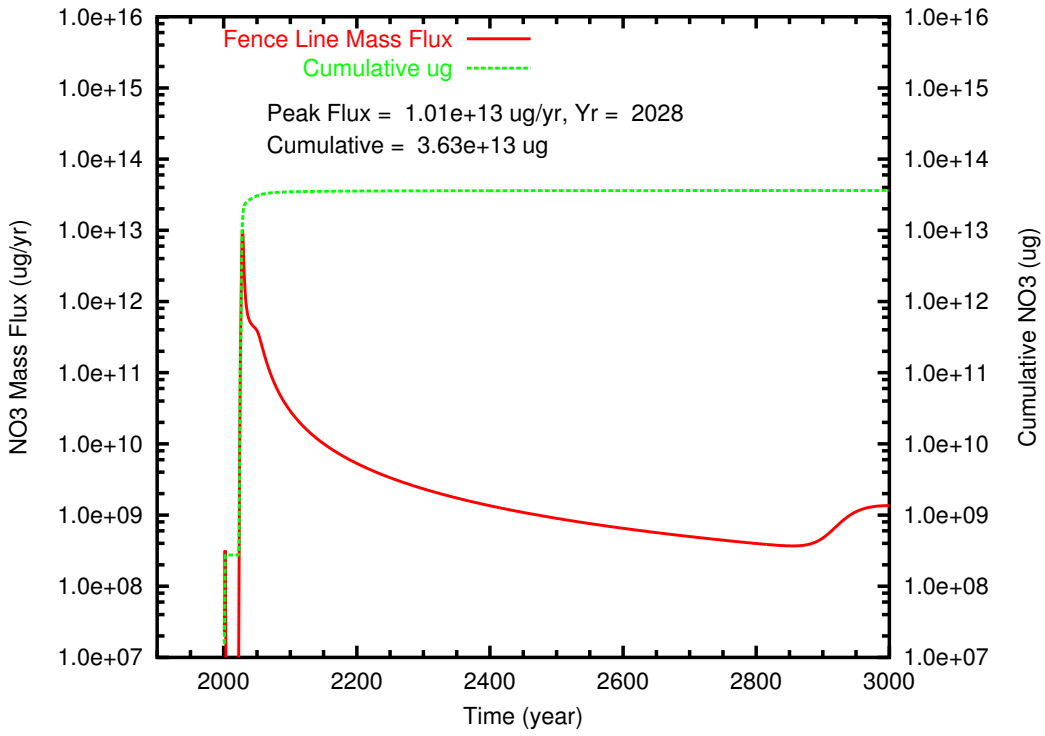

Figure B.17. T Case 3 NO_3 mass flux and cumulative mass at fenceline

(a)

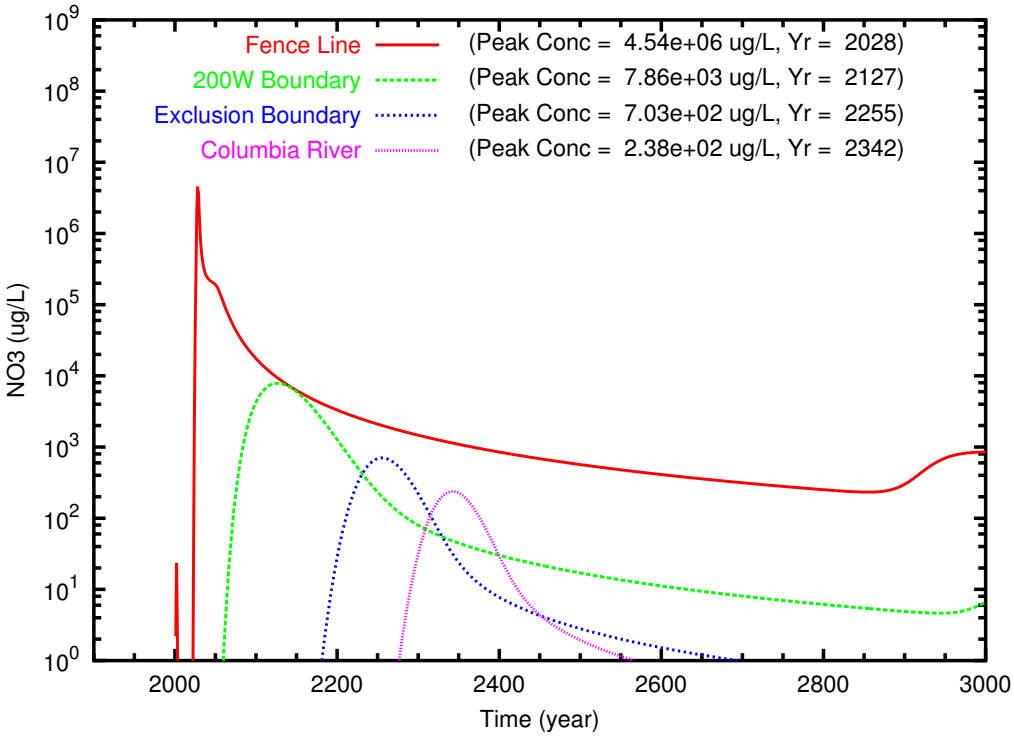

(b)

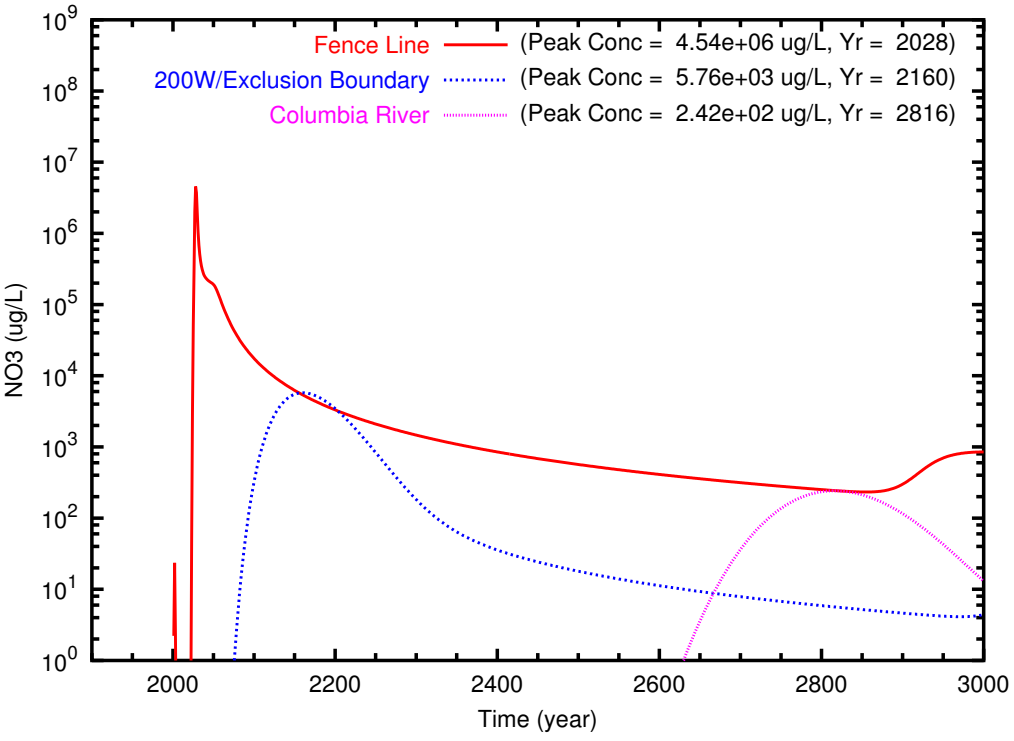

Figure B.18. T Case 3 $\mathbf{NO_3}$ breakthrough curves at fenceline and downgradient points along (a) east path and (b) north path

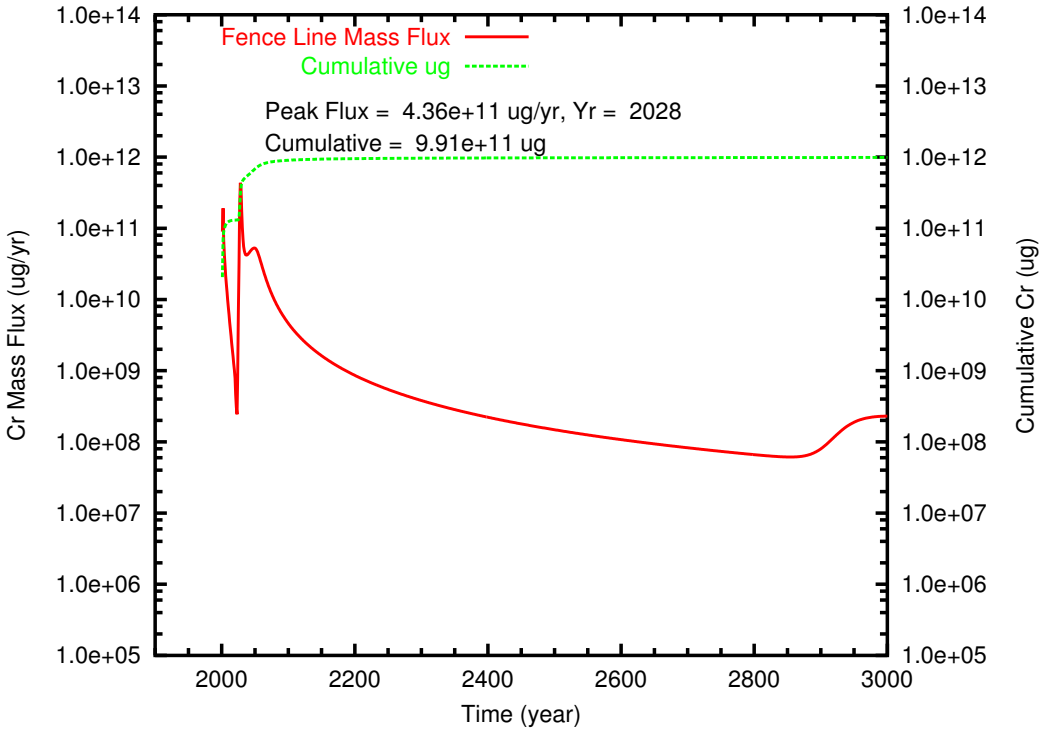

Figure B.19. T Case 3 **Cr** mass flux and cumulative mass at fenceline

(a)

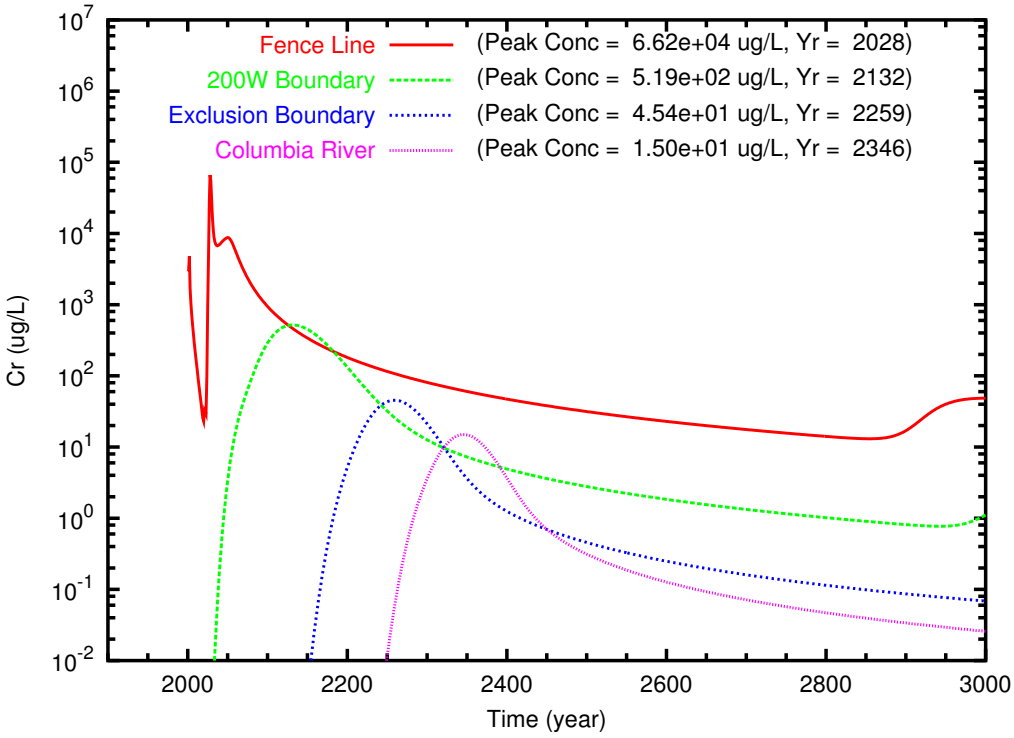

(b)

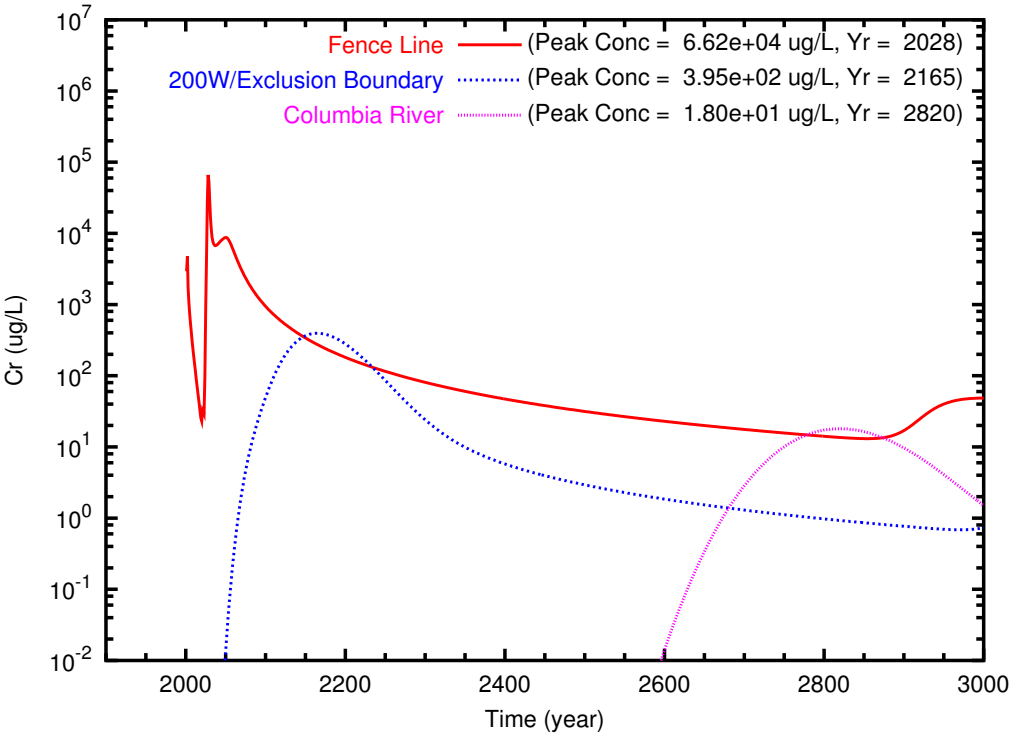

Figure B.20. T Case 3 **Cr** breakthrough curves at fenceline and downgradient points along (a) east path and (b) north path

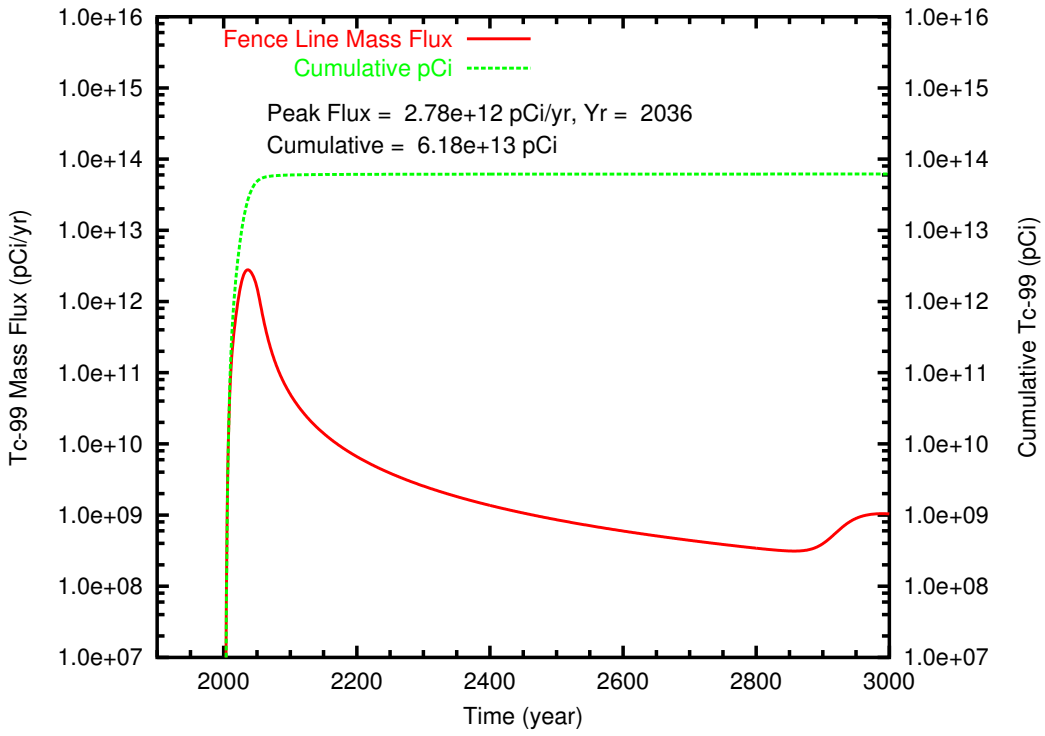

Figure B.21. T Case 4 **Tc-99** mass flux and cumulative mass at fenceline

(a)

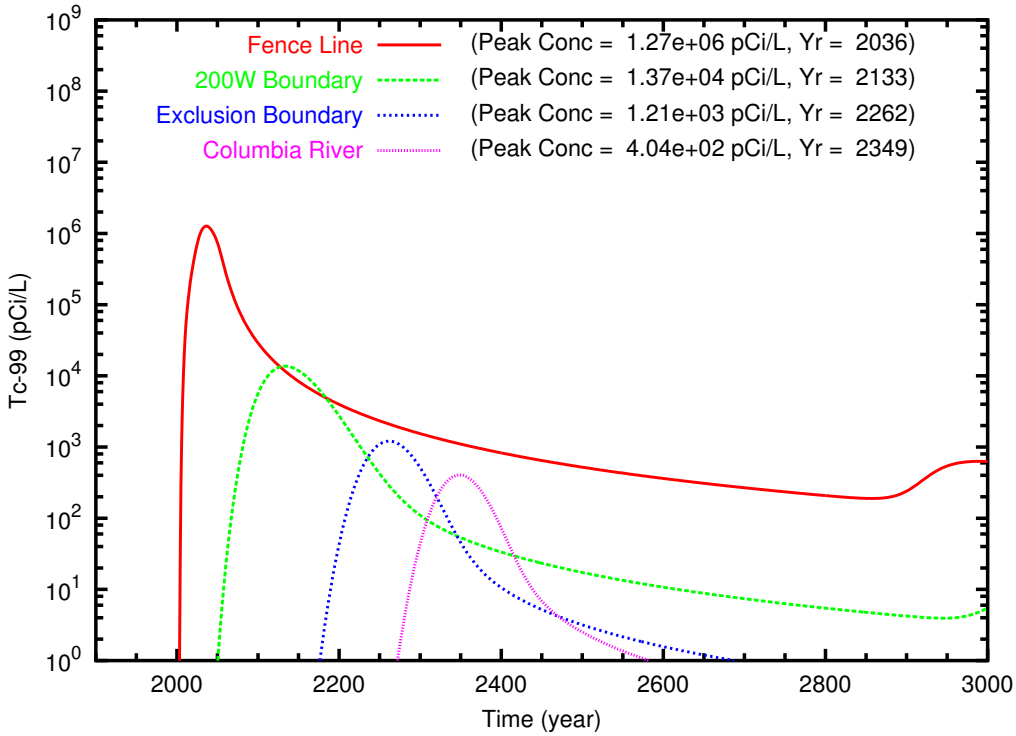

(b)

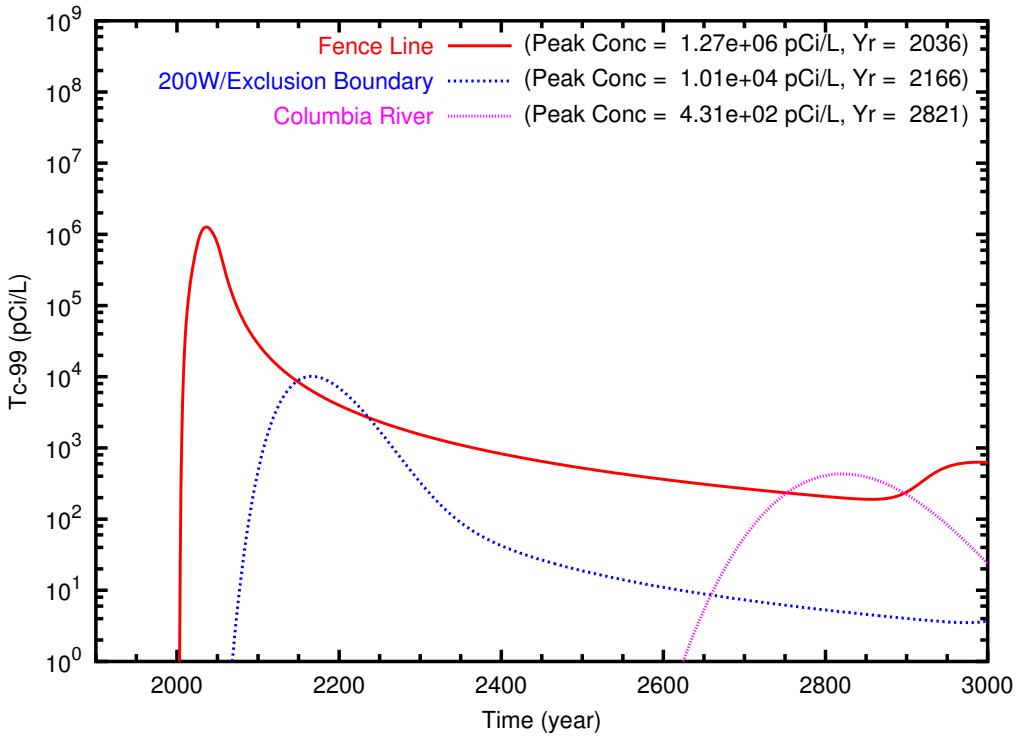

Figure B.22. T Case 4 **Tc-99** breakthrough curves at fenceline and downgradient points along (a) east path and (b) north path

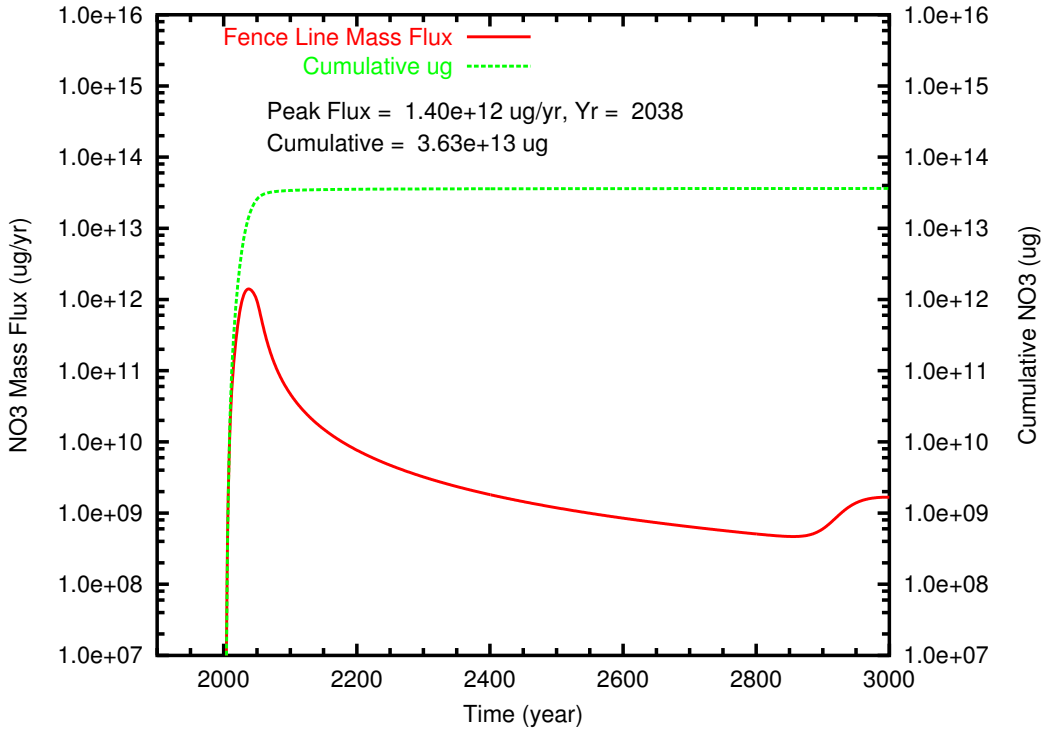

Figure B.23. T Case 4 NO_3 mass flux and cumulative mass at fenceline

(a)

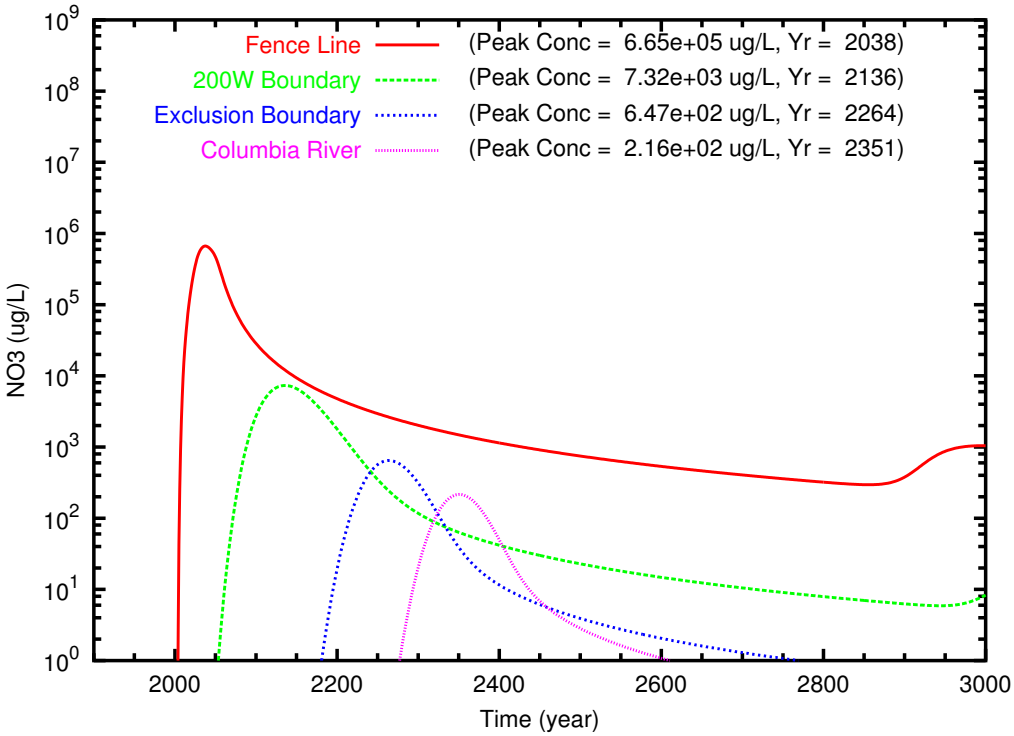

(b)

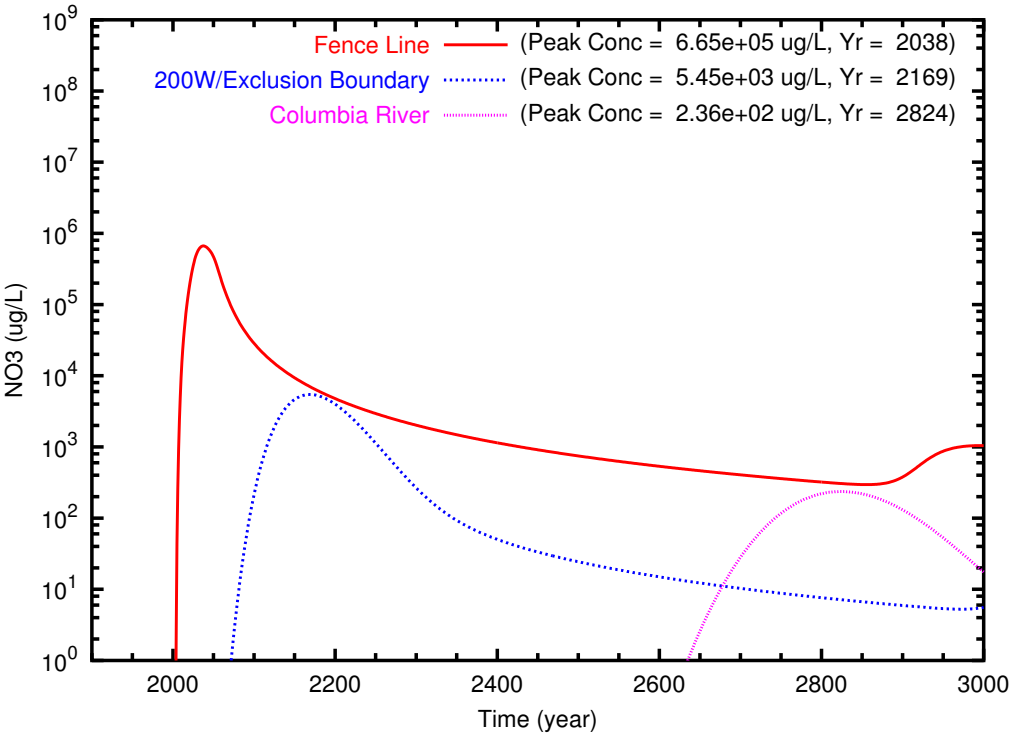

Figure B.24. T Case 4 **NO_3** breakthrough curves at fenceline and downgradient points along (a) east path and (b) north path

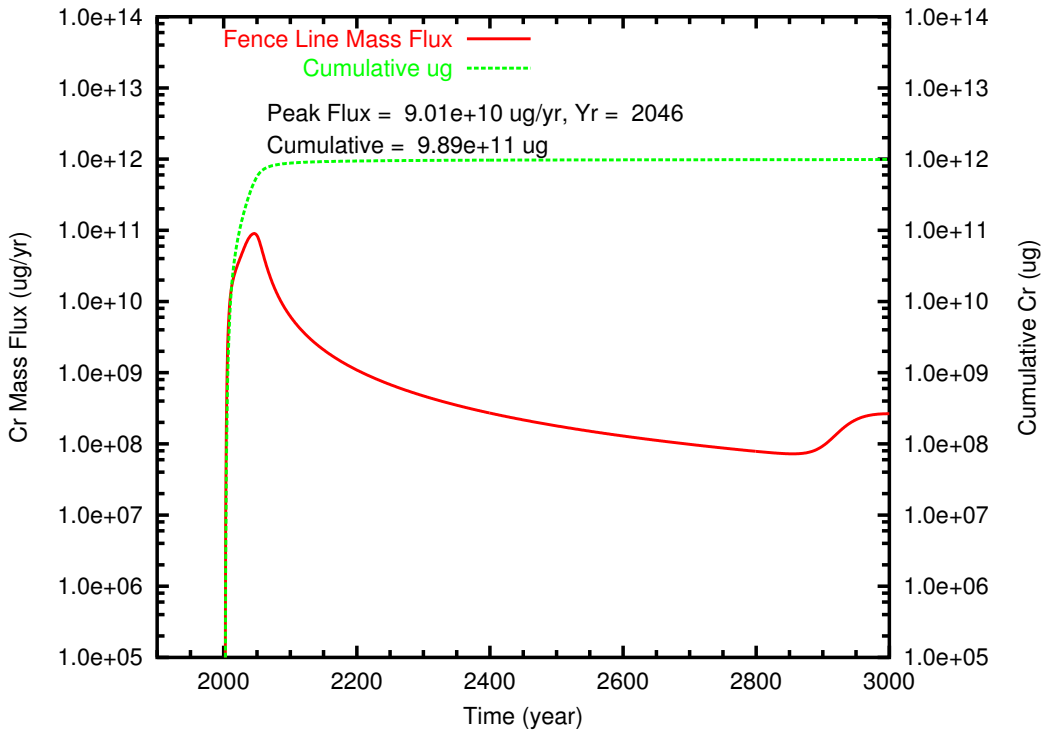

Figure B.25. T Case 4 **Cr** mass flux and cumulative mass at fenceline

(a)

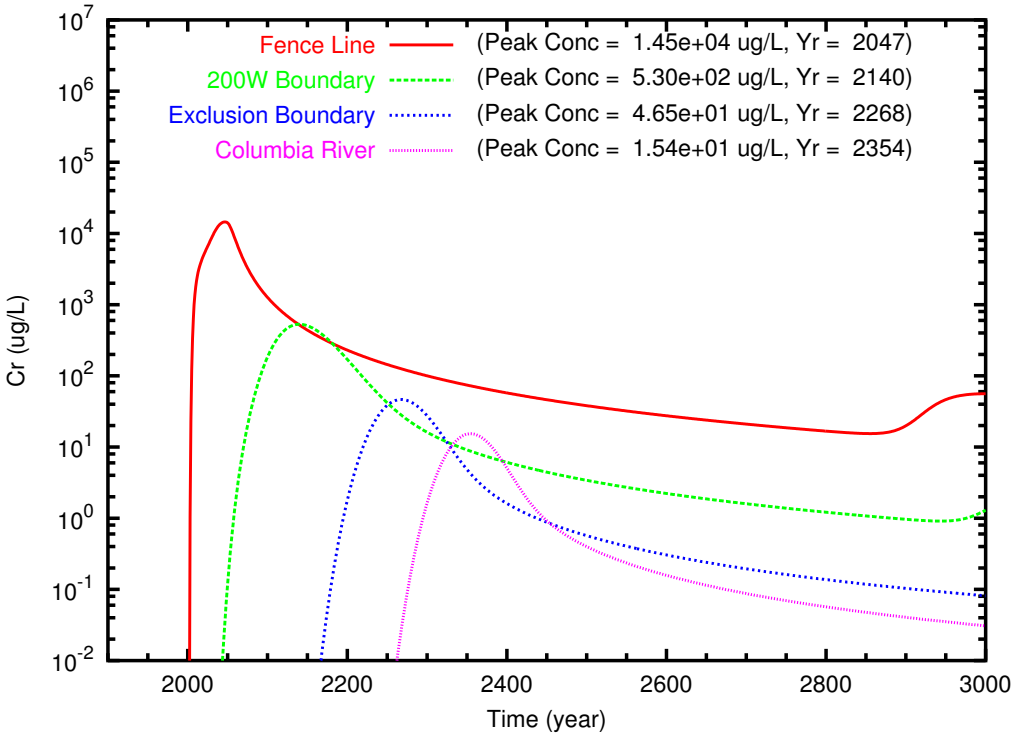

(b)

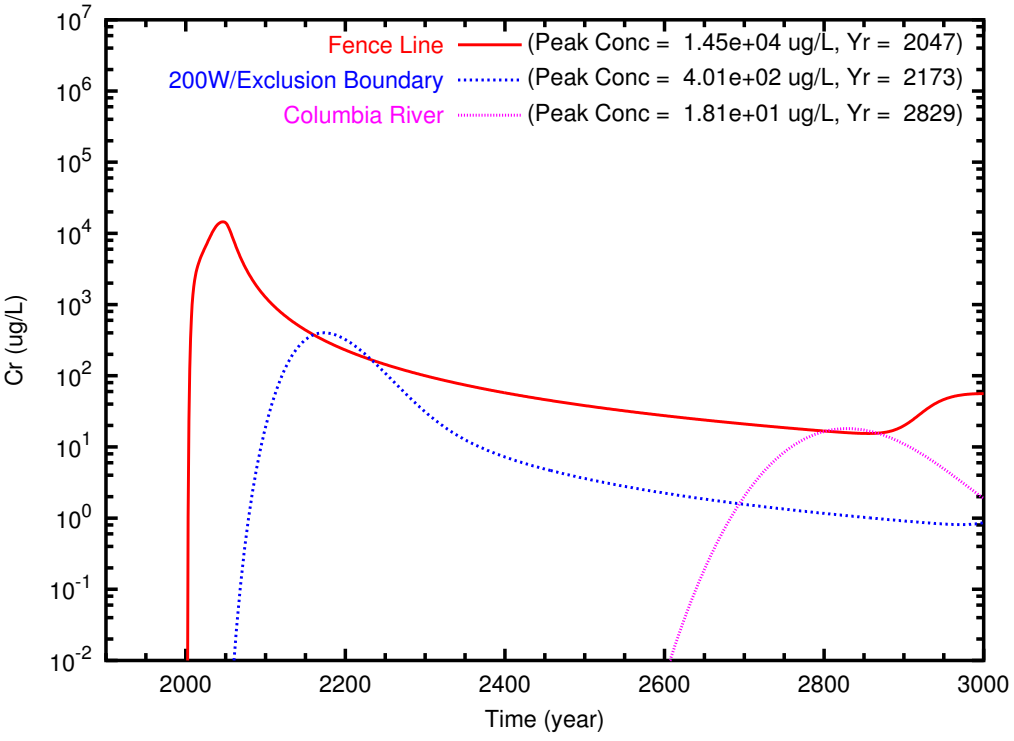

Figure B.26. T Case 4 **Cr** breakthrough curves at fenceline and downgradient points along (a) east path and (b) north path

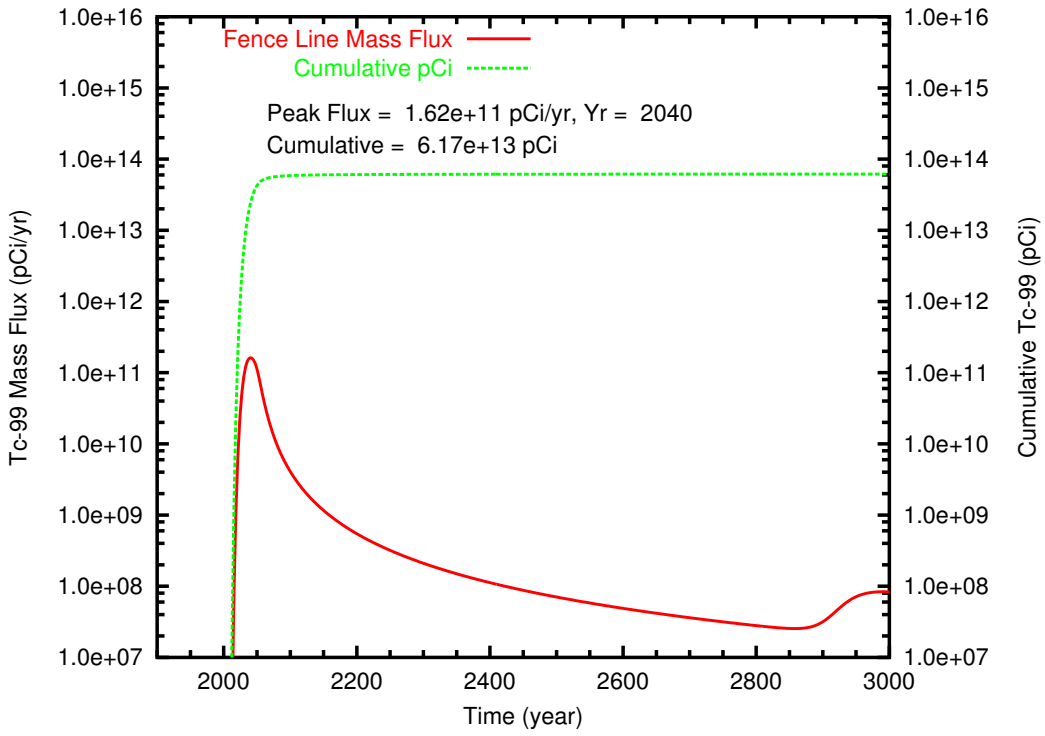

Figure B.27. T Case 5 **Tc-99** mass flux and cumulative mass at fenceline

(a)

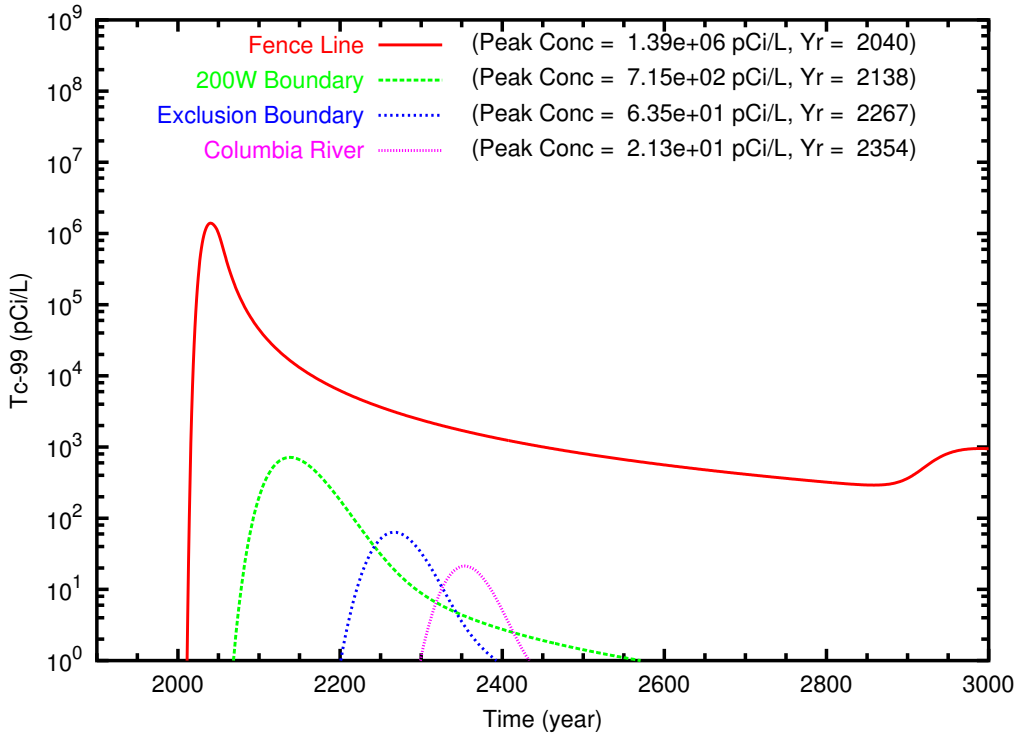

(b)

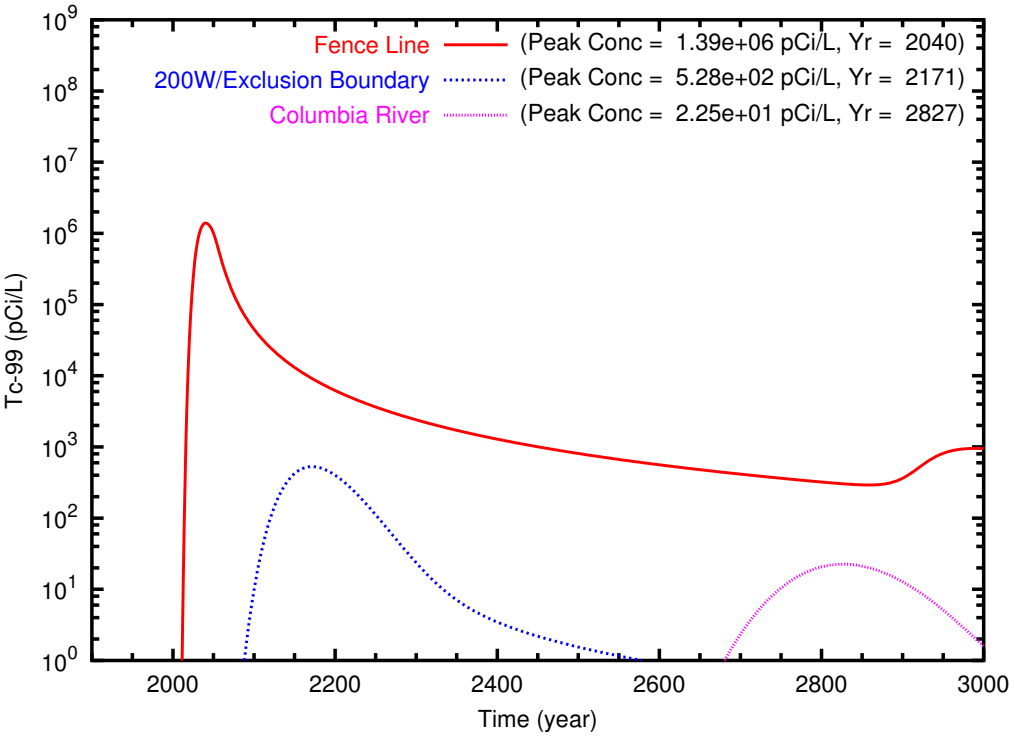

Figure B.28. T Case 5 **Tc-99** breakthrough curves at fenceline and downgradient points along (a) east path and (b) north path

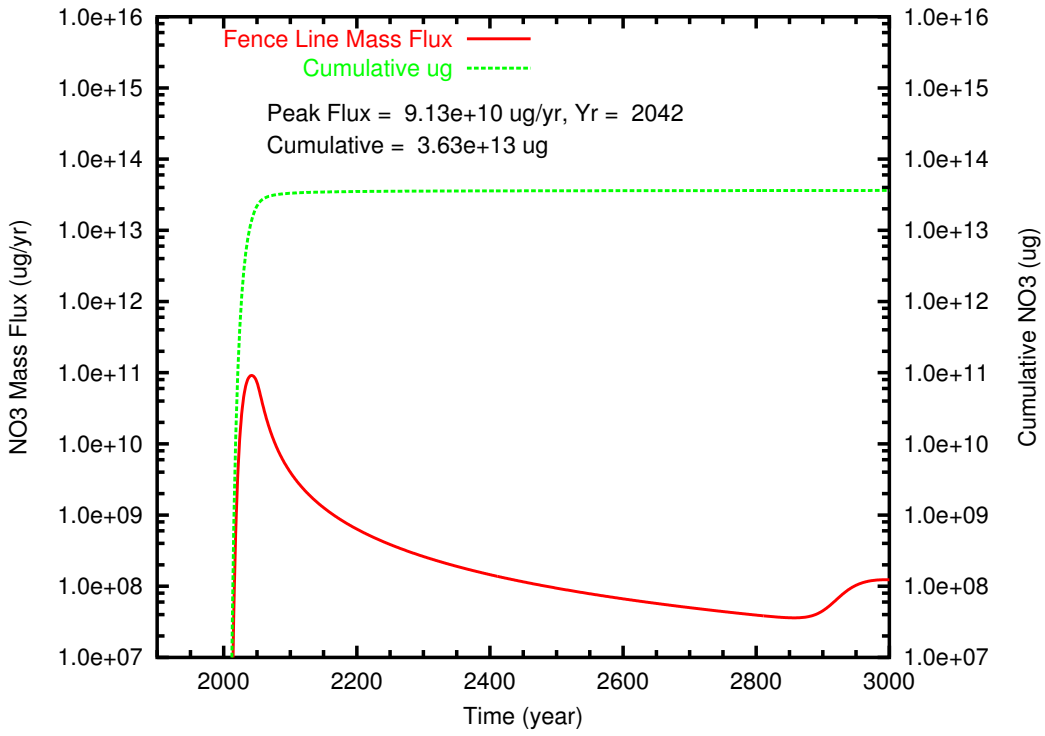

Figure B.29. T Case 5 NO_3 mass flux and cumulative mass at fenceline

(a)

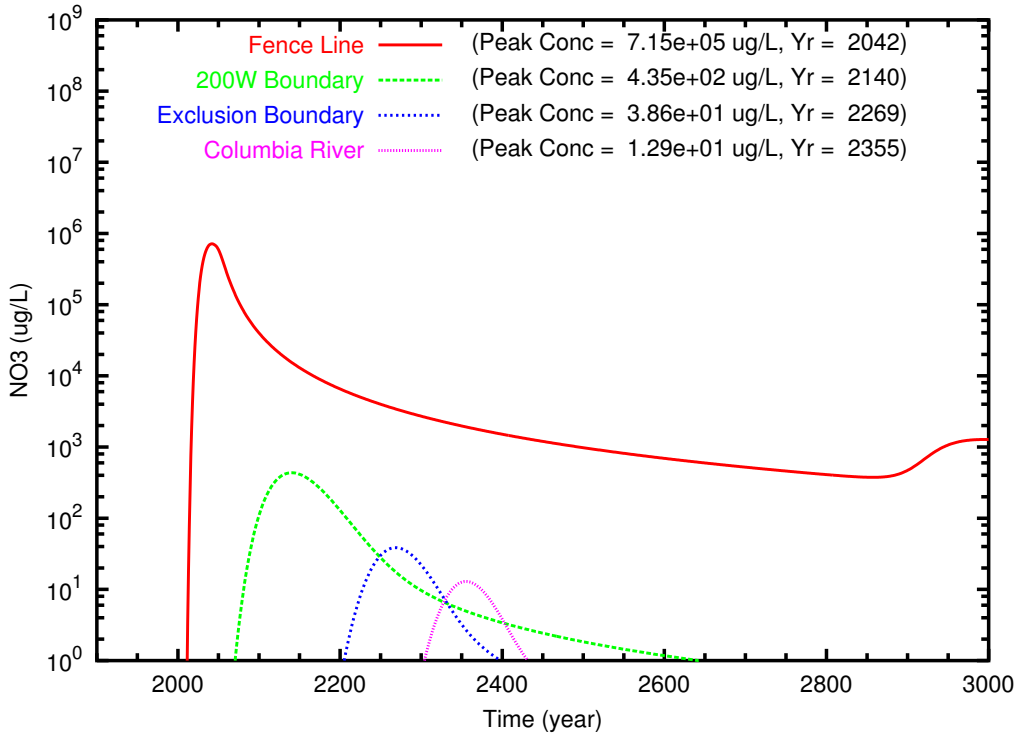

(b)

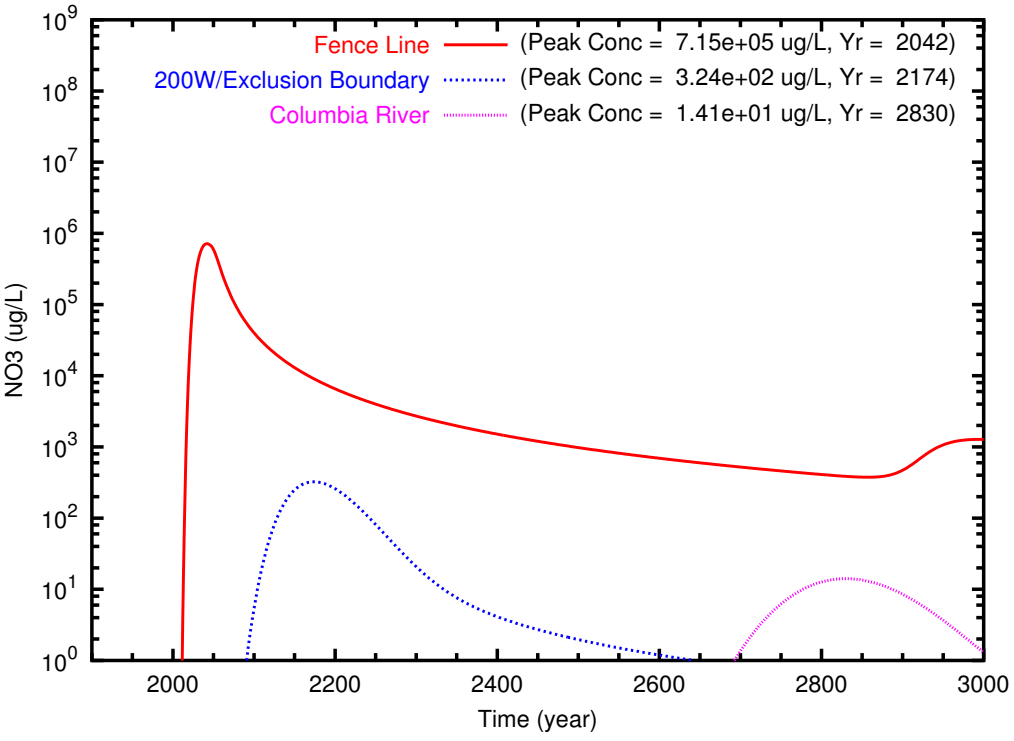

Figure B.30. T Case 5 **NO_3** breakthrough curves at fenceline and downgradient points along (a) east path and (b) north path

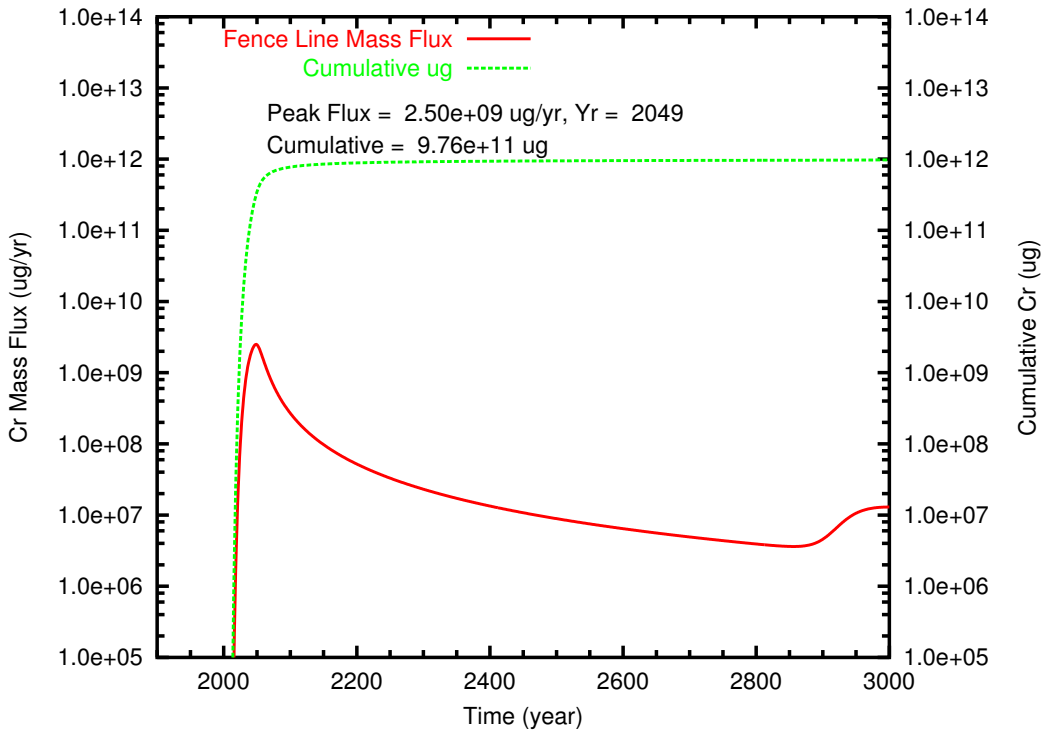

Figure B.31. T Case 5 **Cr** mass flux and cumulative mass at fenceline

(a)

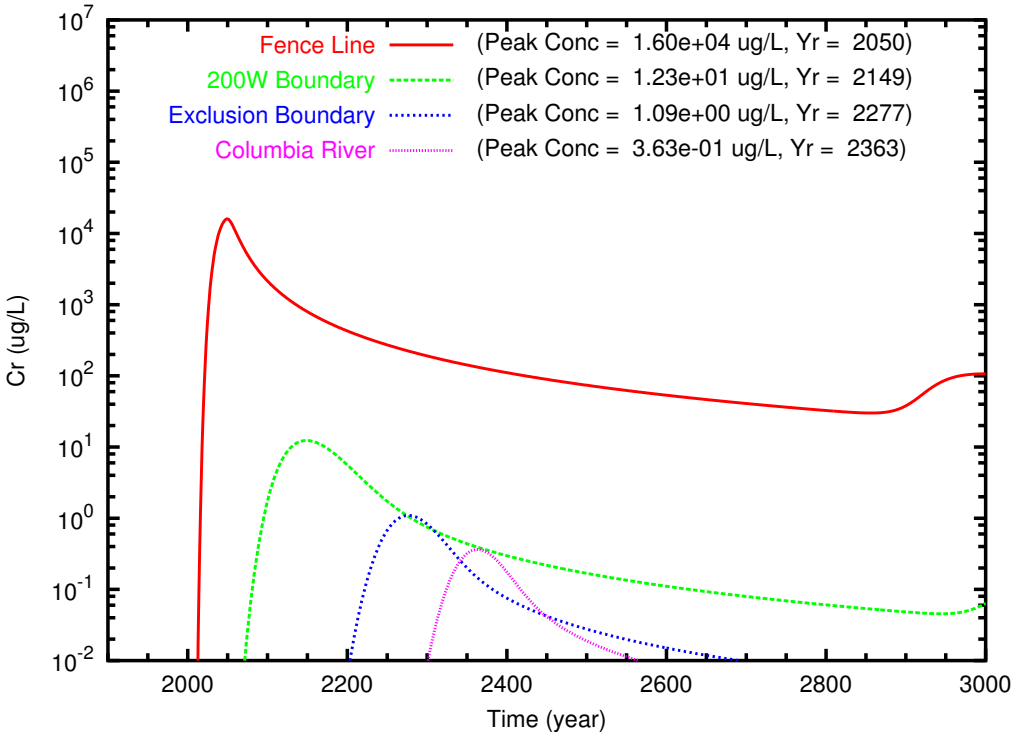

(b)

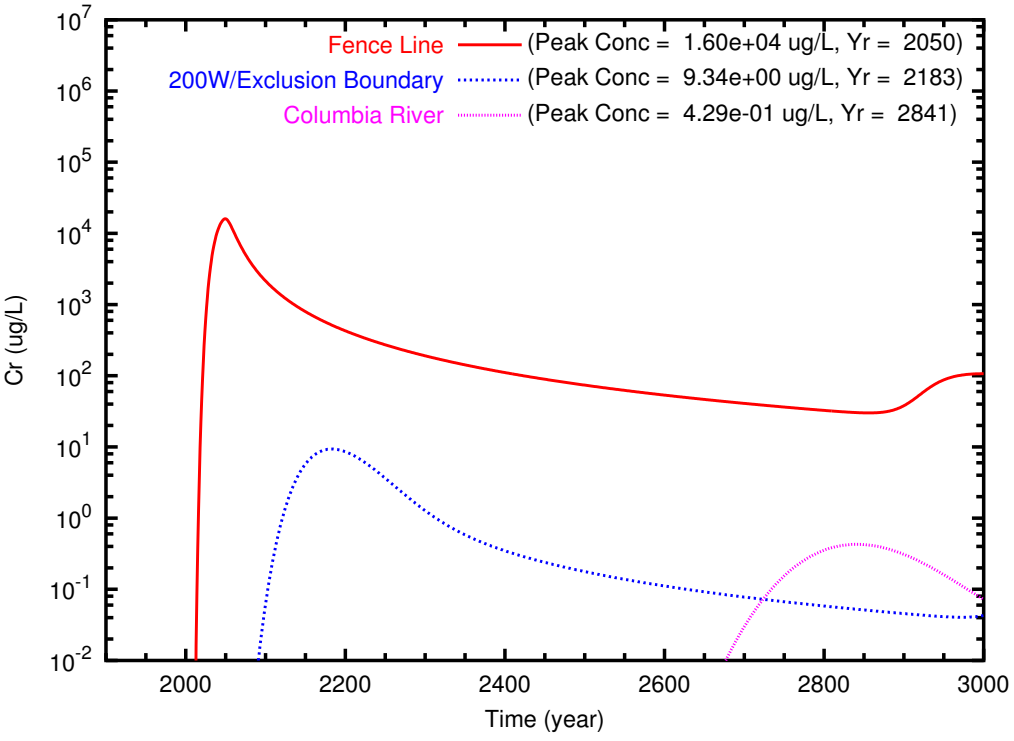

Figure B.32. T Case 5 **Cr** breakthrough curves at fenceline and downgradient points along (a) east path and (b) north path

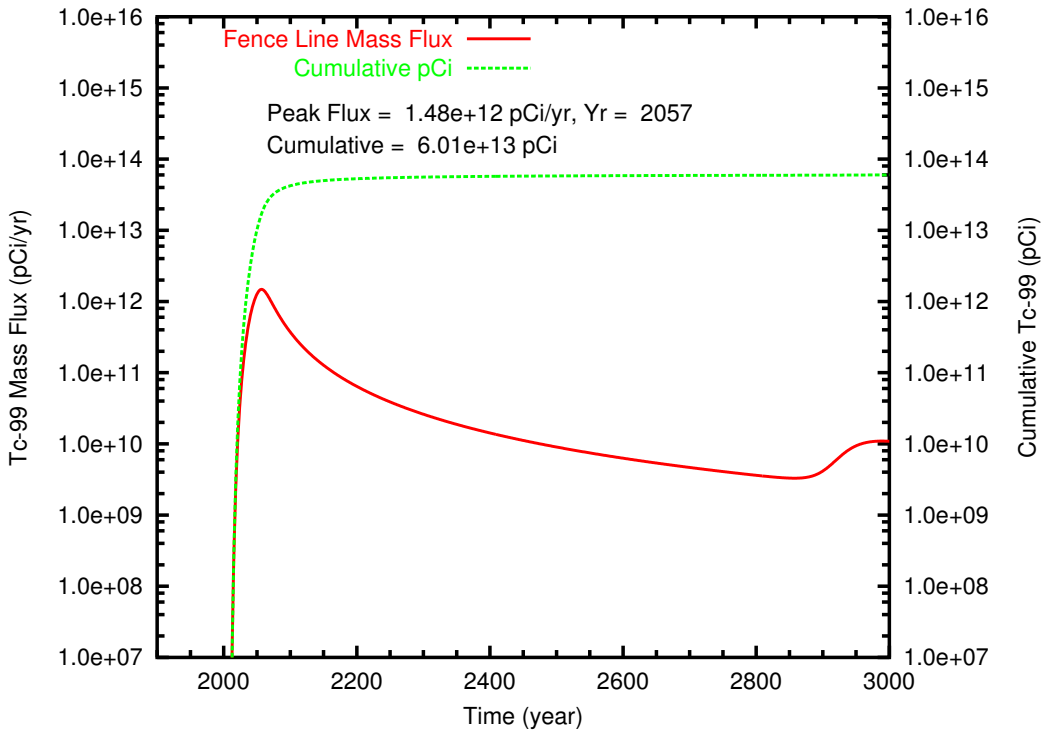

Figure B.33. T Case 6 **Tc-99** mass flux and cumulative mass at fenceline

(a)

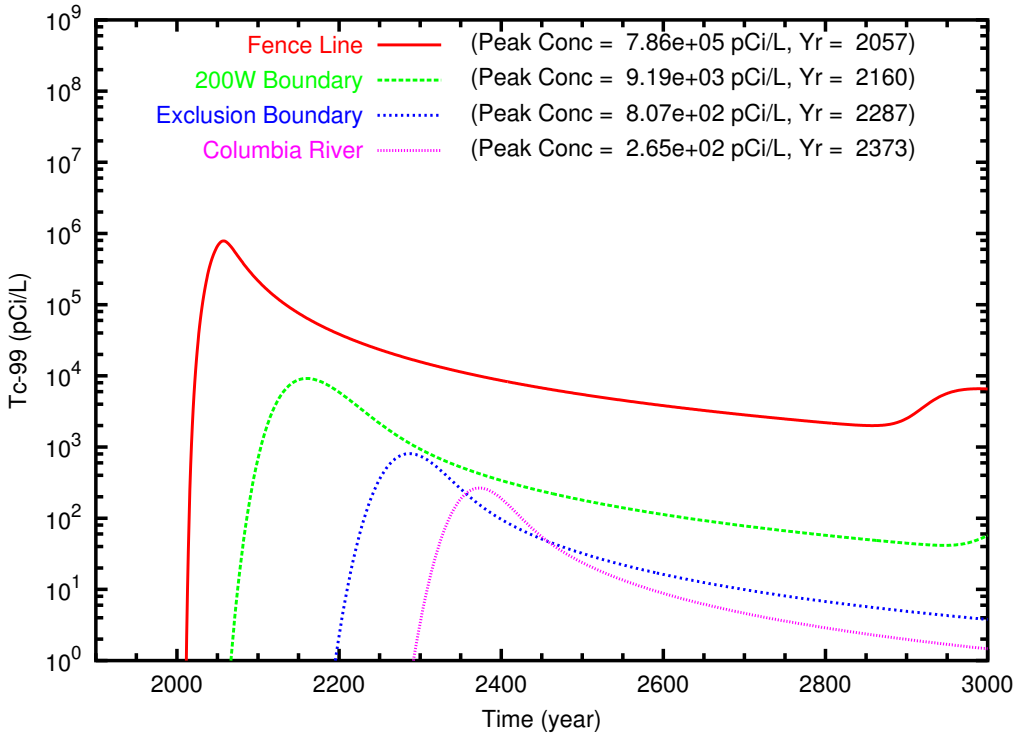

(b)

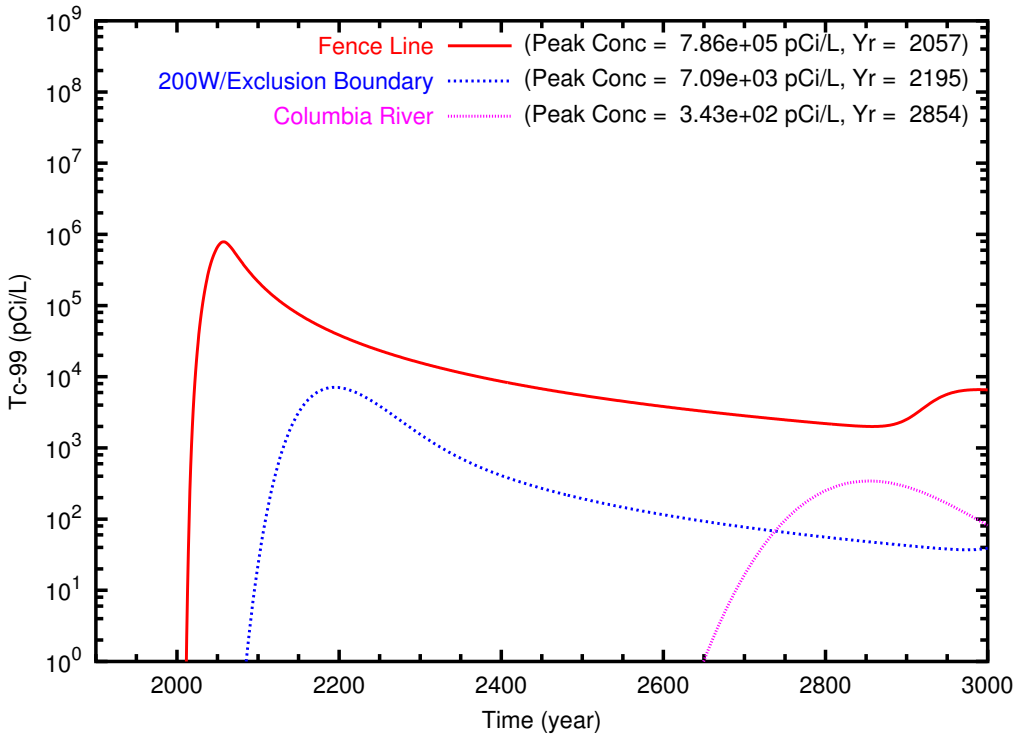

Figure B.34. T Case 6 **Tc-99** breakthrough curves at fenceline and downgradient points along (a) east path and (b) north path

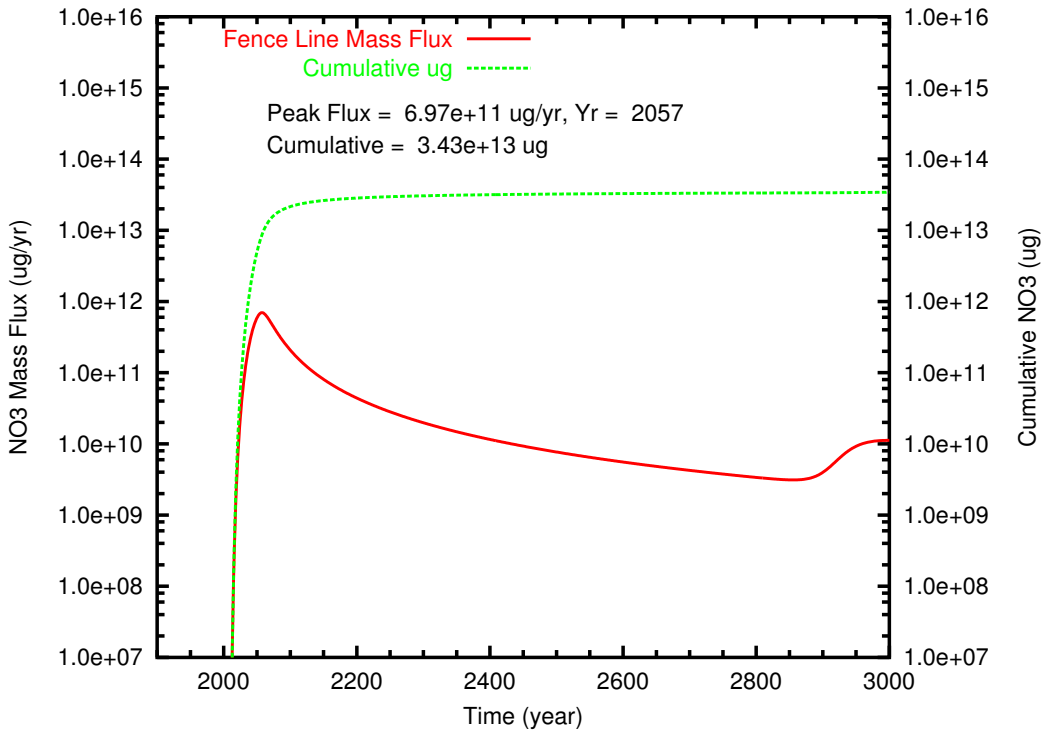

Figure B.35. T Case 6 $\mathbf{NO_3}$ mass flux and cumulative mass at fenceline

(a)

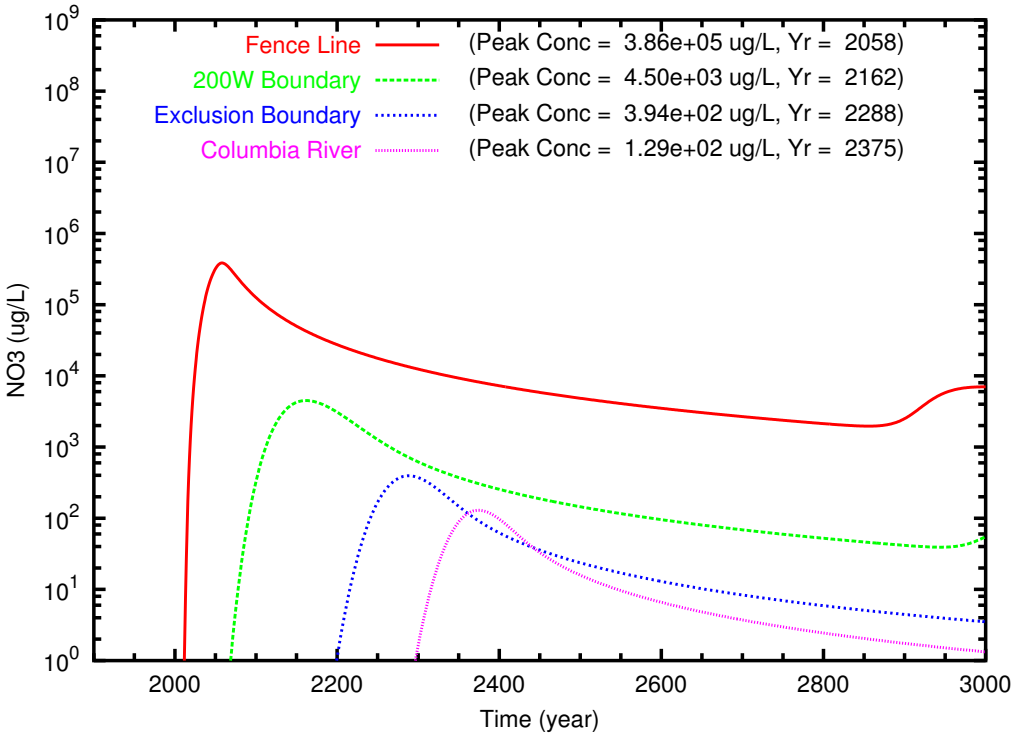

(b)

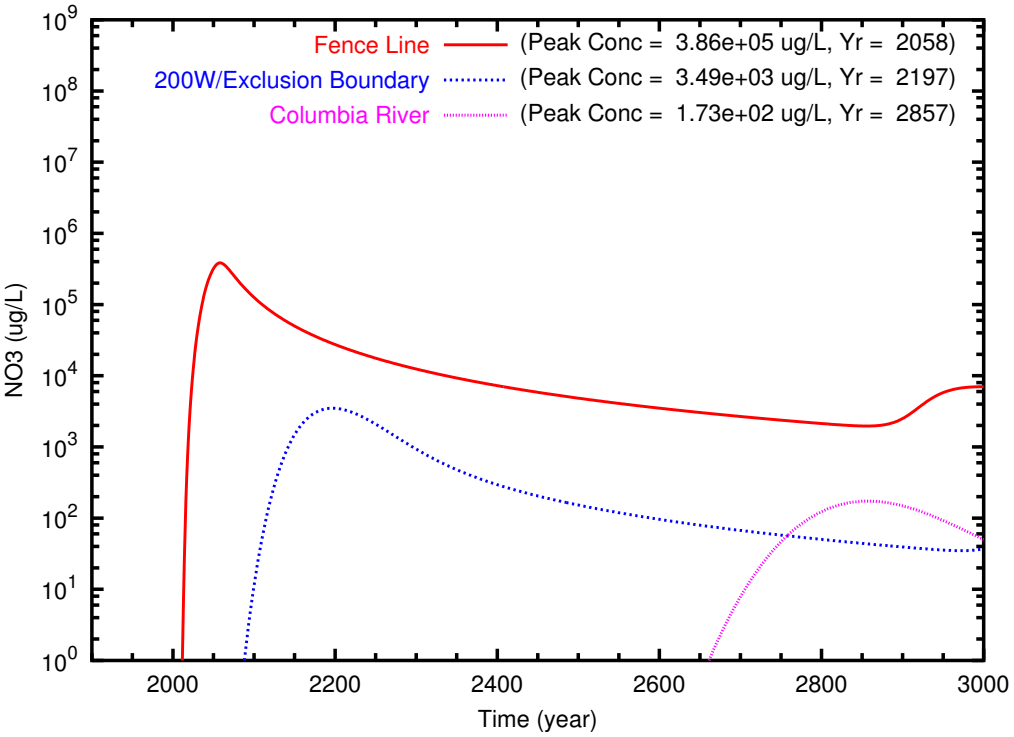

Figure B.36. T Case 6 $\mathbf{NO_3}$ breakthrough curves at fenceline and downgradient points along (a) east path and (b) north path

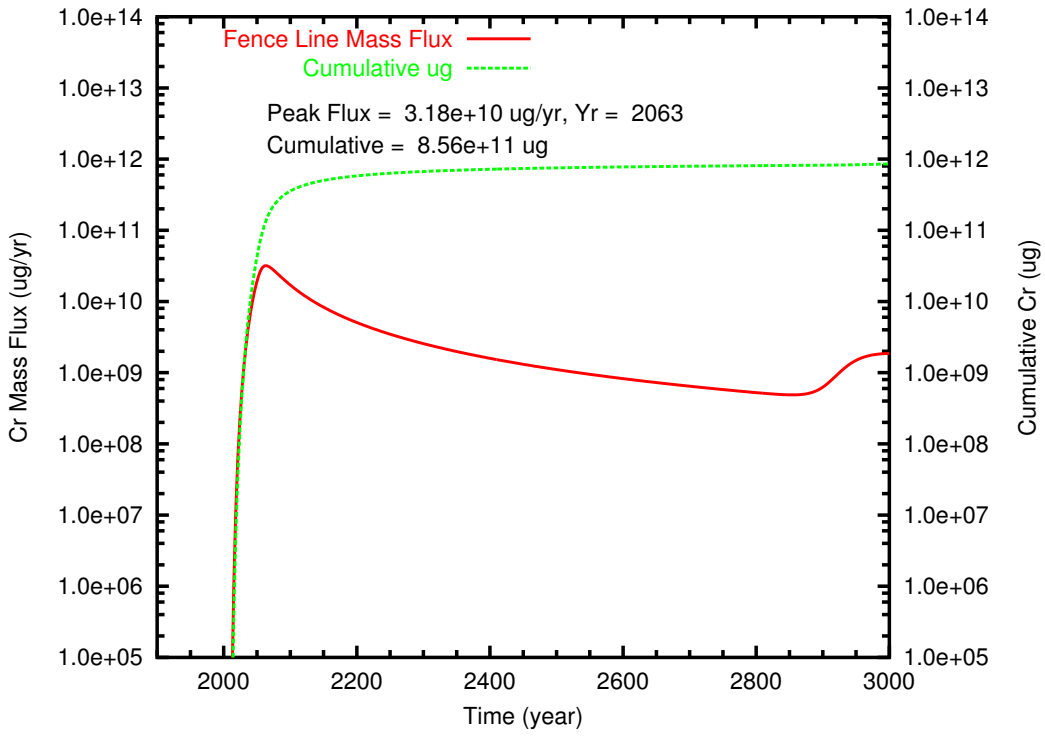

Figure B.37. T Case 6 **Cr** mass flux and cumulative mass at fenceline

(a)

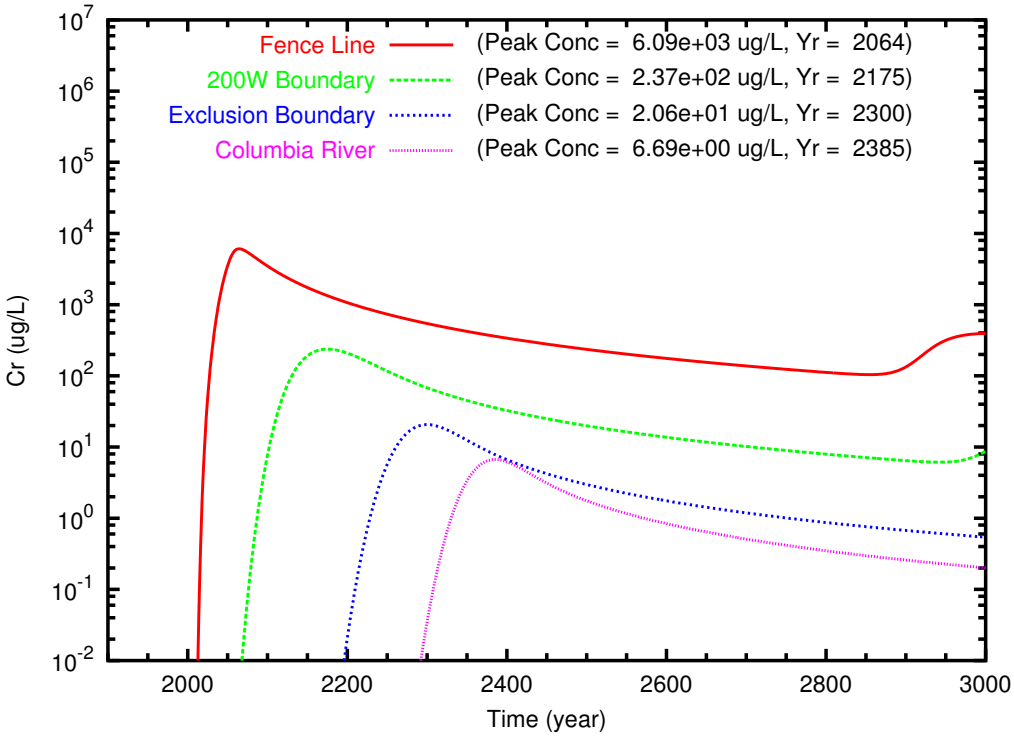

(b)

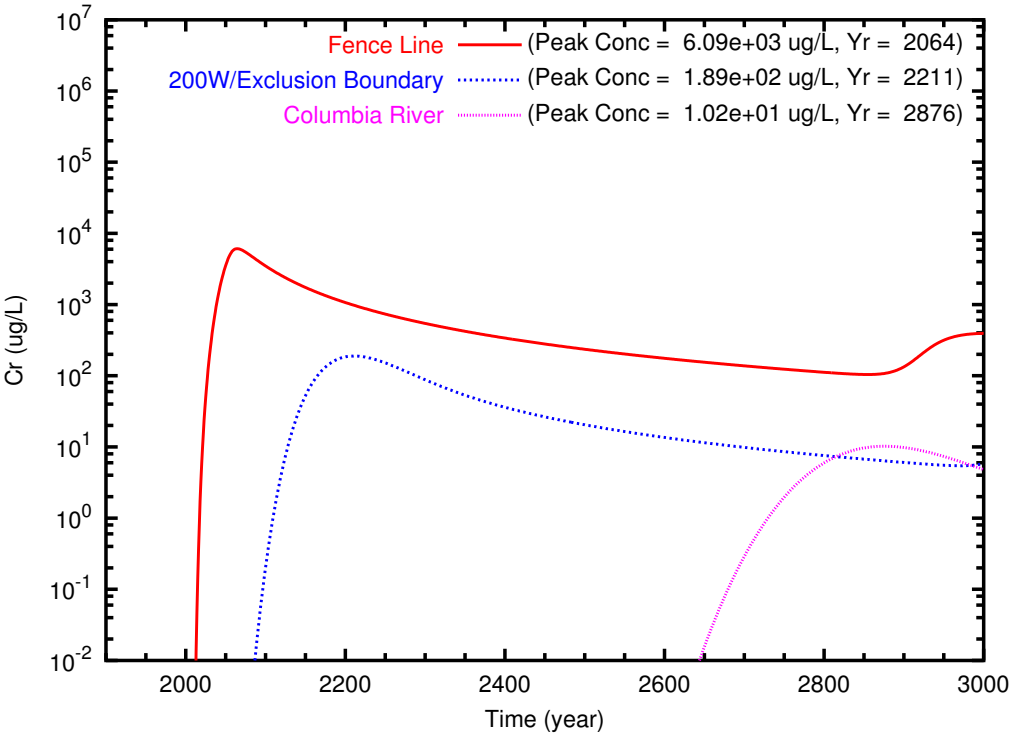

Figure B.38. T Case 6 **Cr** breakthrough curves at fenceline and downgradient points along (a) east path and (b) north path

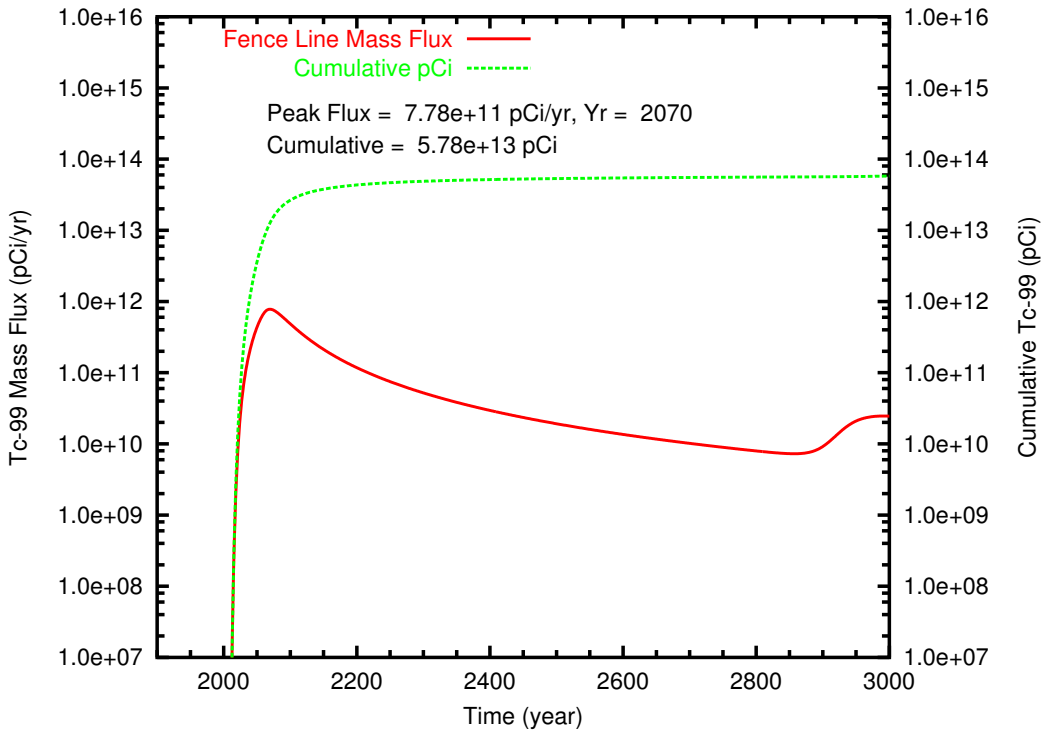

Figure B.39. T Case 7 **Tc-99** mass flux and cumulative mass at fenceline

(a)

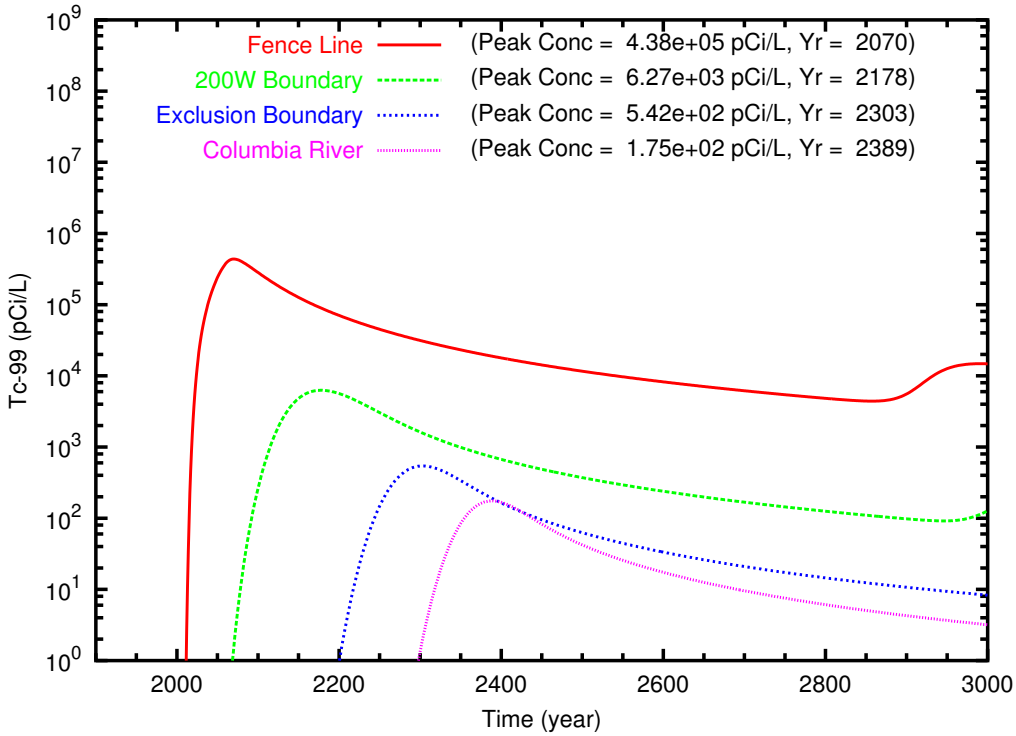

(b)

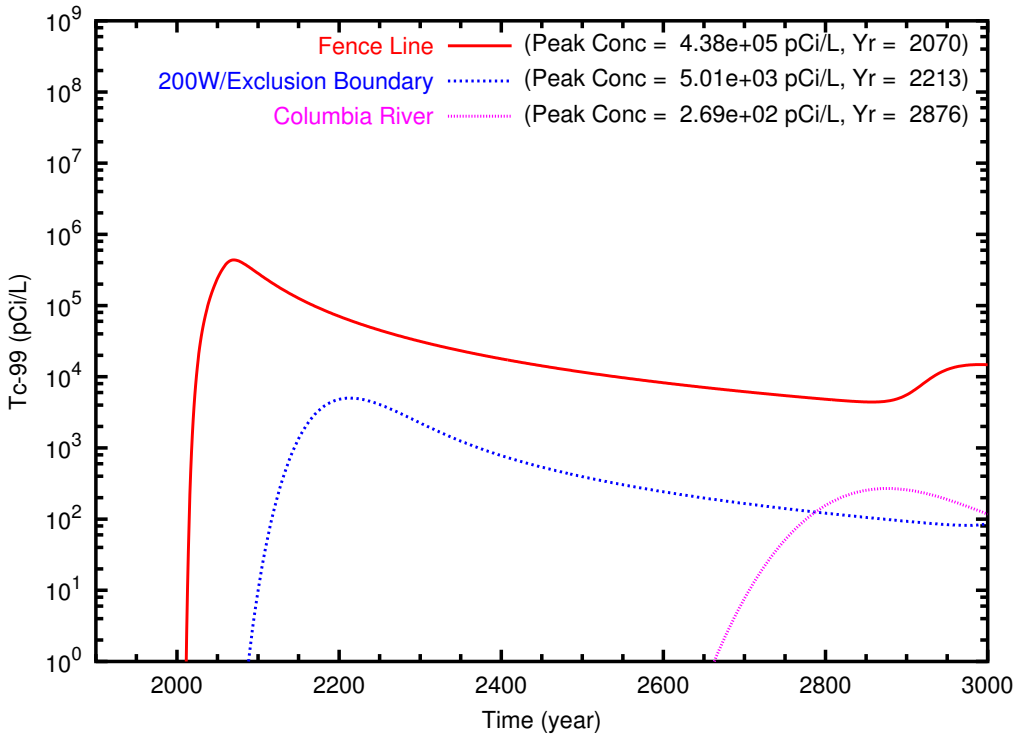

Figure B.40. T Case 7 **Tc-99** breakthrough curves at fenceline and downgradient points along (a) east path and (b) north path

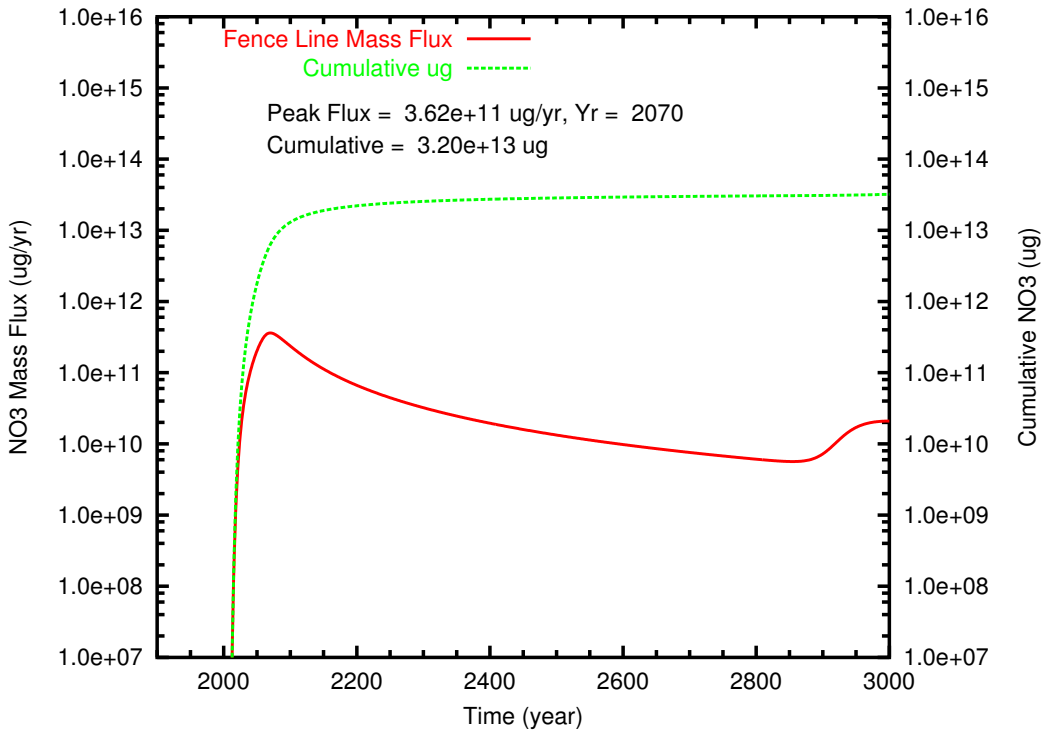

Figure B.41. T Case 7 NO_3 mass flux and cumulative mass at fenceline

(a)

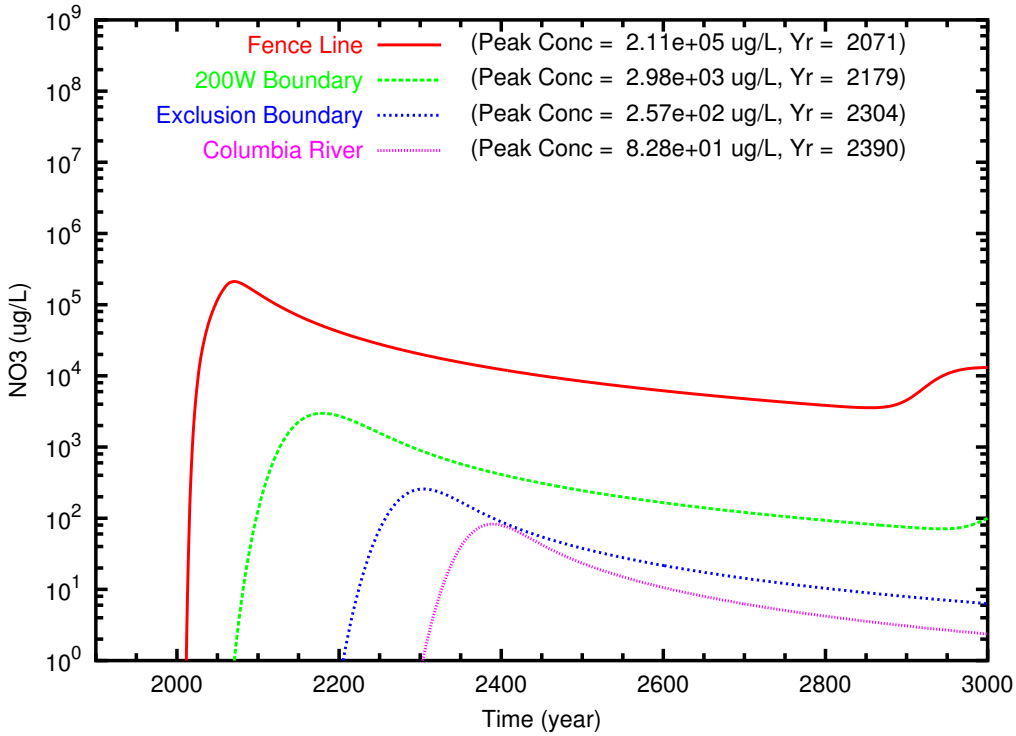

(b)

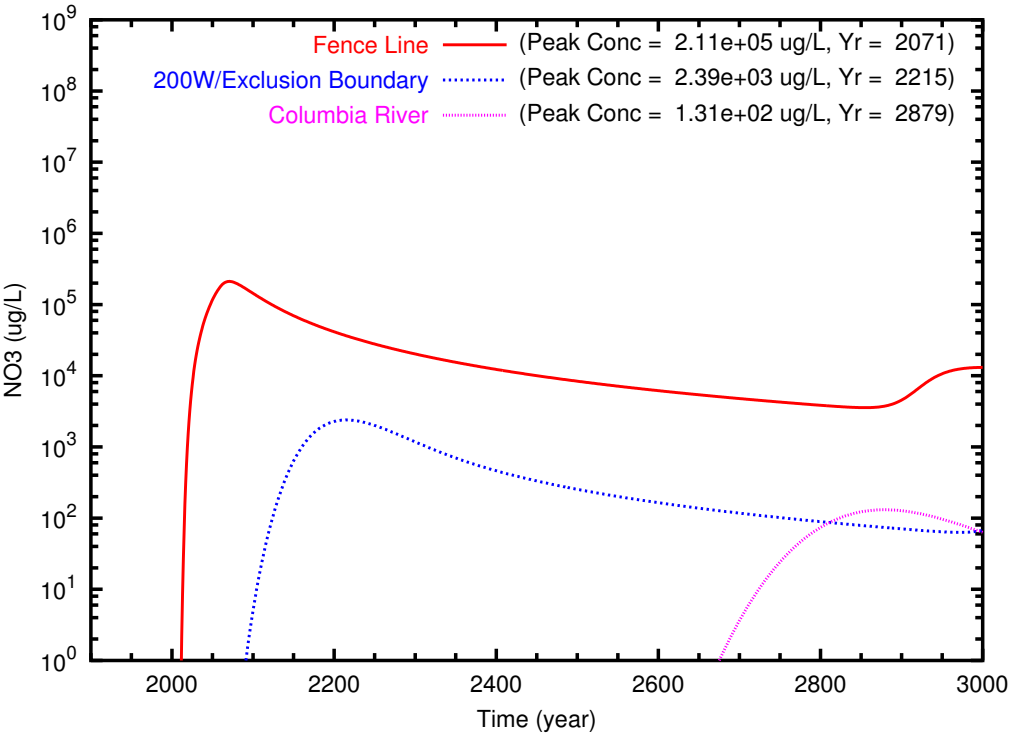

Figure B.42. T Case 7 $\mathbf{NO_3}$ breakthrough curves at fenceline and downgradient points along (a) east path and (b) north path

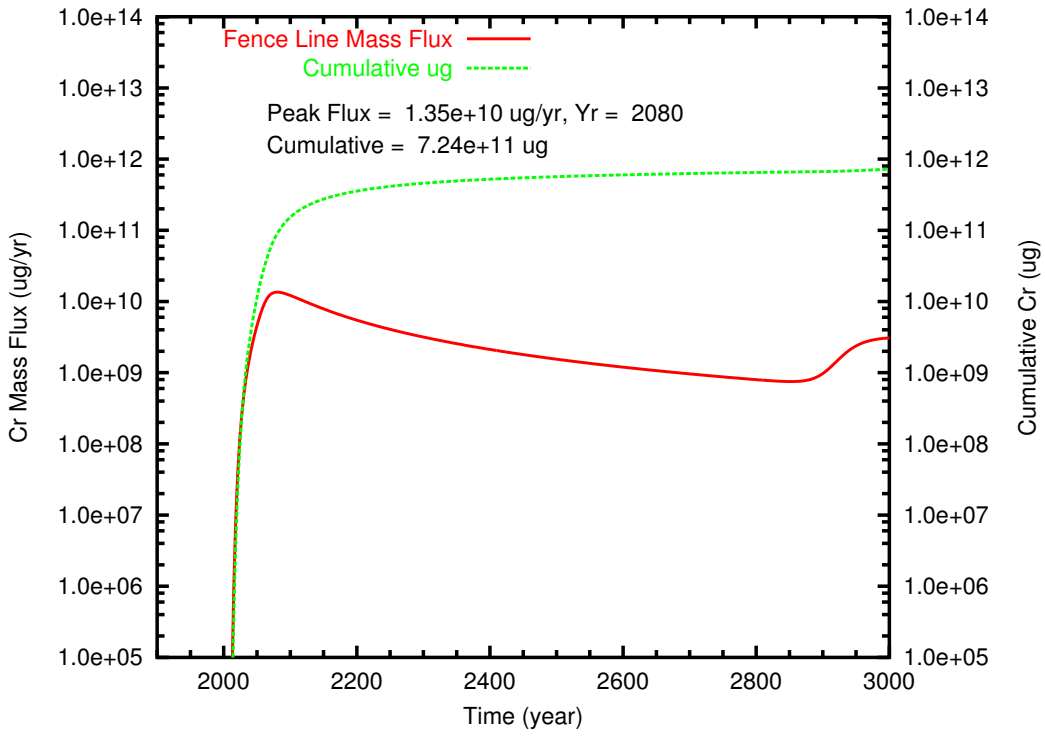

Figure B.43. T Case 7 **Cr** mass flux and cumulative mass at fenceline

(a)

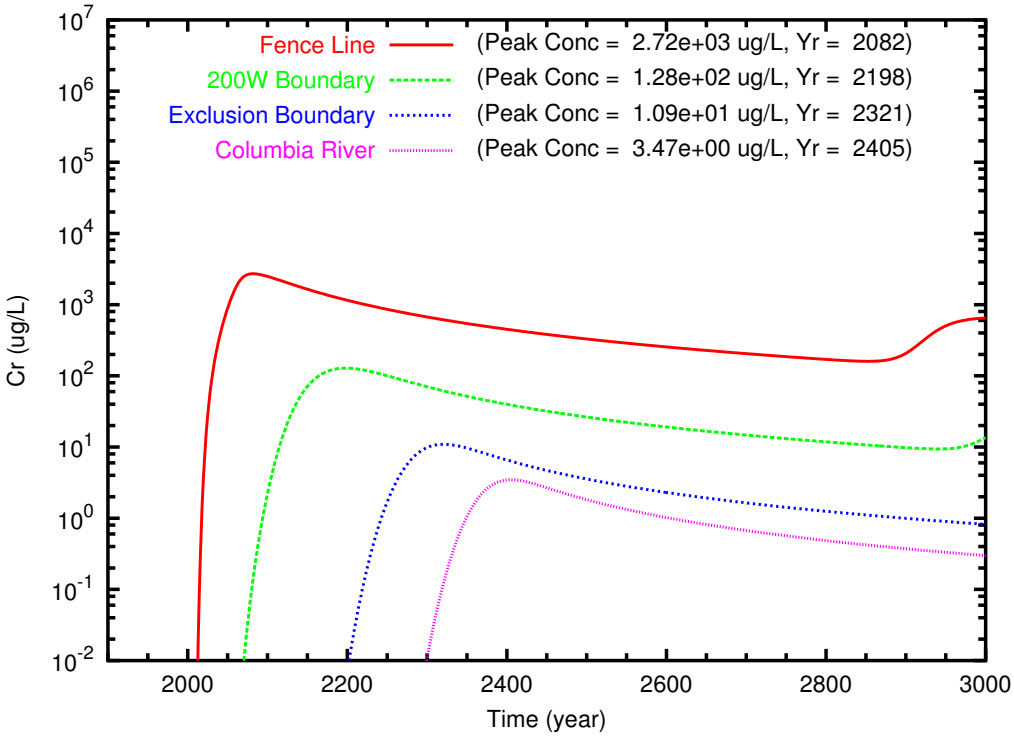

(b)

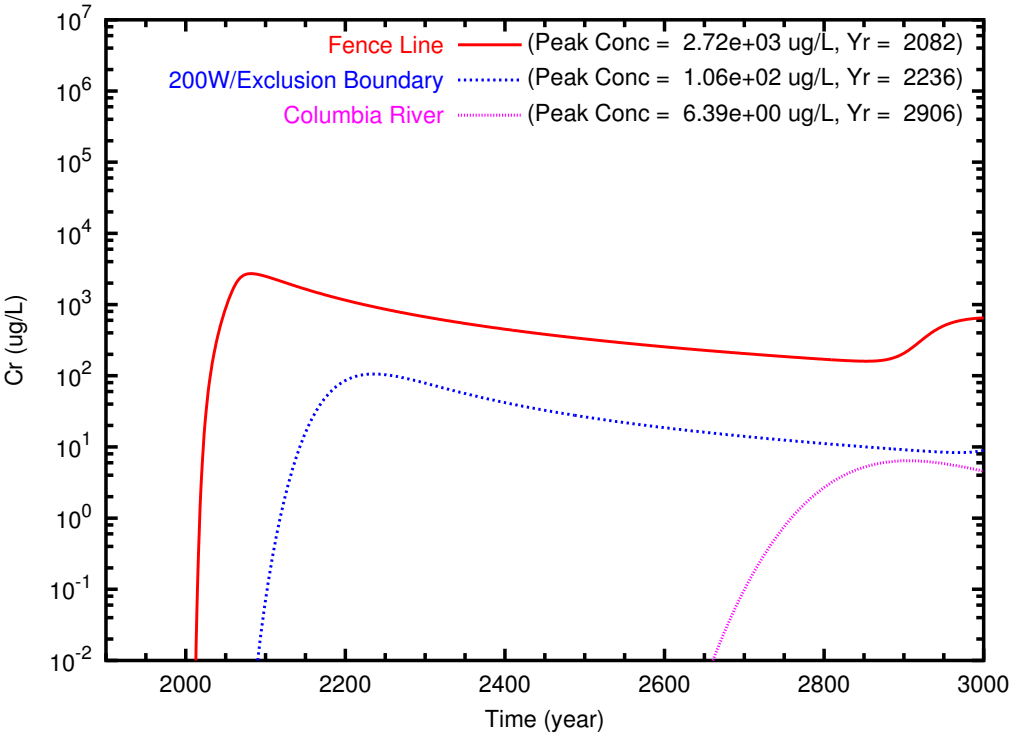

Figure B.44. T Case 7 **Cr** breakthrough curves at fenceline and downgradient points along (a) east path and (b) north path

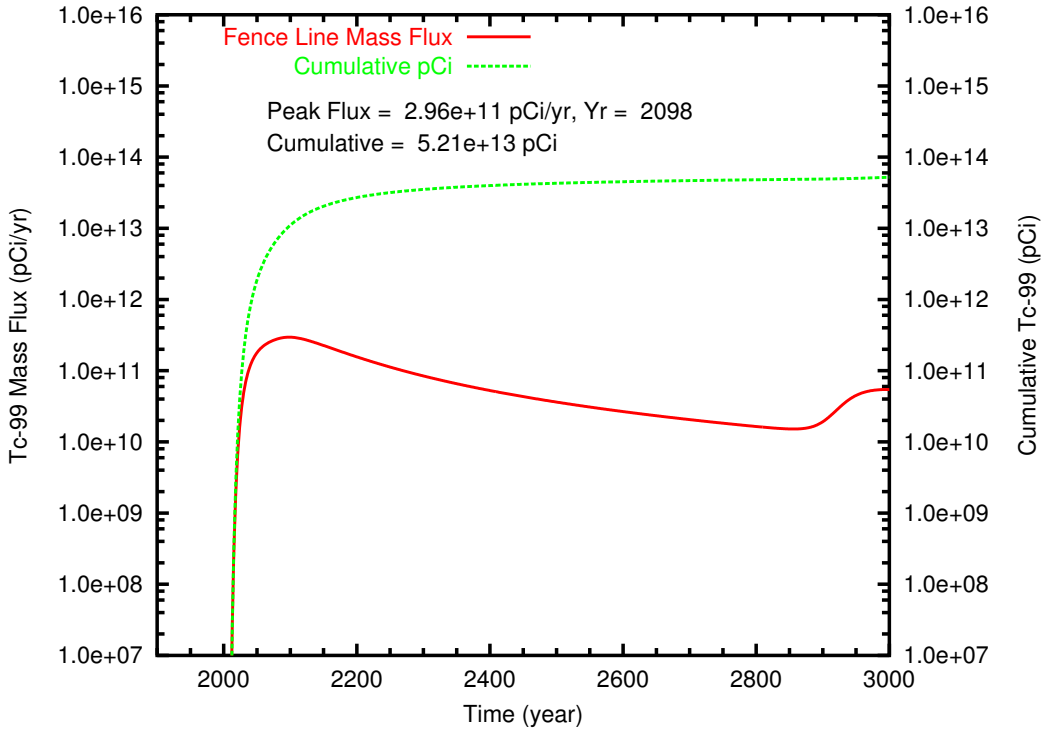

Figure B.45. T Case 8 **Tc-99** mass flux and cumulative mass at fenceline

(a)

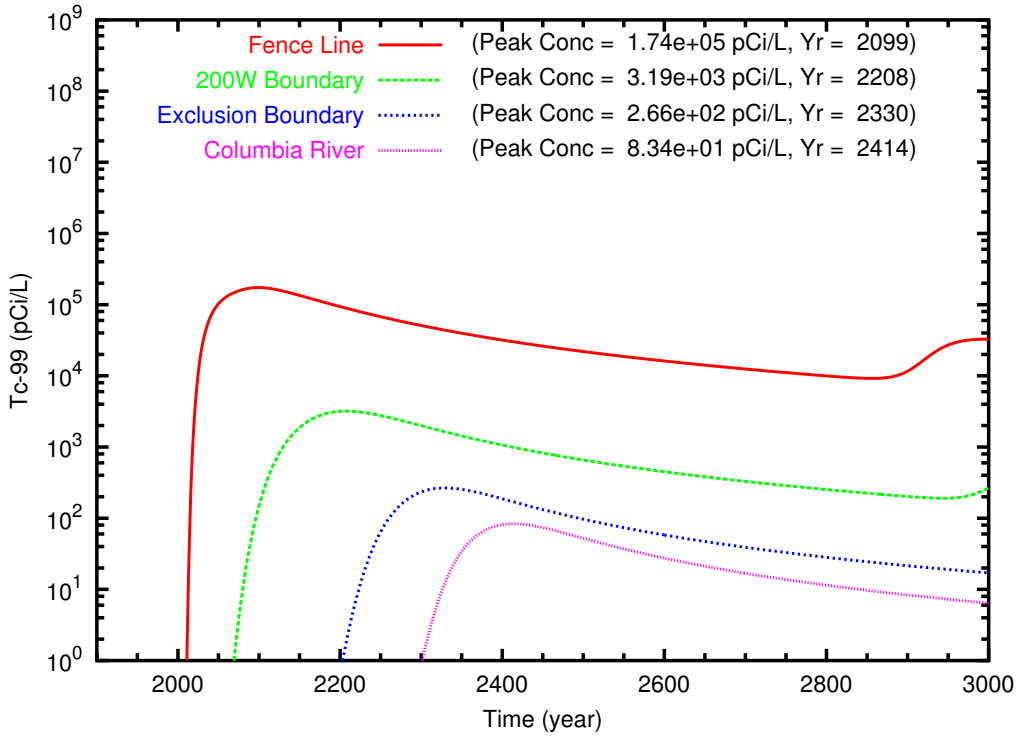

(b)

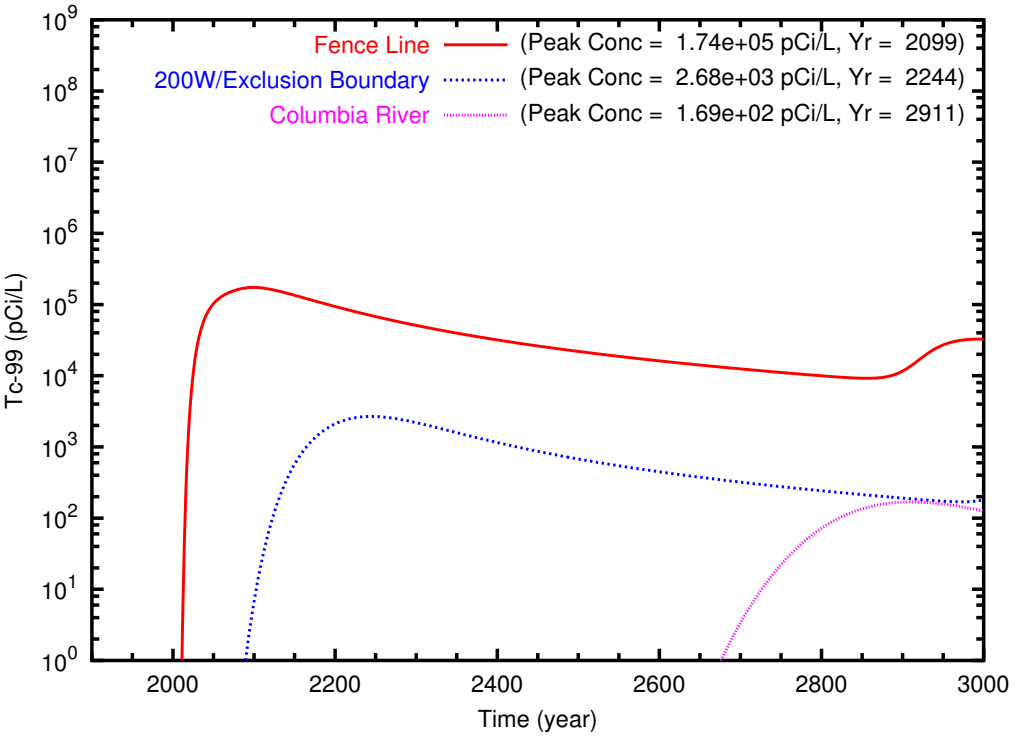

Figure B.46. T Case 8 **Tc-99** breakthrough curves at fenceline and downgradient points along (a) east path and (b) north path

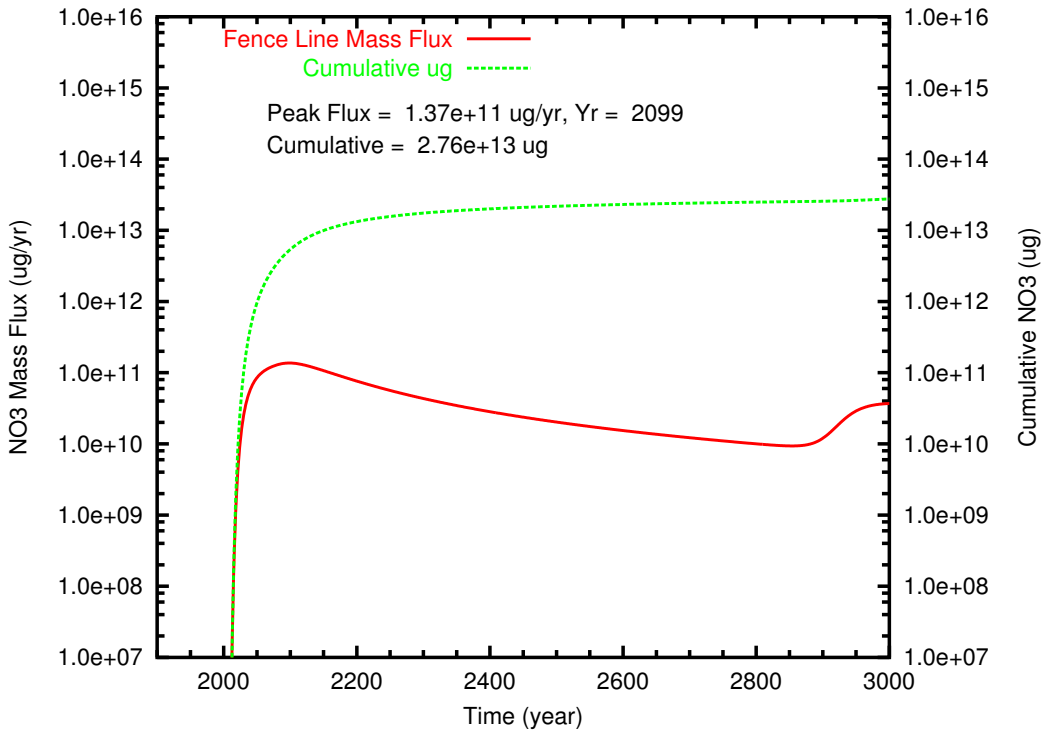

Figure B.47. T Case 8 NO_3 mass flux and cumulative mass at fenceline

(a)

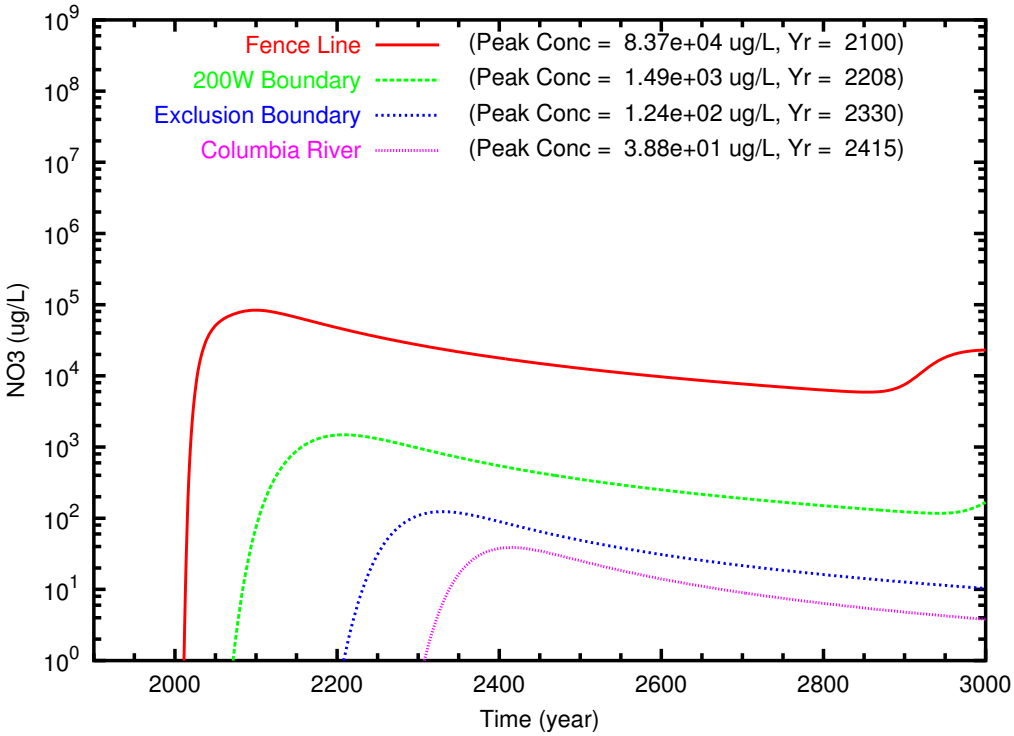

(b)

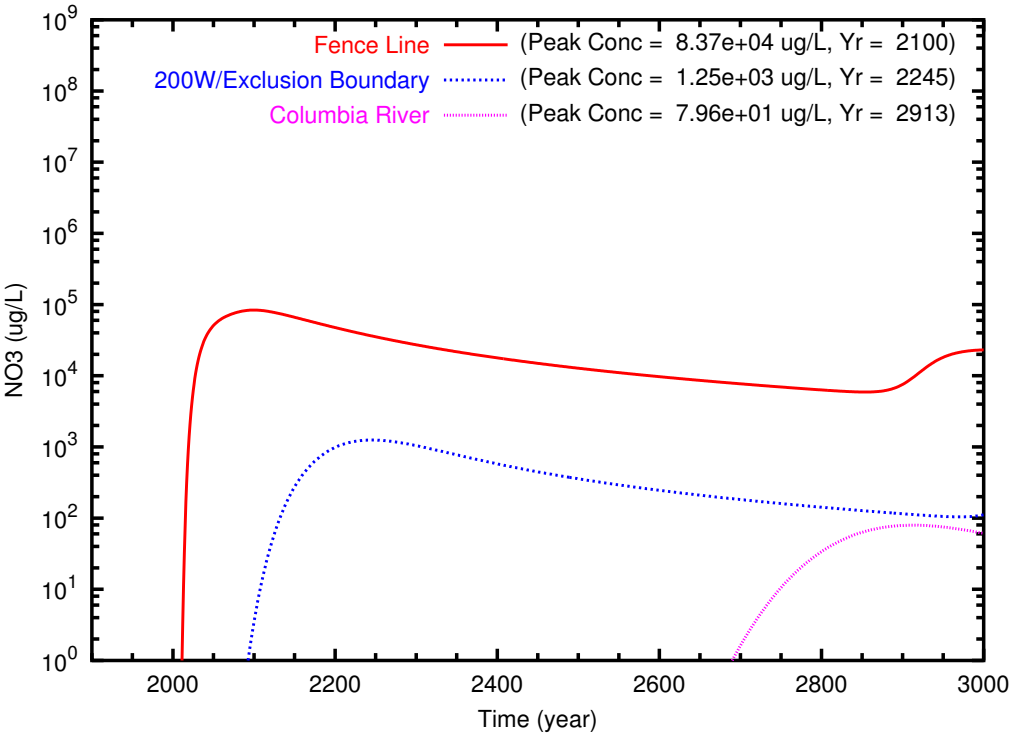

Figure B.48. T Case 8 **NO_3** breakthrough curves at fenceline and downgradient points along (a) east path and (b) north path

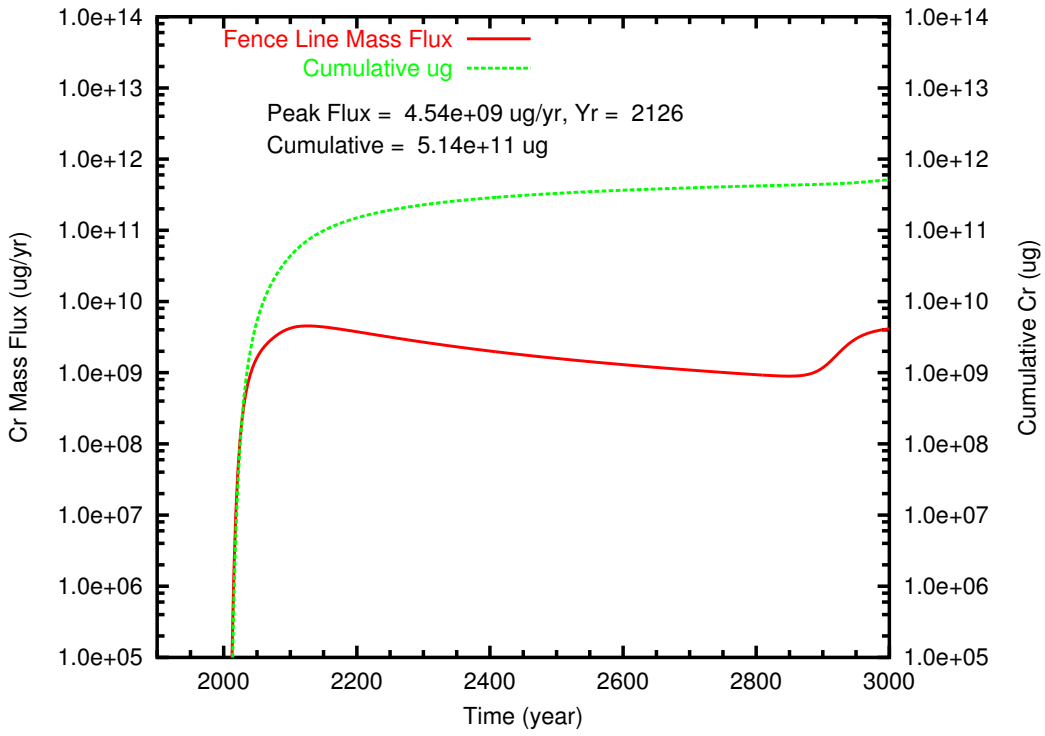

Figure B.49. T Case 8 **Cr** mass flux and cumulative mass at fenceline

(a)

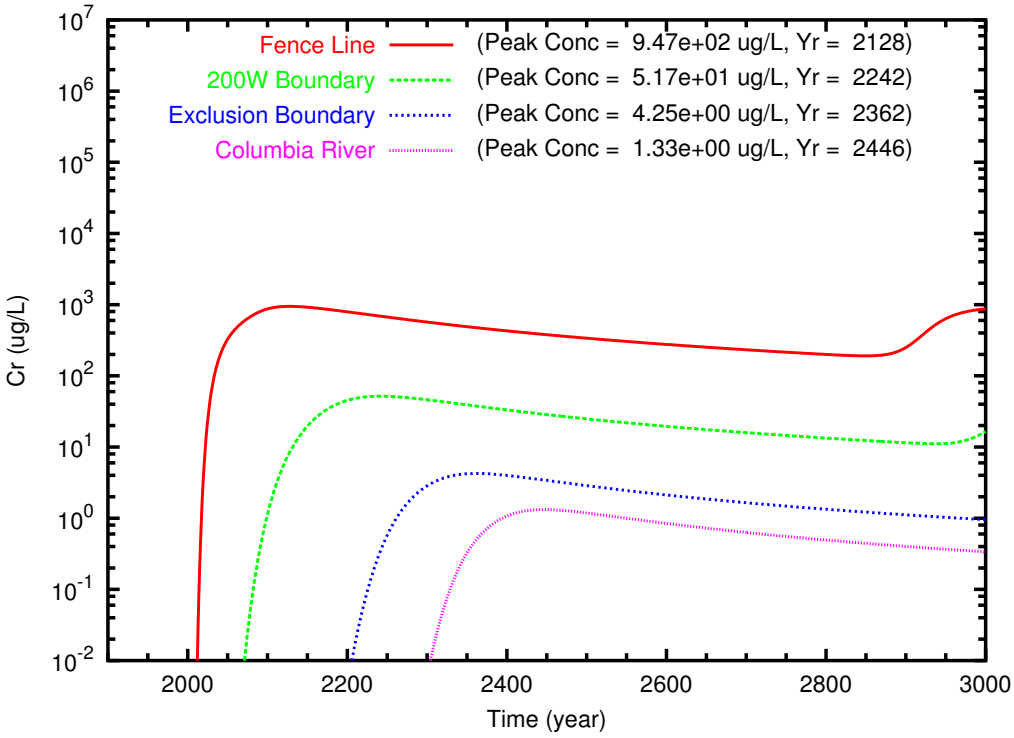

(b)

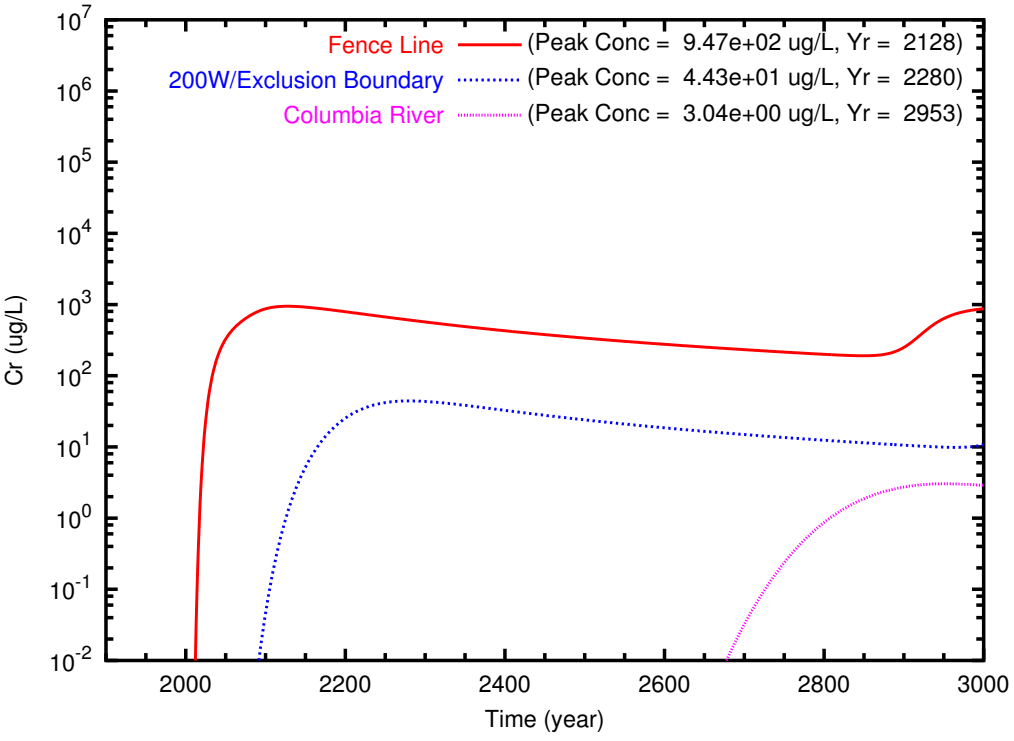

Figure B.50. T Case 8 **Cr** breakthrough curves at fenceline and downgradient points along (a) east path and (b) north path

Appendix C

TX Tank Farm Cross-Section Plots

(a)

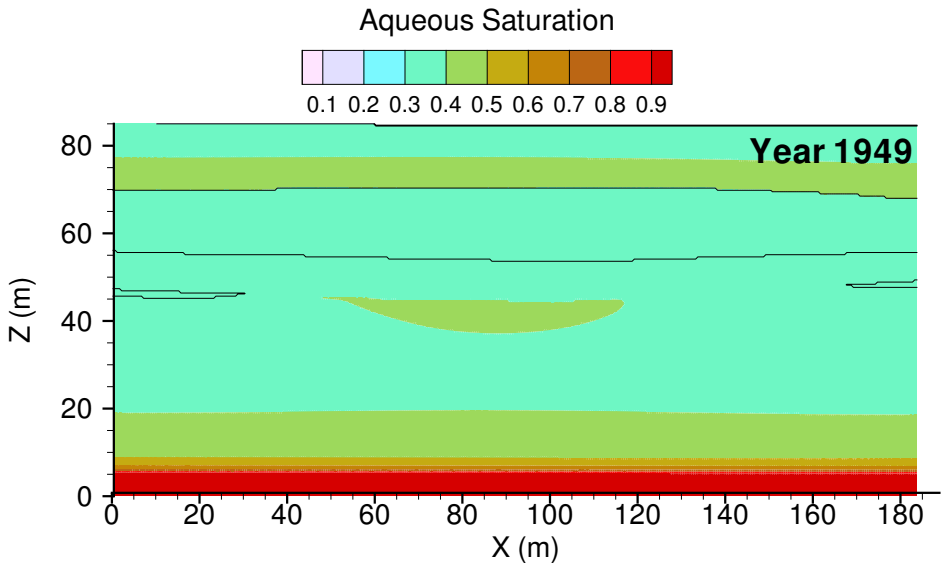

(b)

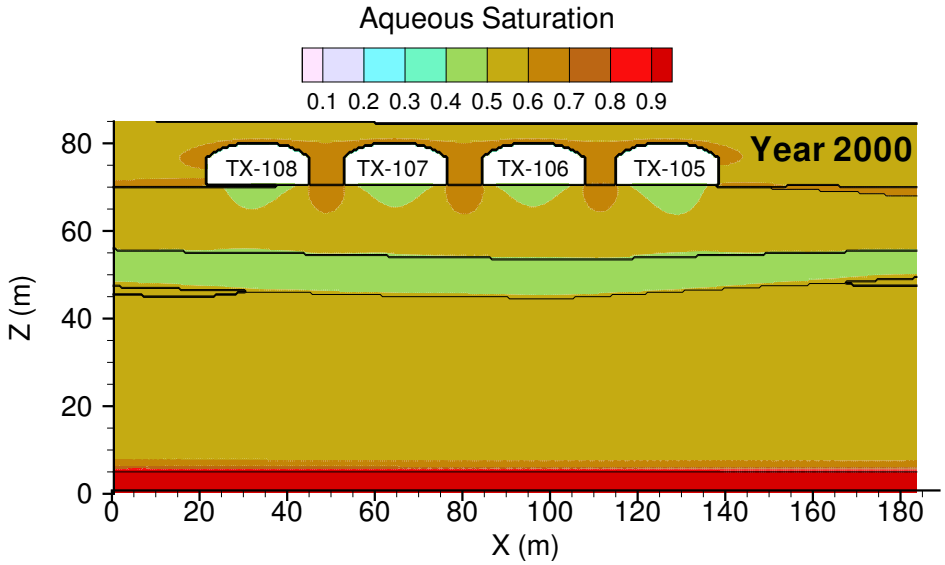

Figure C.1. TX baseline aqueous saturation at (a) year 1949 and (b) 01/01/2000

(a)

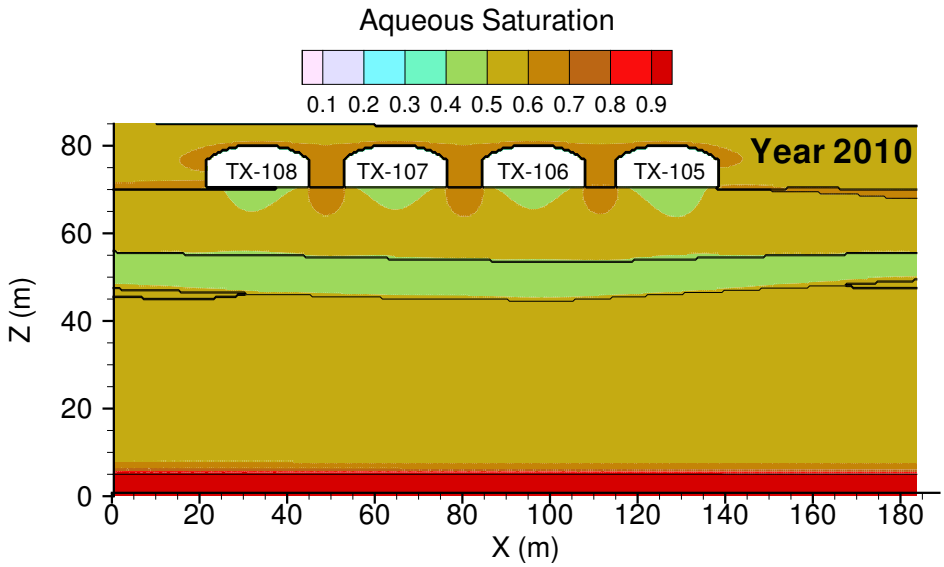

(b)

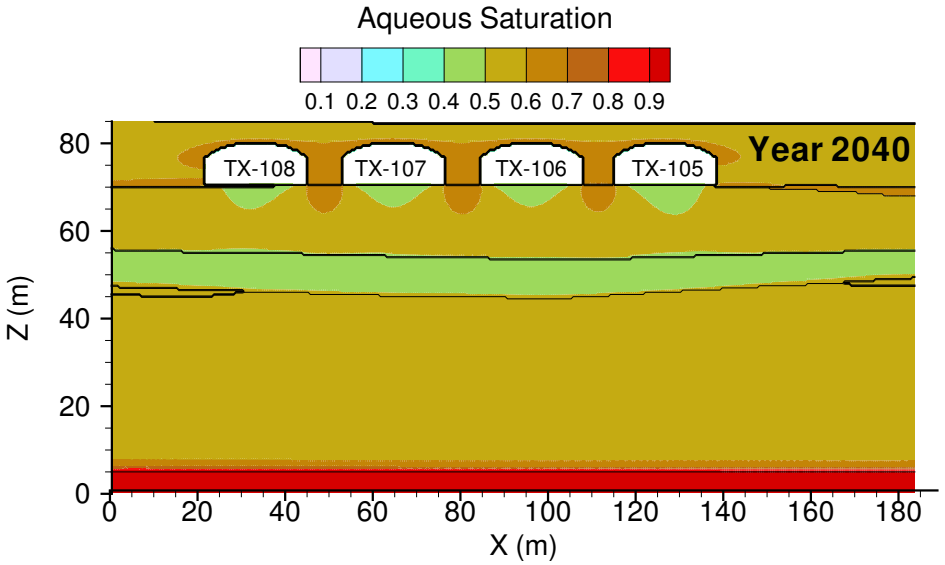

Figure C.2. TX baseline aqueous saturation at (a) year 2010 (current conditions) and (b) year 2040 (no interim barrier)

(a)

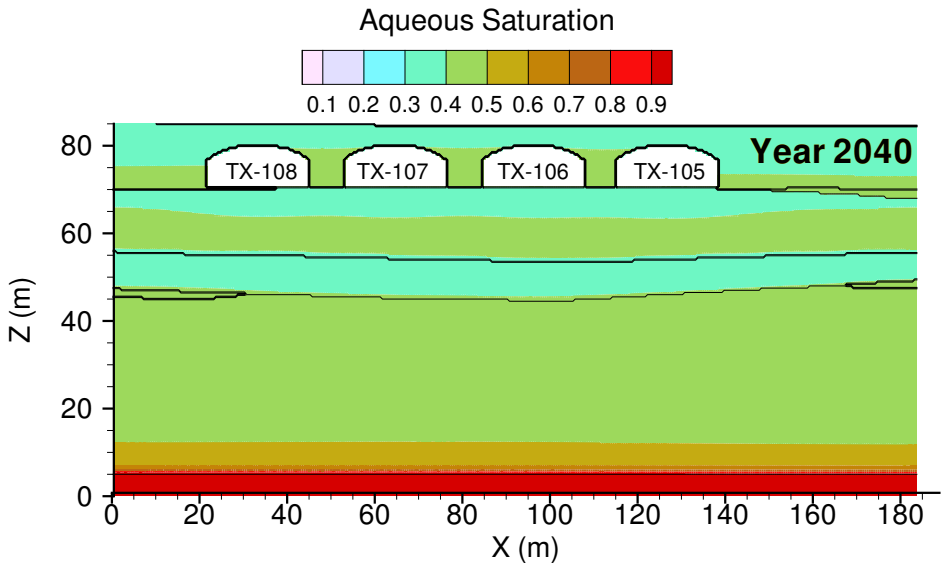

(b)

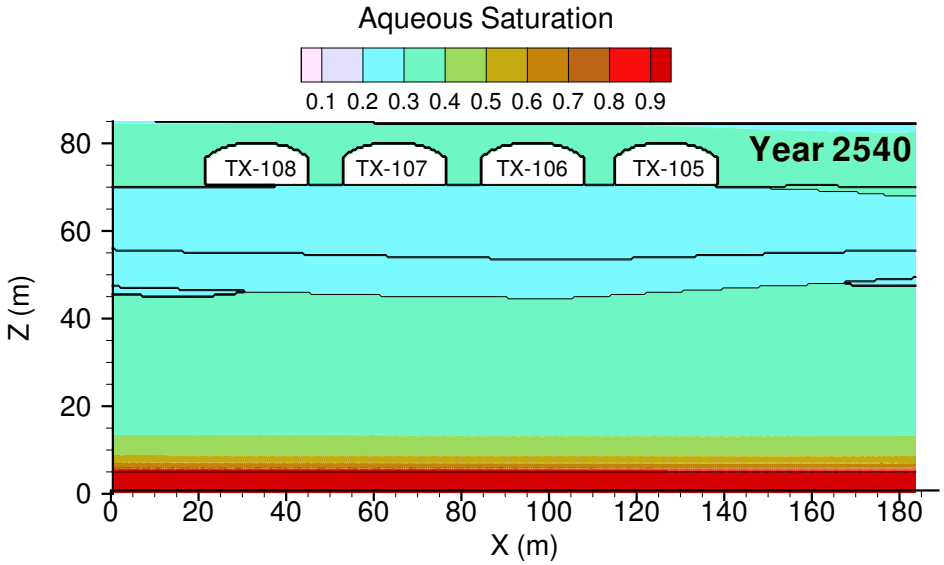

Figure C.3. TX baseline aqueous saturation at (a) year 2040 (interim barrier) and (b) year 2540 (closure barrier)

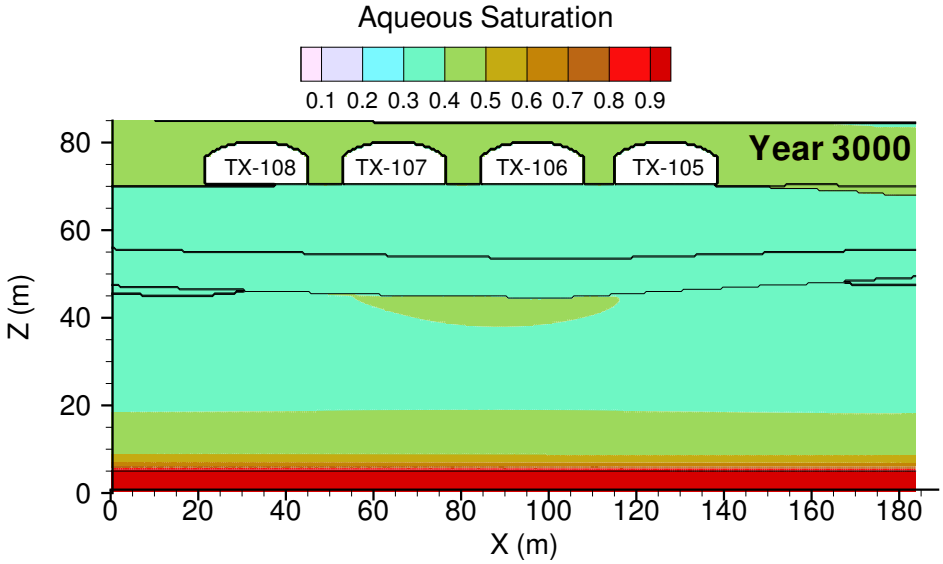

Figure C.4. TX baseline aqueous saturation at year 3000 (degraded barrier)

(a)

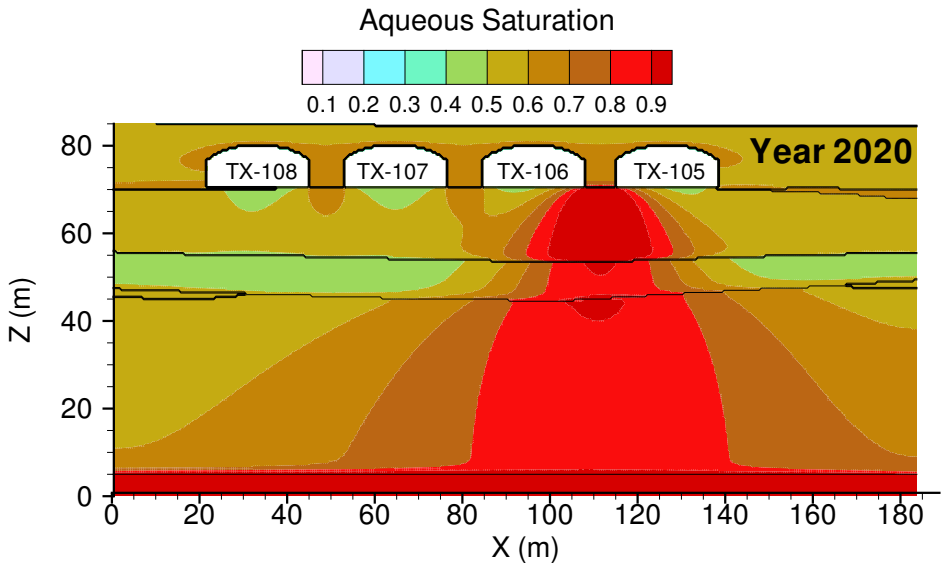

(b)

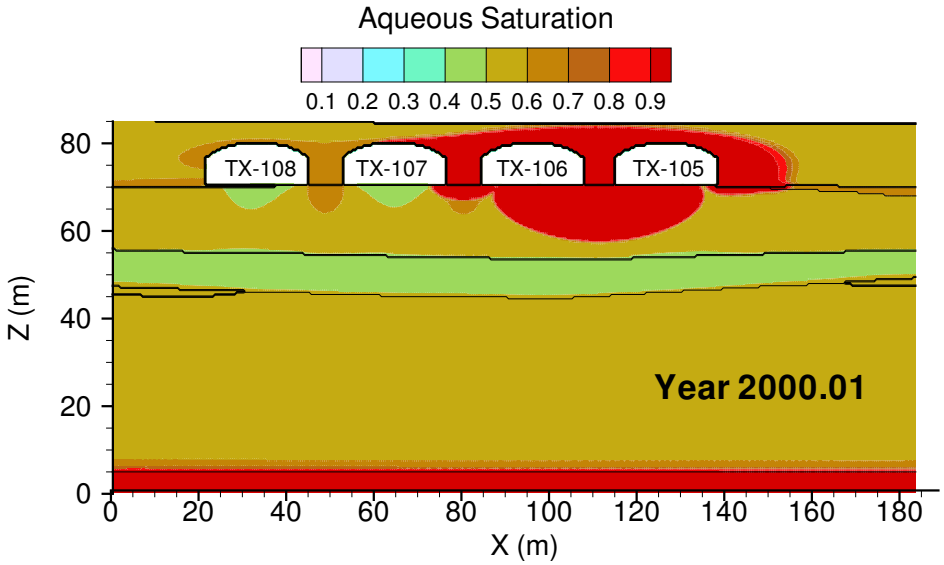

Figure C.5. TX baseline aqueous saturation: (a) Case 3, year 2020 and (b) Case 4, 1/5/2000

(a)

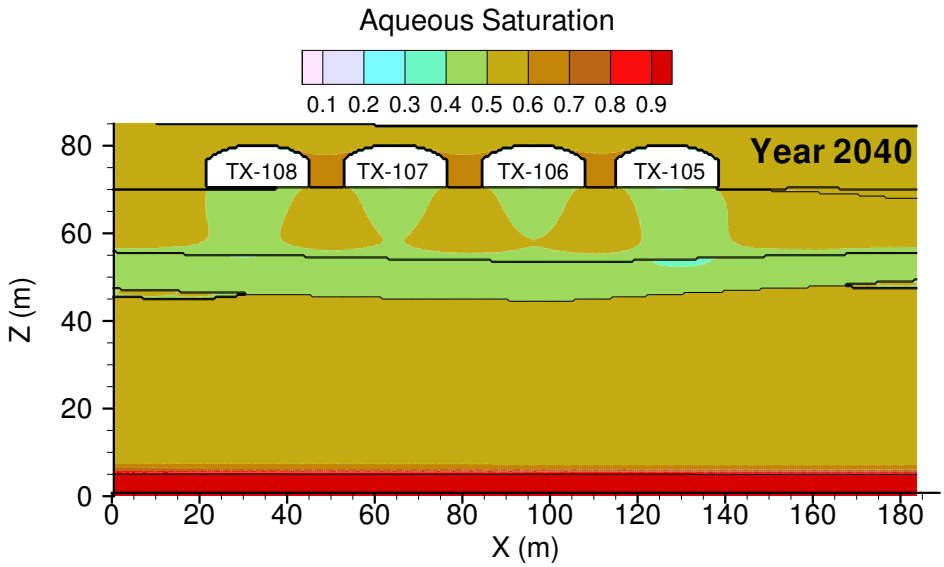

(b)

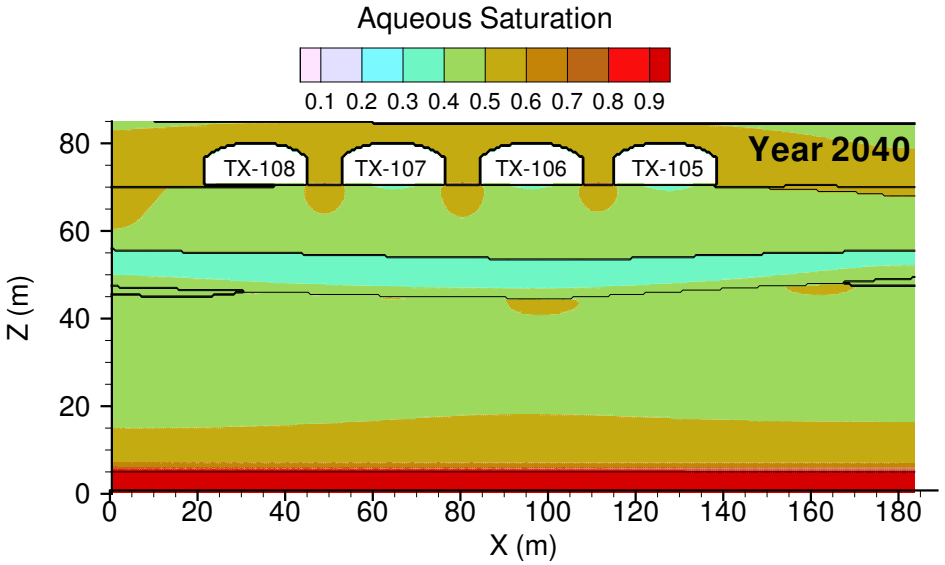

Figure C.6. TX baseline aqueous saturation at year 2040: (a) Case 6 and (b) Case 7

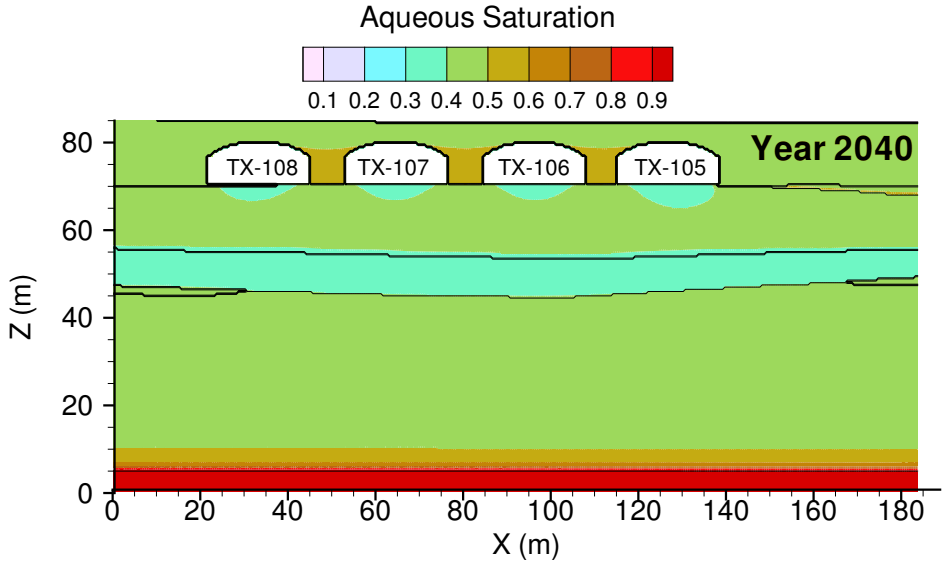

Figure C.7. TX baseline aqueous saturation at year 2040 for Case 8

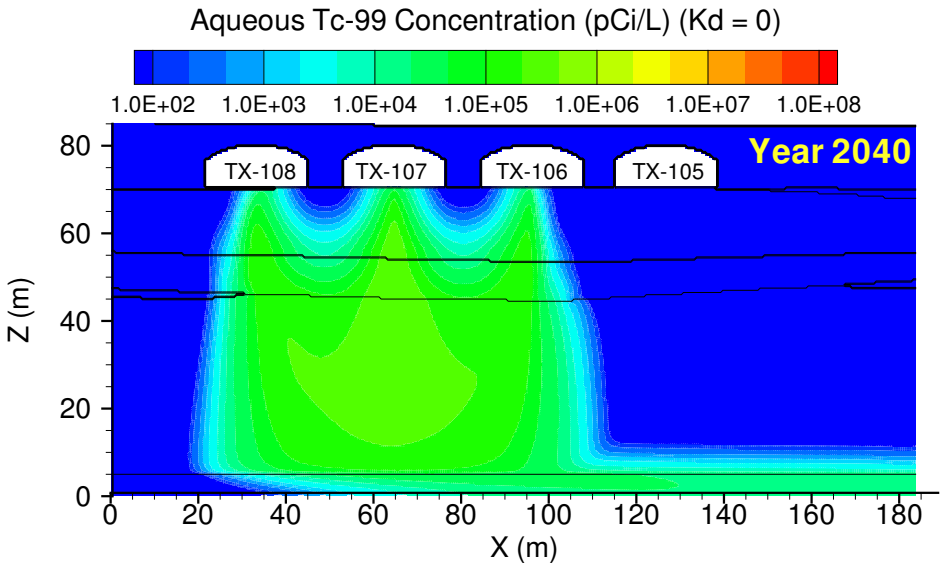

Figure C.8. TX Case 1, **Tc-99** aqueous concentration at year 2040. Year of maximum concentration at fenceline was 2050.

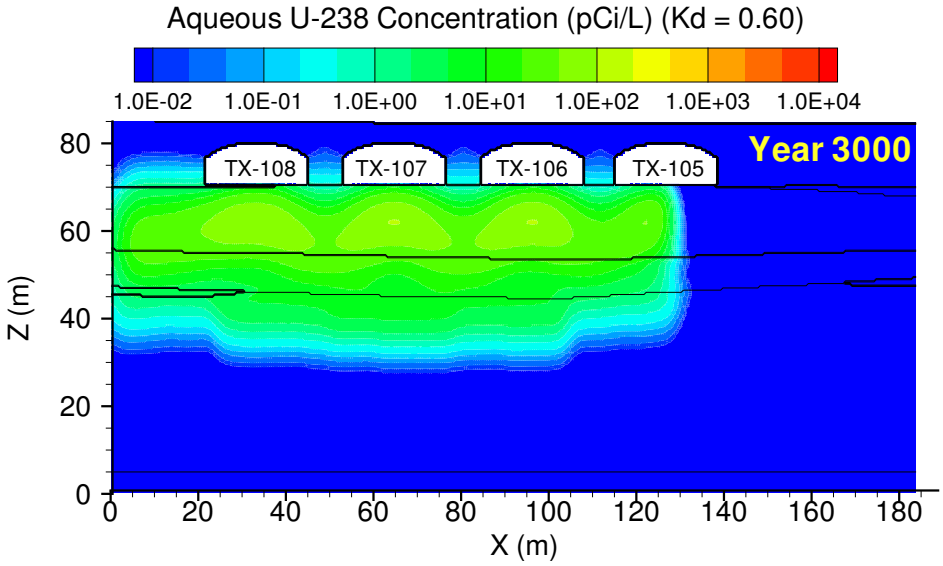

Figure C.9. TX Case 1, **U-238** (K_d = 0.60) aqueous concentration at year 3000. Year of maximum concentration at fenceline was 3000.

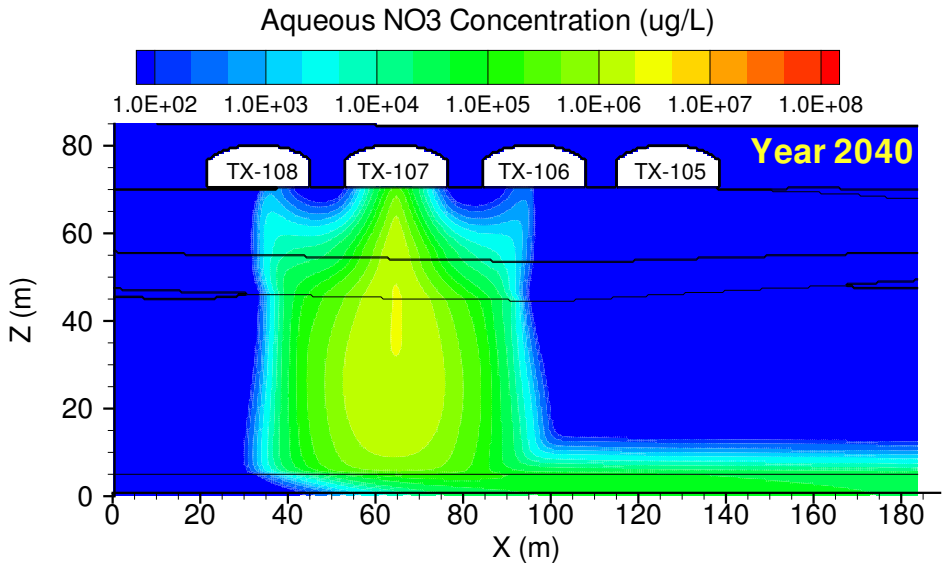

Figure C.10. TX Case 1, **NO_3** aqueous concentration at year 2040. Year of maximum concentration at fenceline was 2051.

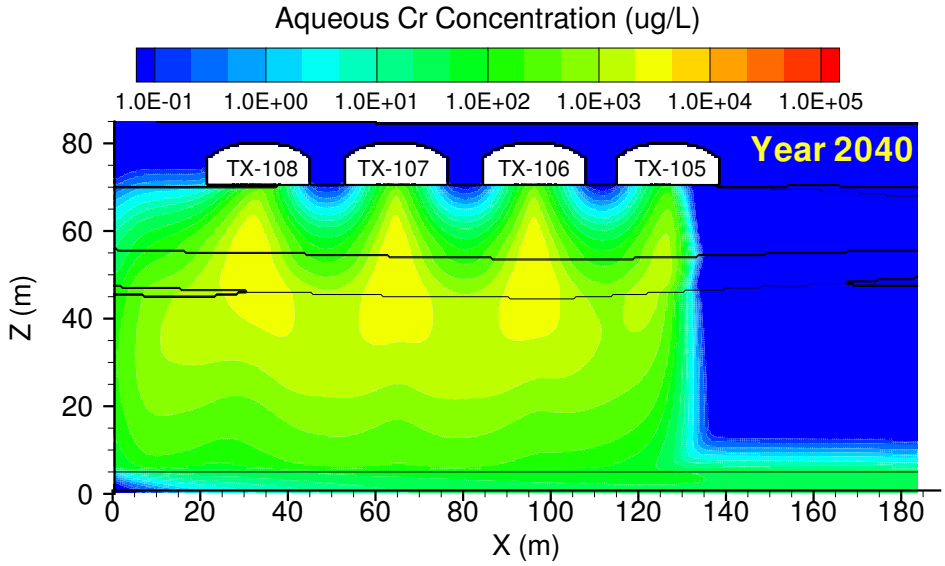

Figure C.11. TX Case 1, **Cr** aqueous concentration at year 2040. Year of maximum concentration at fenceline was 2058.

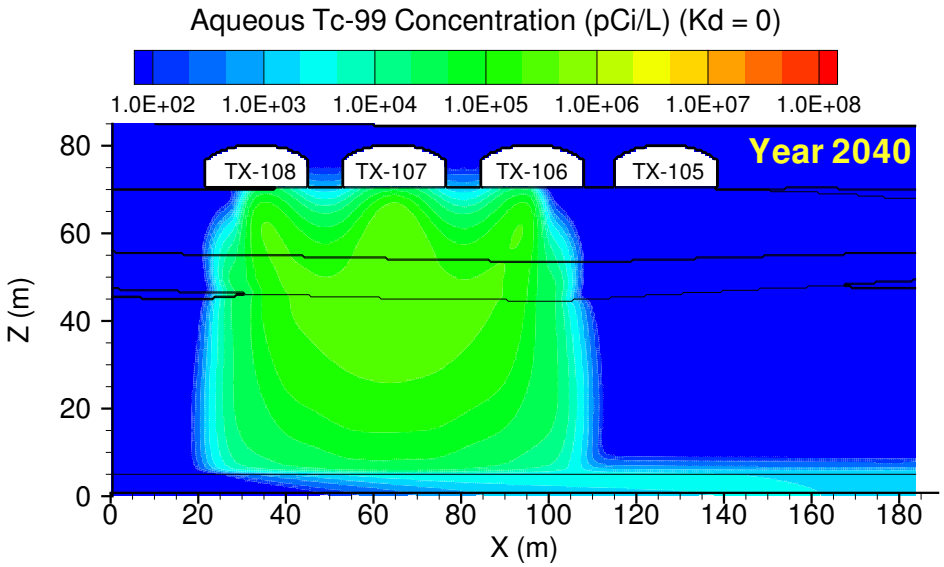

Figure C.12. TX Case 2, **Tc-99** aqueous concentration at year 2040. Year of maximum concentration at fenceline was 2060.

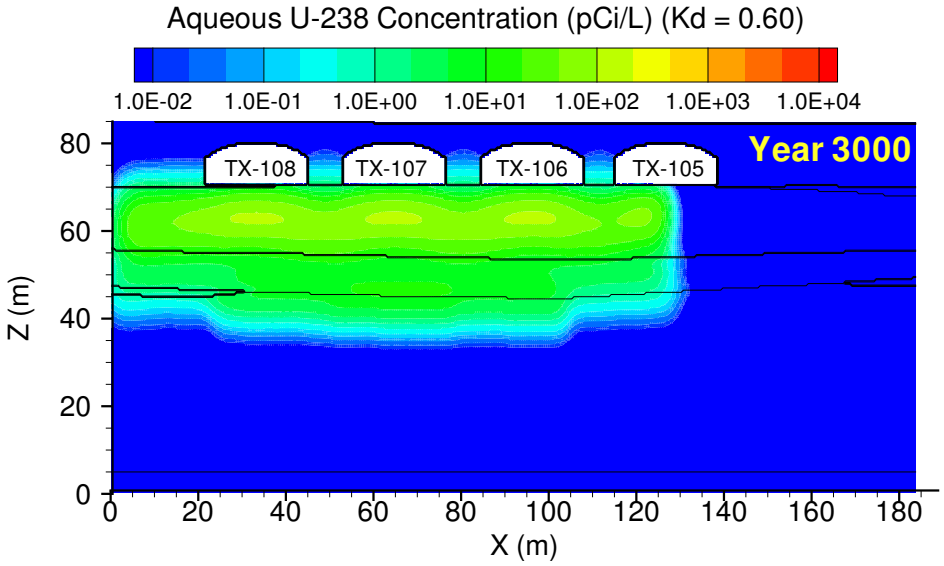

Figure C.13. TX Case 2, **U-238** (K_d = 0.60) aqueous concentration at year 3000. Year of maximum concentration at fenceline was 3000.

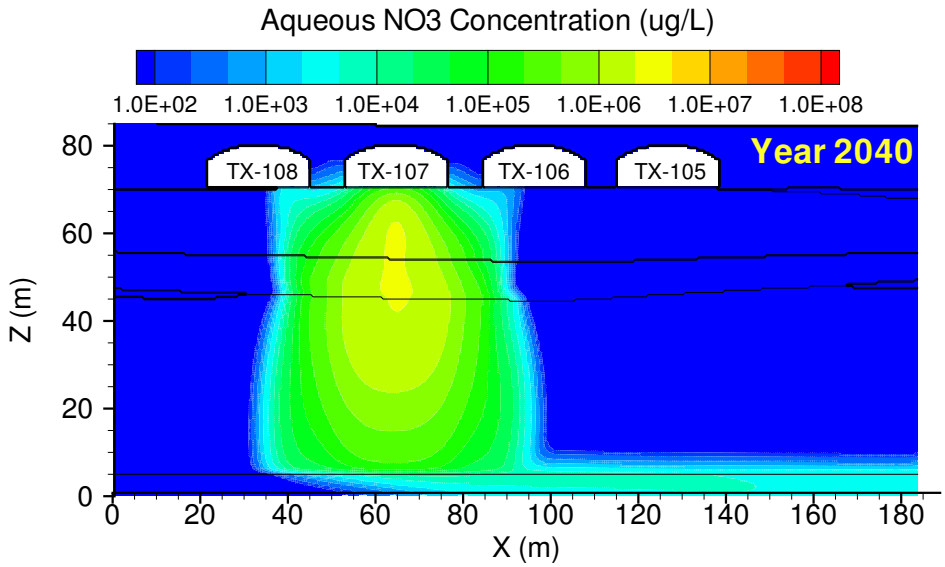

Figure C.14. TX Case 2, **NO_3** aqueous concentration at year 2040. Year of maximum concentration at fenceline was 2067.

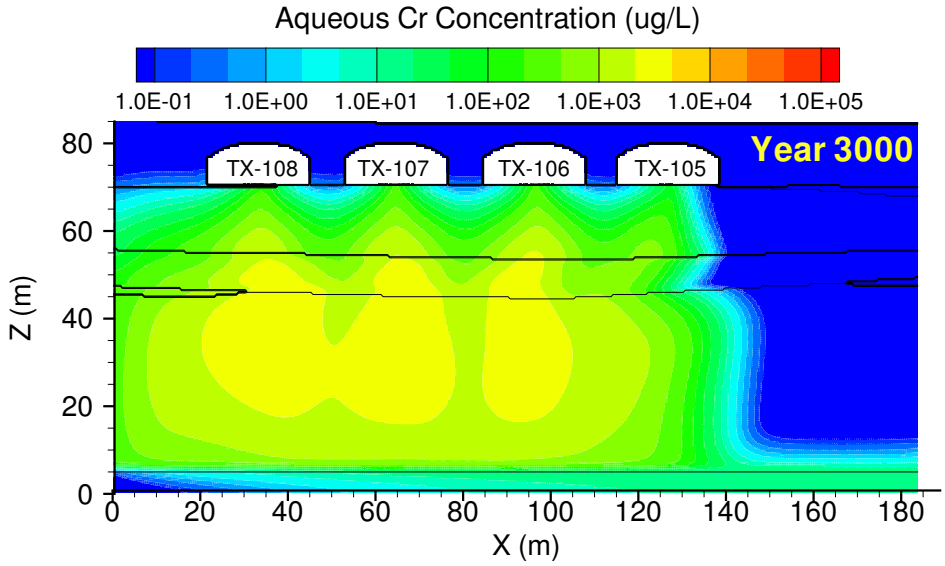

Figure C.15. TX Case 2, **Cr** aqueous concentration at year 3000. Year of maximum concentration at fenceline was 3000.

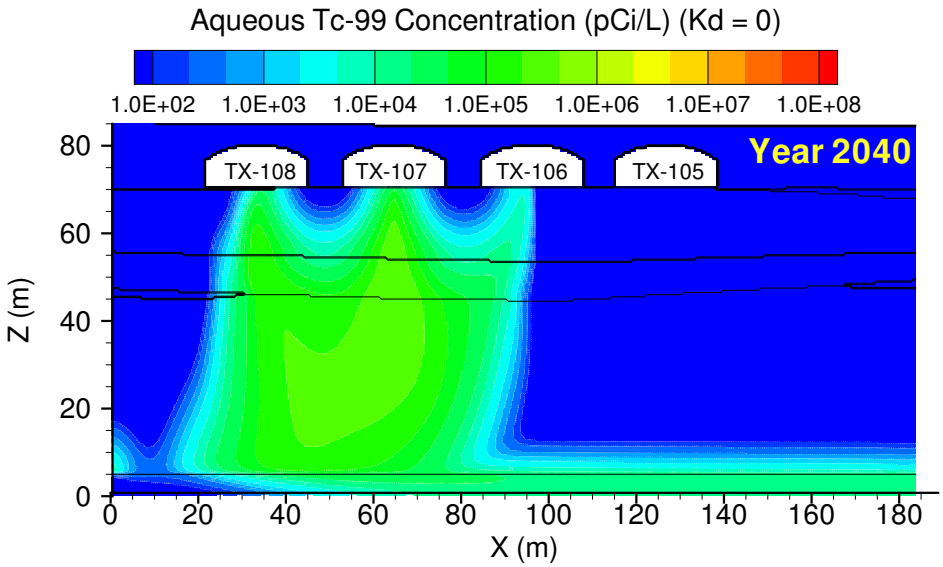

Figure C.16. TX Case 3, **Tc-99** aqueous concentration at year 2040. Year of maximum concentration at fenceline was 2027.

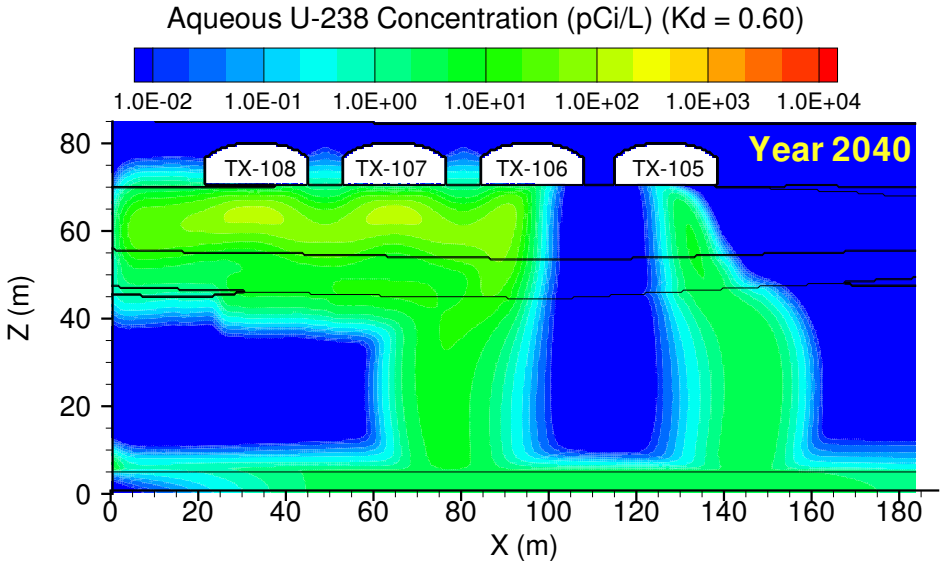

Figure C.17. TX Case 3, **U-238** (K_d = 0.60) aqueous concentration at year 2040. Year of maximum concentration at fenceline was 2062.

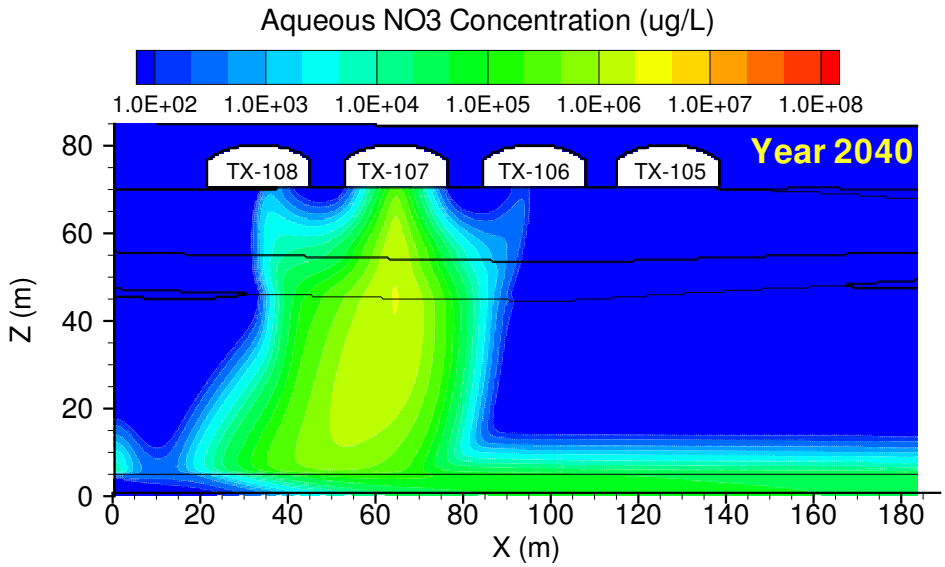

Figure C.18. TX Case 3, **NO_3** aqueous concentration at year 2040. Year of maximum concentration at fenceline was 2027.

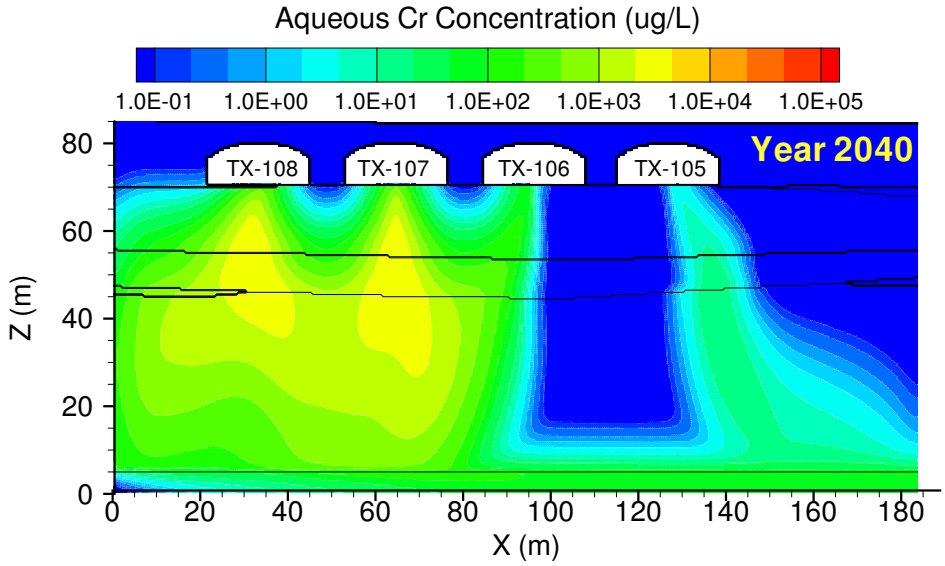

Figure C.19. TX Case 3, **Cr** aqueous concentration at year 2040. Year of maximum concentration at fenceline was 2027.

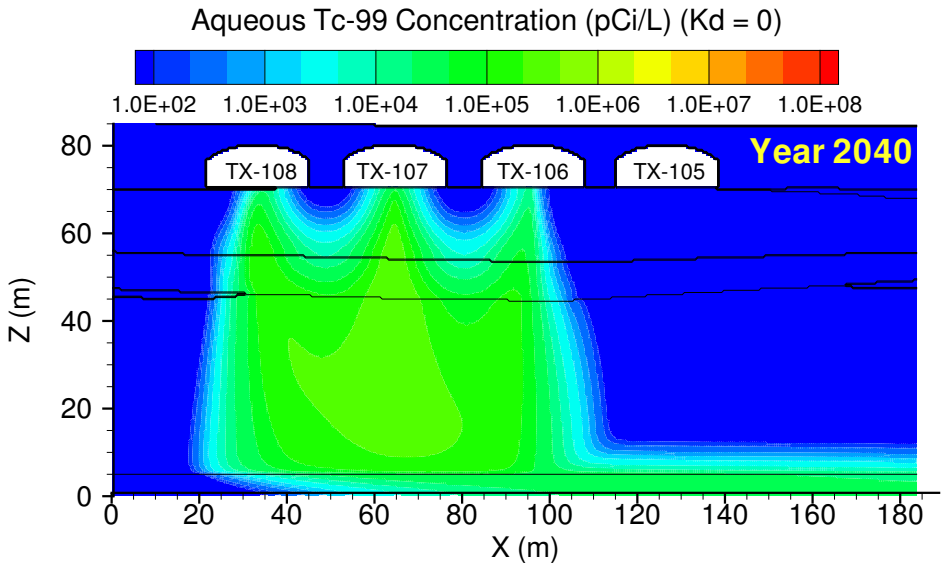

Figure C.20. TX Case 4, **Tc-99** aqueous concentration at year 2040. Year of maximum concentration at fenceline was 2049.

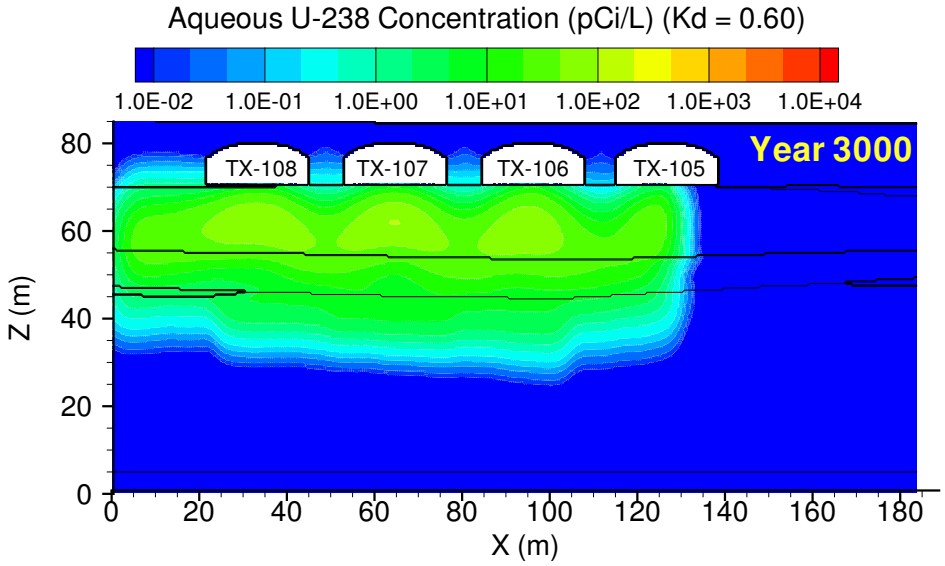

Figure C.21. TX Case 4, **U-238** (K_d = 0.60) aqueous concentration at year 3000. Year of maximum concentration at fenceline was 3000.

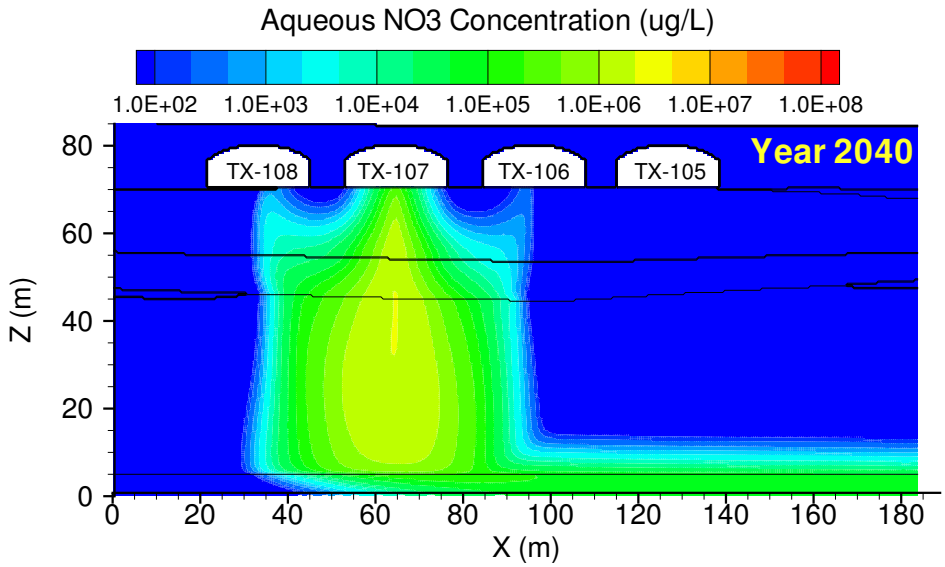

Figure C.22. TX Case 4, **NO_3** aqueous concentration at year 2040. Year of maximum concentration at fenceline was 2050.

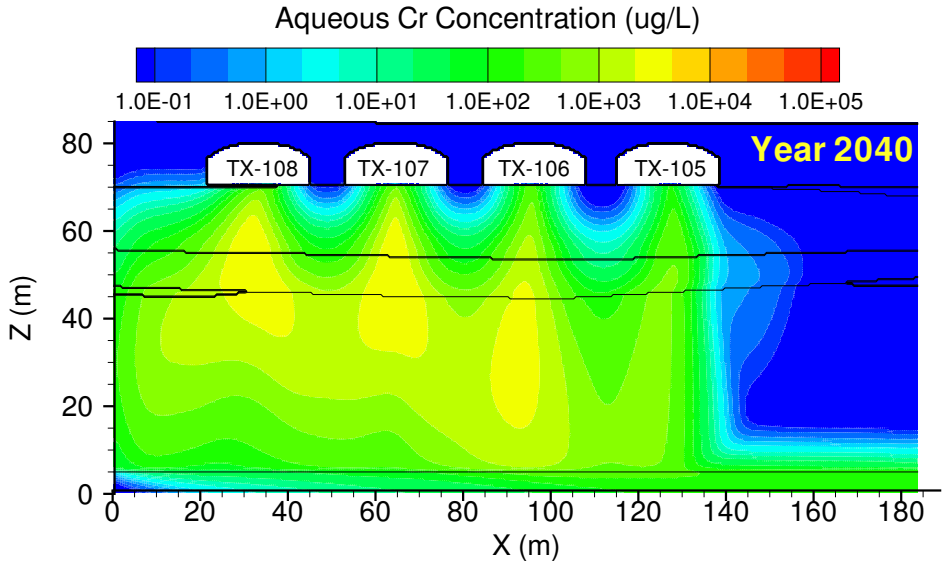

Figure C.23. TX Case 4, **Cr** aqueous concentration at year 2040. Year of maximum concentration at fenceline was 2053.

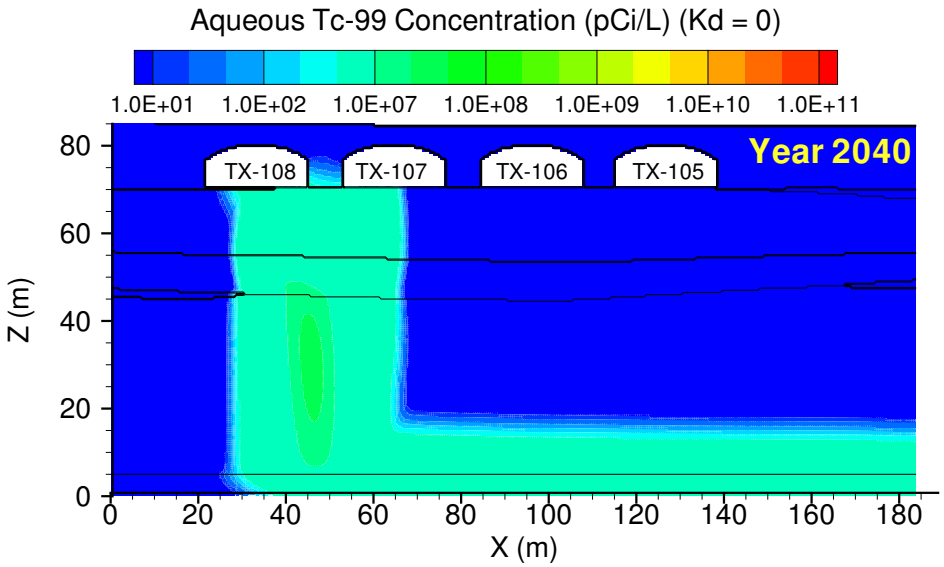

Figure C.24. TX Case 5, **Tc-99** aqueous concentration at year 2040. Year of maximum concentration at fenceline was 2052.

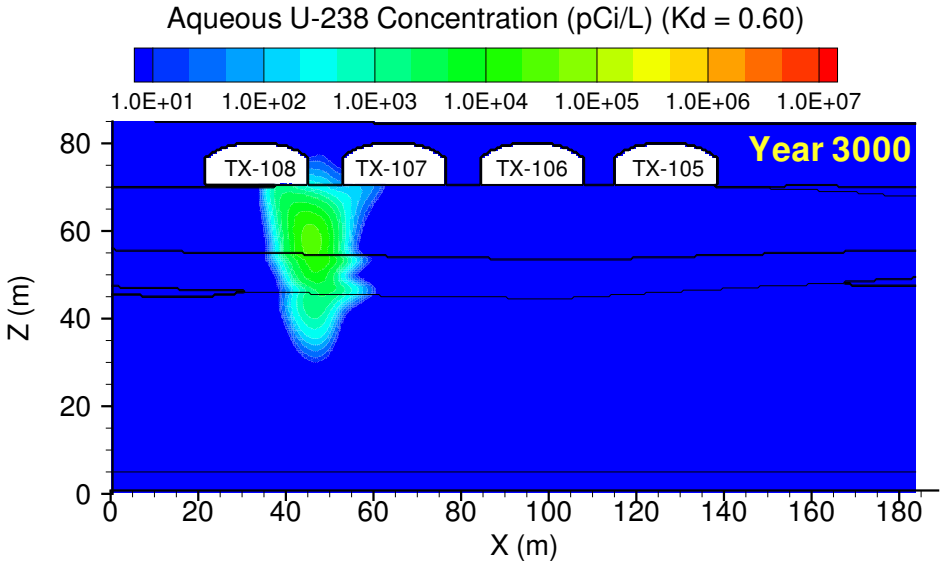

Figure C.25. TX Case 5, **U-238** (K_d = 0.60) aqueous concentration at year 3000. Year of maximum concentration at fenceline was 3000.

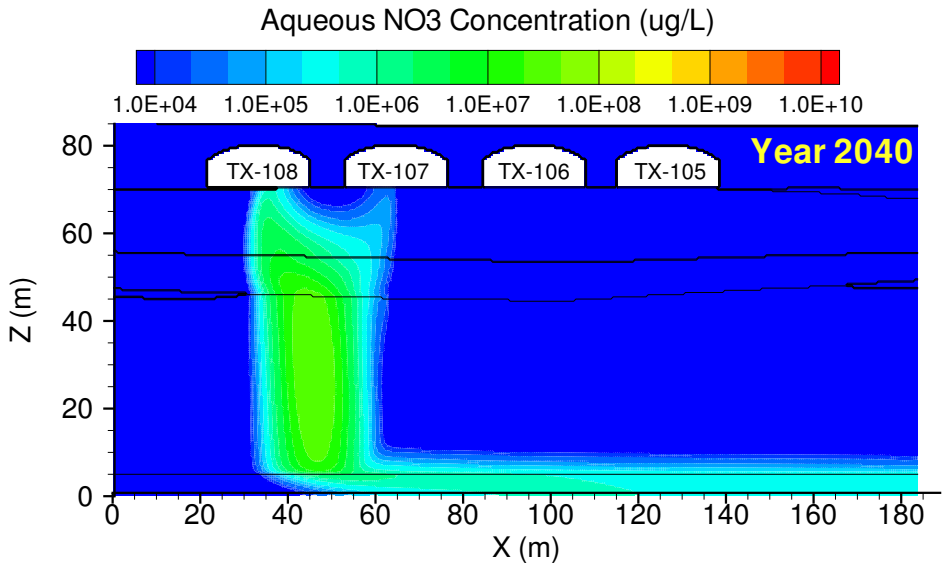

Figure C.26. TX Case 5, **NO_3** aqueous concentration at year 2040. Year of maximum concentration at fenceline was 2052.

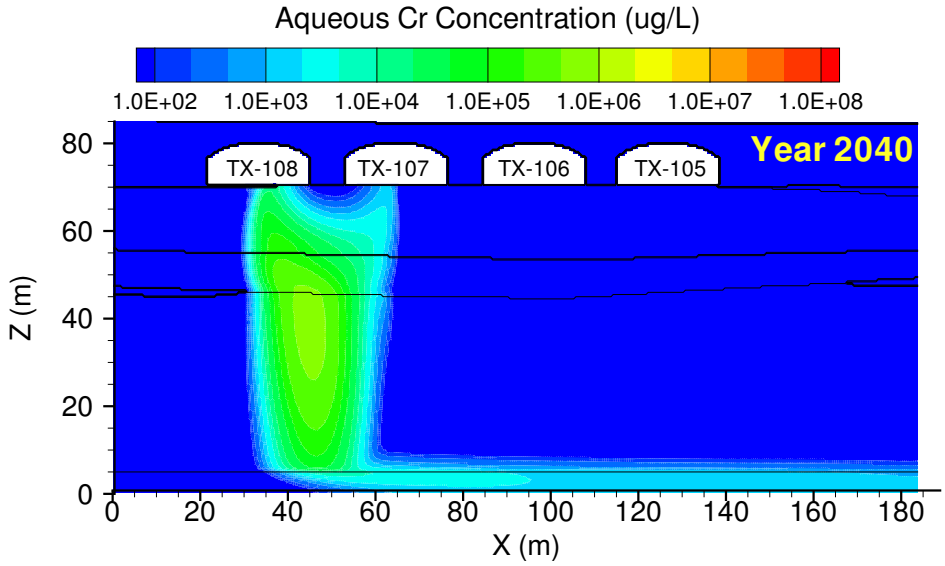

Figure C.27. TX Case 5, **Cr** aqueous concentration at year 2040. Year of maximum concentration at fenceline was 2057.

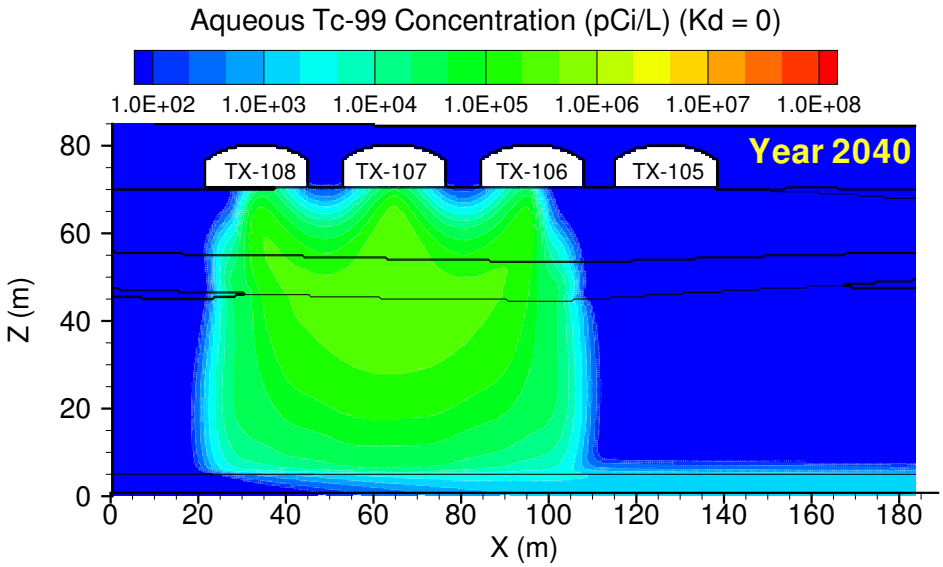

Figure C.28. TX Case 6, **Tc-99** aqueous concentration at year 2040. Year of maximum concentration at fenceline was 2066.

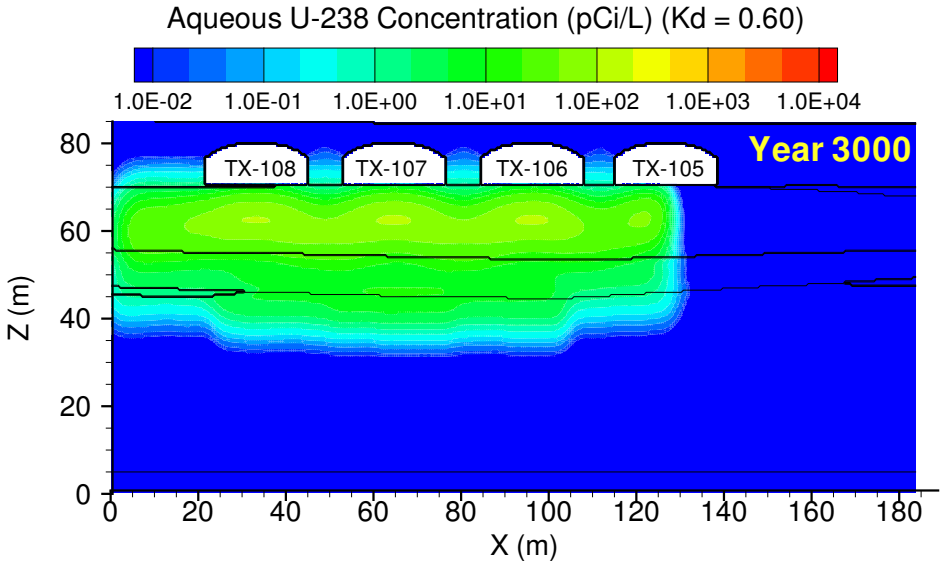

Figure C.29. TX Case 6, **U-238** (K_d = 0.60) aqueous concentration at year 3000. Year of maximum concentration at fenceline was 3000.

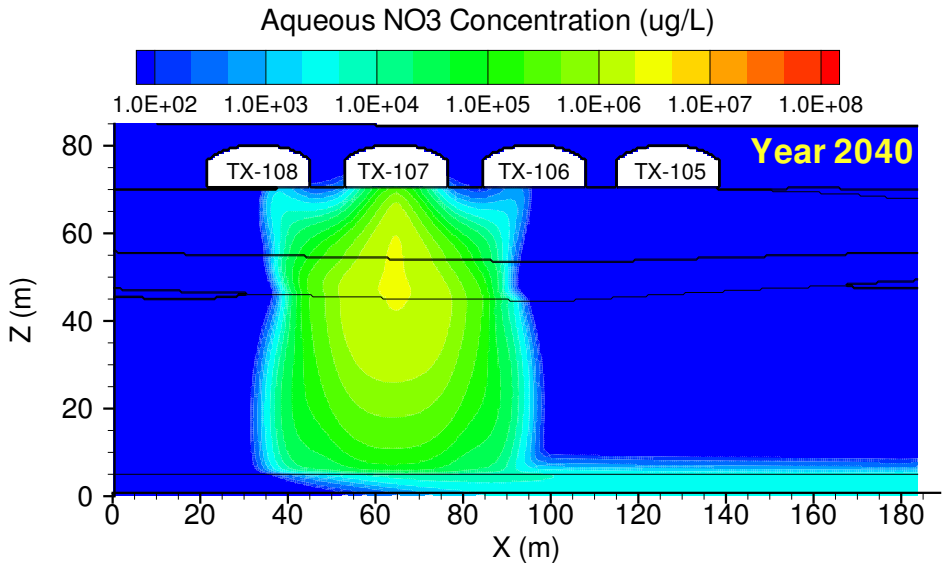

Figure C.30. TX Case 6, **NO_3** aqueous concentration at year 2040. Year of maximum concentration at fenceline was 2069.

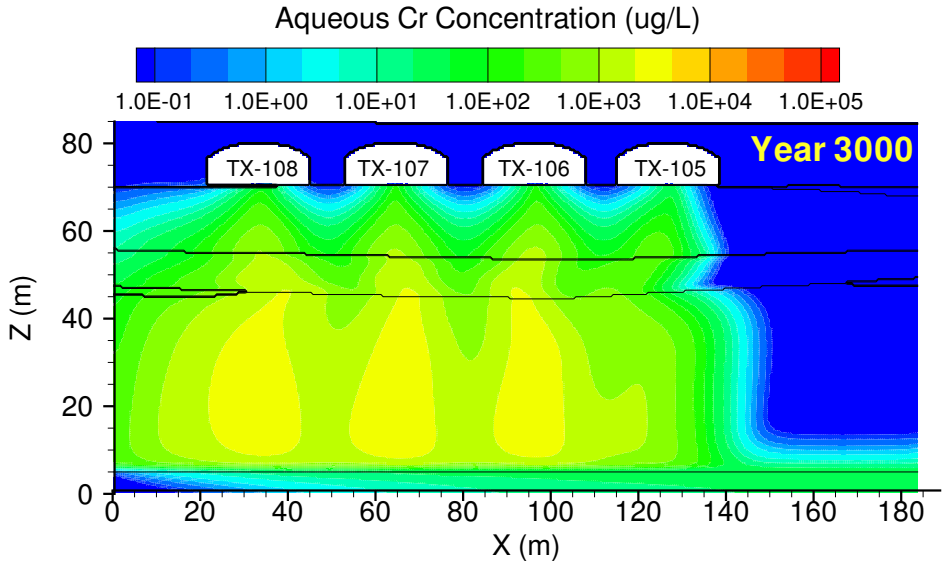

Figure C.31. TX Case 6, **Cr** aqueous concentration at year 3000. Year of maximum concentration at fenceline was 3000.

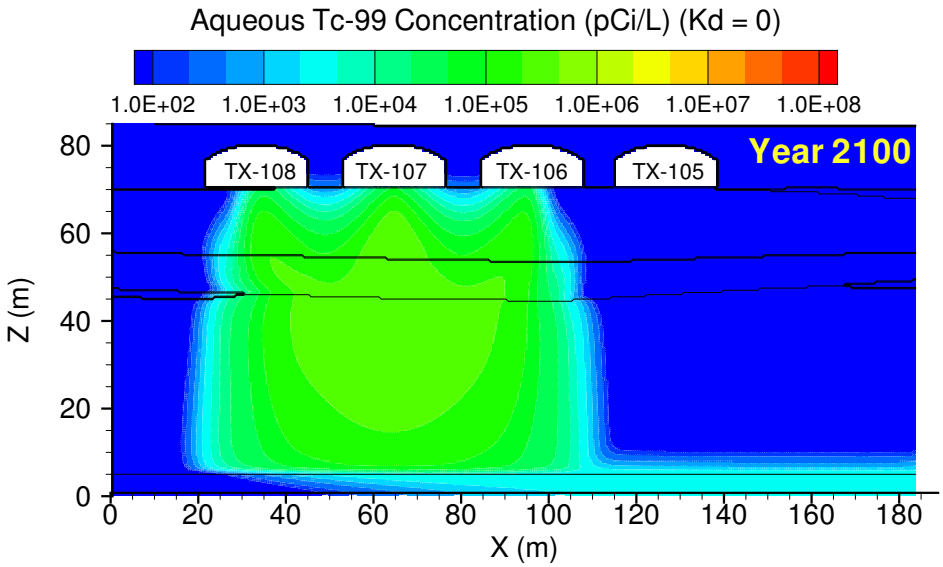

Figure C.32. TX Case 7, **Tc-99** aqueous concentration at year 2100. Year of maximum concentration at fenceline was 2085.

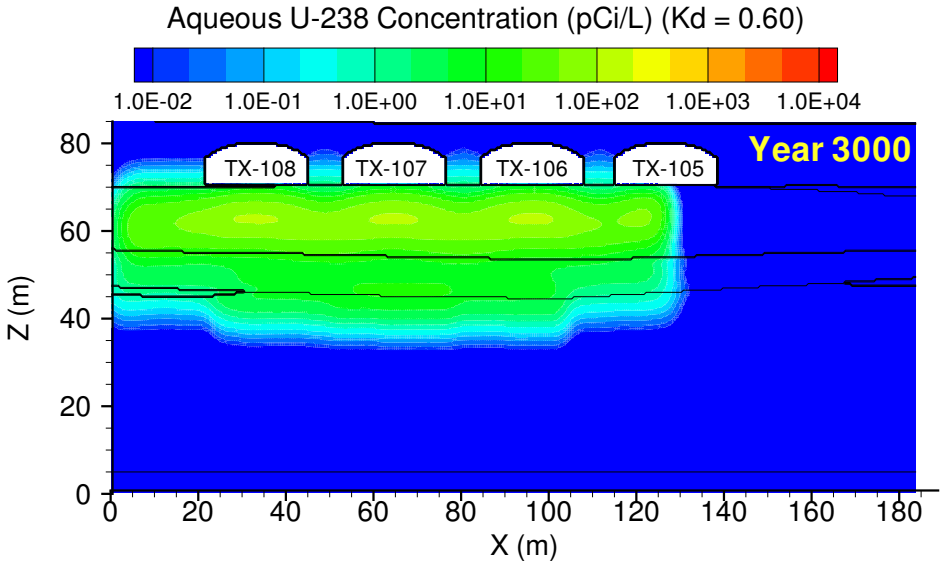

Figure C.33. TX Case 7, **U-238** (K_d = 0.60) aqueous concentration at year 3000. Year of maximum concentration at fenceline was 3000.

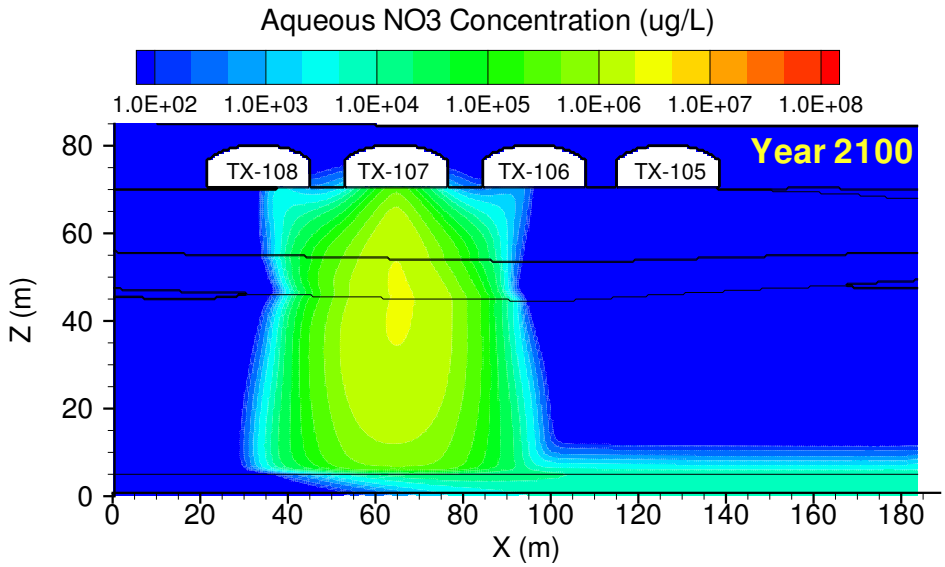

Figure C.34. TX Case 7, **NO_3** aqueous concentration at year 2100. Year of maximum concentration at fenceline was 2092.

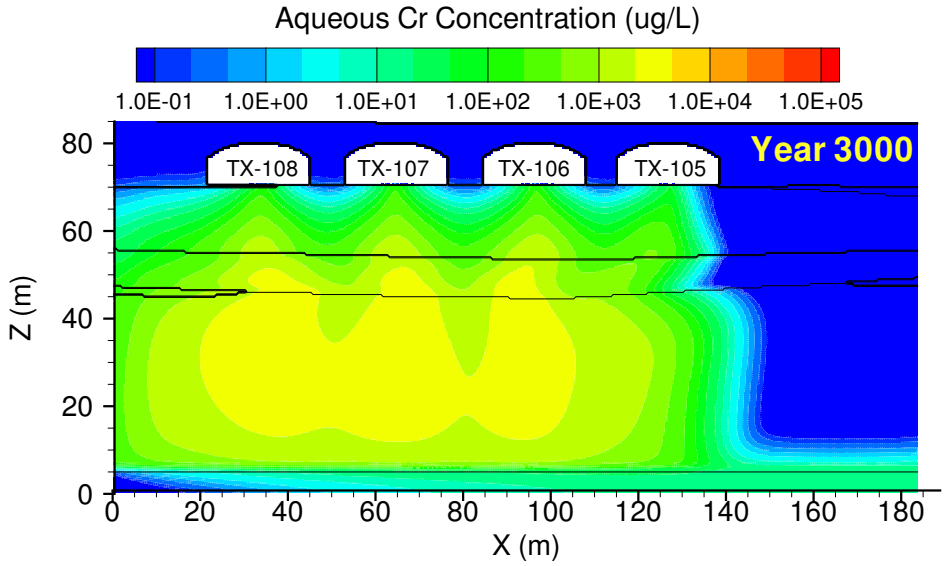

Figure C.35. TX Case 7, **Cr** aqueous concentration at year 3000. Year of maximum concentration at fenceline was 3000.

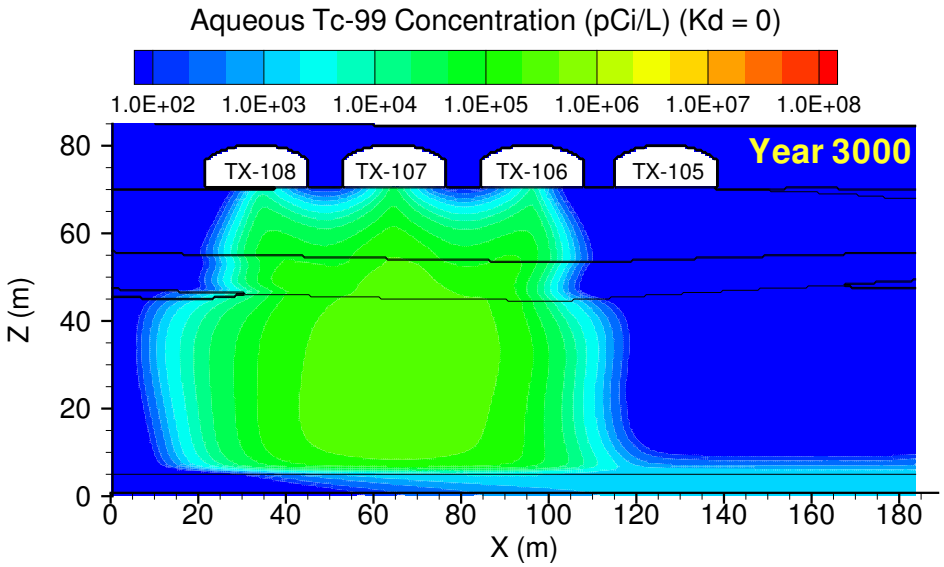

Figure C.36. TX Case 8, **Tc-99** aqueous concentration at year 3000. Year of maximum concentration at fenceline was 3000.

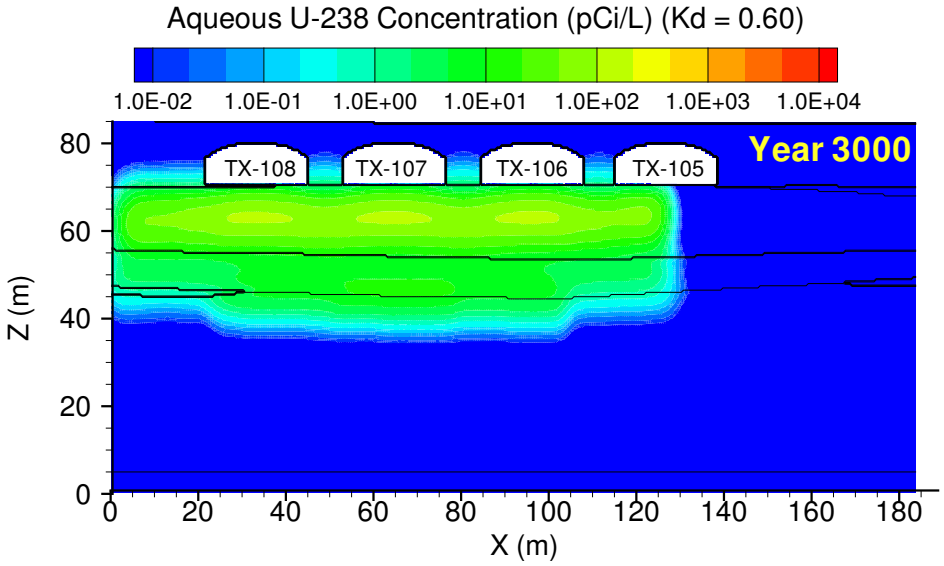

Figure C.37. TX Case 8, **U-238** (K_d = 0.60) aqueous concentration at year 3000. Year of maximum concentration at fenceline was 3000.

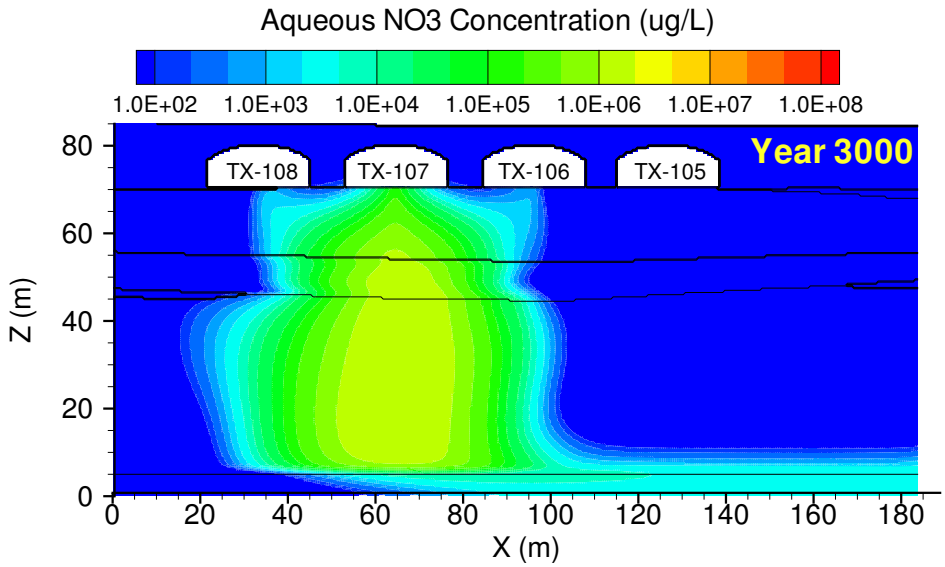

Figure C.38. TX Case 8, **NO_3** aqueous concentration at year 3000. Year of maximum concentration at fenceline was 3000.

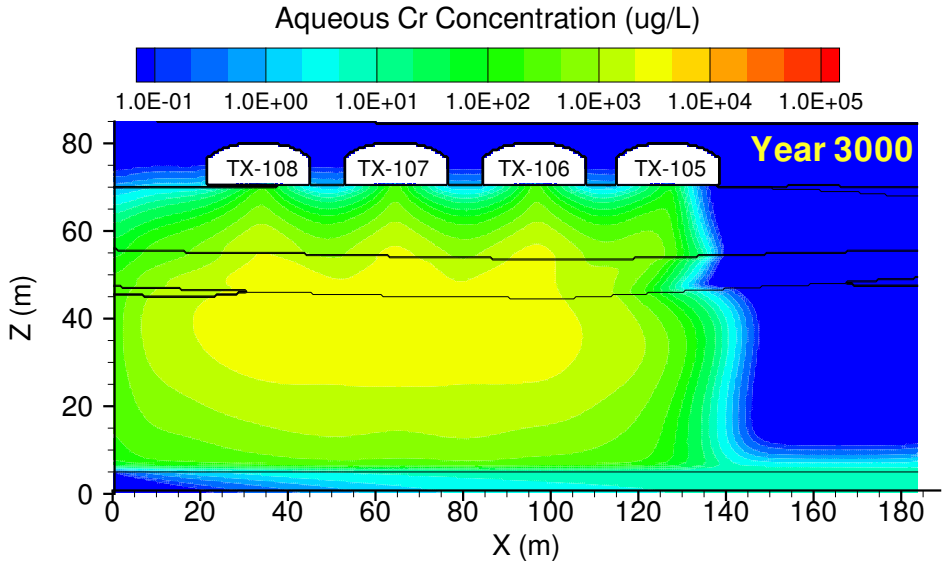

Figure C.39. TX Case 8, **Cr** aqueous concentration at year 3000. Year of maximum concentration at fenceline was 3000.

Appendix D

TX Tank Farm
Contaminant Breakthrough Curves

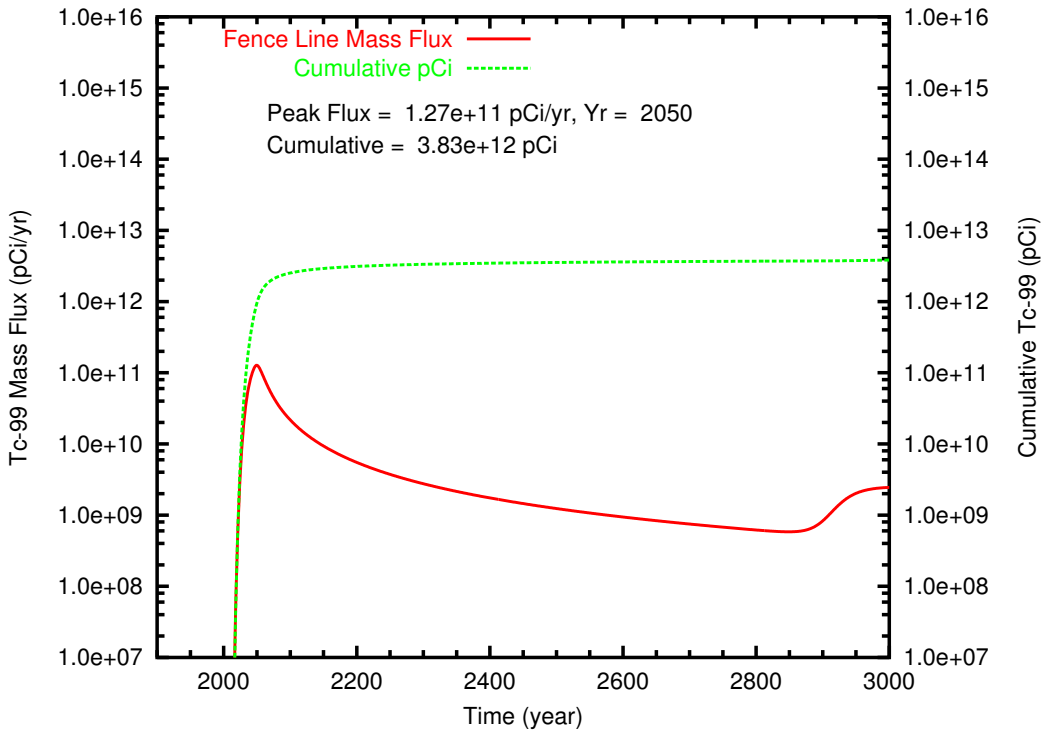

Figure D.1. TX Case 1 **Tc-99** mass flux and cumulative mass at fenceline

(a)

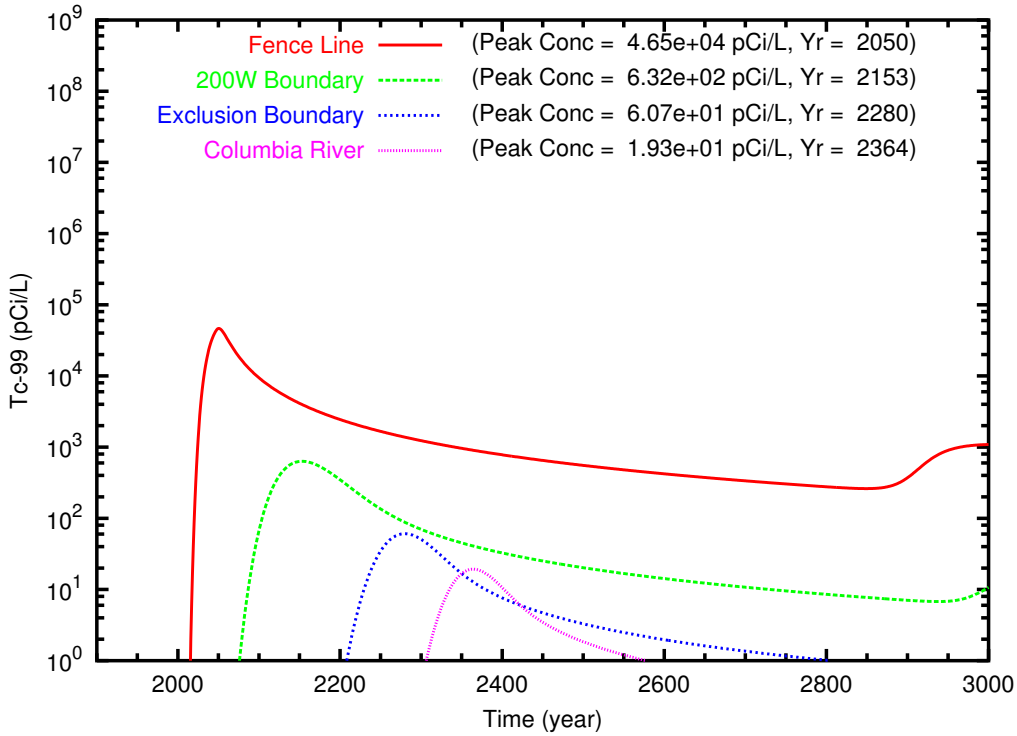

(b)

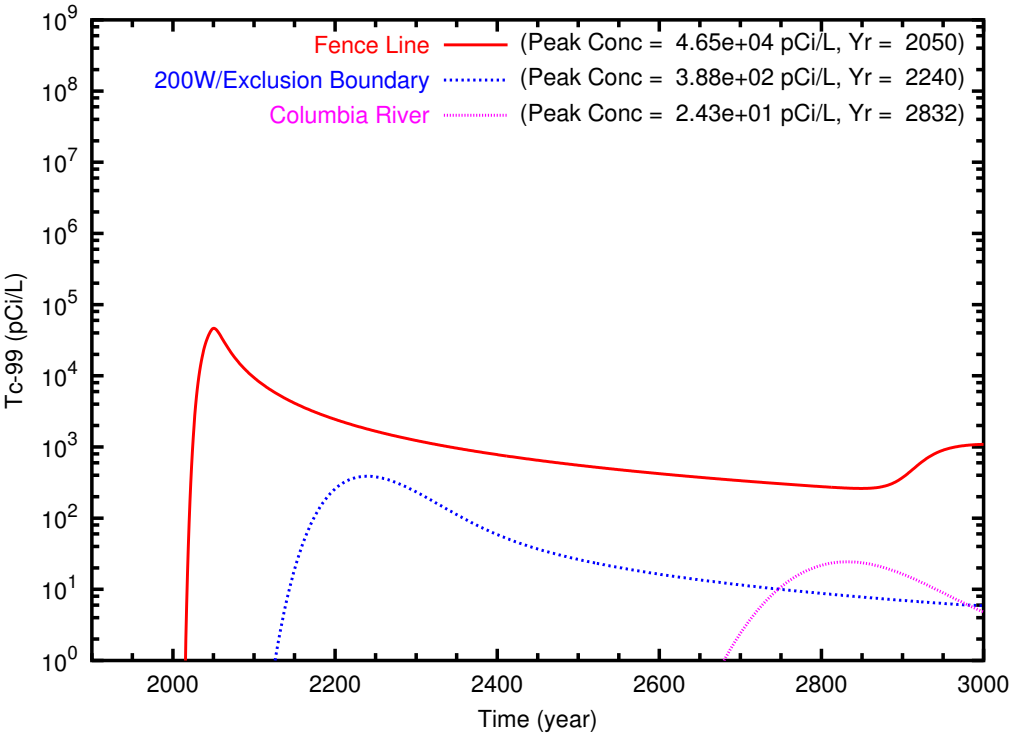

Figure D.2. TX Case 1 **Tc-99** breakthrough curves at fenceline and downgradient points along (a) east path and (b) north path

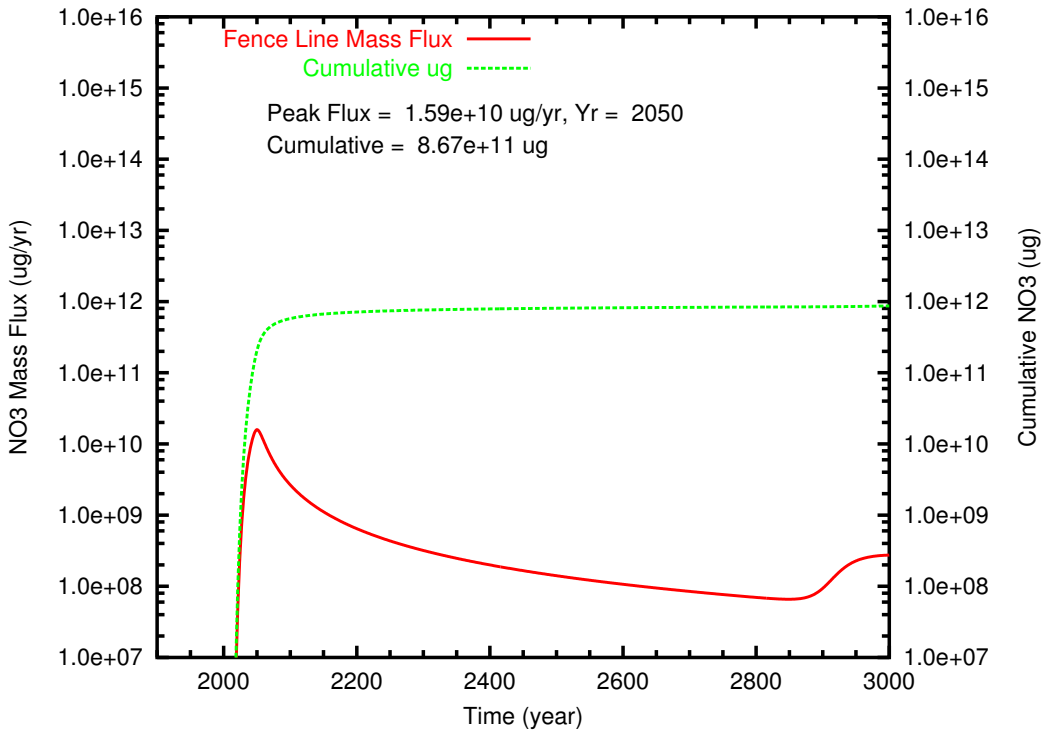

Figure D.3. TX Case 1 $\mathbf{NO_3}$ mass flux and cumulative mass at fenceline

(a)

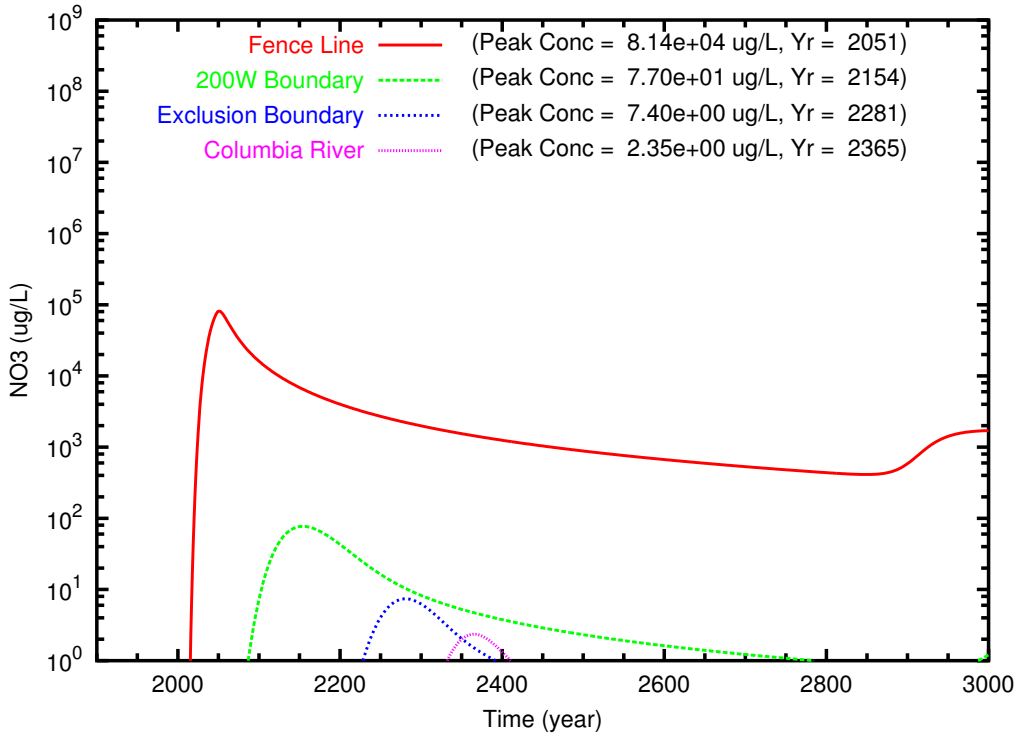

(b)

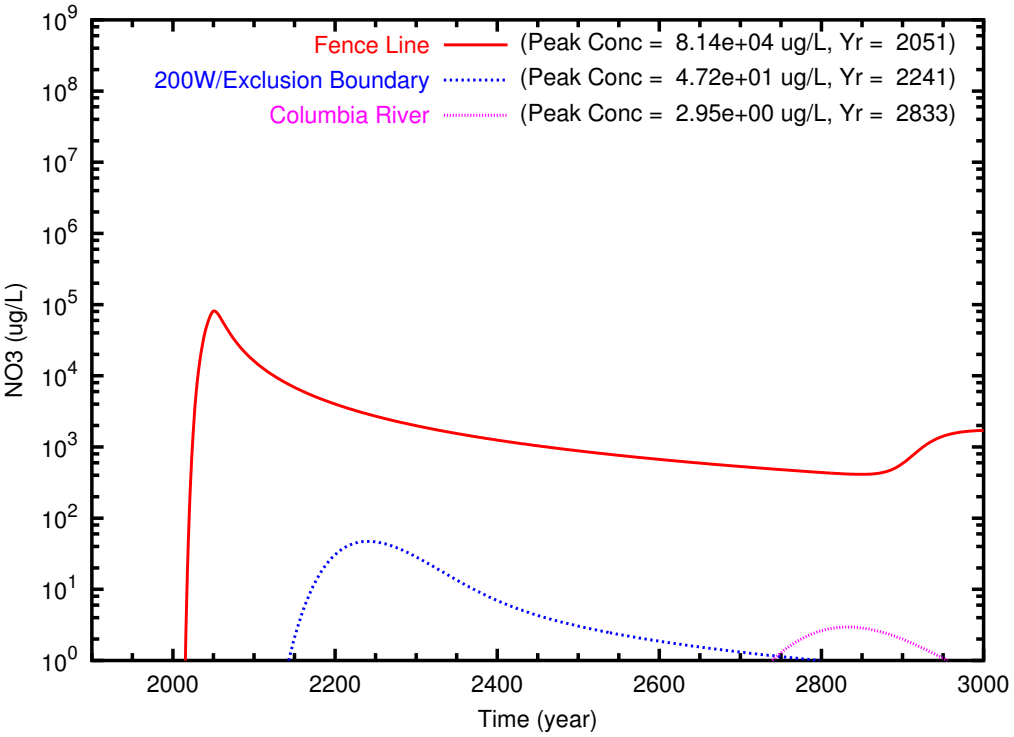

Figure D.4. TX Case 1 **NO_3** breakthrough curves at fenceline and downgradient points along (a) east path and (b) north path

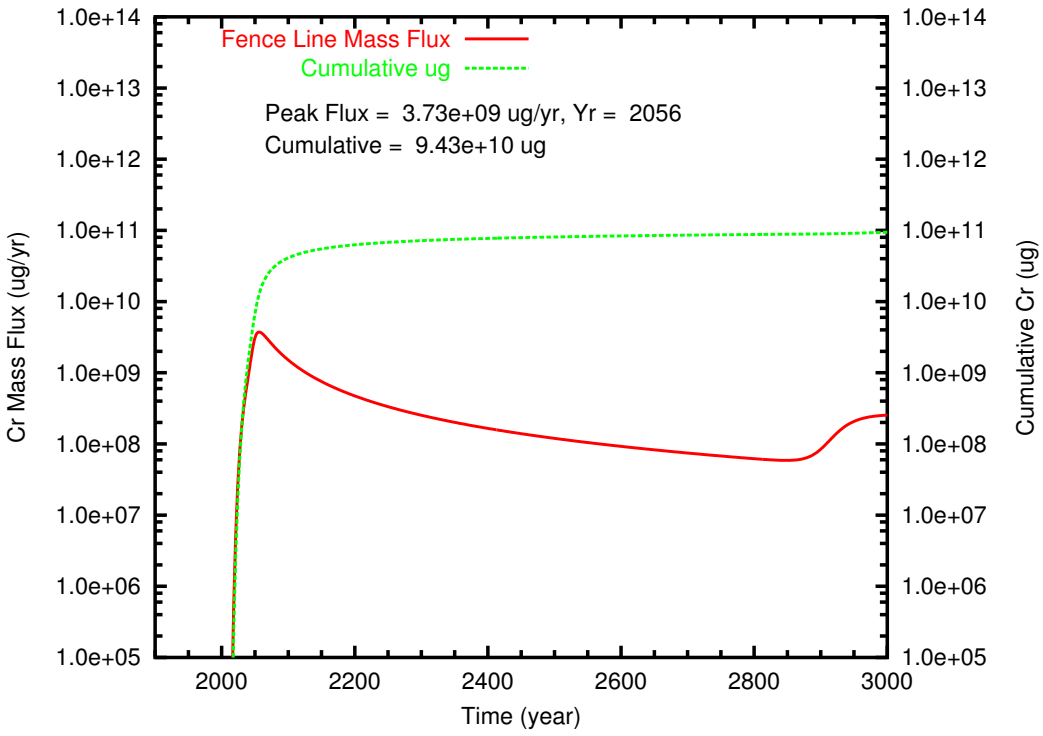

Figure D.5. TX Case 1 **Cr** mass flux and cumulative mass at fenceline

(a)

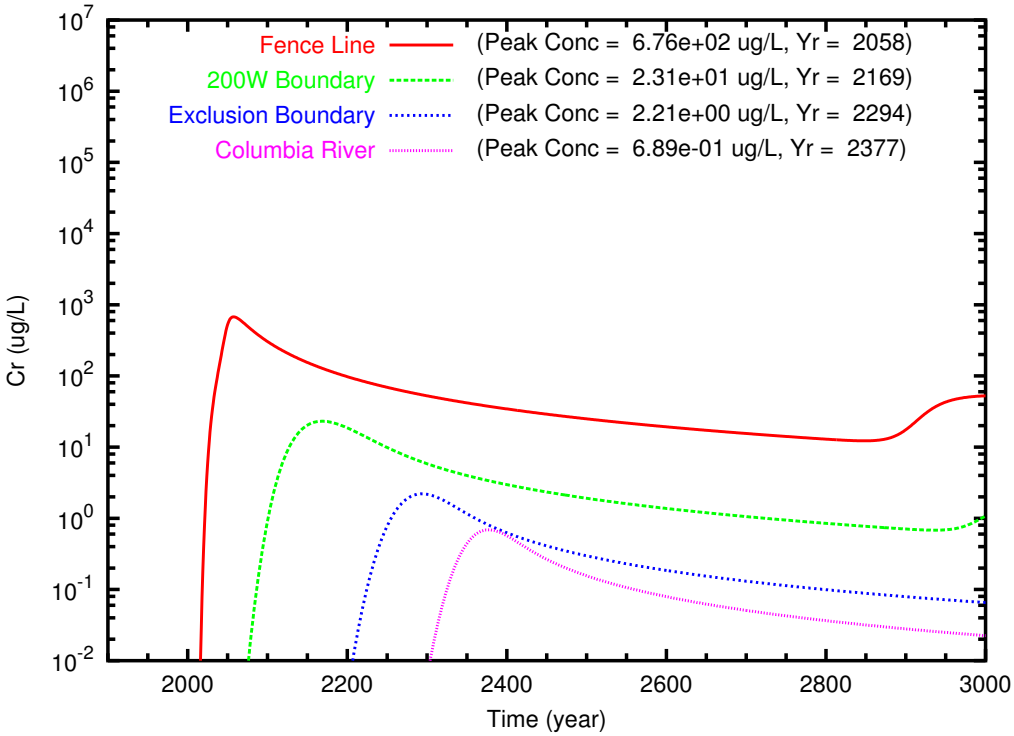

(b)

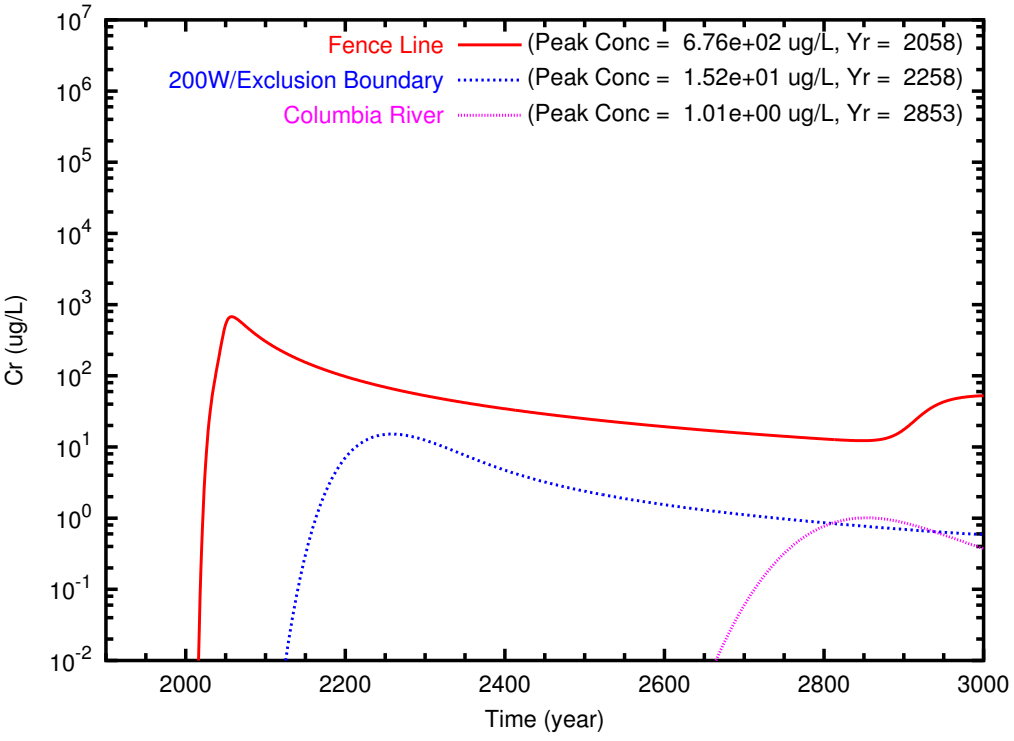

Figure D.6. TX Case 1 **Cr** breakthrough curves at fenceline and downgradient points along (a) east path and (b) north path

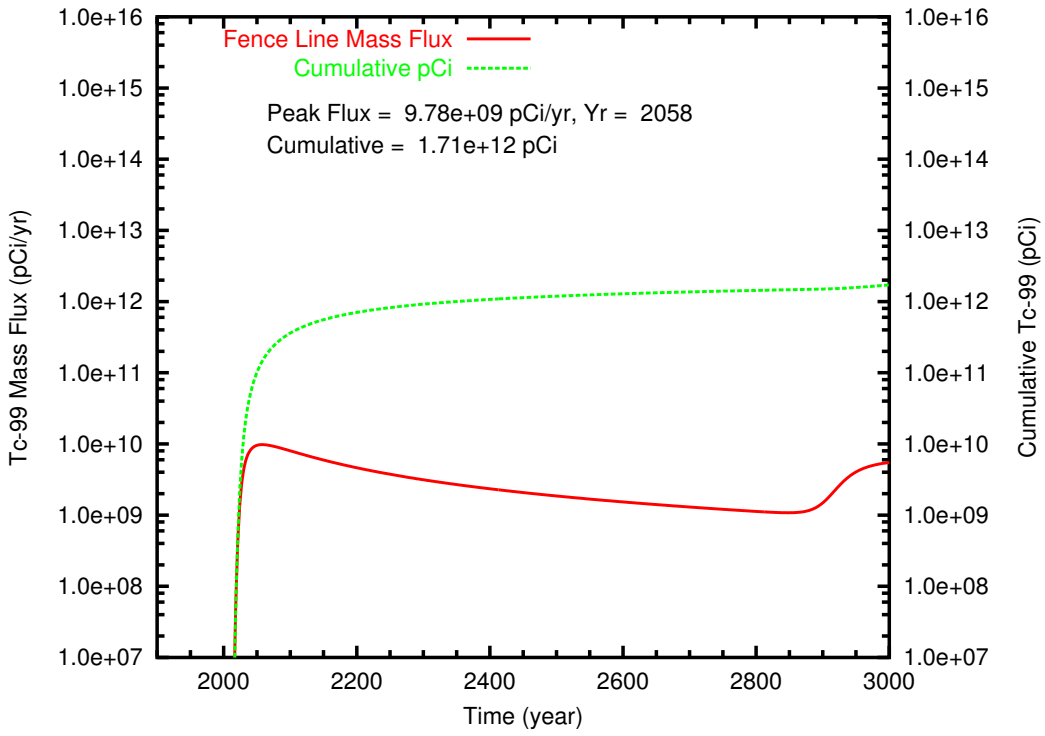

Figure D.7. TX Case 2 **Tc-99** mass flux and cumulative mass at fenceline

(a)

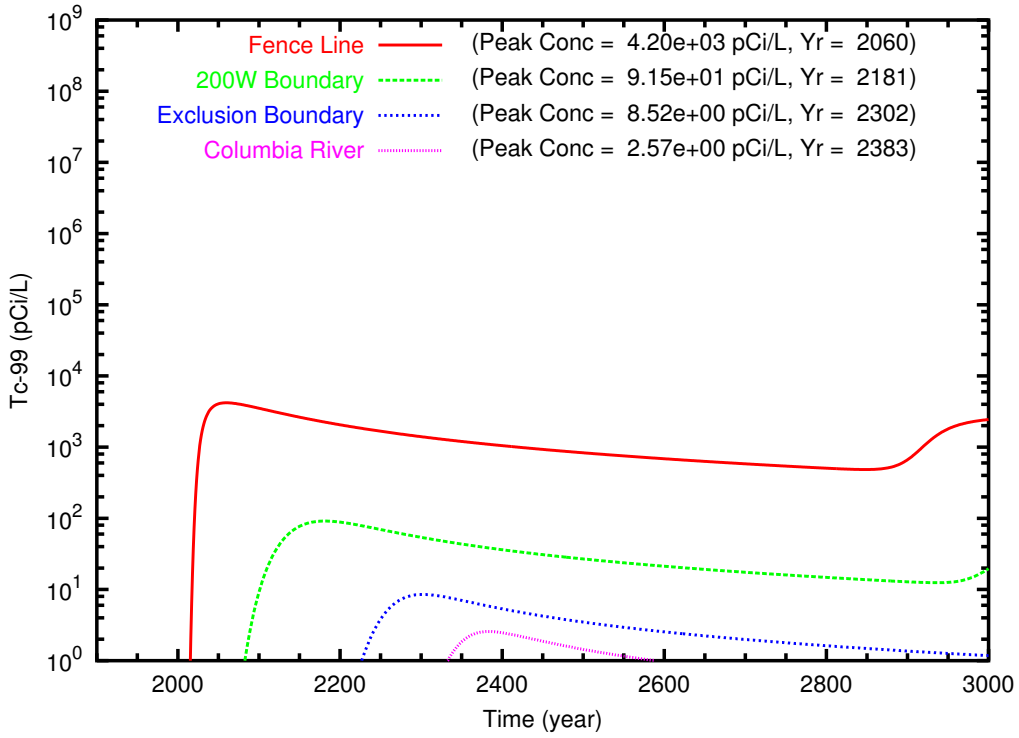

(b)

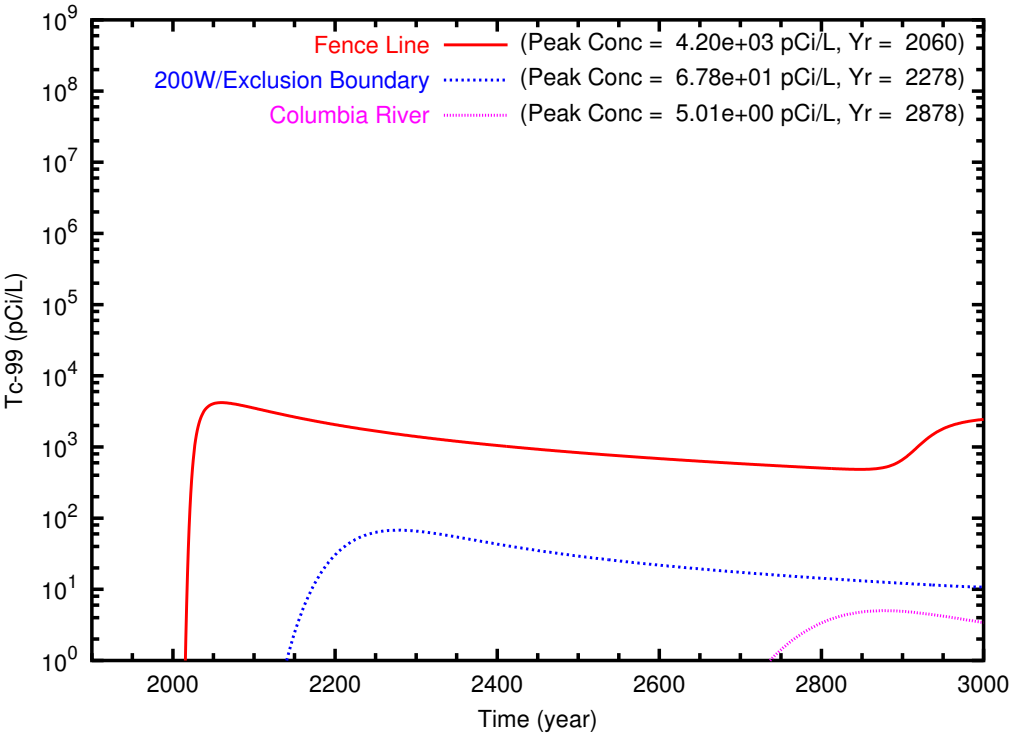

Figure D.8. TX Case 2 **Tc-99** breakthrough curves at fenceline and downgradient points along (a) east path and (b) north path

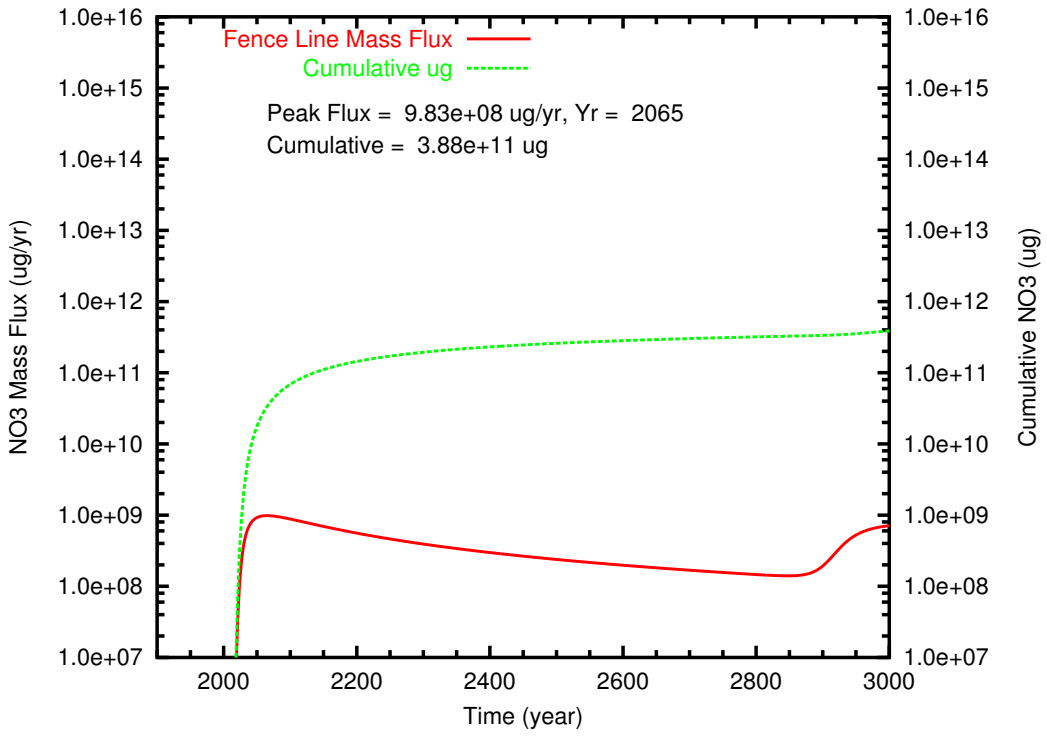

Figure D.9. TX Case 2 $\mathbf{NO_3}$ mass flux and cumulative mass at fenceline

(a)

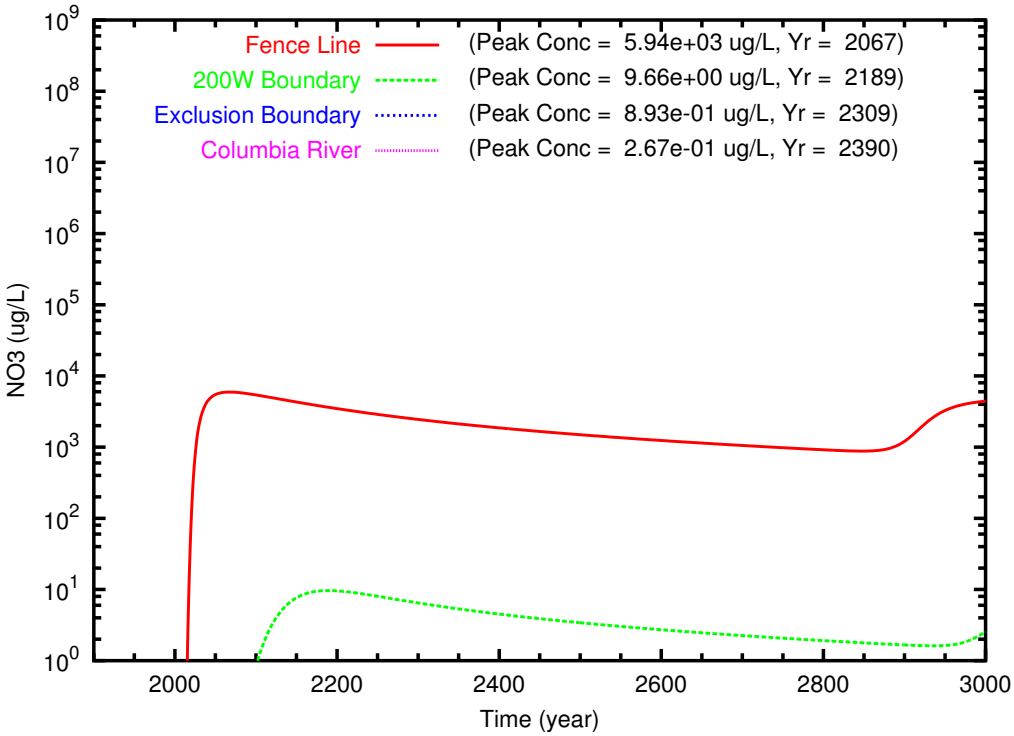

(b)

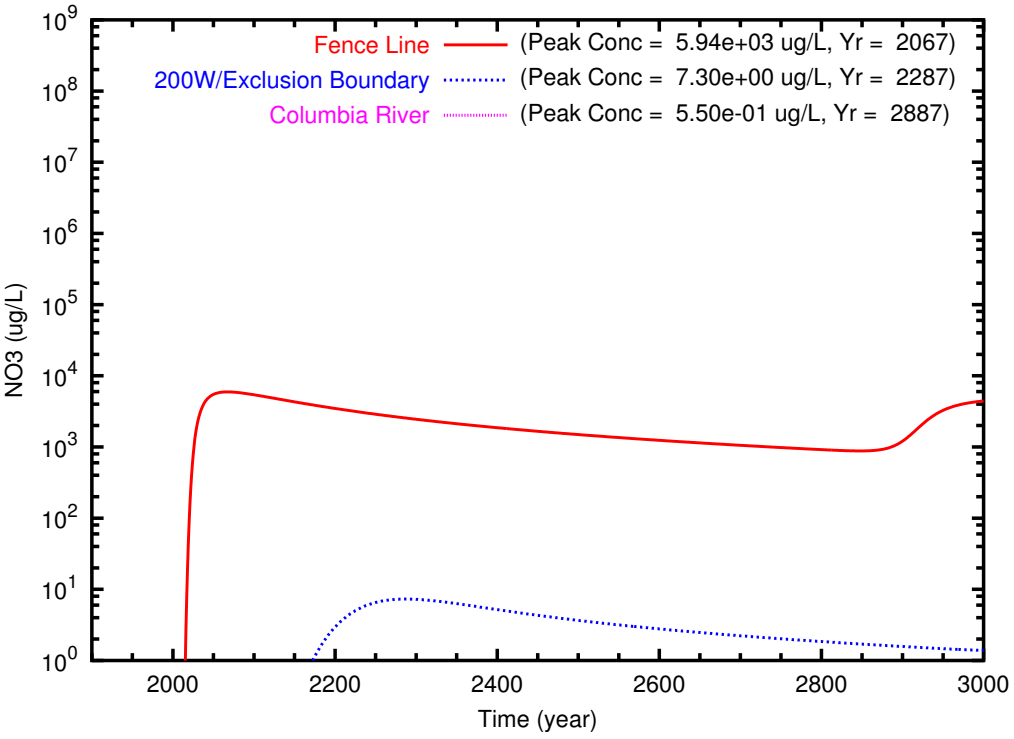

Figure D.10. TX Case 2 **NO_3** breakthrough curves at fenceline and downgradient points along (a) east path and (b) north path

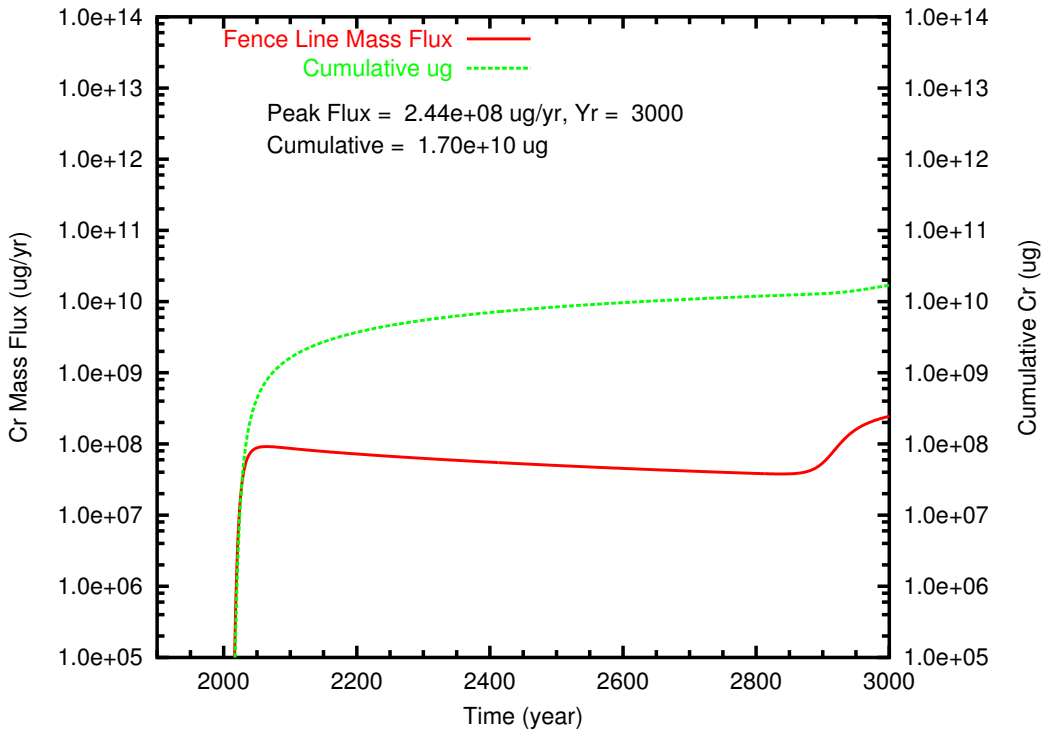

Figure D.11. TX Case 2 **Cr** mass flux and cumulative mass at fenceline

(a)

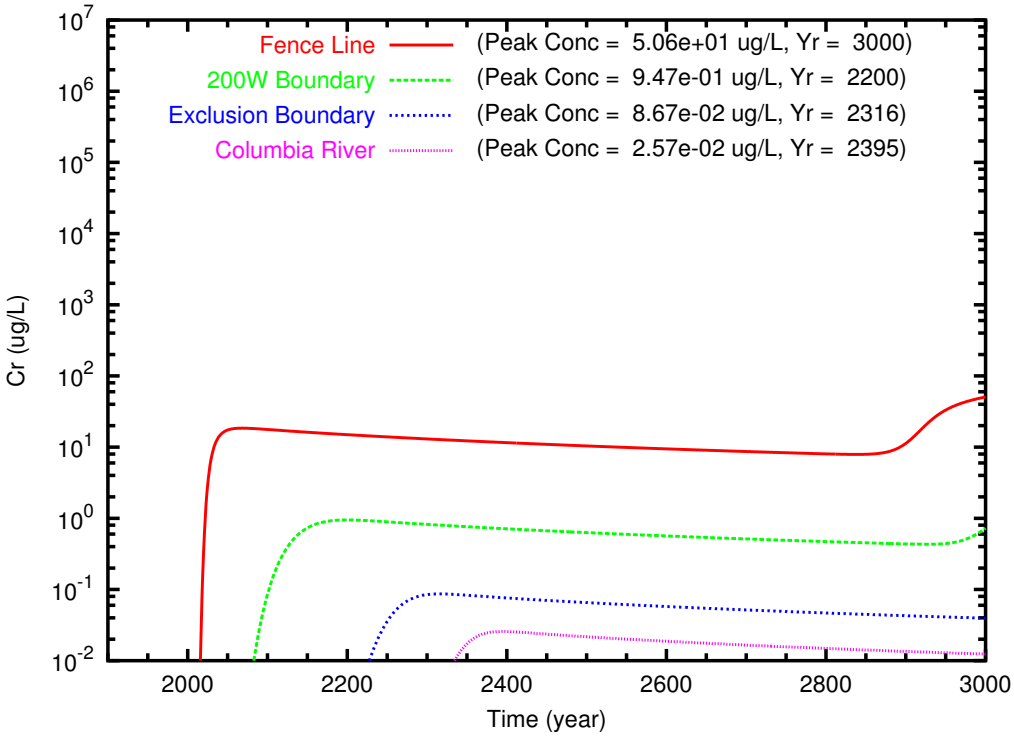

(b)

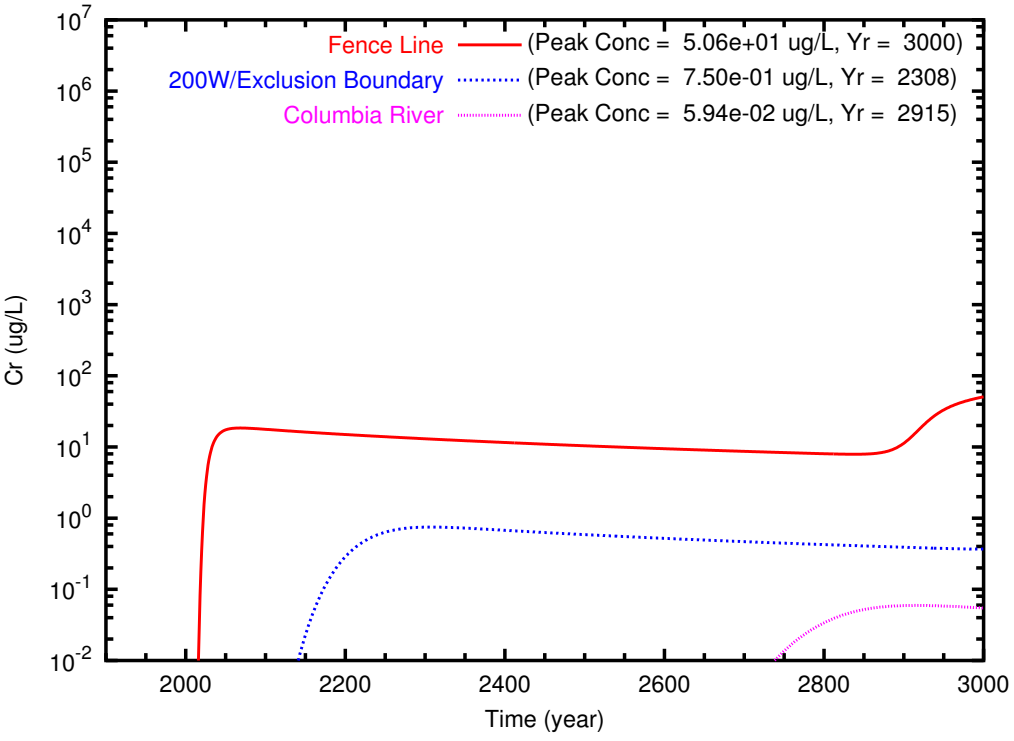

Figure D.12. TX Case 2 **Cr** breakthrough curves at fenceline and downgradient points along (a) east path and (b) north path

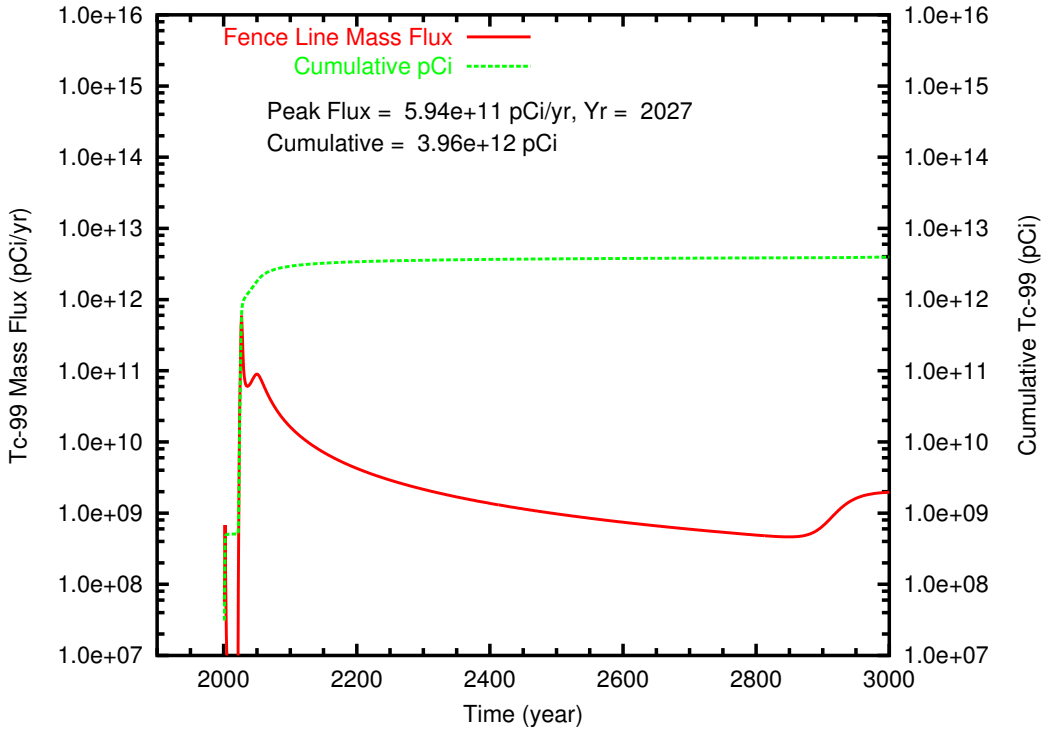

Figure D.13. TX Case 3 **Tc-99** mass flux and cumulative mass at fenceline

(a)

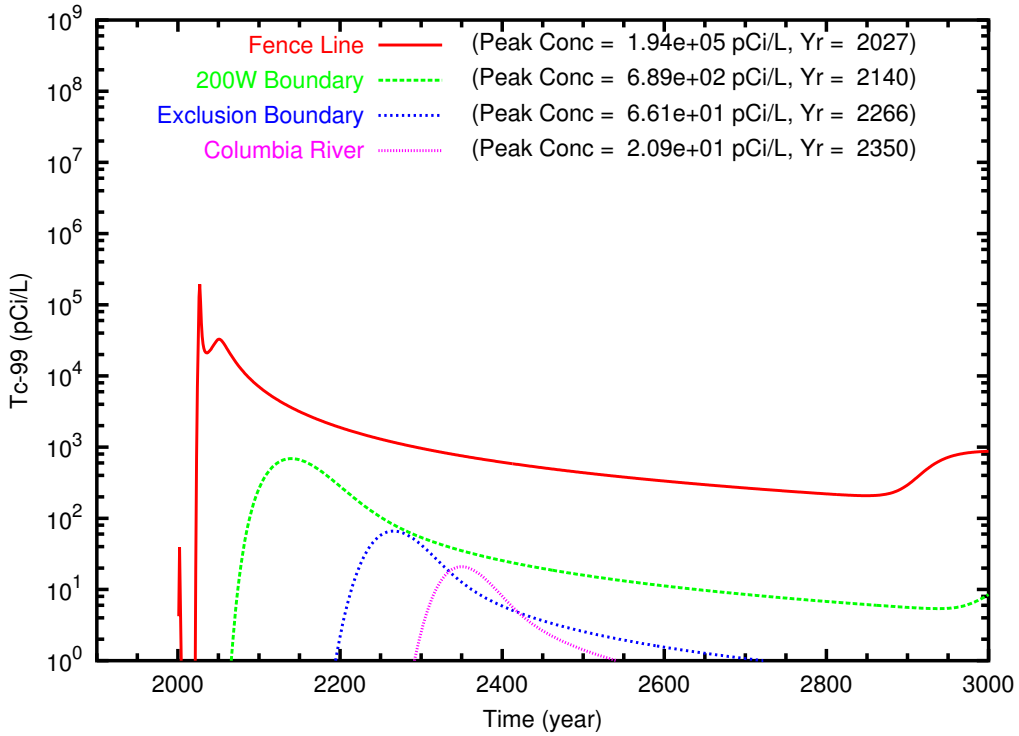

(b)

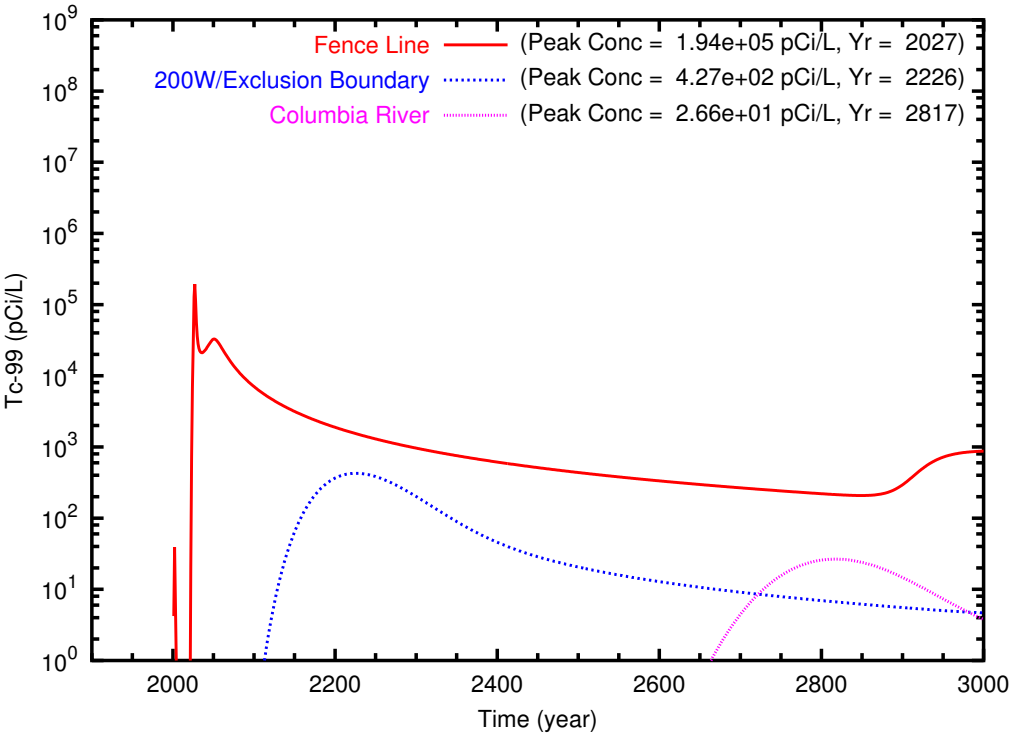

Figure D.14. TX Case 3 **Tc-99** breakthrough curves at fenceline and downgradient points along (a) east path and (b) north path

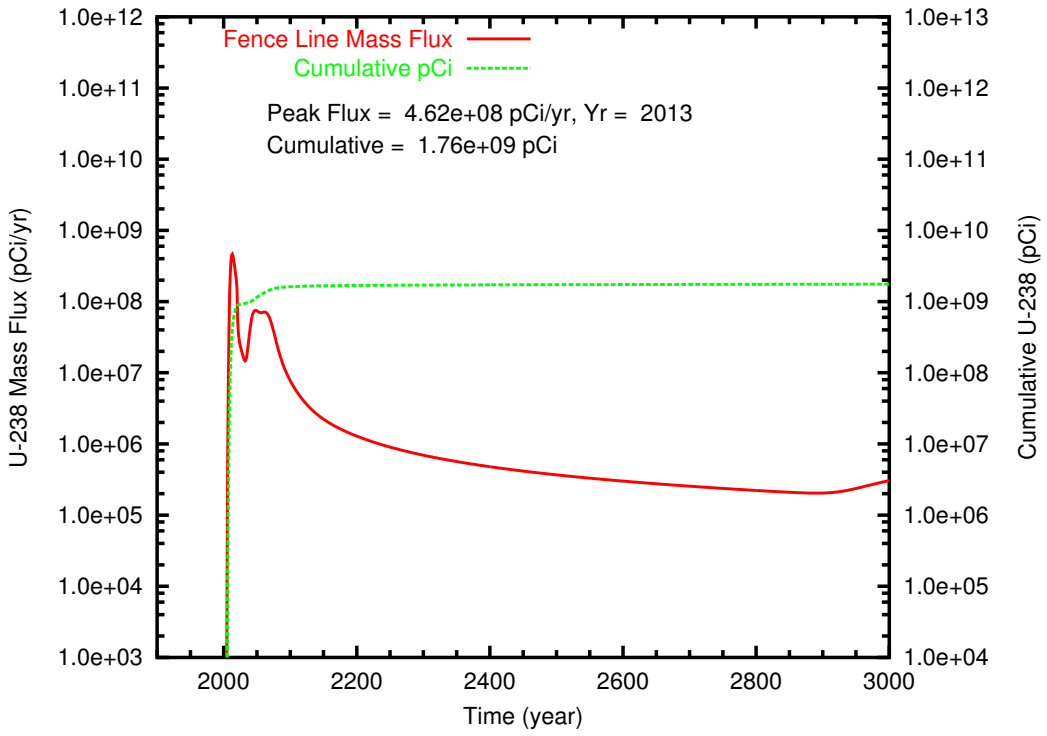

Figure D.15. TX Case 3 **U-238** (K_d = 0.60) mass flux and cumulative mass at fenceline

(a)

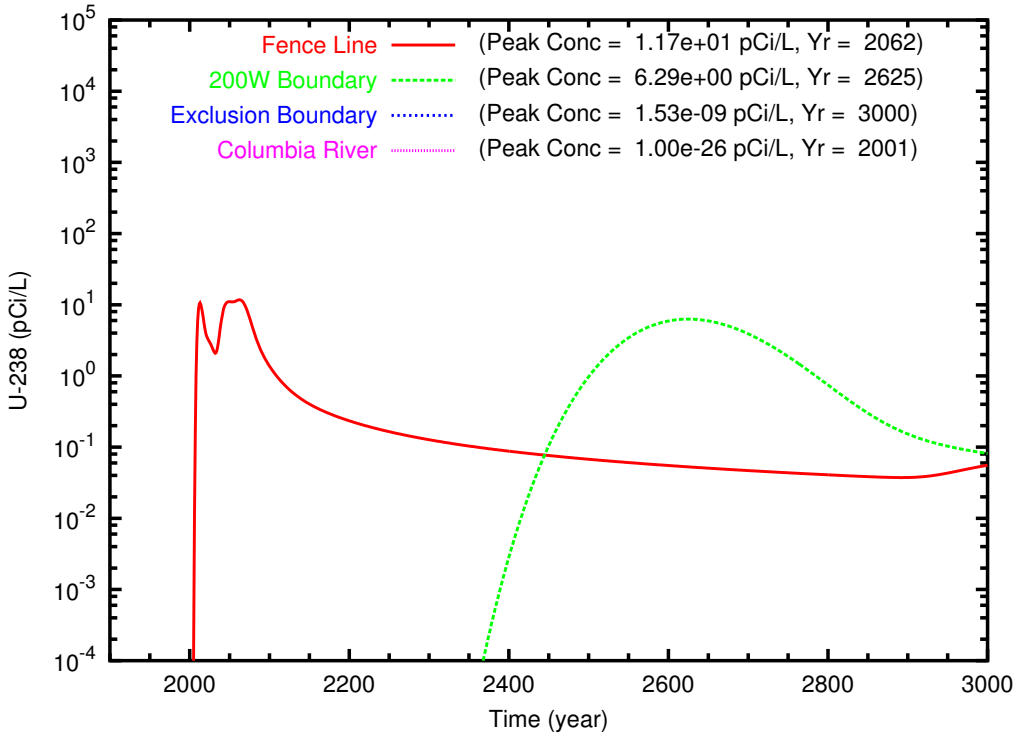

(b)

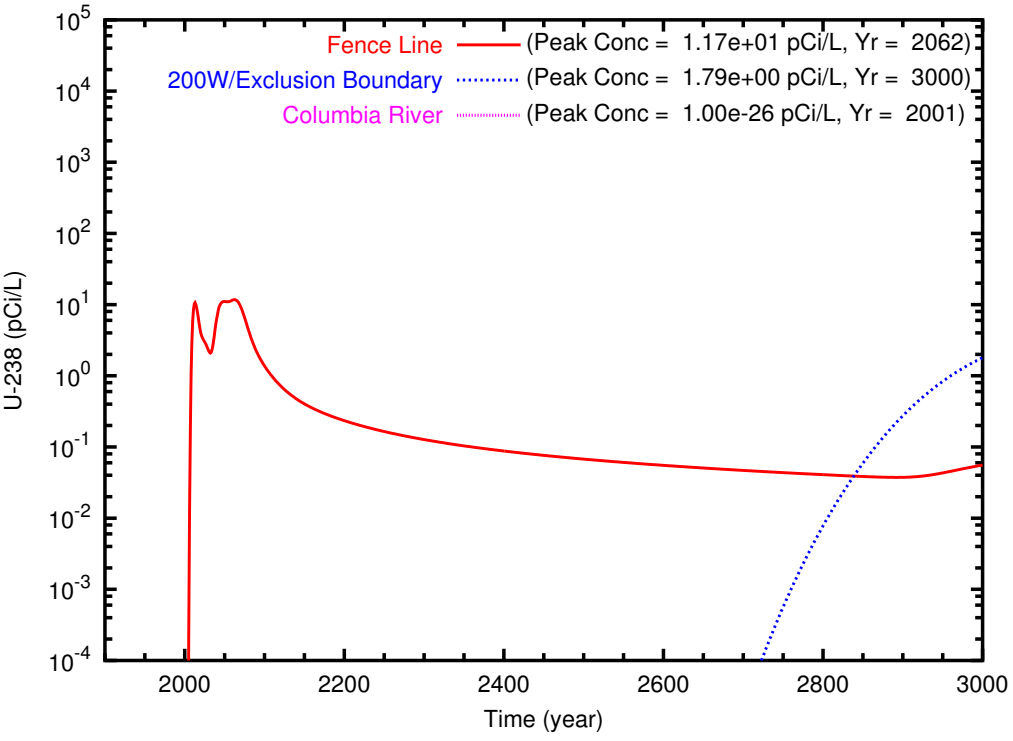

Figure D.16. TX Case 3 **U-238** (K_d = 0.60) breakthrough curves at fenceline and downgradient points along (a) east path and (b) north path

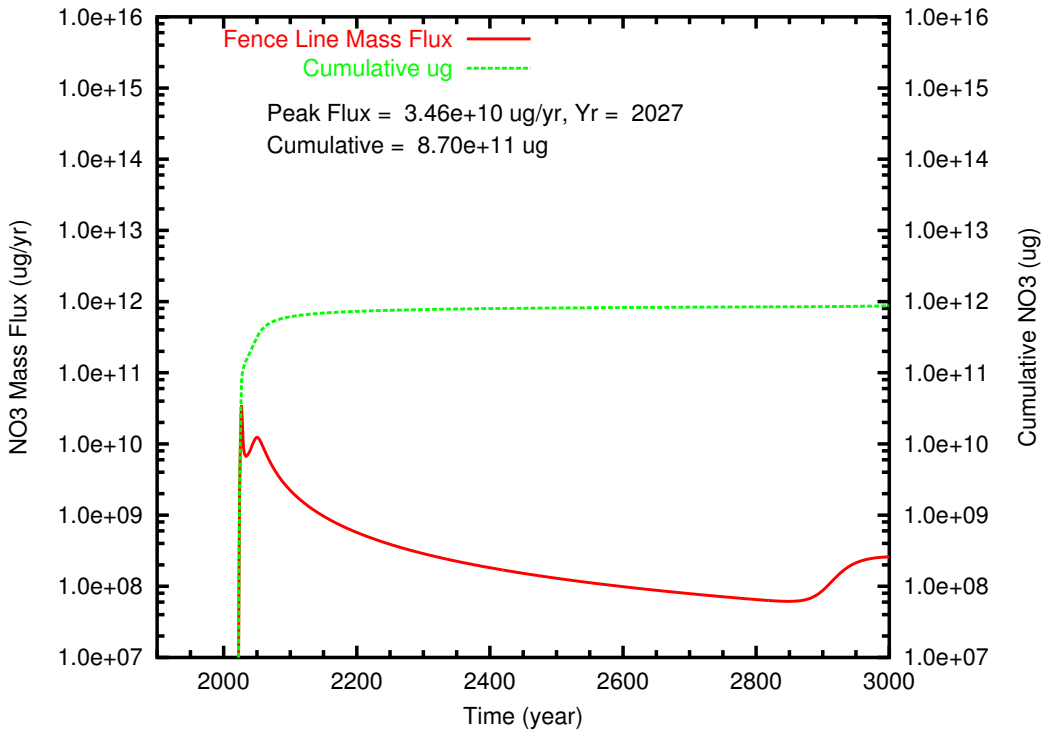

Figure D.17. TX Case 3 $\mathbf{NO_3}$ mass flux and cumulative mass at fenceline

(a)

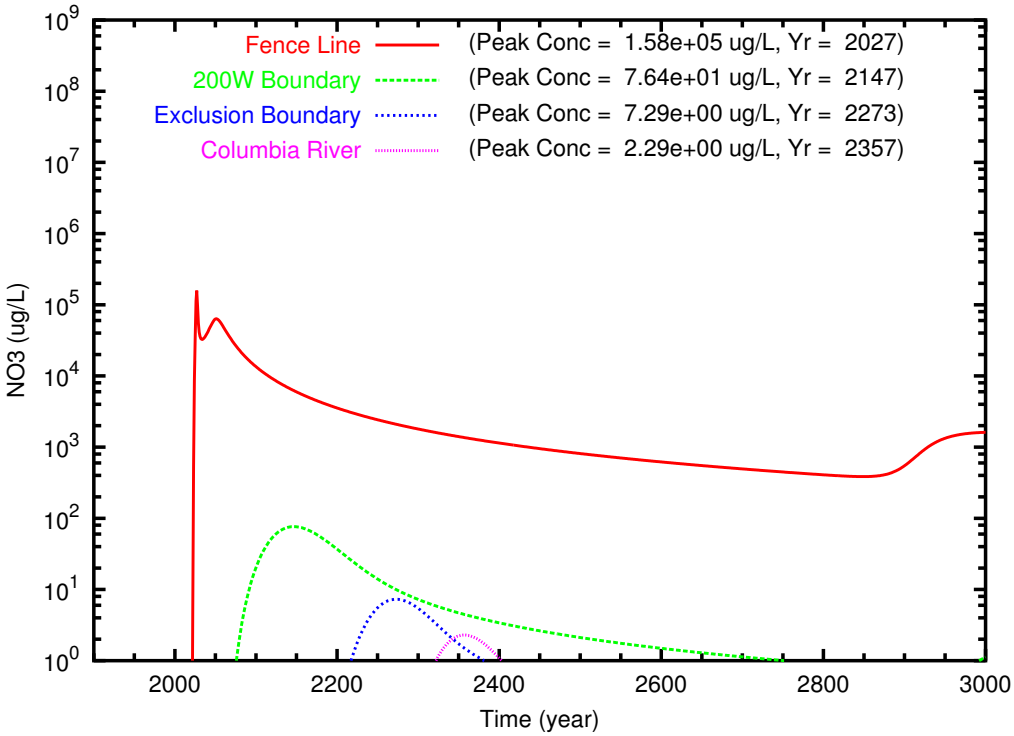

(b)

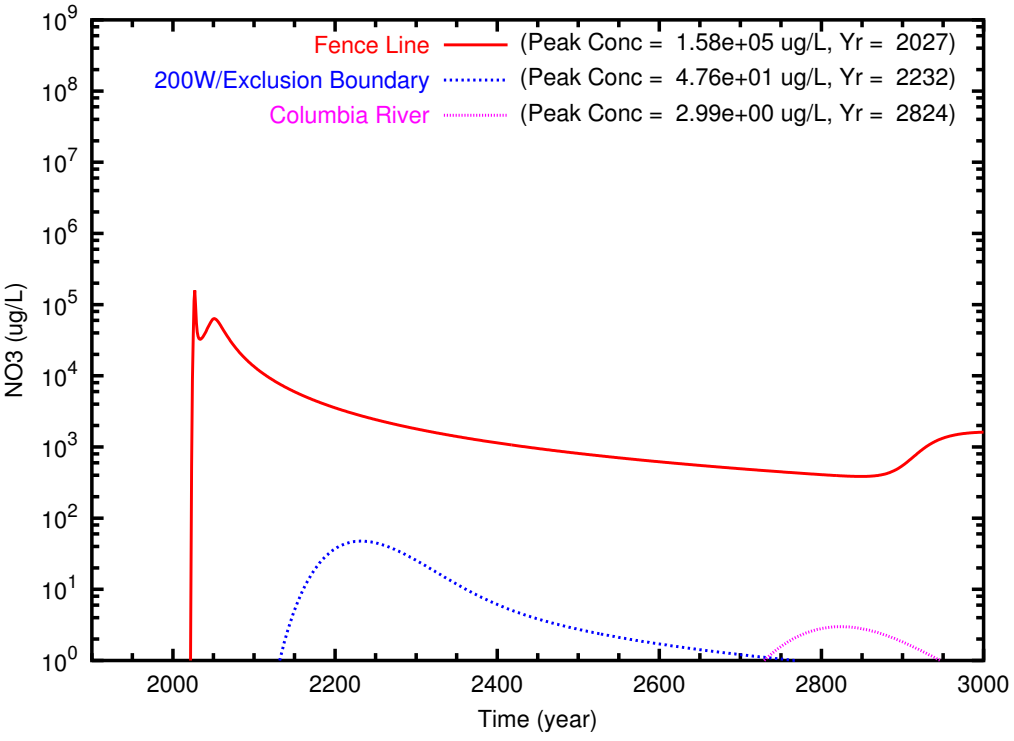

Figure D.18. TX Case 3 **NO_3** breakthrough curves at fenceline and downgradient points along (a) east path and (b) north path

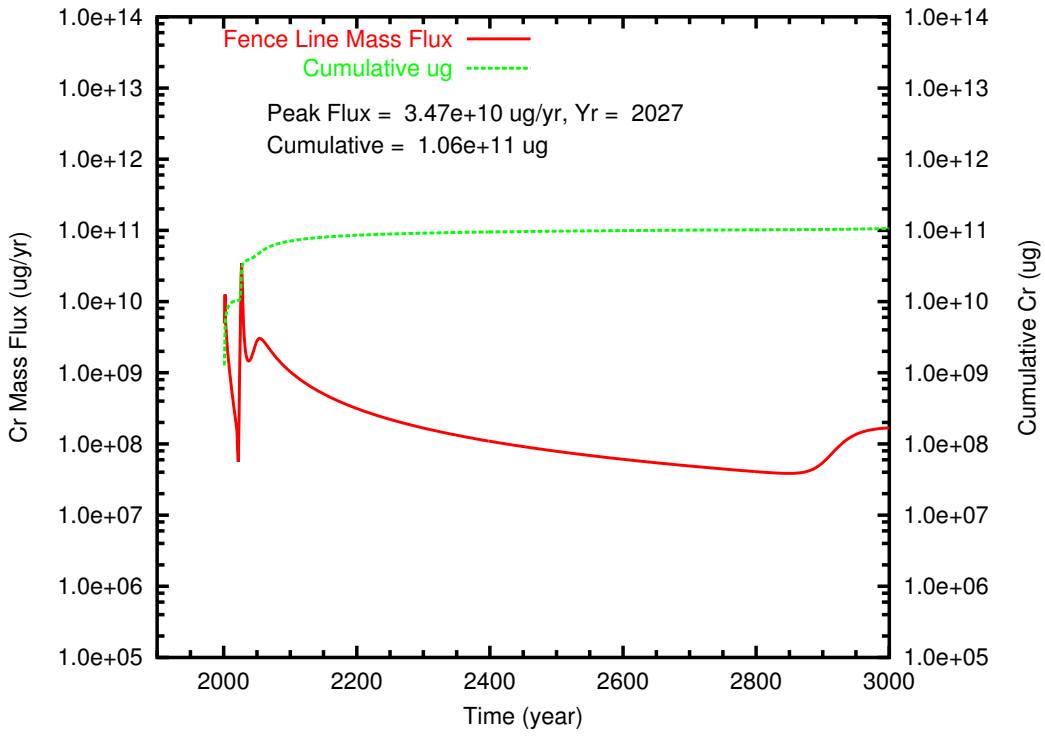

Figure D.19. TX Case 3 **Cr** mass flux and cumulative mass at fenceline

(a)

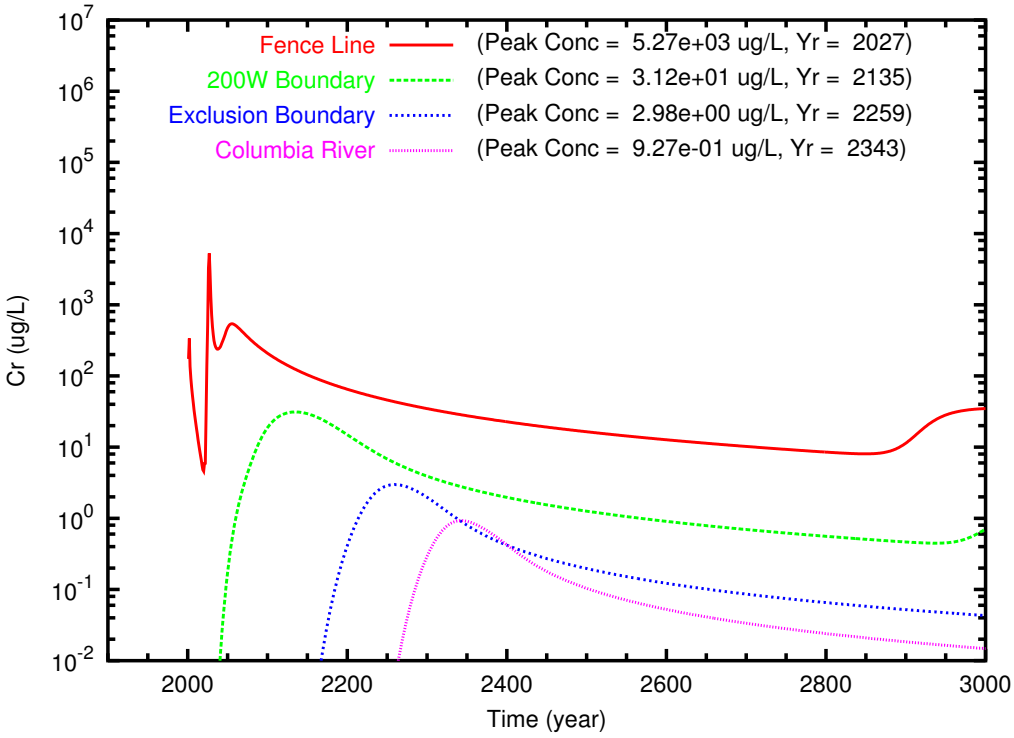

(b)

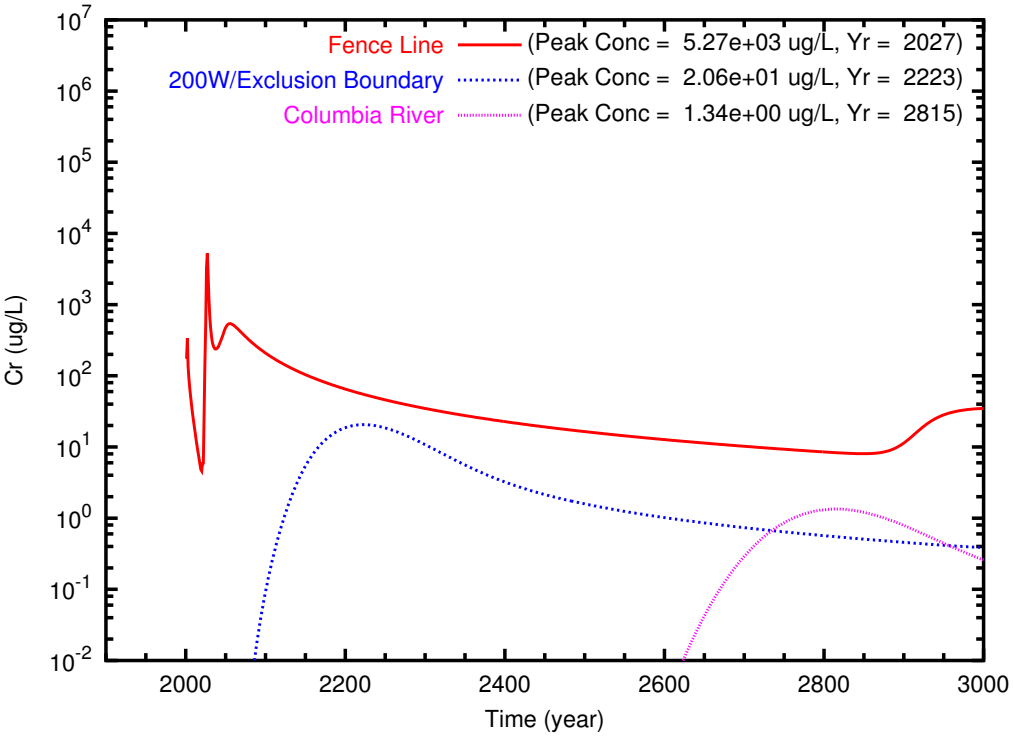

Figure D.20. TX Case 3 **Cr** breakthrough curves at fenceline and downgradient points along (a) east path and (b) north path

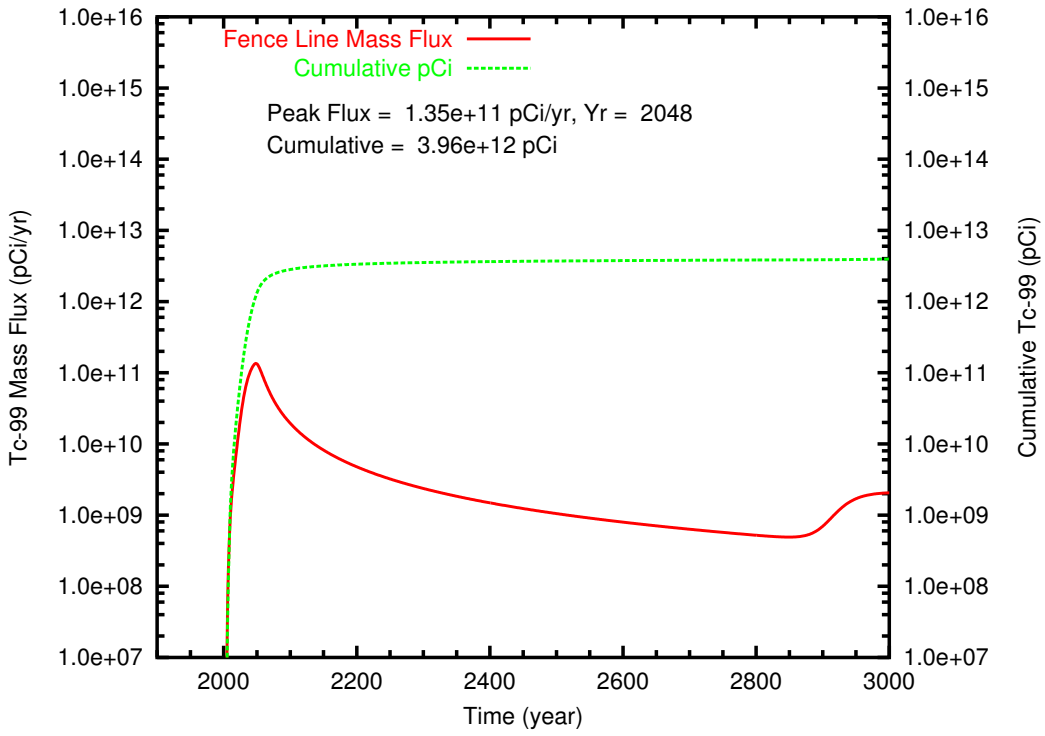

Figure D.21. TX Case 4 **Tc-99** mass flux and cumulative mass at fenceline

(a)

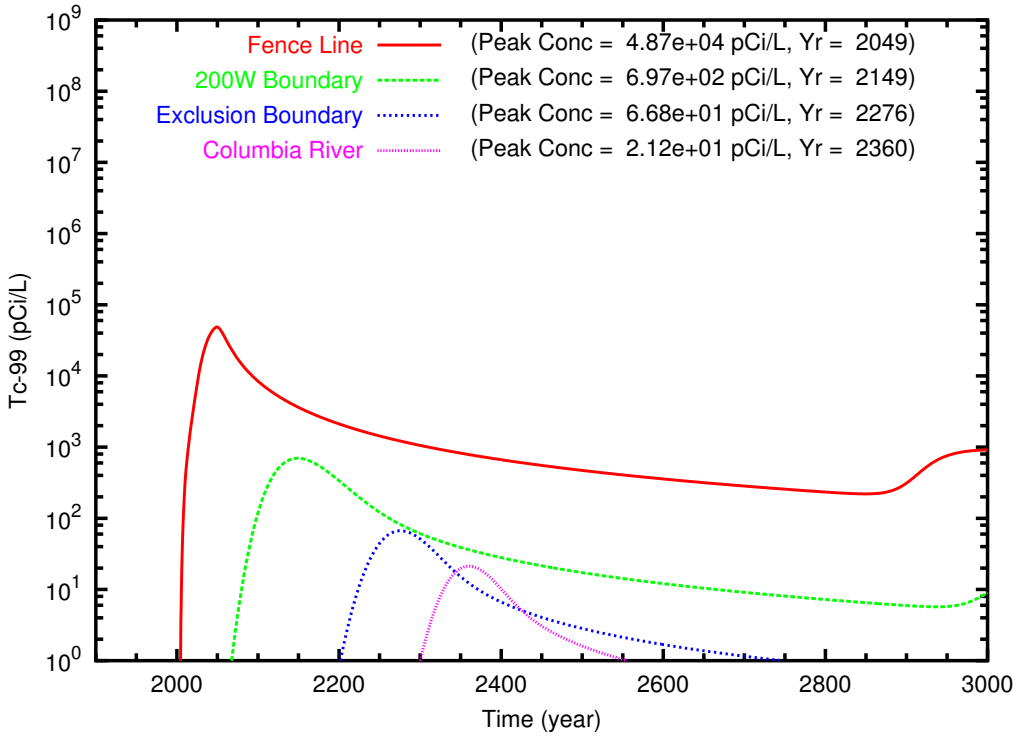

(b)

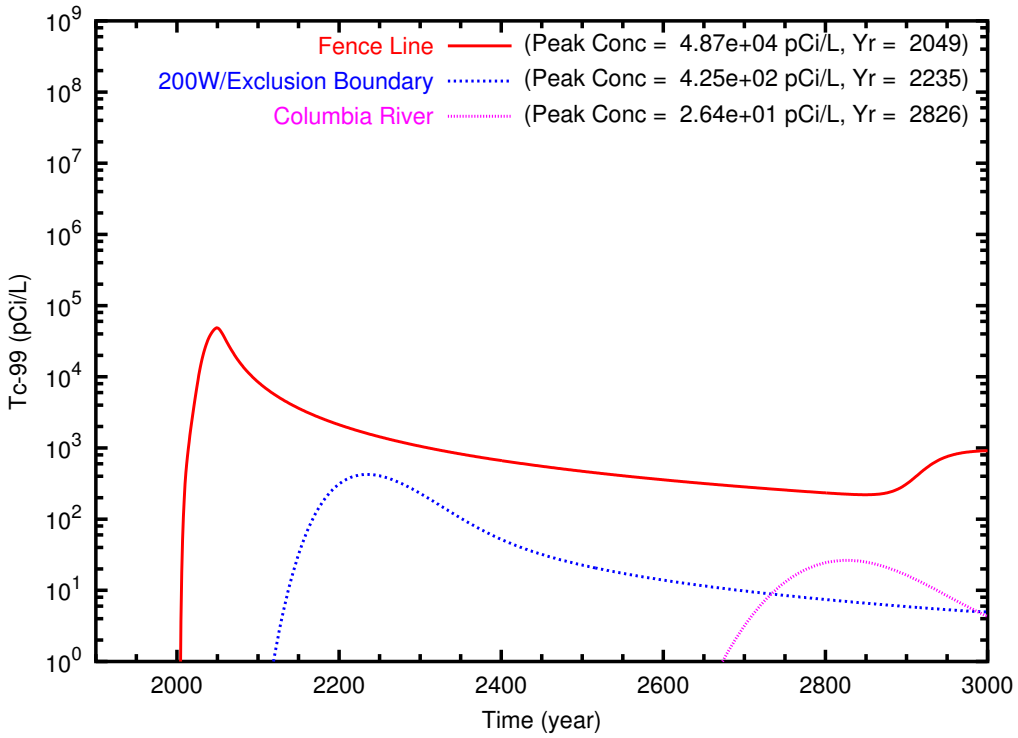

Figure D.22. TX Case 4 **Tc-99** breakthrough curves at fenceline and downgradient points along (a) east path and (b) north path

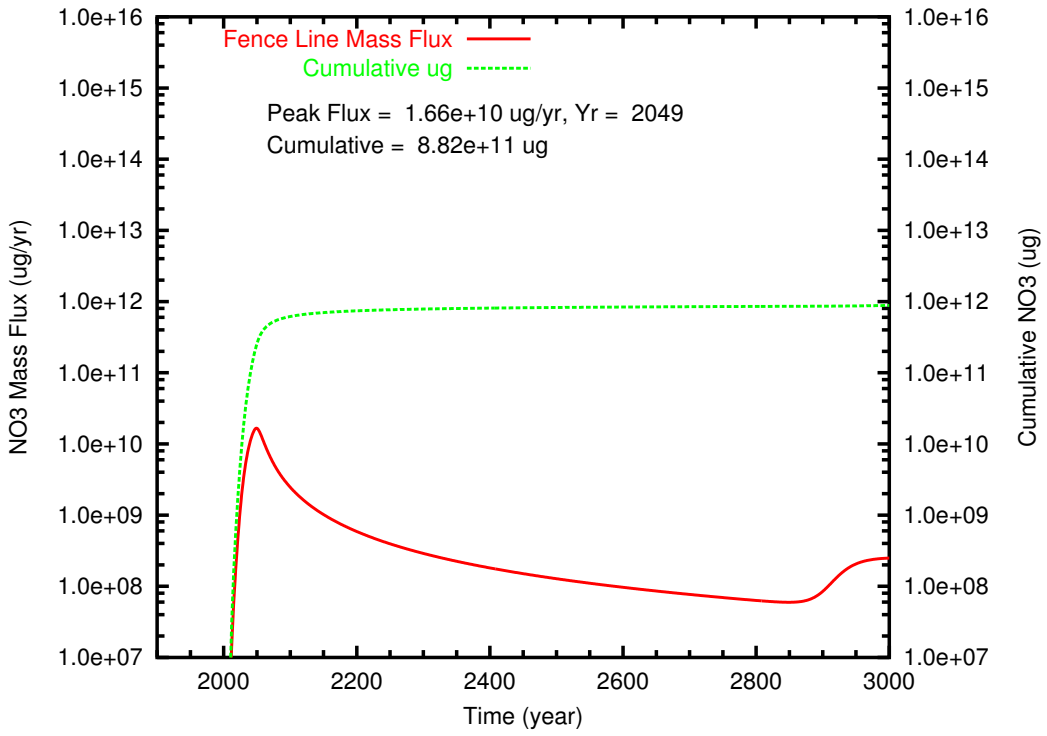

Figure D.23. TX Case 4 $\mathbf{NO_3}$ mass flux and cumulative mass at fenceline

(a)

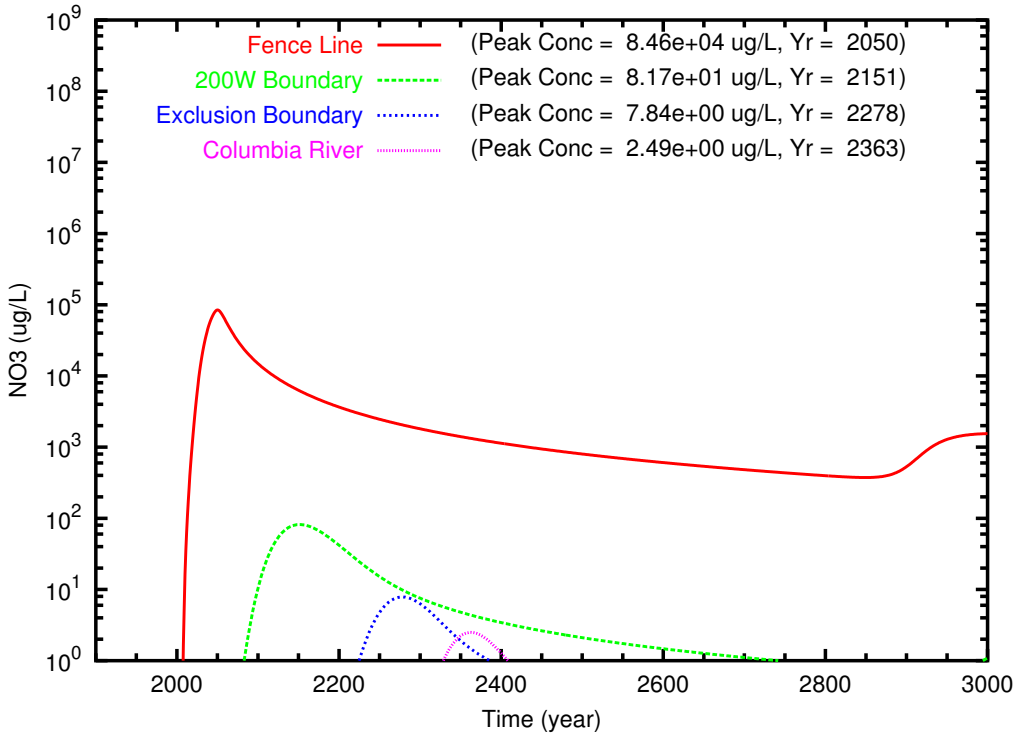

(b)

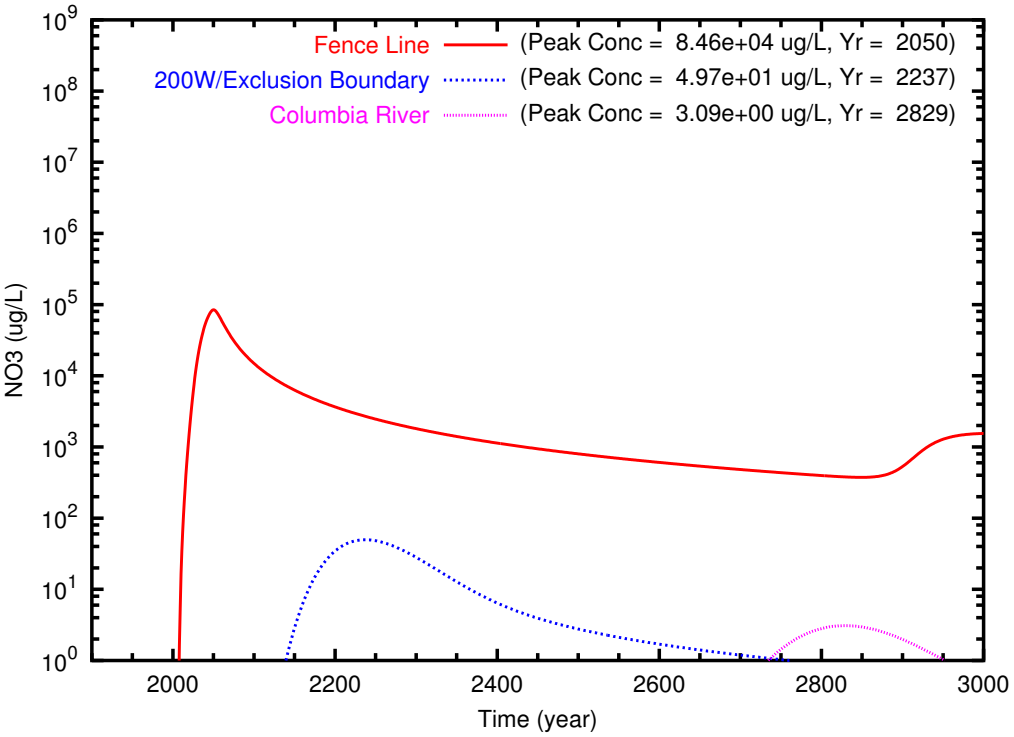

Figure D.24. TX Case 4 **NO_3** breakthrough curves at fenceline and downgradient points along (a) east path and (b) north path

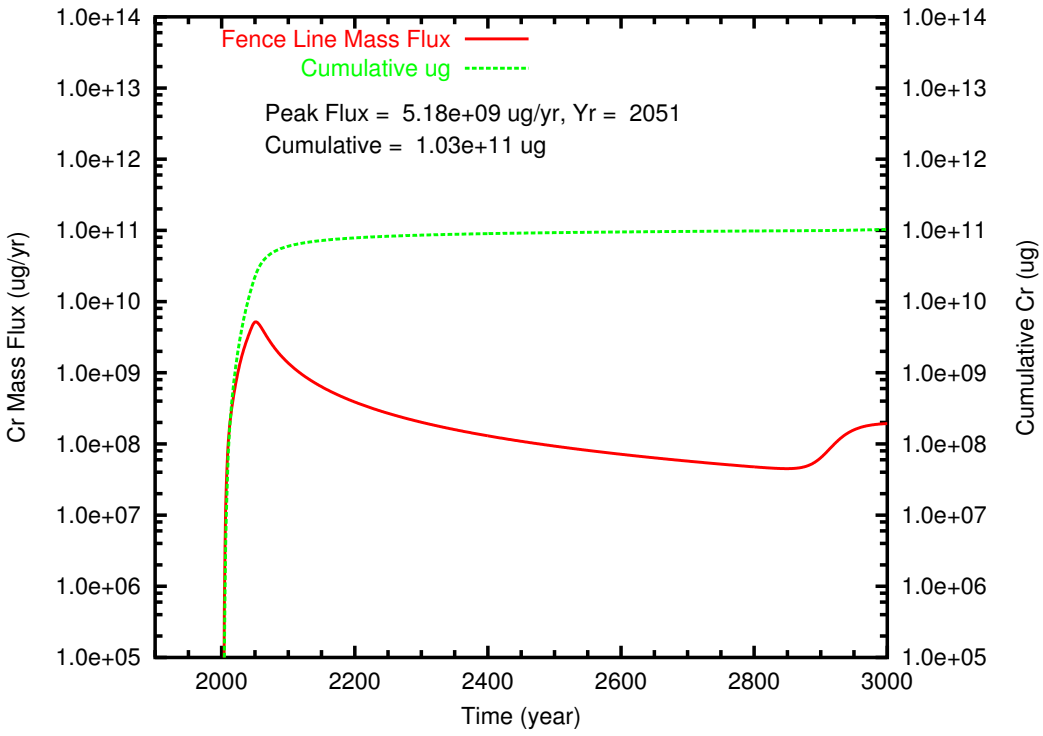

Figure D.25. TX Case 4 **Cr** mass flux and cumulative mass at fenceline

(a)

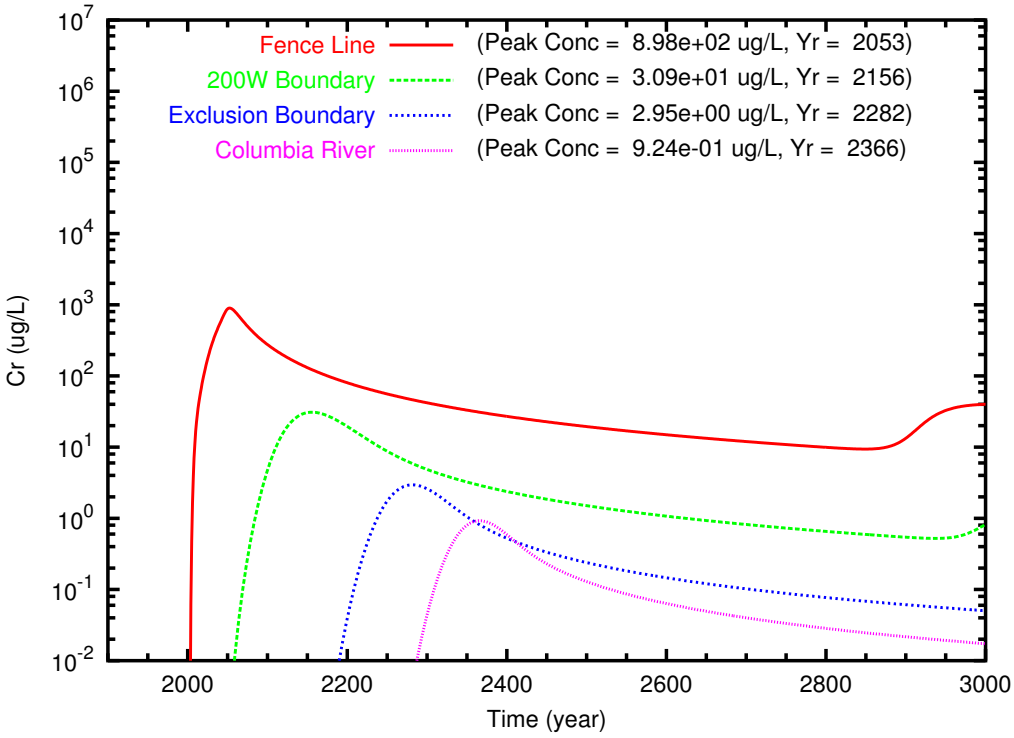

(b)

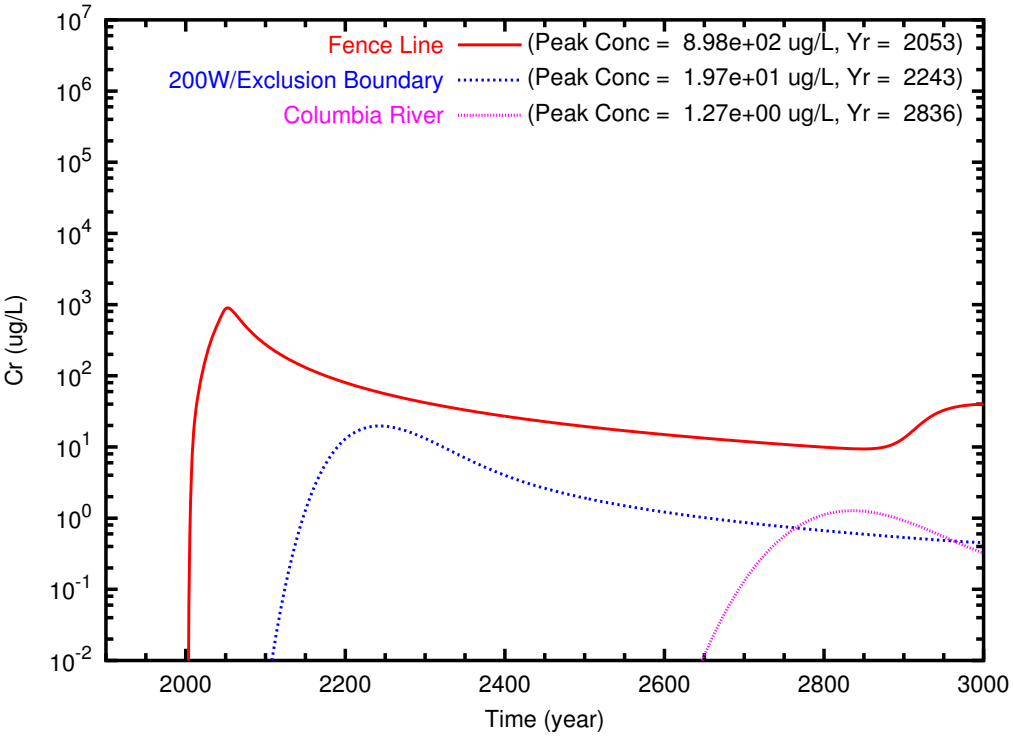

Figure D.26. TX Case 4 **Cr** breakthrough curves at fenceline and downgradient points along (a) east path and (b) north path

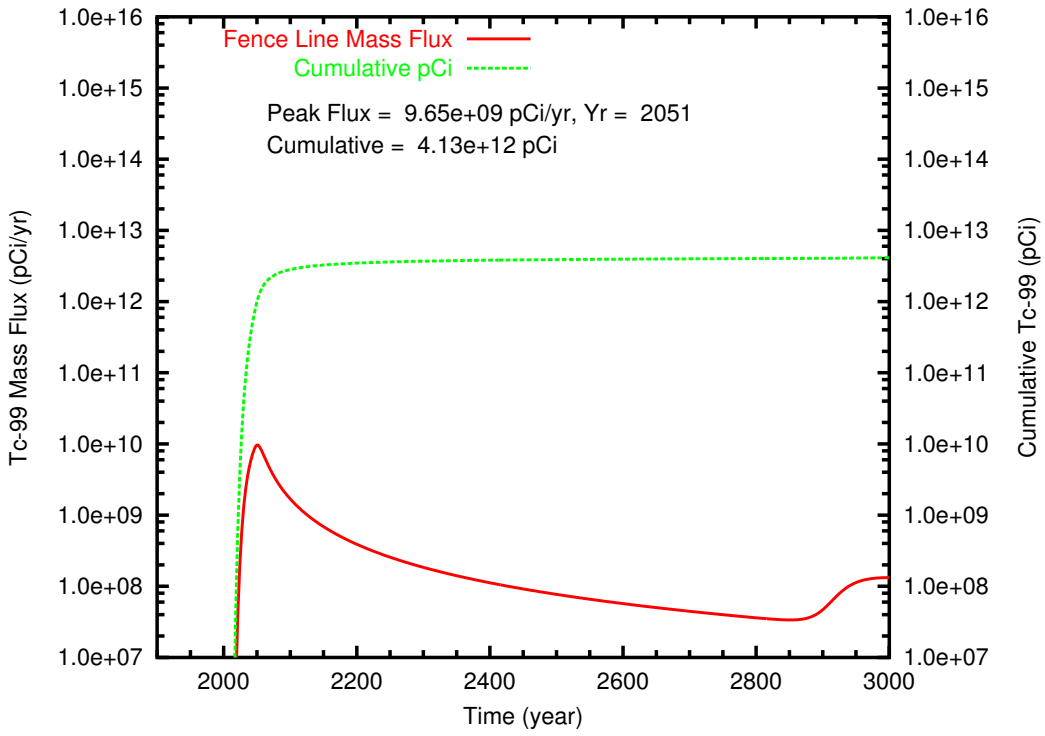

Figure D.27. TX Case 5 **Tc-99** mass flux and cumulative mass at fenceline

(a)

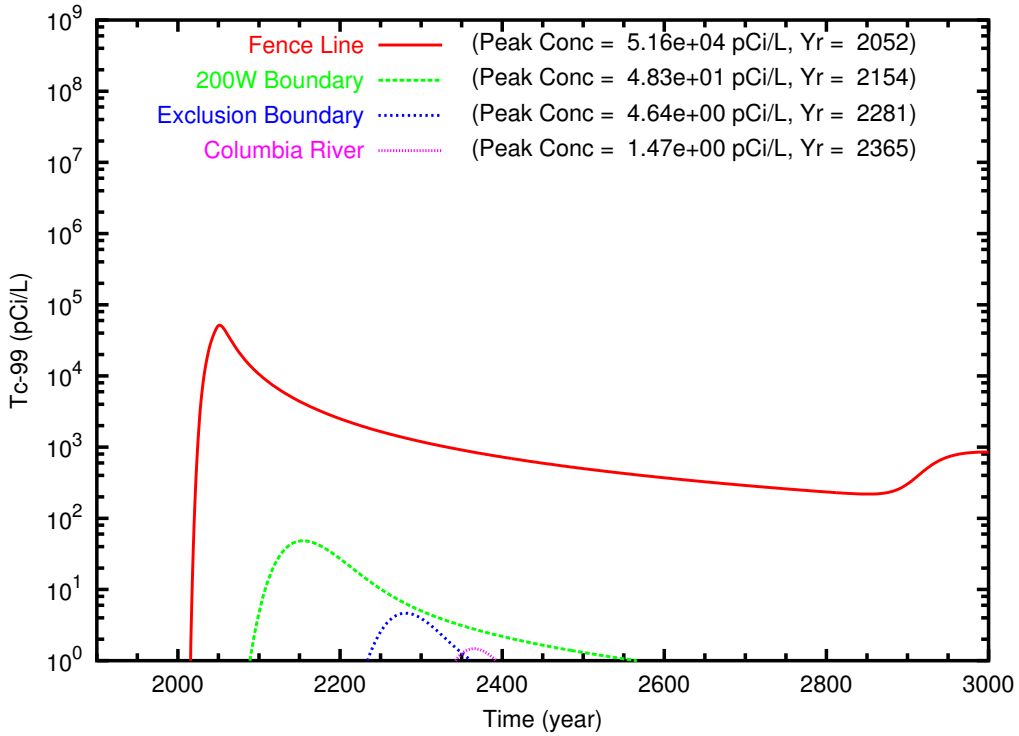

(b)

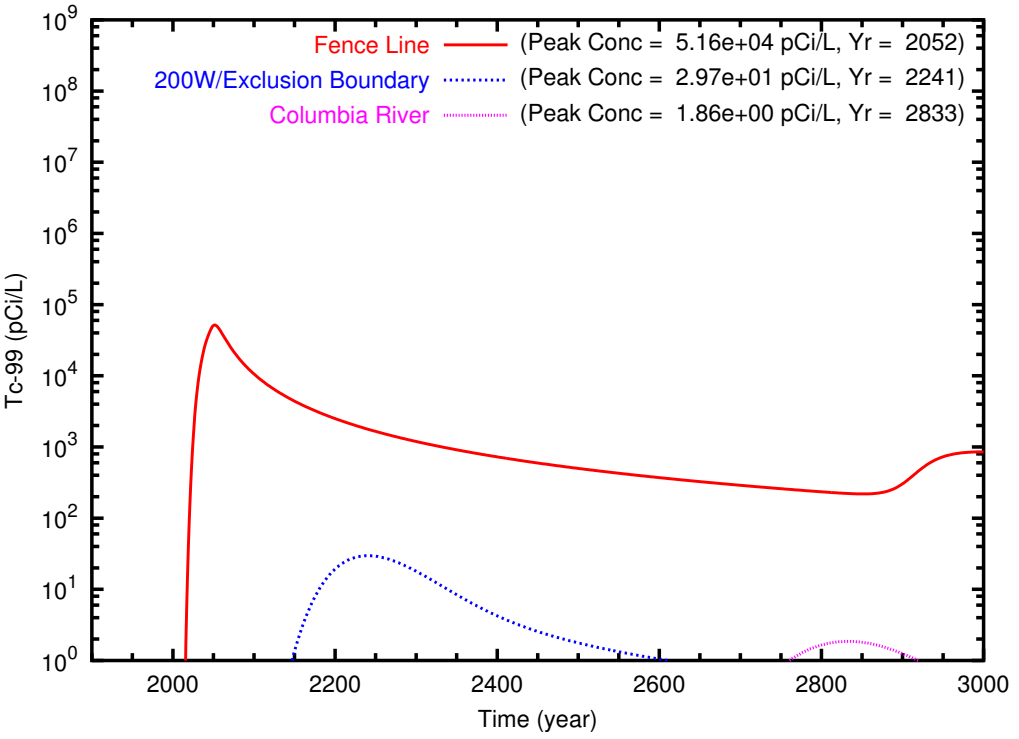

Figure D.28. TX Case 5 **Tc-99** breakthrough curves at fenceline and downgradient points along (a) east path and (b) north path

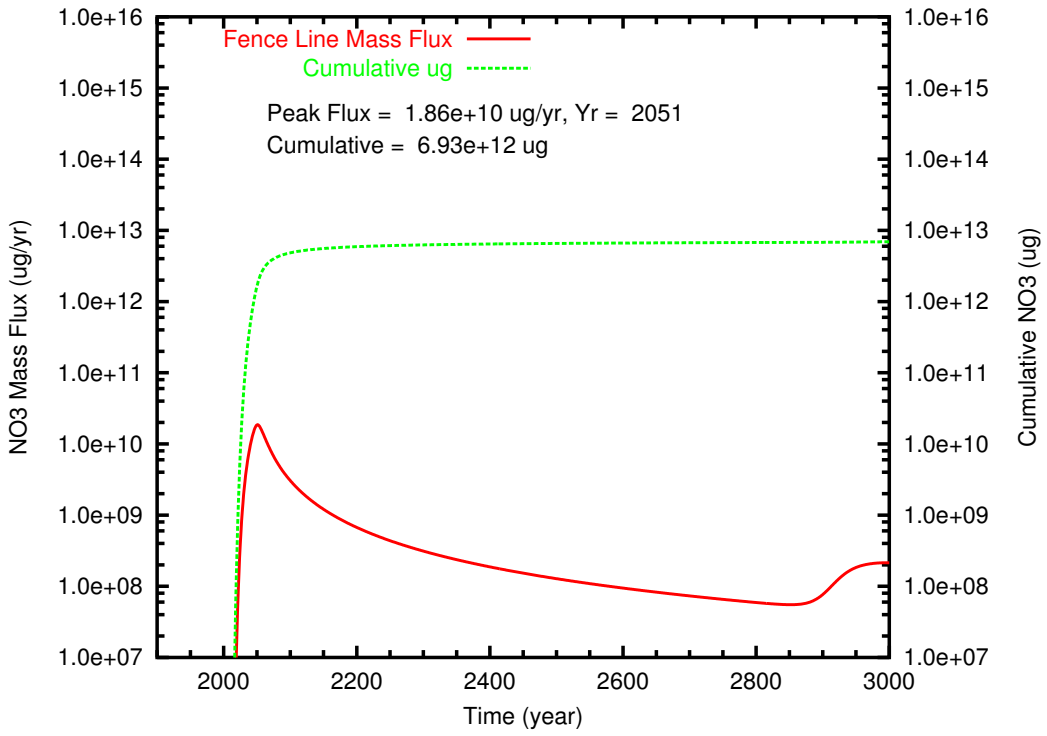

Figure D.29. TX Case 5 $\mathbf{NO_3}$ mass flux and cumulative mass at fenceline

(a)

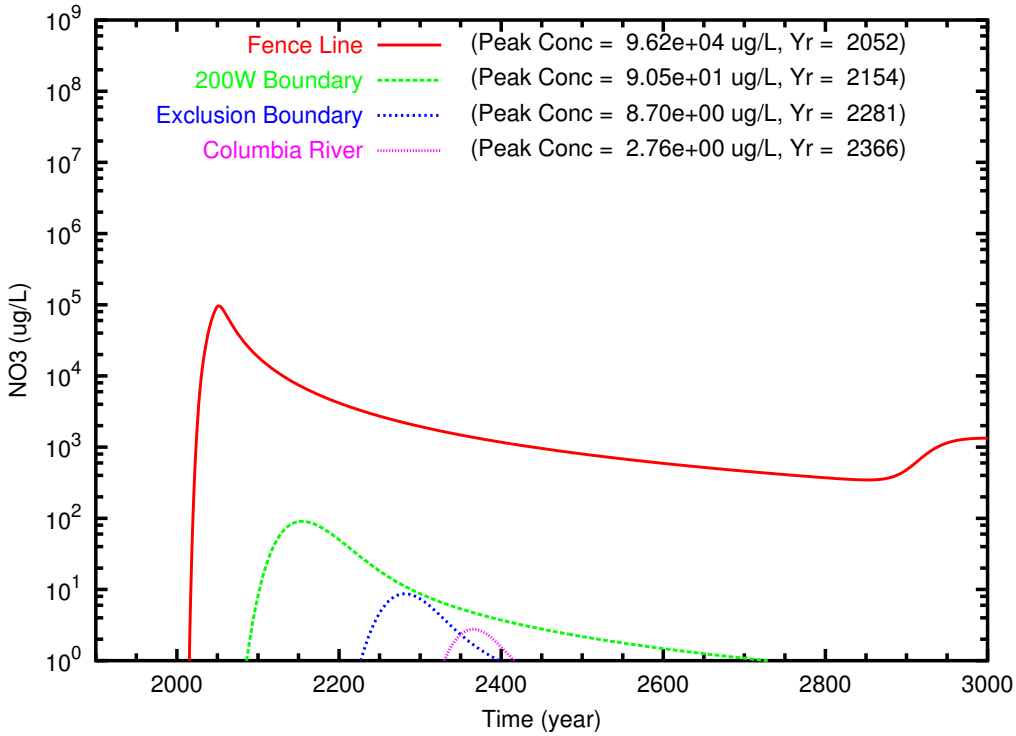

(b)

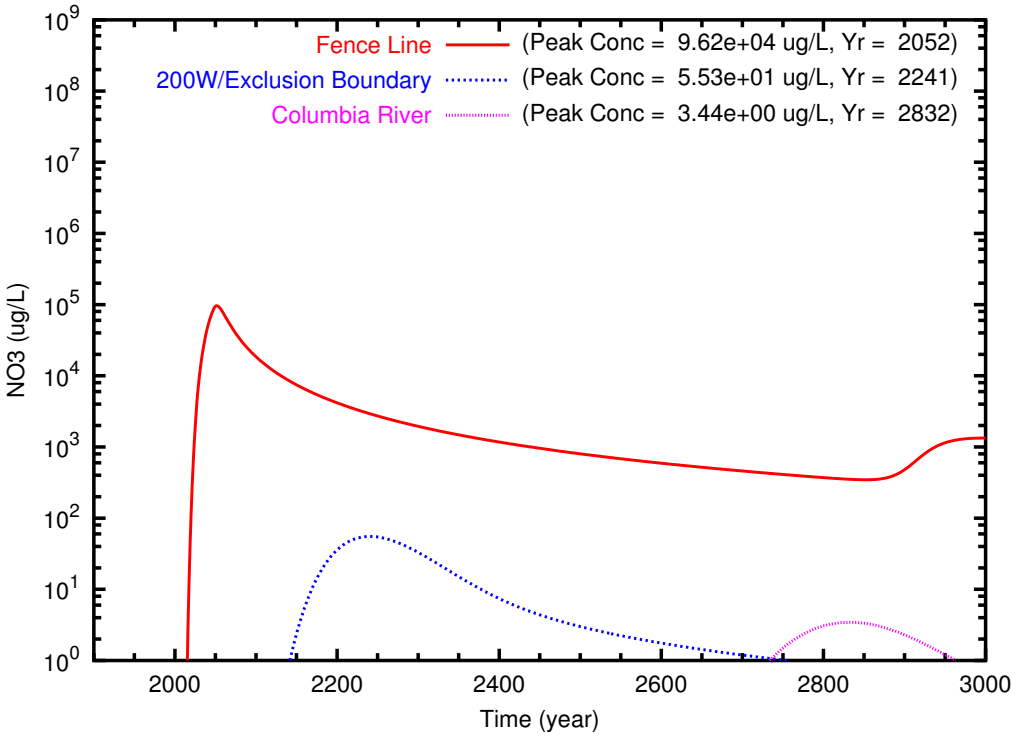

Figure D.30. TX Case 5 **NO_3** breakthrough curves at fenceline and downgradient points along (a) east path and (b) north path

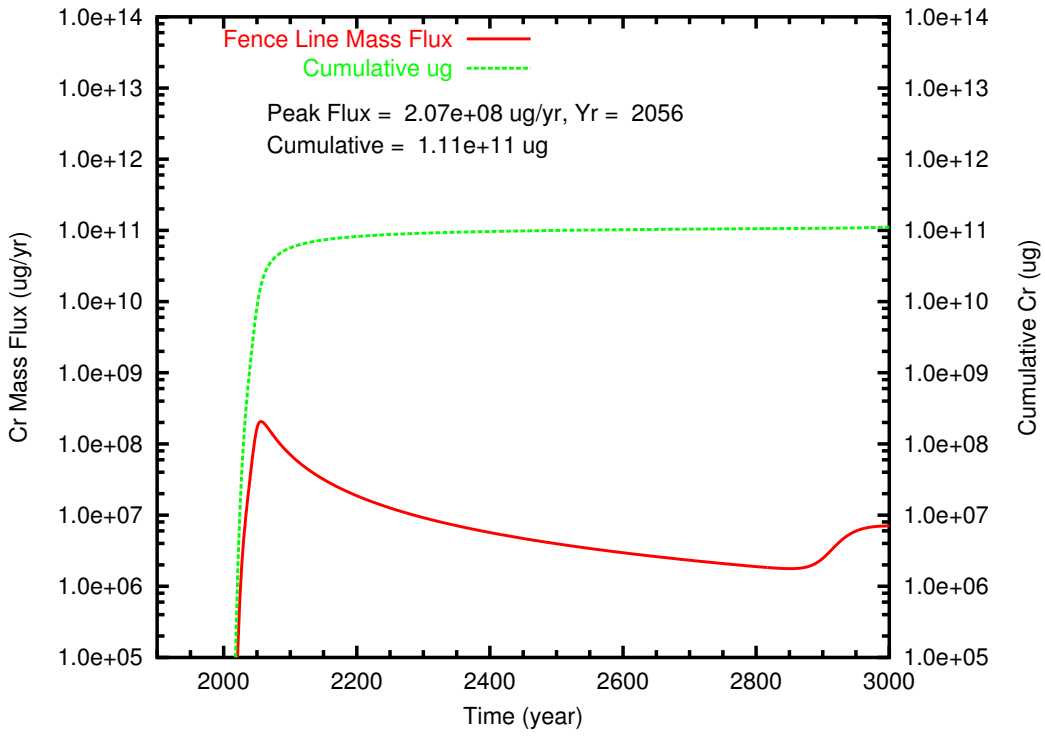

Figure D.31. TX Case 5 **Cr** mass flux and cumulative mass at fenceline

(a)

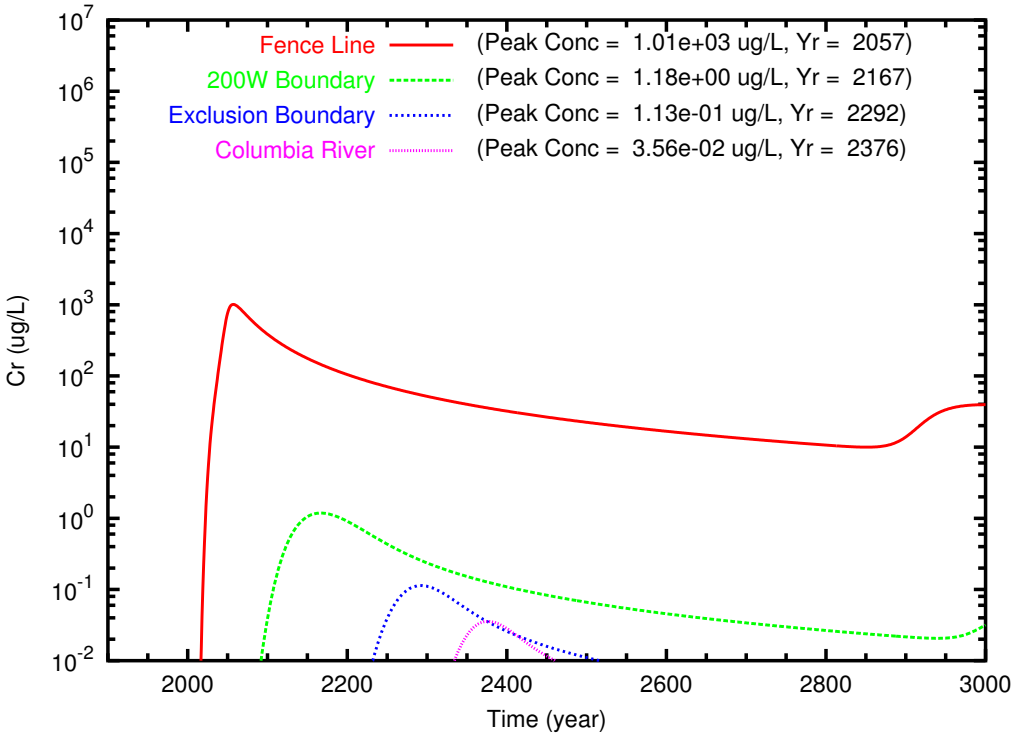

(b)

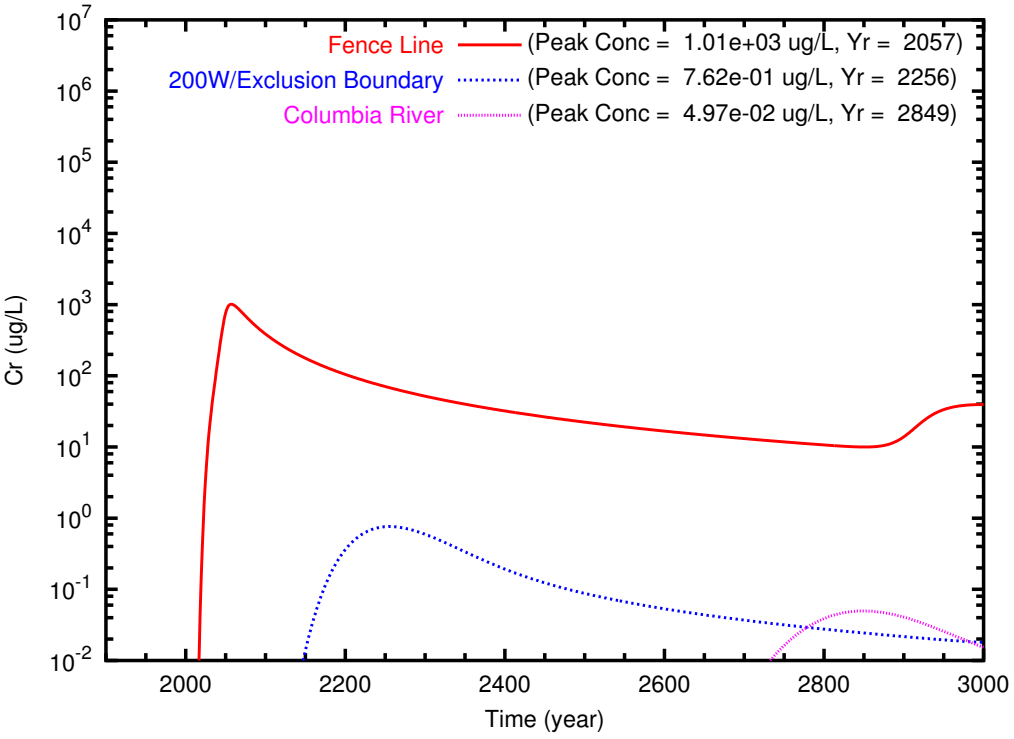

Figure D.32. TX Case 5 **Cr** breakthrough curves at fenceline and downgradient points along (a) east path and (b) north path

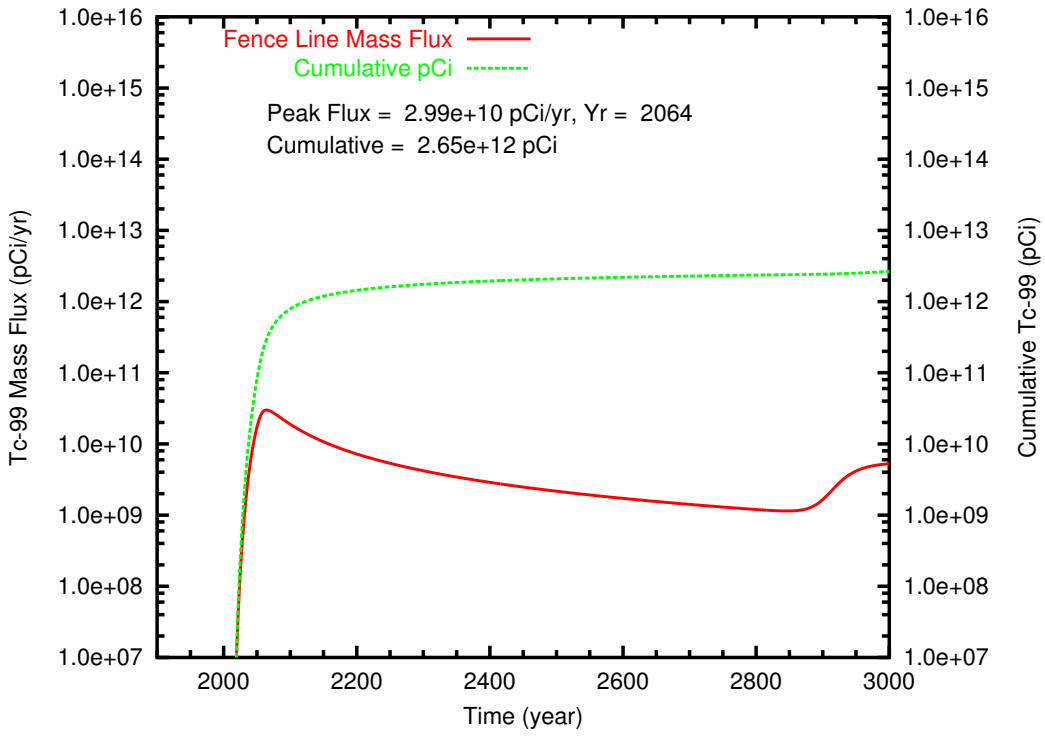

Figure D.33. TX Case 6 **Tc-99** mass flux and cumulative mass at fenceline

(a)

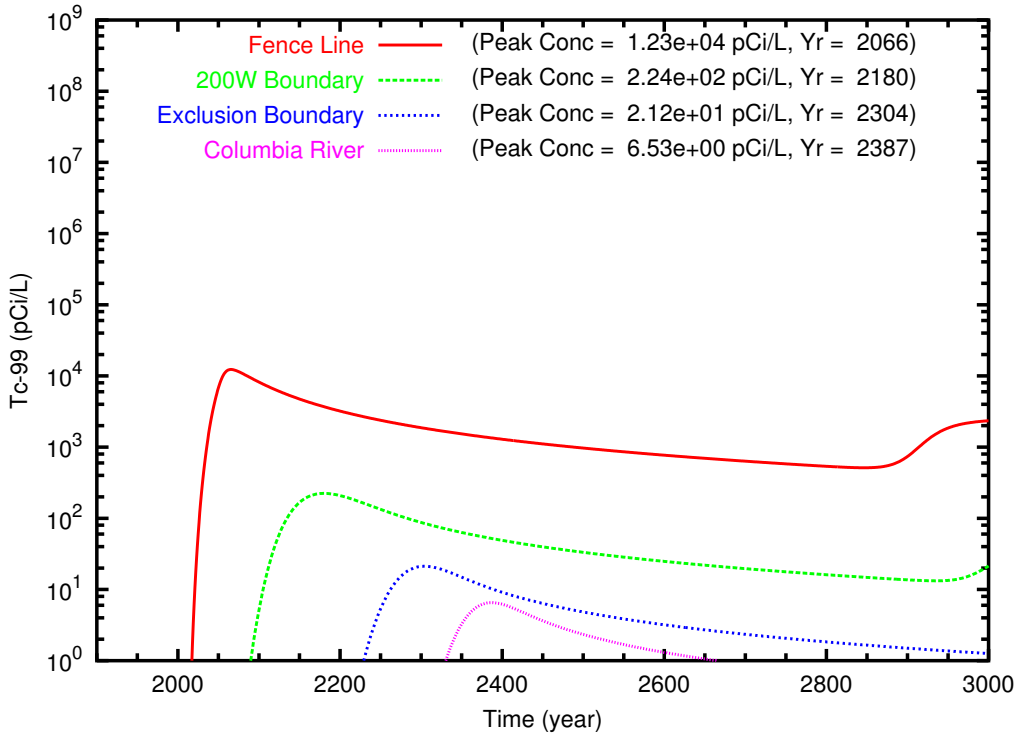

(b)

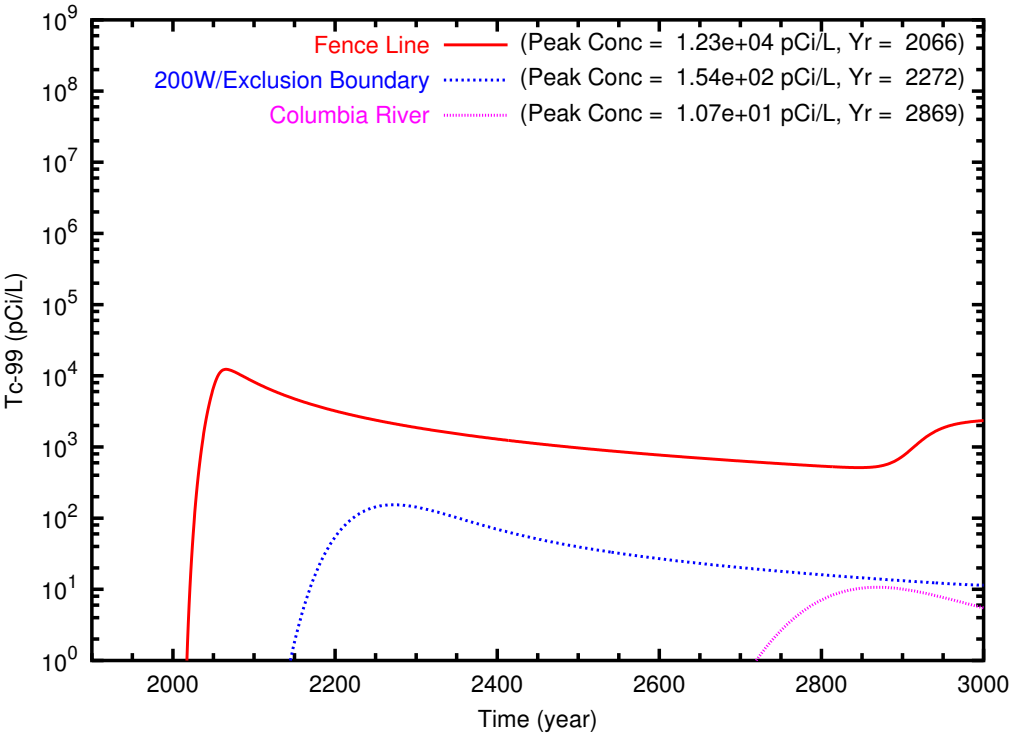

Figure D.34. TX Case 6 **Tc-99** breakthrough curves at fenceline and downgradient points along (a) east path and (b) north path

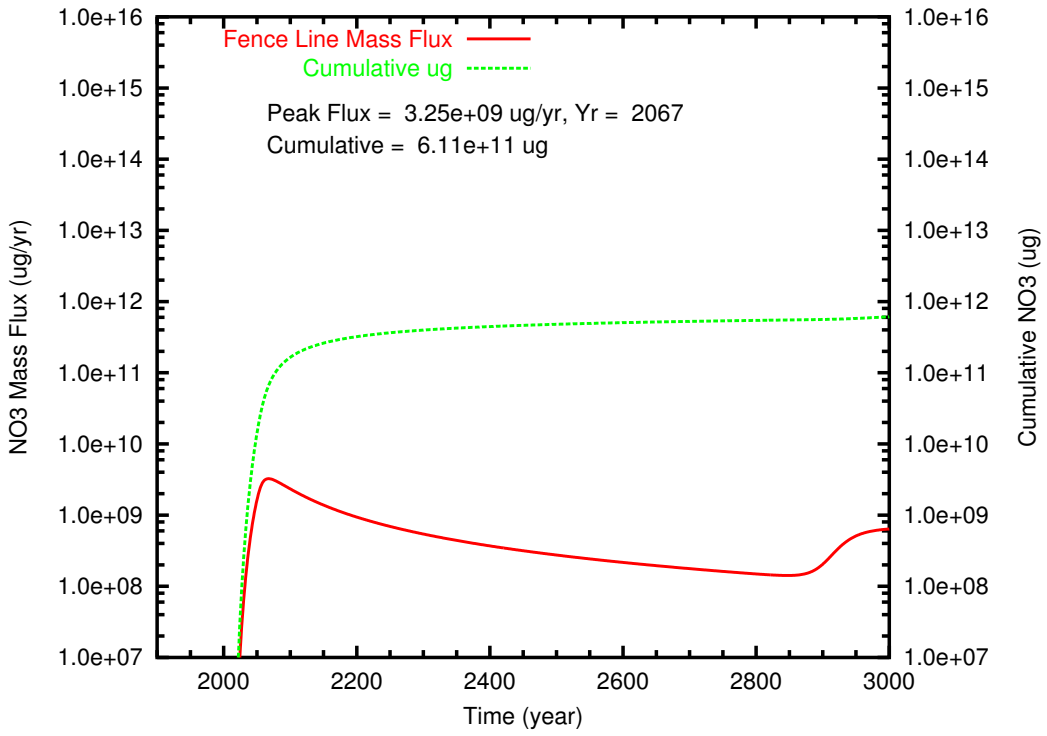

Figure D.35. TX Case 6 $\mathbf{NO_3}$ mass flux and cumulative mass at fenceline

(a)

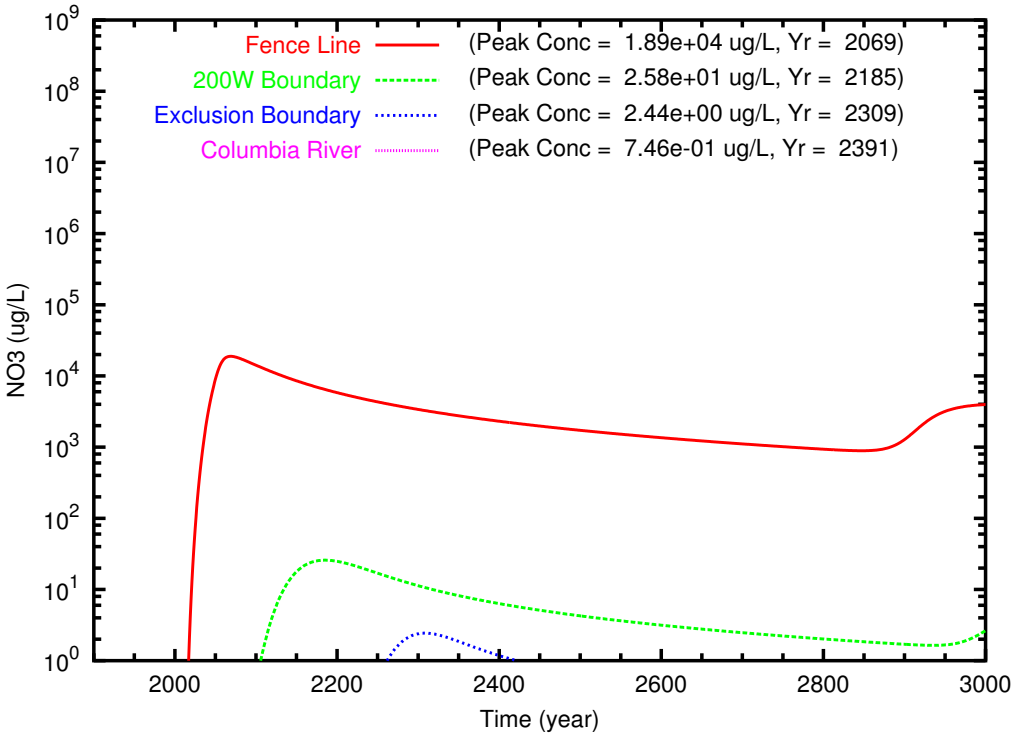

(b)

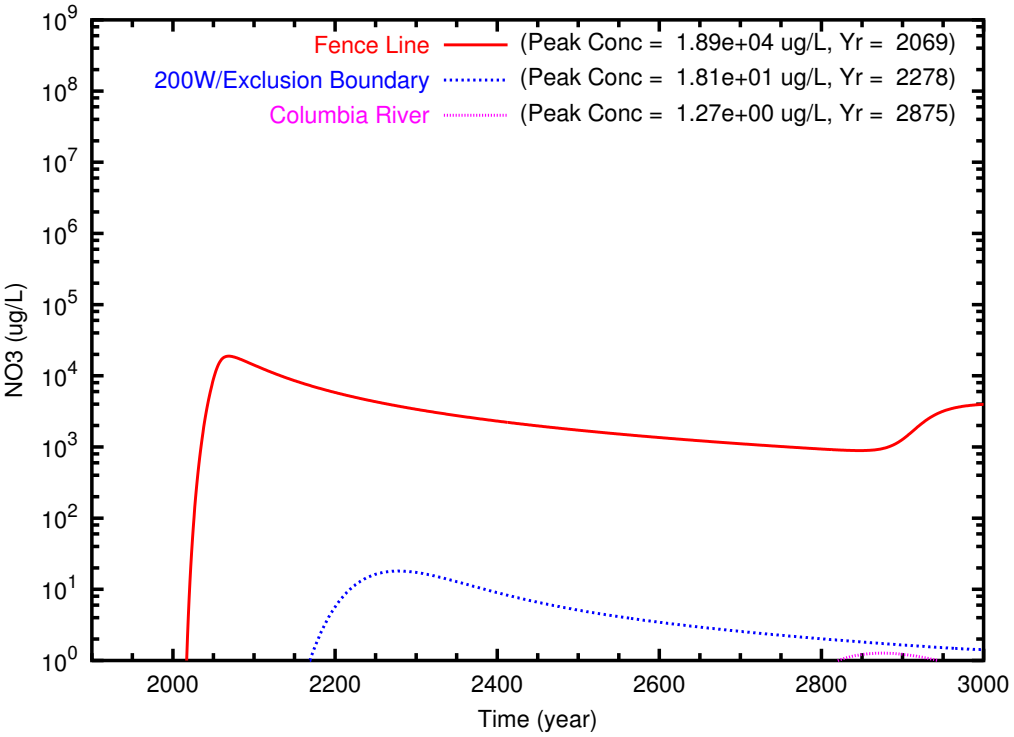

Figure D.36. TX Case 6 **NO_3** breakthrough curves at fenceline and downgradient points along (a) east path and (b) north path

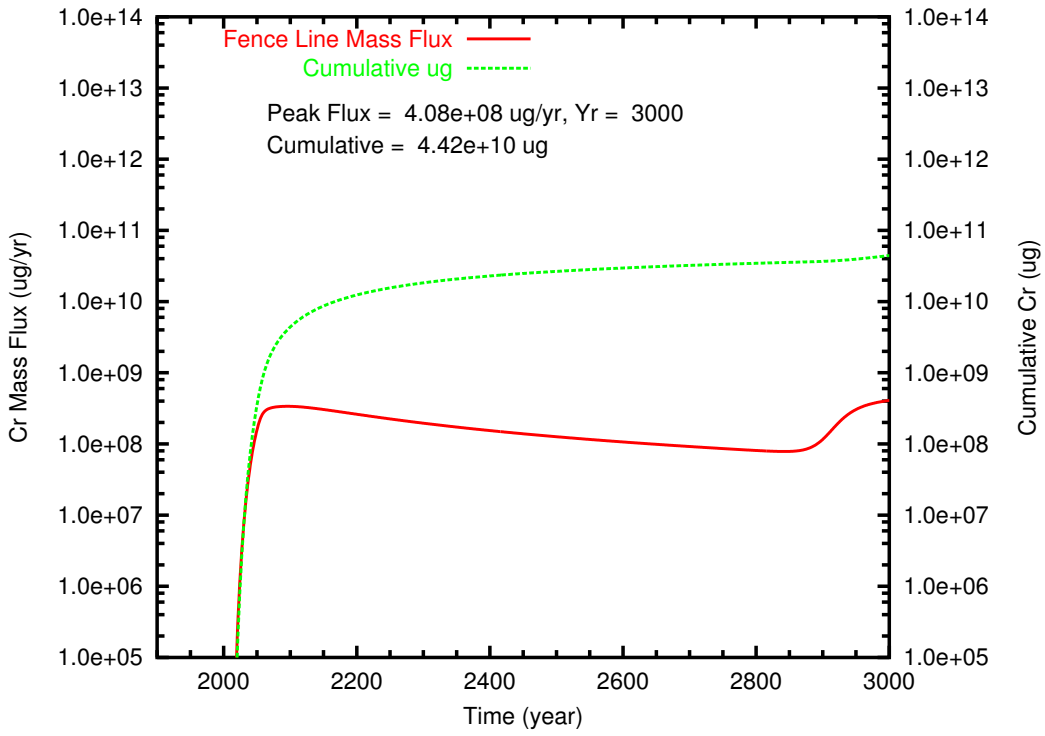

Figure D.37. TX Case 6 **Cr** mass flux and cumulative mass at fenceline

(a)

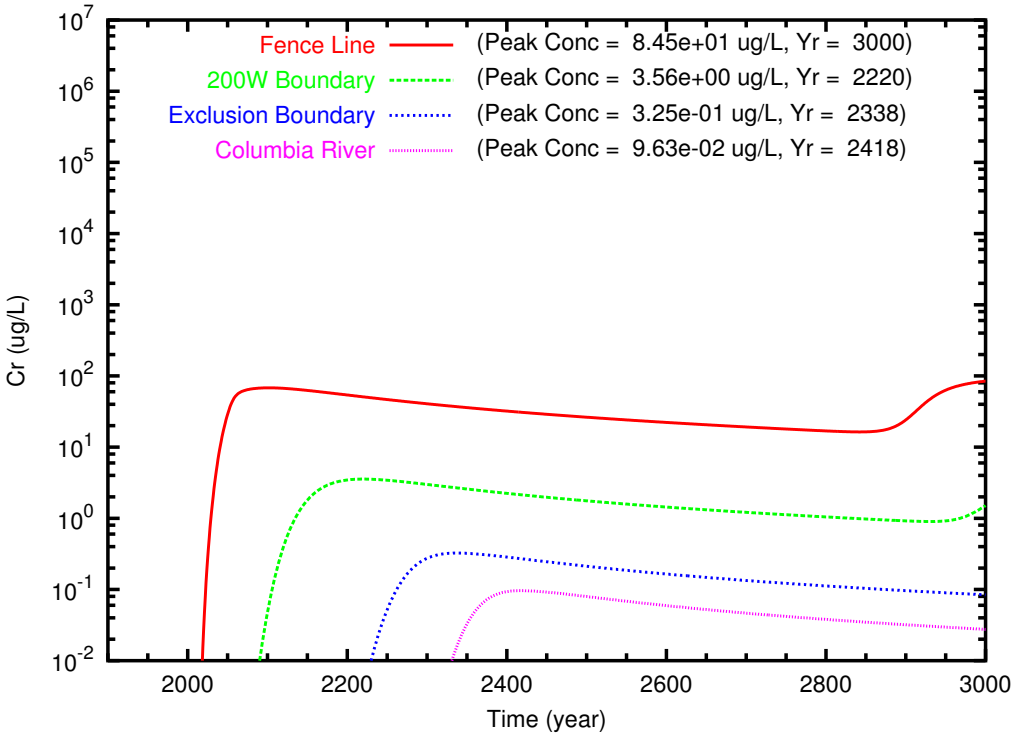

(b)

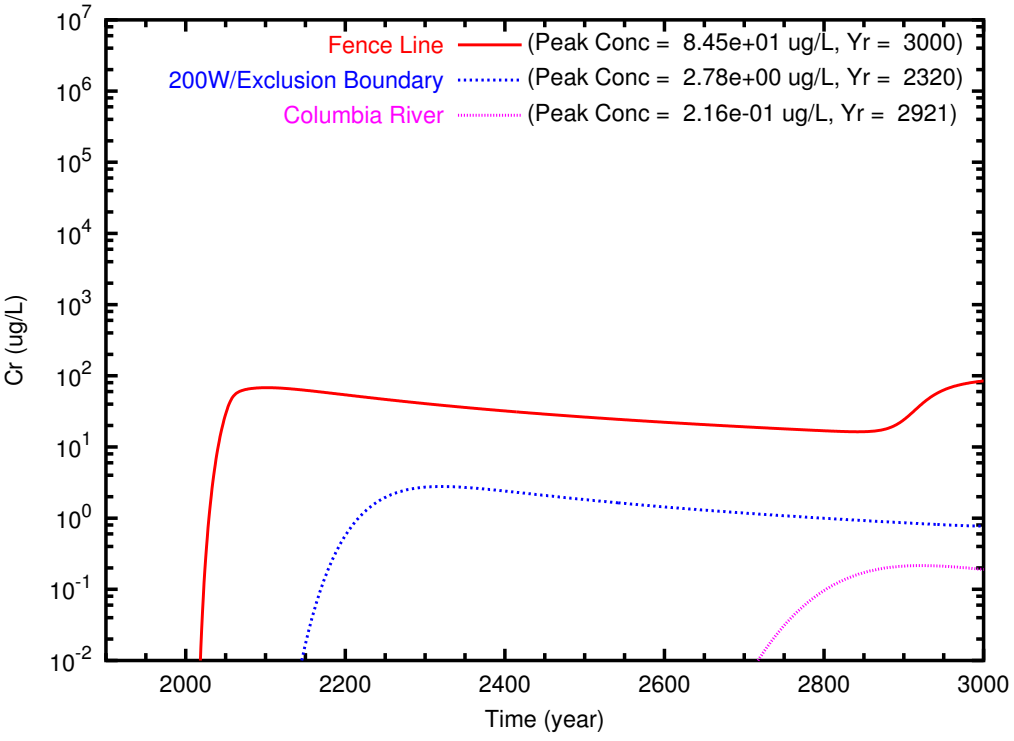

Figure D.38. TX Case 6 **Cr** breakthrough curves at fenceline and downgradient points along (a) east path and (b) north path

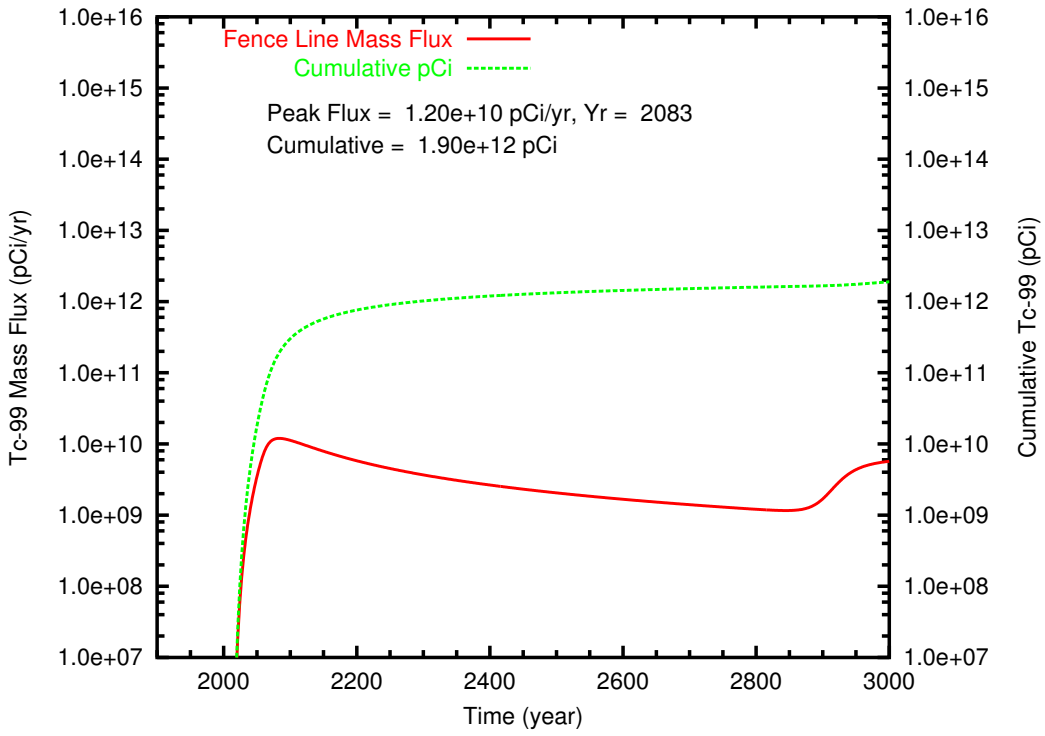

Figure D.39. TX Case 7 **Tc-99** mass flux and cumulative mass at fenceline

(a)

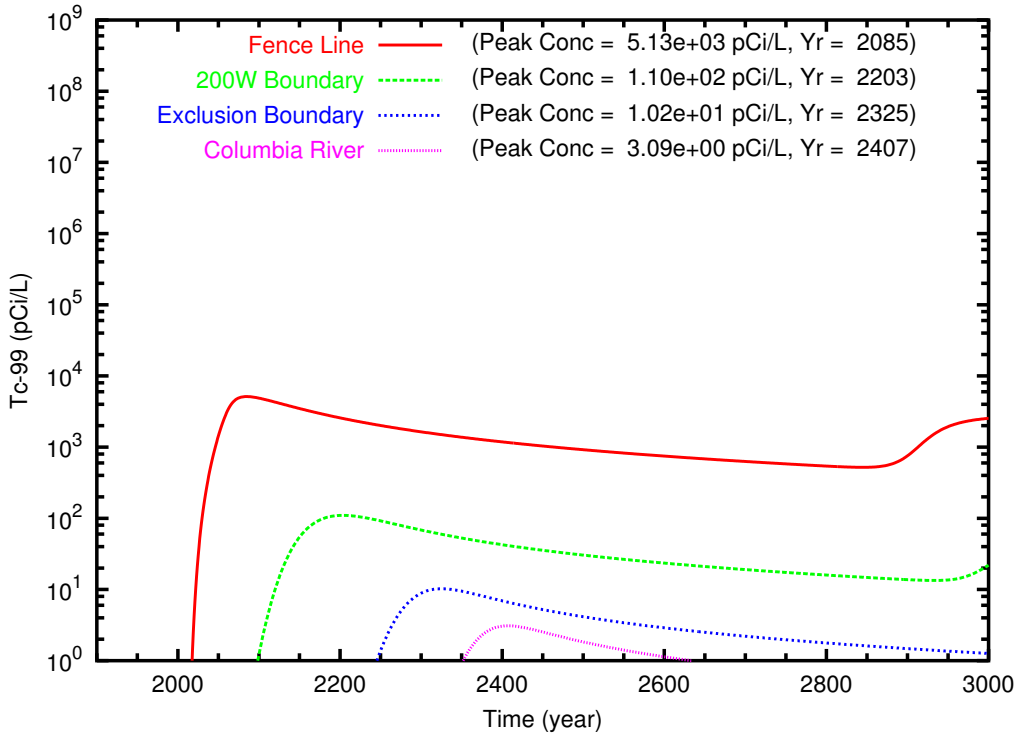

(b)

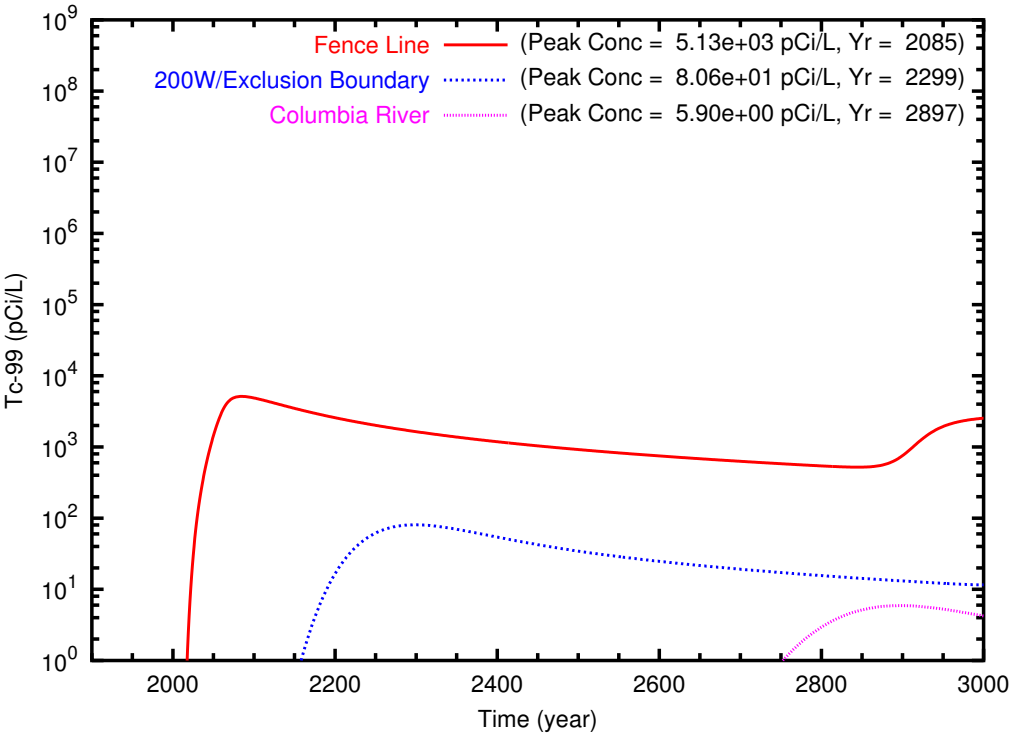

Figure D.40. TX Case 7 **Tc-99** breakthrough curves at fenceline and downgradient points along (a) east path and (b) north path

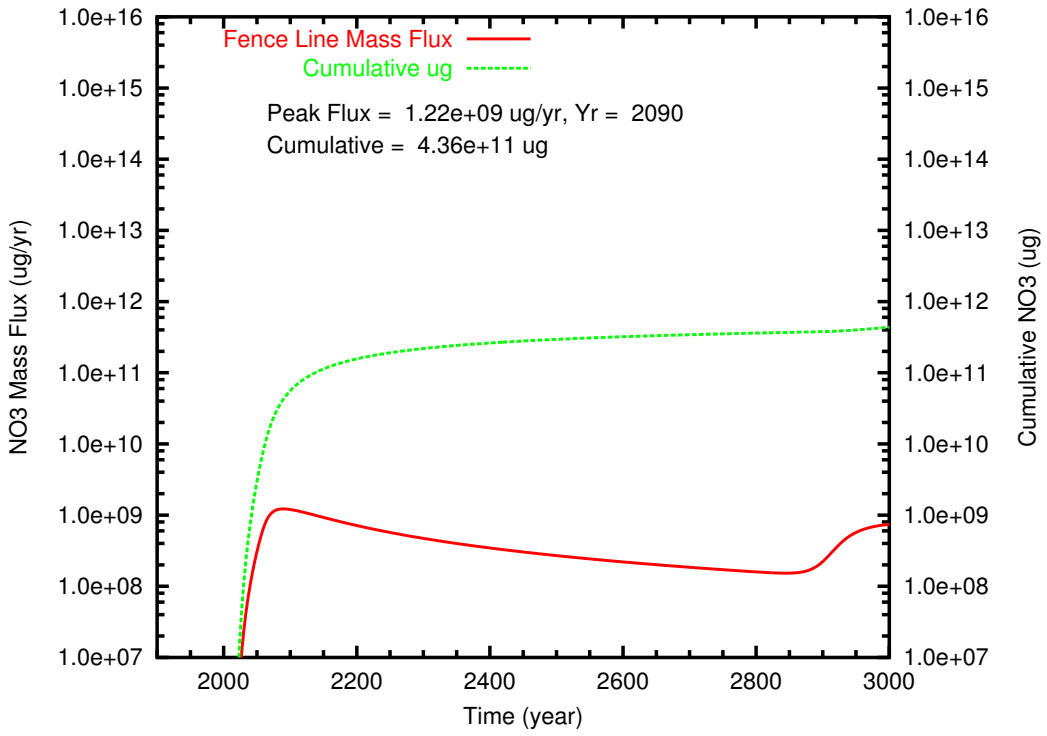

Figure D.41. TX Case 7 $\mathbf{NO_3}$ mass flux and cumulative mass at fenceline

(a)

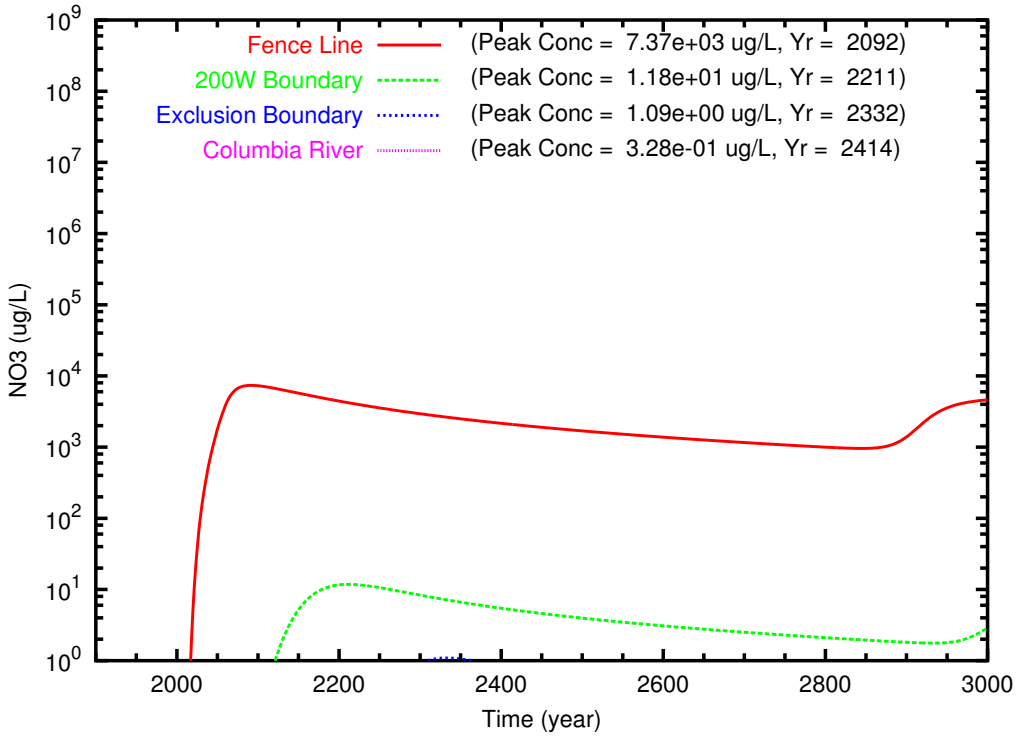

(b)

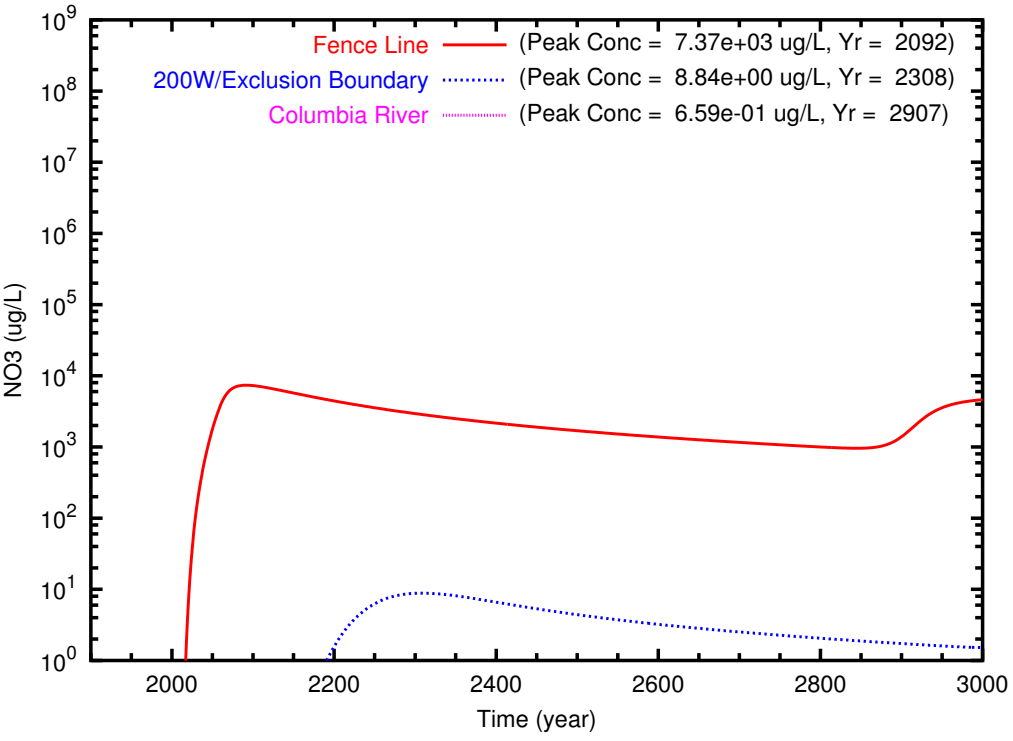

Figure D.42. TX Case 7 **NO_3** breakthrough curves at fenceline and downgradient points along (a) east path and (b) north path

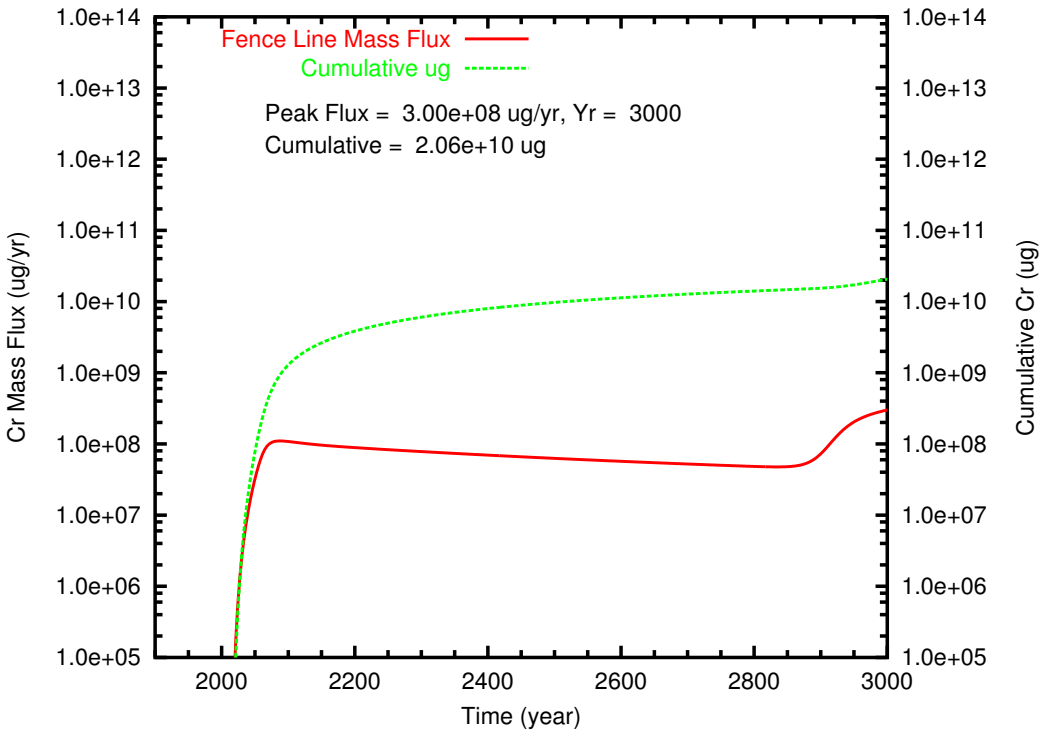

Figure D.43. TX Case 7 **Cr** mass flux and cumulative mass at fenceline

(a)

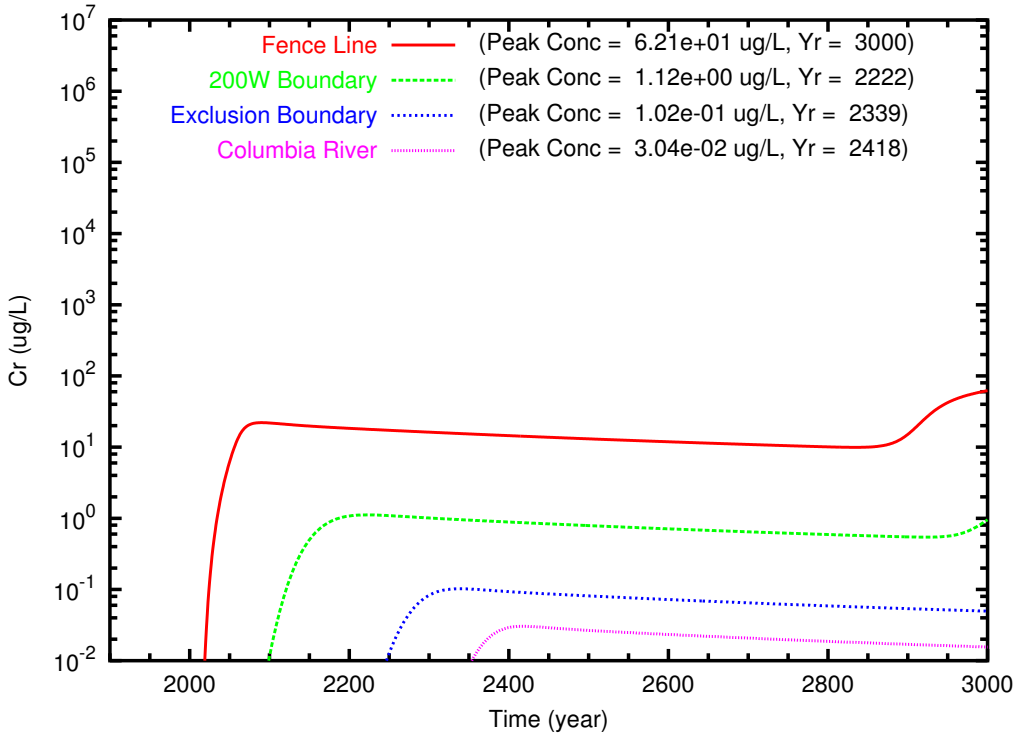

(b)

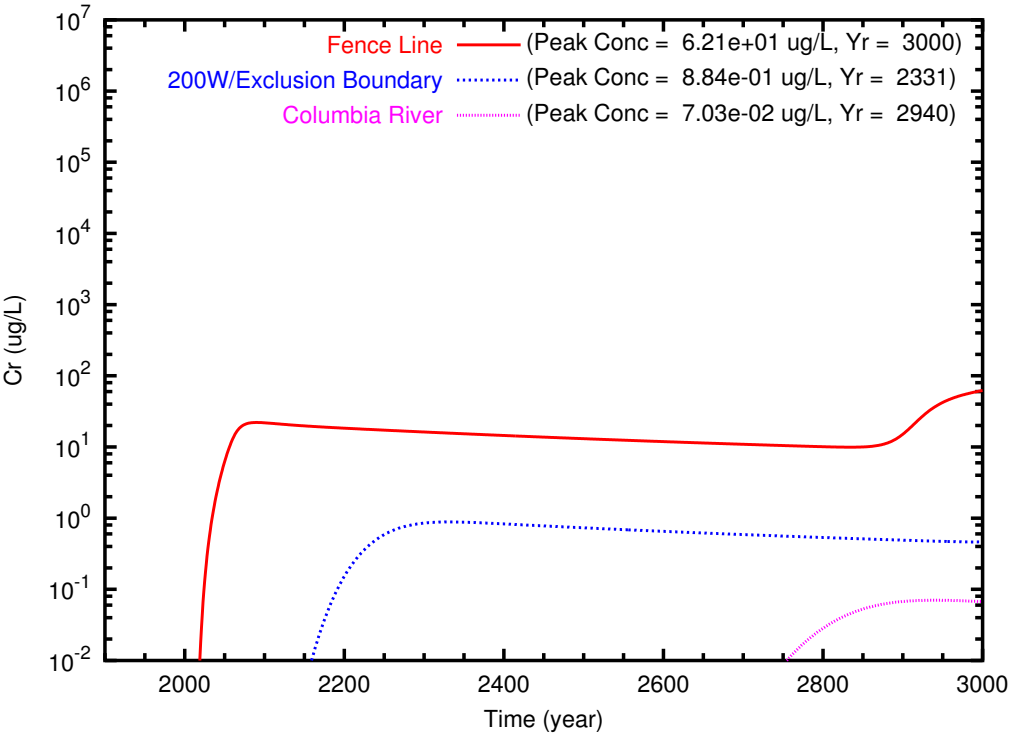

Figure D.44. TX Case 7 **Cr** breakthrough curves at fenceline and downgradient points along (a) east path and (b) north path

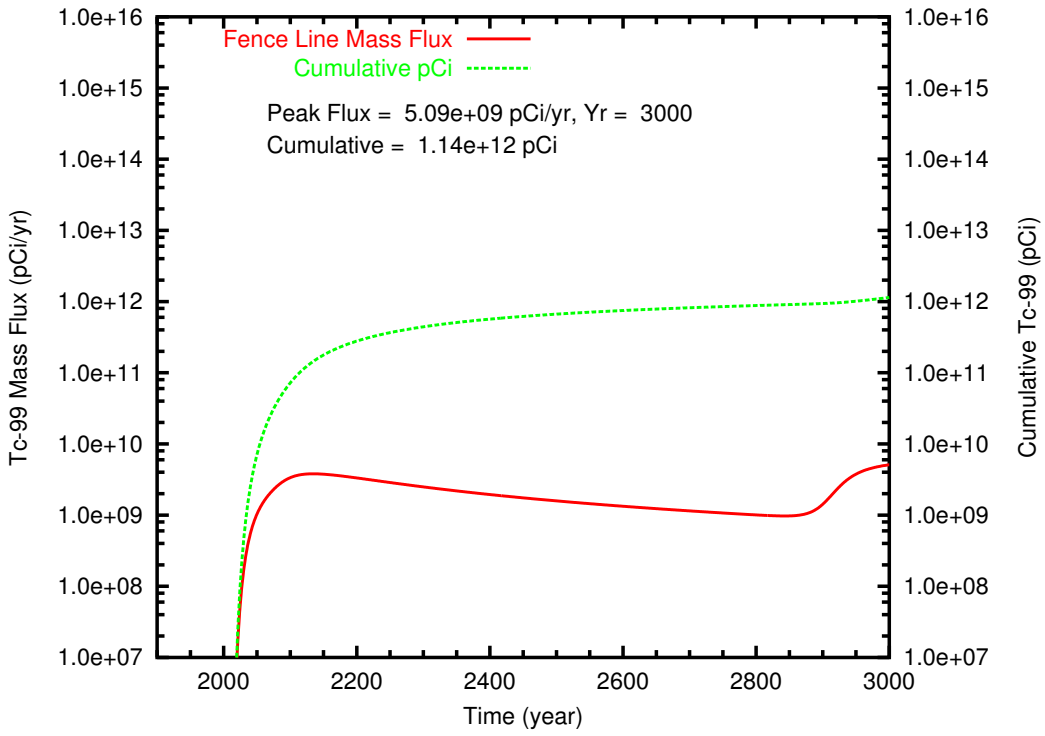

Figure D.45. TX Case 8 **Tc-99** mass flux and cumulative mass at fenceline

(a)

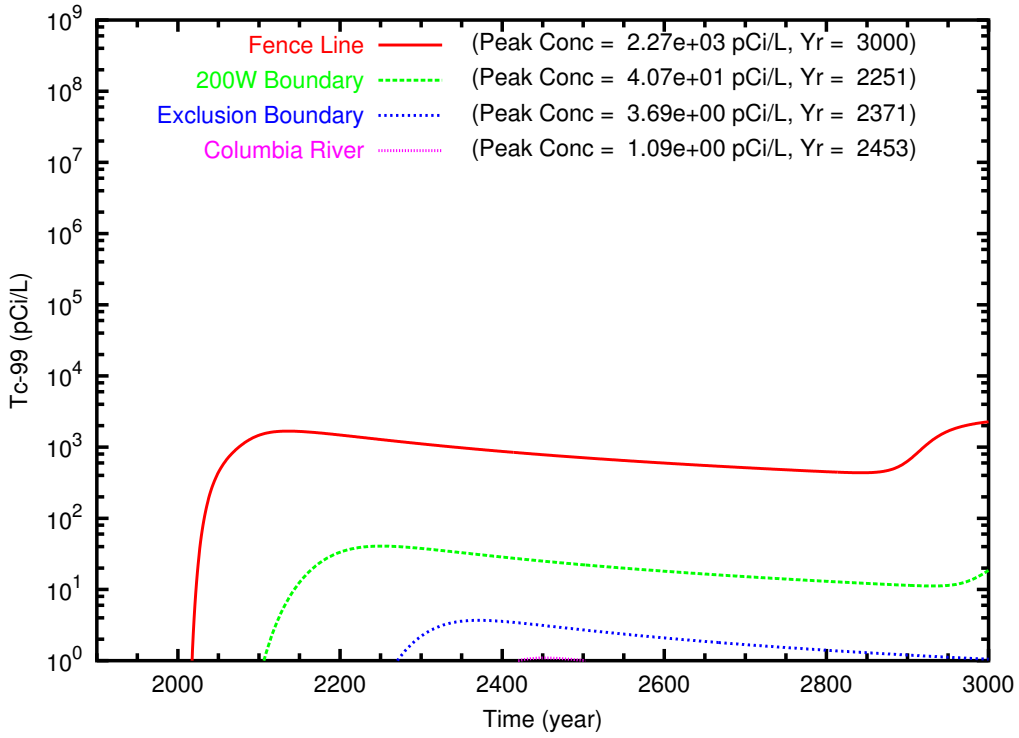

(b)

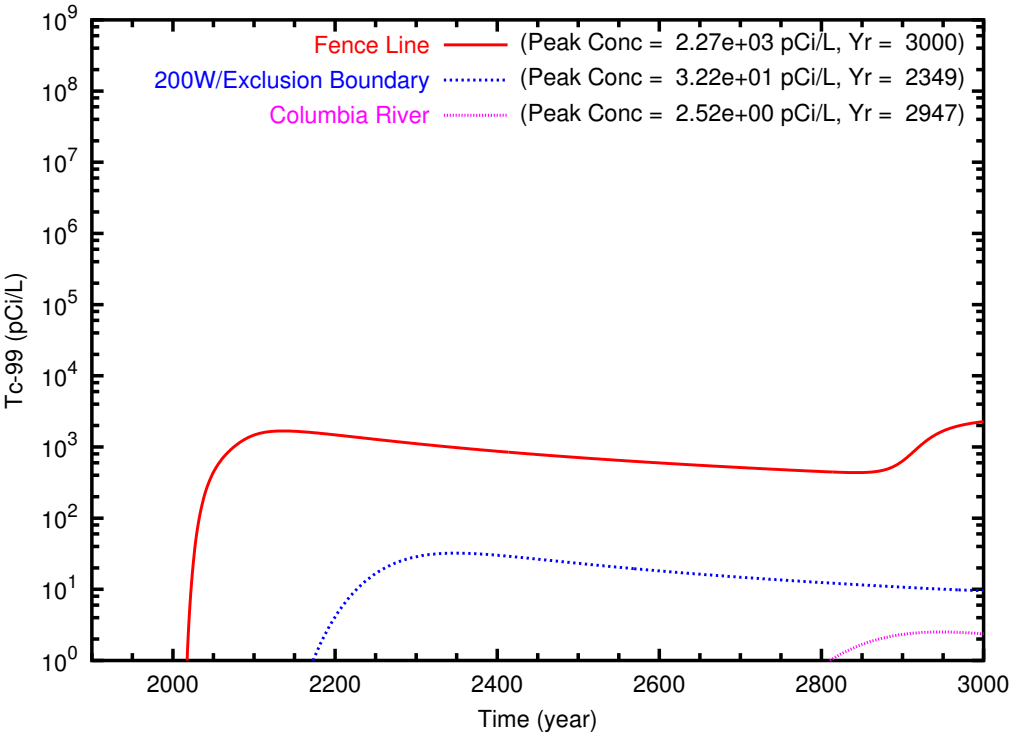

Figure D.46. TX Case 8 **Tc-99** breakthrough curves at fenceline and downgradient points along (a) east path and (b) north path

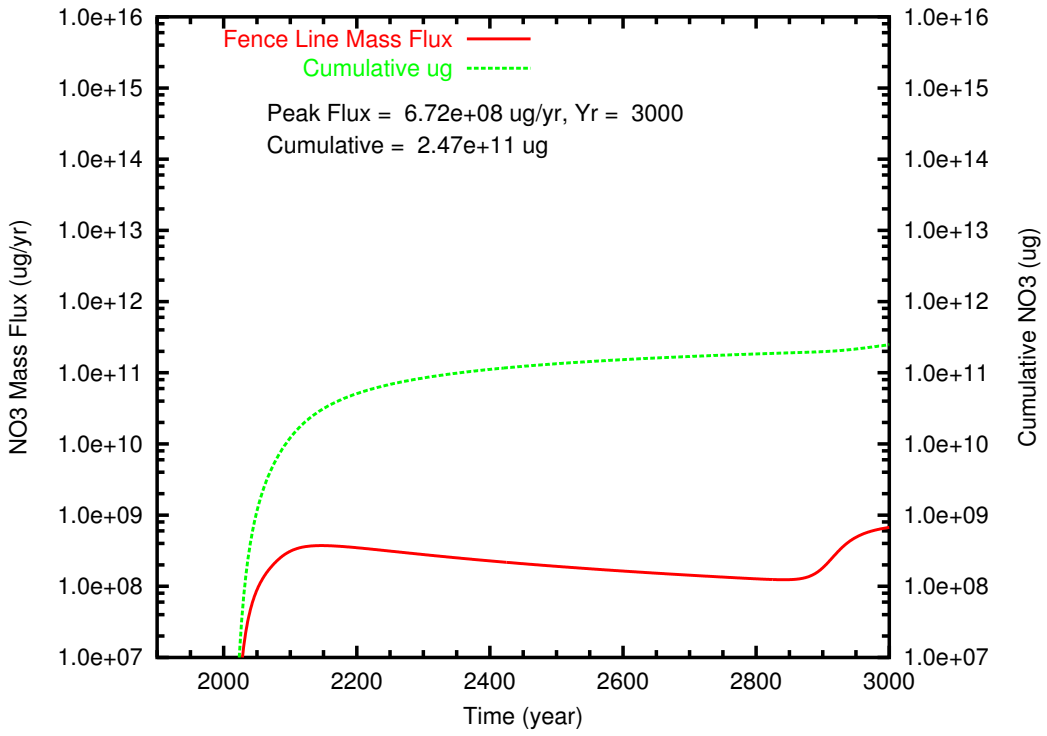

Figure D.47. TX Case 8 $\mathbf{NO_3}$ mass flux and cumulative mass at fenceline

(a)

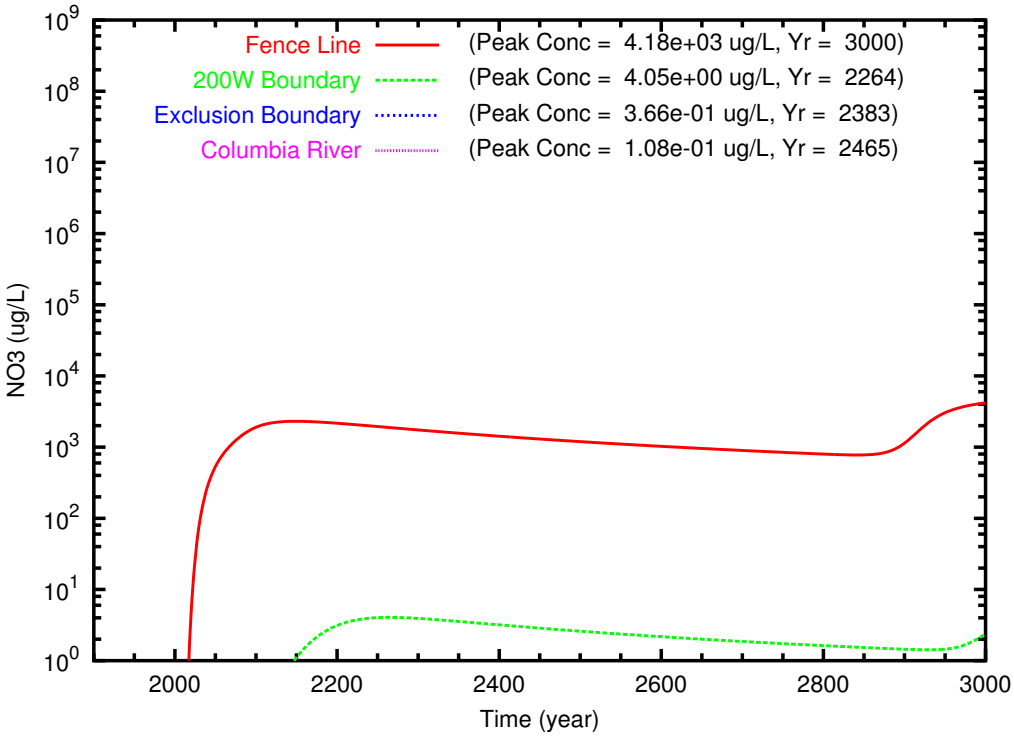

(b)

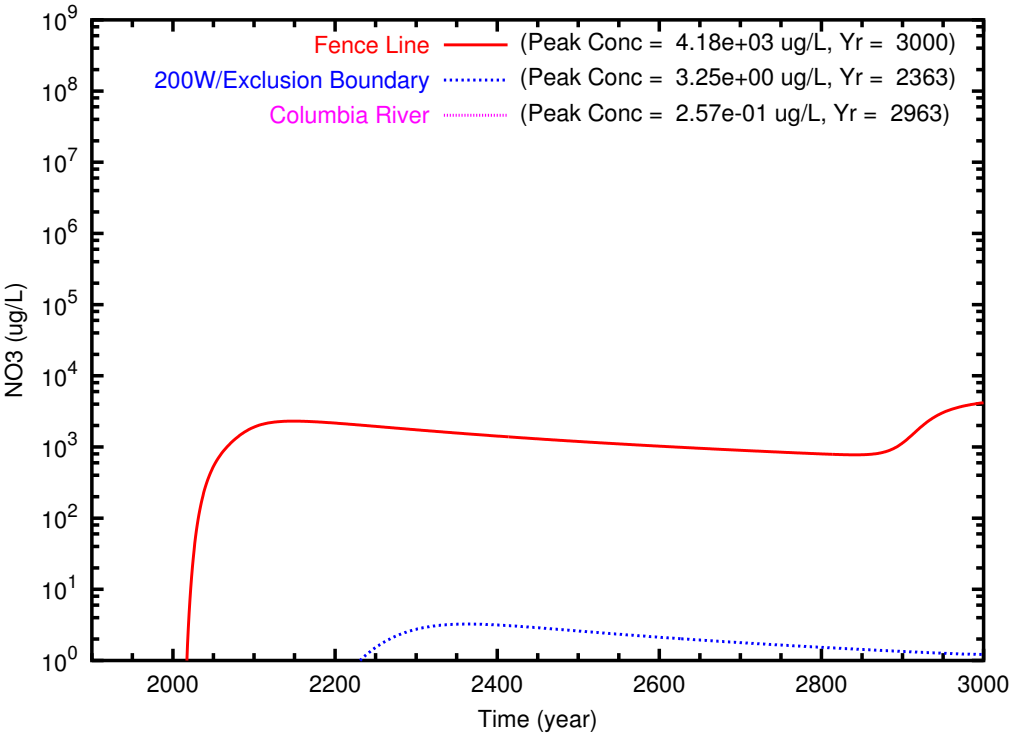

Figure D.48. TX Case 8 **NO_3** breakthrough curves at fenceline and downgradient points along (a) east path and (b) north path

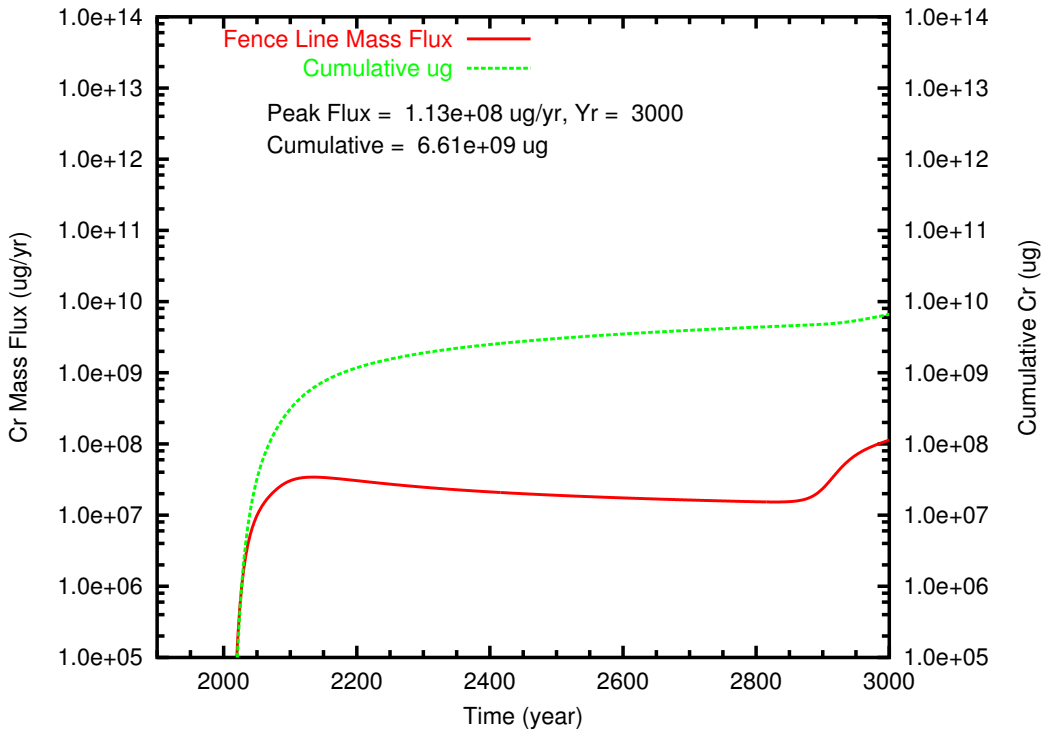

Figure D.49. TX Case 8 **Cr** mass flux and cumulative mass at fenceline

(a)

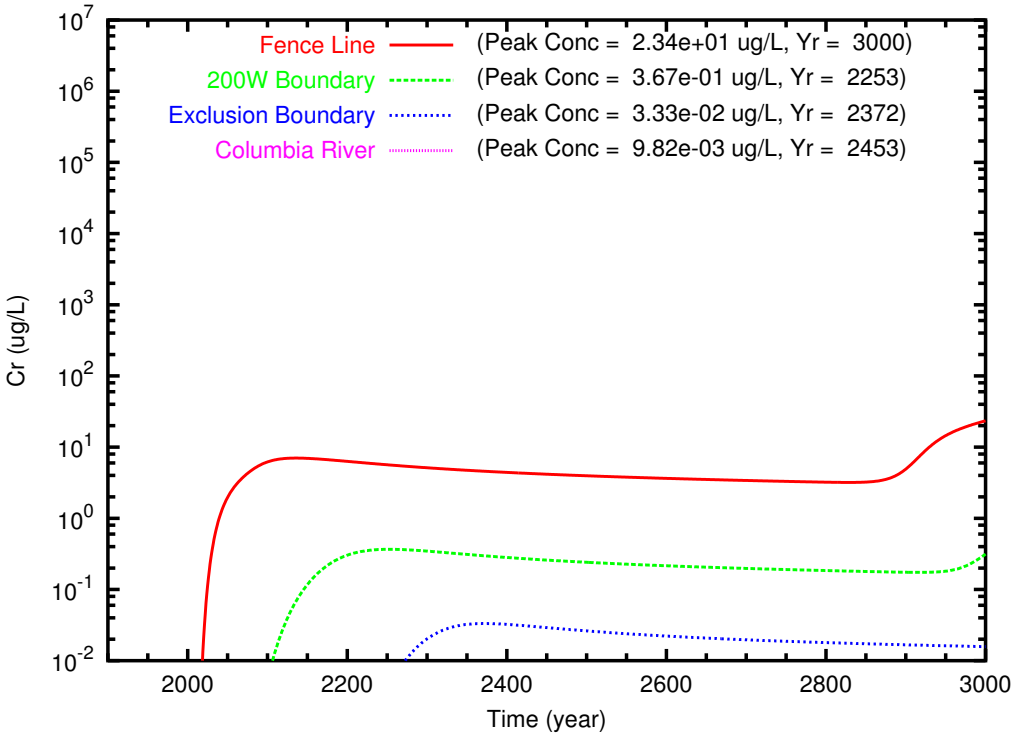

(b)

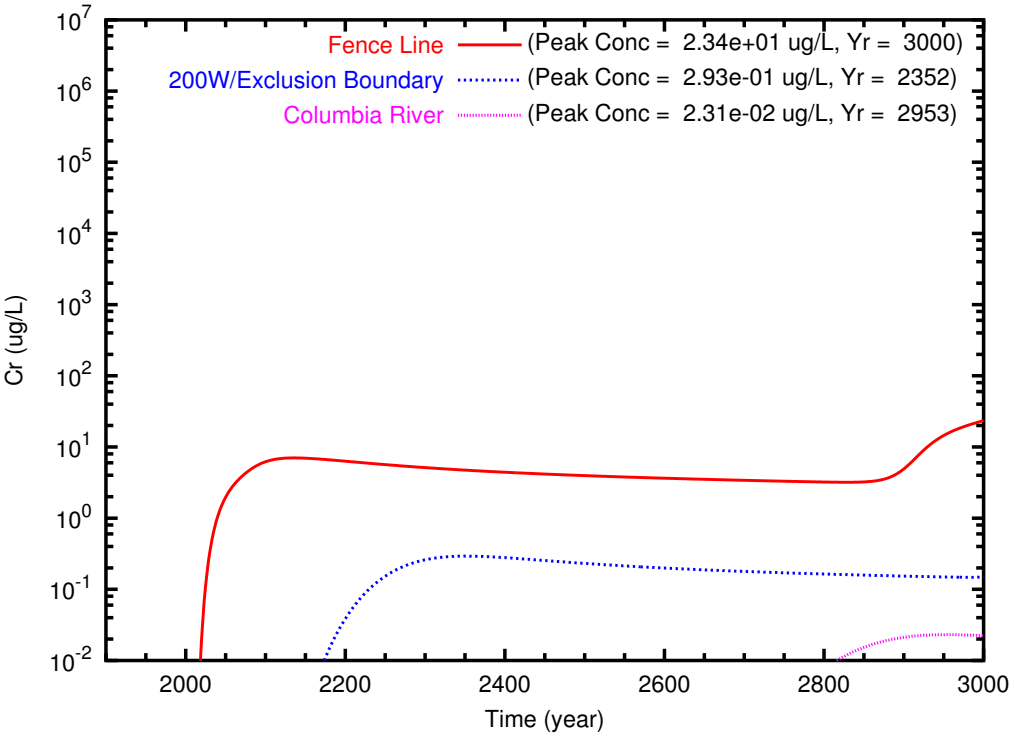

Figure D.50. TX Case 8 **Cr** breakthrough curves at fenceline and downgradient points along (a) east path and (b) north path

Distribution

No. of Copies

Onsite

3 Fluor Federal Services

R. Khaleel E6-17

5 CH2M-HILL Group, Inc.

F.J. Anderson E6-35

8 Pacific Northwest National Laboratory

Z.F. Zhang (3)	K9-36
V.L. Freedman	K9-36
S.R. Waichler	K9-36
M.P. Bergeron	K9-36
Information Release (2)	K1-06